

HZDR-022

BRILLIANT RADIATION SOURCES BY LASER-PLASMA ACCELERATORS AND OPTICAL UNDULATORS

Alexander Debus

Wissenschaftlich-Technische Berichte
HZDR-022 · ISSN 2191-8708

**WISSENSCHAFTLICH-
TECHNISCHE BERICHTE**

hZDR



**HELMHOLTZ
ZENTRUM DRESDEN
ROSSENDORF**

Druckausgabe: ISSN 2191-8708

Elektronische Ausgabe: ISSN 2191-8716

Die elektronische Ausgabe erscheint unter Creative Commons License (CC BY-NC-ND):

Qucosa: <http://fzd.qucosa.de/startseite/>

Die vorliegende Arbeit wurde sowohl als Dissertation an der Fakultät Mathematik und Naturwissenschaften der Technischen Universität Dresden, sowie als Wissenschaftlich-Technischer Bericht des Helmholtz-Zentrum Dresden-Rossendorf mit der Berichtsnummer **HZDR-022** veröffentlicht.

2012

Herausgegeben vom

Helmholtz-Zentrum Dresden-Rossendorf e.V.

Postfach 51 01 19

D-01314 Dresden

Bundesrepublik Deutschland/Germany



Dissertation

Brilliant radiation sources by laser-plasma accelerators and optical undulators

Eingereicht von

Alexander Debus, M.A.

geboren am 23.05.1980 in Heilbronn-Neckargartach

zur Erlangung des akademischen Grades

Doctor rerum naturalium (Dr. rer. nat.)

vorgelegt der

Fakultät Mathematik und Naturwissenschaften
der Technischen Universität Dresden

Die Dissertation wurde in der Zeit von 9/2007 bis 9/2011 am
Helmholtz-Zentrum Dresden-Rossendorf im Institut für Strahlenphysik angefertigt.

Erster Gutachter

Prof. Dr. Roland Sauerbrey

Zweiter Gutachter

Prof. Dr. Jan-Michael Rost

Eingereicht am

7. Oktober 2011

Tag der Verteidigung

18. April 2012

This work is dedicated to my parents.

"Let's think the unthinkable, let's do the undoable, let us prepare to grapple with the ineffable itself, and see if we may not eff it after all."

Douglas Adams

Author of the *Hitchhiker's guide to the Galaxy*
Quotation from *Dirk Gently's Holistic Detective Agency*

ZUSAMMENFASSUNG

Die vorliegende Arbeit beschäftigt sich in Experiment und Theorie mit Laser-Plasma beschleunigten Elektronen und optischen Undulatoren zur Erzeugung von brillianter Synchrotronstrahlung. Zum ersten Mal wird experimentell nachgewiesen, dass laserbeschleunigte Elektronenpulse kürzer als 30 fs sind. Ferner werden solche Elektronenpulse erstmalig in einem Demonstrationsexperiment durch einen magnetischen Undulator als Synchrotronstrahlenquelle genutzt.

Aufbauend auf diesen experimentellen Erkenntnissen, sowie umfangreichen numerischen Simulationen zur Thomsonstreuung, werden die theoretischen Grundlagen einer neuartigen Interaktionsgeometrie für Laser-Materie Wechselwirkungen entwickelt. Diese neue, in der Anwendbarkeit sehr allgemeine Methode basiert auf raum-zeitlicher Laserpulsformung durch nicht-lineare Winkeldispersion wie diese durch VLS- (*varied-line spacing*) Gitter erzeugt werden kann und hat den Vorteil nicht durch die Fokussierbarkeit des Lasers (Rayleighlänge) begrenzt zu sein. Zusammen mit laserbeschleunigten Elektronen ermöglicht dieser *traveling-wave Thomson scattering* (TWTS) benannte Ansatz neuartige, nur auf optischer Technologie basierende Synchrotronstrahlenquellen mit Zentimeter bis Meter langen optische Undulatoren. Die hierbei mit existierenden Lasern erzielbaren Brillianzen übersteigen diese bestehender Thomsonquellen-Designs um 2-3 Größenordnungen.

Die hier vorgestellten Ergebnisse weisen weit über die Grenzen der vorliegenden Arbeit hinaus. Die Möglichkeit Laser als Teilchenbeschleuniger und auch optischen Undulator zu verwenden führt zu bauartbedingt sehr kompakten und energieeffizienten Synchrotronstrahlungsquellen. Die hieraus resultierende monochromatische Strahlung hoher Brillanz in einem Wellenlängenbereich von extremen ultraviolett (EUV) zu harten Röntgenstrahlen ist für die Grundlagenforschung, medizinische Anwendungen, Material- und Lebenswissenschaften von fundamentaler Bedeutung und wird maßgeblich zu einer neuen Generation ultrakurzer Strahlungsquellen und freien Elektronenlasern (FELs) beitragen.

ABSTRACT

This thesis investigates the use of high-power lasers for synchrotron radiation sources with high brilliance, from the EUV to the hard X-ray spectral range. Hereby lasers accelerate electrons by laser-wakefield acceleration (LWFA), act as optical undulators, or both. Experimental evidence shows for the first time that LWFA electron bunches are shorter than the driving laser and have a length scale comparable to the plasma wavelength. Furthermore, a first proof of principle experiment demonstrates that LWFA electrons can be exploited to generate undulator radiation.

Building upon these experimental findings, as well as extensive numerical simulations of Thomson scattering, the theoretical foundations of a novel interaction geometry for laser-matter interaction are developed. This new method is very general and when tailored towards relativistically moving targets not being limited by the focusability (Rayleigh length) of the laser, while it does not require a waveguide.

In a theoretical investigation of Thomson scattering, the optical analogue of undulator radiation, the limits of Thomson sources in scaling towards higher peak brilliances are highlighted. This leads to a novel method for generating brilliant, highly tunable X-ray sources, which is highly energy efficient by circumventing the laser Rayleigh limit through a novel traveling-wave Thomson scattering (TWTS) geometry. This new method suggests increases in X-ray photon yields of 2-3 orders of magnitudes using existing lasers and a way towards efficient, optical undulators to drive a free-electron laser.

The results presented here extend far beyond the scope of this work. The possibility to use lasers as particle accelerators, as well as optical undulators, leads to very compact and energy efficient synchrotron sources. The resulting monoenergetic radiation of high brilliance in a range from extreme ultraviolet (EUV) to hard X-ray radiation is of fundamental importance for basic research, medical applications, material and life sciences and is going to significantly contribute to a new generation of radiation sources and free-electron lasers (FELs).

CONTENTS

1	Introduction	1
2	Basics of synchrotron radiation and electron acceleration	7
2.1	Undulator radiation	8
2.2	Free-electron lasers	12
2.3	High-power lasers	29
2.4	Thomson scattering radiation	31
2.5	Electron acceleration by Laser wakefields	36
3	Ultrashort electron bunches from laser wakefield-acceleration	49
3.1	Basics of transition radiation	51
3.2	Electro-optical experiment for measuring the electron bunch duration	54
3.3	Limitations in resolution	57
3.4	Ab-initio transition radiation modeling of the experiment	61
3.5	Error analysis using Monte-Carlo methods	63
3.6	Measured electron bunch durations	64
3.7	Complementary approaches: spectroscopic determination of the bunch duration	65
3.8	Synchrotron radiation from laser-wakefield accelerated electrons	71

4 Thomson scattering – Lasers as optical undulators	79
4.1 Numerical modeling of Thomson scattering	80
4.2 Non-ideal effects	84
4.3 High-repetition Thomson sources for high average photon yields	88
4.4 Single-shot Thomson sources with ELBE and laser-wakefield accelerated beams .	97
5 Scalable optical undulators with traveling-wave Thomson scattering	105
5.1 Photon yield limitations in head-on Thomson scattering geometries	106
5.2 Traveling-wave Thomson scattering	108
5.3 Experimental approaches and constraints	110
5.4 Theoretical Tools for designing VLS gratings	117
5.5 Interaction distances using VLS gratings – calculation results	119
5.6 Scaling for incoherent TWTS sources	122
5.7 Traveling-wave Thomson scattering FEL	125
5.8 Outlook on traveling-wave Thomson scattering	133
6 Conclusions	137
A Ray-tracing of VLS gratings	141
Bibliography	147

1 INTRODUCTION

New light sources have consistently driven progress in science. On the one hand X-ray light sources based on electron synchrotrons have developed into indispensable tools in many fields of natural science, medicine and engineering, revealing the inner structure of atoms, molecules and solids. On the other hand, the invention of the laser in the 1960s [1] as a bright, coherent light source has triggered a revolution in optics, has become ubiquitous and permeates everyday life. Since the 1960s laser intensities have increased by more than ten orders of magnitudes to about 10^{21} – 10^{22} **W/cm²** today. With the advent of chirped laser pulse amplification [2, 3] it became possible to attain peak laser powers up to the terawatt and petawatt range. In fact today's laser powers can be used to ionize matter, create plasmas and accelerate electrons to relativistic energies.

This rapid progress in laser technology and pump-probe diagnostics has led to a growing interest in combining ultrafast lasers and X-ray pulses [4] to examine processes on the femtosecond time scales that are characteristic for atoms and molecules. Main drivers of this development are electron linac driven X-FEL projects, such as FLASH, XFEL and LCLS. Yet, smaller scale projects providing tunable ultrafast X-ray sources on a closer time horizon and for de-centralized research could significantly enrich the scientific landscape. In most of the scenarios under discussion, ultrafast Thomson scattering sources using high power lasers play a dominant role, either using electrons from small-scale linear accelerators [5–9] or laser wakefield accelerators (LWFA) [10–14] providing compact and low emittance electron bunches [15–20].

The aim of this work is to combine laser and accelerator technology to realize synchrotron light sources that give access to ultrashort brilliant X-ray sources that enable temporal and spatial resolutions, both on **fs** temporal and **sub-nm** spatial scales. Hereby, the laser acts either as a particle accelerator, as an optical undulator, or both. The vision is synchrotron light sources as table-top devices that are less expensive and more readily available both for research and industry than large sources based on conventional accelerators.

In fundamental research, ultrashort, monoenergetic X-ray sources of high-efficiency are important for examining atomic and nuclear processes on ultrafast time scales. These could also be

used for X-ray backlighting in time-resolved diagnostics of warm-dense matter in inertial confinement fusion plasmas or pulsed positron production. A compact, laser-driven synchrotron radiation source is interesting for phase-contrast X-ray imaging in medicine and material sciences and Thomson-based sources used in semiconductor industry could provide a debris-free, collimated EUV source, fully compatible with high-vacuum environments.

LASERS AS PARTICLE ACCELERATORS

In order to accelerate electrons over short distances, Tajima and Dawson [21] proposed to use lasers to excite a charge density wave within a plasma, which travels with almost the speed of light behind the laser. The extreme axial field gradients that are generated are of excess 100 GV/m [10], which is 3-4 orders of magnitudes more than available in today's conventional accelerators, where the maximum accelerating gradient is limited by the break down field of the accelerating cavities (50 – 150 MV/m) [22, 23]. A plasma on the other hand which is already fully ionized can sustain much higher fields.

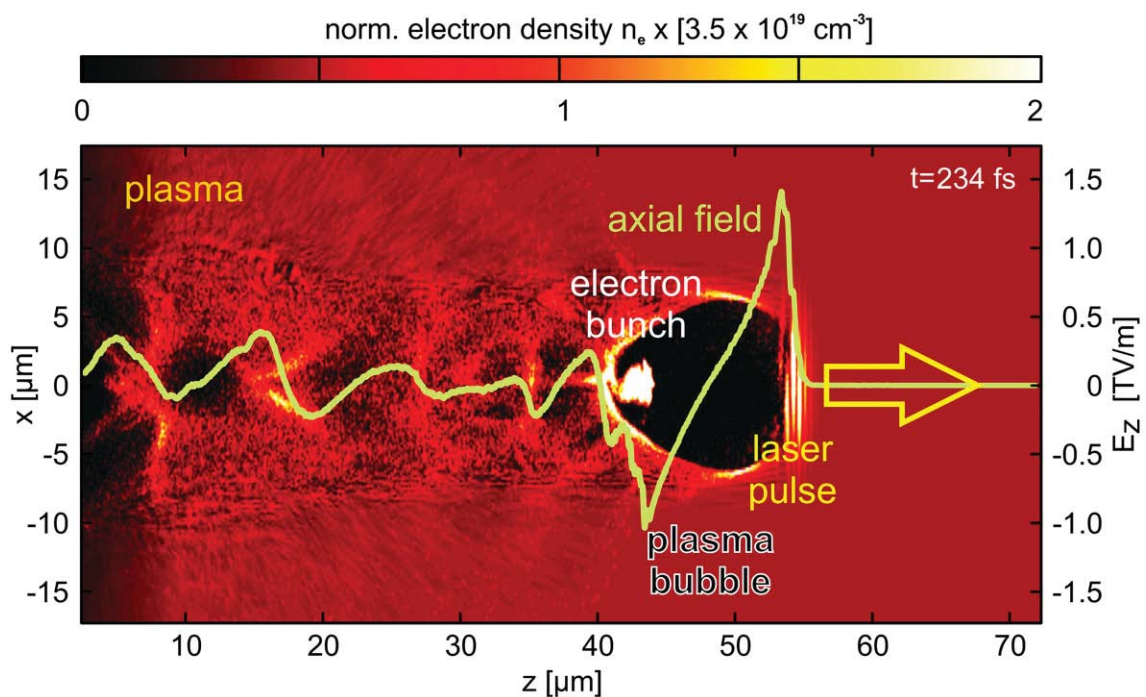


Figure 1.1: Cross-section output of the electron density on the axis of laser propagation from 3D Particle-in-Cell simulation (ILLUMINATION) showing a snapshot of a laser-generated plasma. The laser pulse has excited a comoving, nonlinear charge-density wave (“bubble”) in the plasma. This structure provides a high, on axis electric field $E_z(z)$ (green) on the order of TV/m for electron acceleration. The electron bunch inside that acceleration gradient has originated from the backside of the bubble through wavebreaking and subsequent self-injection.

Such a plasma-based acceleration scheme is depicted in Fig. 1.1, where the laser drives a plasma wave. In this wave electrons can be injected either by wavebreaking [15–17], optical [24] or external injection [25], which are then accelerated by the field until the electrons either outrun the wave or the accelerated electrons leave the plasma, when the plasma terminates. With

these mechanisms it is possible to accelerate electrons up to **GeV** energies over **cm** distances [18], which makes this a compact accelerator with the highest acceleration gradients realized by mankind.

What makes these electron bunches unique are its small dimensions, which are generally comparable to the laser focal spot in diameter and the plasma period in length, which is on the order of μm [26–28]. Due to this small source size, the normalized emittances and electron pulse durations are expected to be about one order of magnitude smaller than those achievable by today’s conventional accelerators [10, 29].

LASERS AS OPTICAL UNDULATORS

Such small source size and short duration make these electron bunches particularly interesting for secondary radiation sources. By undulators or a counterpropagating laser the electrons in the bunch undergo a wiggling motion and thus emit synchrotron radiation into a narrow forward angle cone $\sim 1/\gamma$ at a wavelength $\simeq \lambda_0/2\gamma^2$. According to electron energies the resulting radiation can reach far into the X-ray regime to hard radiation at **keV** and **MeV** energies. The ultrashort time-scale on the order of **fs** of these X-ray flashes potentially leads to peak brilliances that are competitive with advanced and large-scale accelerators.

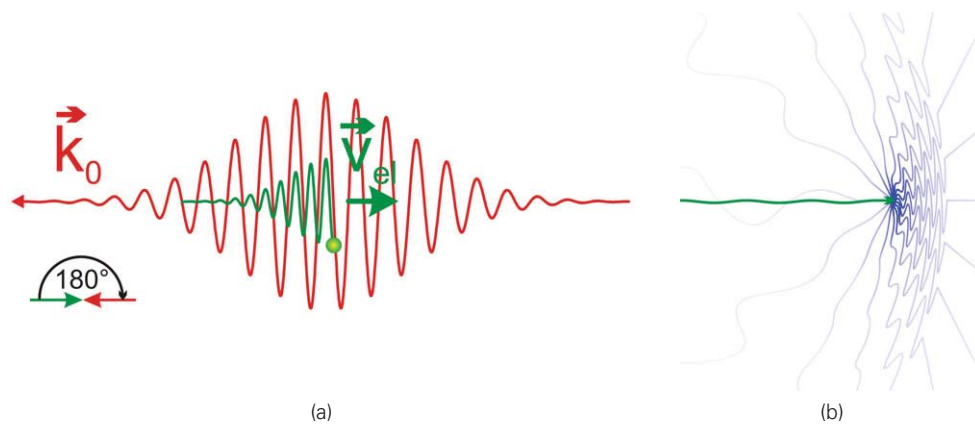


Figure 1.2: (a) A laser (red field) scatters at an ultrashort, relativistic electron (green trajectory) at $\gamma = 2$, thus acting as an optical undulator. (b) In that process the electron (green) emits an ultrashort, bright X-ray flash (blue). The blue field lines depict the radiation field originating from the electron.

The quantity of the peak brilliance

$$B_{\text{phot}} = \frac{N_p}{\tau_{\text{beam}} \cdot \Delta A[\text{mm}^2] \cdot \Delta\Omega[\text{mrad}^2] \cdot (\Delta E/E_{\text{phot}})[0.1\%]} \quad (1.1)$$

is used as to compare photon sources, such as X-ray beams from third-generation synchrotrons or free-electron lasers. Here, N_p denotes the total photon number, $\Delta E/E_{\text{phot}}$ the relative spread in photon energy and τ_{beam} the X-ray pulse duration. The area and the solid angle from which the radiation originates are ΔA and $\Delta\Omega$ respectively. The higher the number, the higher the phase

space resolution for experiments, and since phase space volume is a conserved quantity in ideal imaging systems, that number is a useful indicator on experimental trade-offs with regard to the photon source.

Fig. 1.3 shows the peak brilliance of a number of synchrotrons and free-electron lasers. Laser-accelerated electrons combined with a small-scale undulator could potentially be used to drive an FEL. Since the laser would be the largest part of such a *table-top FEL* [30], the main benefit compared to a conventional FEL would be the large size reduction in required infrastructure. The costs of such a laser-driven FEL would be by 1-2 orders of magnitudes lower – on a scale below 10 Mio EUR, rather than several 100 million EUR for a linac-driven FEL.

Thomson scattering sources on the other hand have the potential to become the brightest sources available in the hard X-ray range beyond 100 keV. There already exist several projects, such as PLEIADES [7, 31], T-REX and MEGa-Ray [32] that aim for a Thomson source, based on electrons from linear accelerators. The MEGa-Ray design goal of $1.5 \times 10^{21} \text{ mm}^2 \text{ mrad}^2 \text{ s}^{-1}$ at 2 MeV would constitute the world brightest source in that range. However, all current Thomson scattering designs are limited in peak brilliance (red line in Fig. 1.3) by the onset of nonlinear Thomson scattering [33] at laser intensities beyond 10^{17} W/cm^2 , which negatively affects the small spectral bandwidth of the X-ray pulse.

THESIS OUTLINE

This work focuses on how lasers can advance both electron beams and synchrotron sources to boost the overall photon yields of ultrashort X-ray sources of high brilliance. Experimentally, first experimental proof of laser accelerated electron bunches being shorter than the drive laser pulse, but comparable to the plasma wavelength is presented. Furthermore, the first synchrotron light source realized by such laser-accelerated electrons is shown. On a theoretical side the emphasis is shifted towards the laser as an optical undulator. It is shown that present Thomson scattering designs using high-power lasers have fundamental scaling issues, that make high-yield Thomson sources prohibitively expensive. As a way to avoid these limitations, a novel traveling-wave Thomson scattering (TWTS) scheme is presented, which not only boosts per shot photon numbers by several orders of magnitudes (Fig. 1.3), but also provides the possibility of obtaining coherent light sources.

With high-power lasers becoming a versatile tool as both electron source and optical undulator, this leads to a broad range of applications: from ultrashort, all-optical pink-beam sources with tunability at X-ray energies for pump-probe studies, to debris-free radiation sources operating at high-average photon fluxes in the extreme ultraviolet (EUV).

As a guide to the reader, the thesis is organized as follows: Chapter 2 provides a brief digest on the radiation physics required in the following chapters, as well as some basics on laser-plasma wakefield accelerators. In chapter 3 the experiment measuring the electron bunch duration through electro-optic detection of transition radiation in the time-domain is shown. Chapter 4 then shifts the focus on the laser, where head-on Thomson scattering is the optical analogue of

an undulator. First non-ideal effects and the simulation code CLARA for modeling Thomson scattering are introduced and, second, simulation results for high-average power, as well as high-peak power sources are presented. Chapter 5 explains how to eliminate scaling limitations of Thomson scattering discussed in the previous chapter by a novel traveling-wave Thomson scattering (TWTS) method and describes its consequences for both Thomson sources and potential free-electron lasers based on optical undulators. In the conclusion future directions and consequences beyond this work are touched.

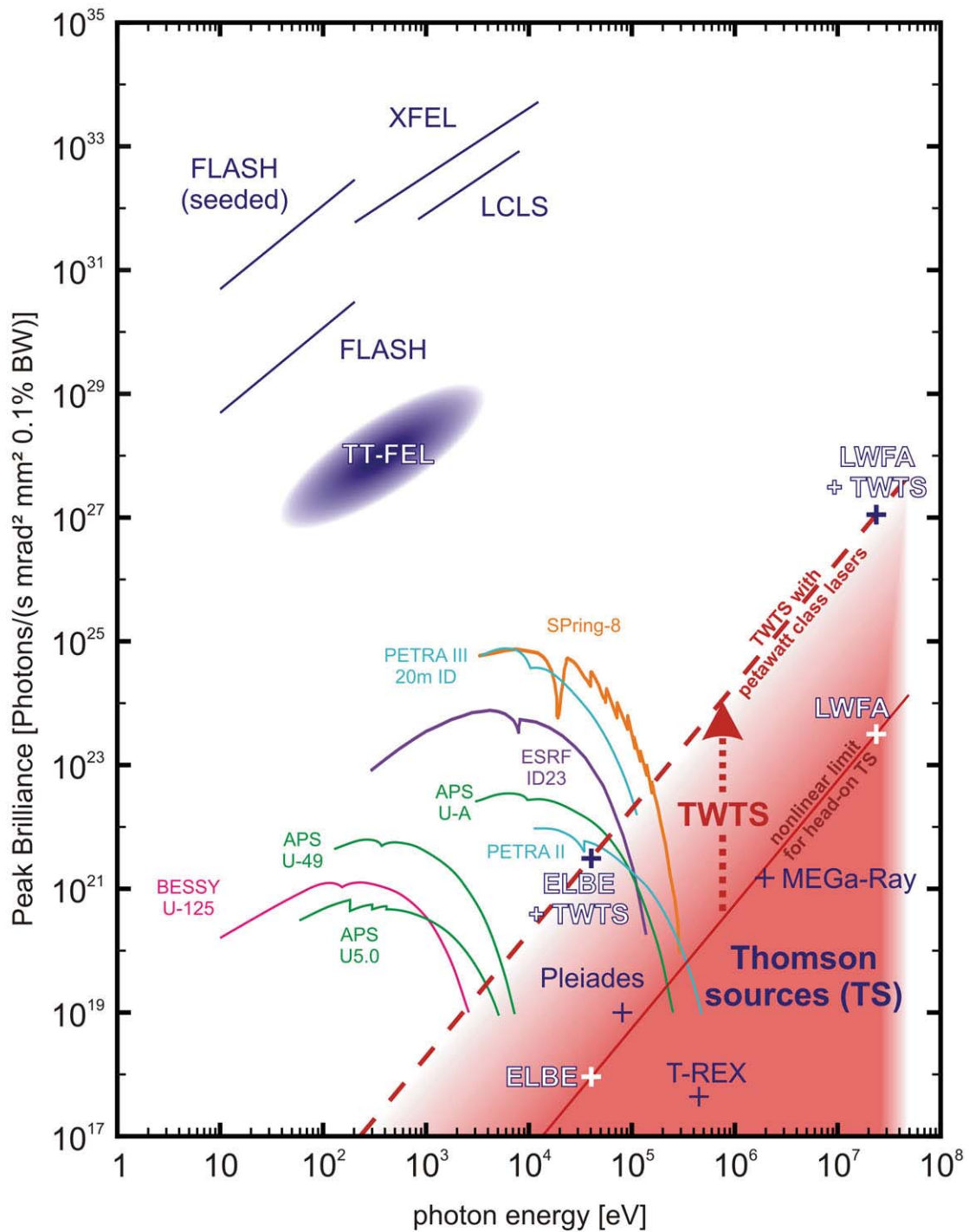


Figure 1.3: Compares synchrotron, FEL and laser-driven X-ray sources by peak brilliance. Table-top free-electron lasers driven by laser wakefield accelerated electrons (TT-FELs) could become interesting as soon as electron energy spread improves. At high X-ray energies, where Thomson sources are the brightest sources to date, the nonlinear Thomson regime so far limits brilliances to or below the red line. The new traveling-wave Thomson scattering geometry circumvents this bottleneck (dashed line), such that peak brilliance is only limited by laser power and electron focusability.

2 BASICS OF SYNCHROTRON RADIATION AND ELECTRON ACCELERATION

According to (1.1) the *peak spectral brightness* or *brilliance*, of a light source is defined as a photon number density over phase-space, emission duration and the radiated energy spectrum. Therefore, brilliant light sources are favorably directed, ultrashort, monochromatic and originate from a small spatial region.

At optical frequencies, high-power lasers are the prime example for such light sources. Current petawatt class lasers at 800 nm and 100 fs duration achieve brilliances

$$B_{\text{laser}} = \frac{P[\text{W}]/(\hbar\omega)}{\lambda^2[\mu\text{m}] \cdot \Delta\omega/\omega[0.1\% \text{BW}]} \quad \text{on the order of } 10^{33} - 10^{34} \text{ mm}^{-1} \text{ mrad}^{-2} \text{ s}^{-1} [0.1\% \text{BW}]. \quad (2.1)$$

In the X-ray range however, where the shorter radiative life times of excited states, as well as the scarcity in X-ray pump-light sources make amplified stimulated emission schemes largely impracticable, brilliant X-ray sources are obtained by synchrotron radiation from particle accelerators, such as PETRA III, ESRF, LCLS or Spring-8. Here, relativistically moving electrons are accelerated by electric or magnetic fields. Analogous to the example of the Hertzian dipole, this acceleration and the finite speed of light leads to emission of classical radiation. The main feature though, is that synchrotron sources exploit special relativity. On the one hand the Doppler effect experienced by the relativistic charge with respect to the accelerating field gives rise to a massive blueshift in the emitted radiation, which often ends up in the X-ray range. The “searchlight effect” on the other hand causes the radiation to be directed primarily into a narrow angle cone around the direction of the moving charge. This is the physical basis for virtually all brilliant X-Ray sources at high energies.

Following the aim of this work, which is using high-power lasers for brilliant, potentially all-

optical X-ray sources, first the basic physics of synchrotron radiation with emphasis on undulators and free-electron lasers (FELs) is reviewed. Then, the laser-driven electron accelerators and optical undulators are introduced and discussed with respect to advantages and challenges in experiment.

2.1 UNDULATOR RADIATION

Undulator or wiggler radiation is one of the most common types of synchrotron radiation and can be found in almost all synchrotron facilities. It is emitted when an relativistic electron beam passes through a static magnetic field with spatial periodicity. In practice, undulators are realized by a linear succession of electric or permanent magnets that are positioned consecutively with alternating north-south orientations. The electrons that pass through an undulator undergo a wiggling motion perpendicular to their direction of flight and, due to the relativistic Doppler upshift, emit high-energy radiation into a narrow angle cone into the electron direction of propagation.

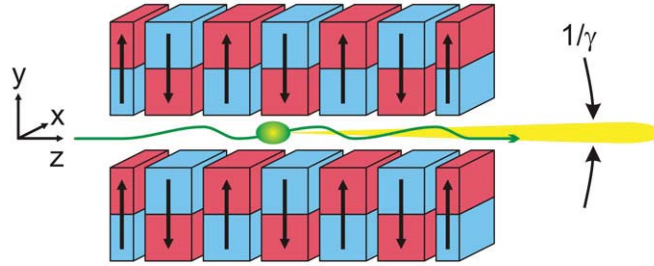


Figure 2.1: An undulator provides an alternating magnetic field with a period of λ_u with a gap g between the magnets for an electron to pass through. This magnetic field causes an electron passing along the undulator axis to undergo an oscillating motion according to the Lorentz force (2.5). Analogues to classic dipole radiation, an electro-magnetic wave is emitted. The relativistic motion of the electron $\gamma \gg 1$ gives rise to the search light effect, which is forward emission into a narrow $1/\gamma$ cone and the Doppler effect, a massive contraction by $\sim (2\gamma)^{-1}$ of the radiated wavelength λ_r with respect to the undulator period λ_u .

In the following, expressions for the energy radiated by a single relativistic electron in a planar undulator are derived. The undulator magnetic field $\mathbf{B}(y, z) = B_x(y, z)\mathbf{e}_x + B_y(y, z)\mathbf{e}_y$ with an undulator period of λ_u , a gap g between the magnet poles and a maximum field \hat{B} without a gap can be approximated by [1]

$$B_y(y, z) = \frac{\hat{B}}{\cosh(k_u g/2)} \cosh(k_u y) \cos(k_u z) \quad (2.2)$$

$$B_x(y, z) = \frac{\hat{B}}{\cosh(k_u g/2)} \sinh(k_u y) \cos(k_u z), \quad (2.3)$$

where $k_u = 2\pi/\lambda_u$. More specifically, the magnetic field on the z-axis is given by

$$\mathbf{B}(0, z) = \underbrace{\frac{\hat{B}}{\cosh(k_u g/2)}}_{B_0} \cos(k_u z) \mathbf{e}_y. \quad (2.4)$$

For relativistic electrons, velocity and momentum are customary written as normalized, dimensionless quantities. The velocity is normalized with respect to the speed of light $\boldsymbol{\beta} = \mathbf{v}/c$ and the relativistic momentum $\mathbf{p} = \gamma \cdot m\mathbf{v} = \gamma mc\boldsymbol{\beta}$ with the Lorentz factor $\gamma = 1/\sqrt{1 - \beta^2}$ is normalized to mc . Hence, the normalized relativistic momentum is defined as $\mathbf{u} = \gamma\boldsymbol{\beta}$.

For an electron moving along this axis with relativistic speeds $\gamma_0 \gg 1$, integration of (2.4) according to the equation of motion

$$\frac{d}{dt}(\gamma mc\boldsymbol{\beta}) = e \left(\underbrace{\mathbf{E}}_{=0} + c\boldsymbol{\beta} \times \mathbf{B} \right), \quad (2.5)$$

yields for $u_x \ll 1$ the normalized longitudinal and transversal velocities

$$\beta_x(t) = \frac{K}{\gamma_0} \cos(k_u \underbrace{c\beta_0 t}_{\simeq z(t)}) \quad (2.6)$$

$$\beta_z(t) = \underbrace{\beta_0 \left(1 - \frac{K^2}{4\gamma_0^2} \right)}_{\bar{\beta}_z} - \frac{K^2}{4\gamma_0^2} \cos(2k_u c\beta_0 t) \quad (2.7)$$

and the time-dependent coordinates of the electron

$$x(t) = \frac{K}{k_u \gamma} \sin(k_u c\beta_0 t) \quad (2.8)$$

$$z(t) = \beta_0 \left(1 - \frac{K^2}{4\gamma_0^2} \right) c\beta_0 t - \frac{K^2}{8k_u \gamma_0^2} \sin(2k_u c\beta_0 t) \quad (2.9)$$

and thus its trajectory. The dimensionless undulator strength parameter is defined as

$$K = \frac{|e|B_0\lambda_u}{2\pi mc} = 0.934 \cdot B_0[\text{T}]\lambda_u[\text{cm}], \quad (2.10)$$

which according to (2.6) denotes the maximum normalized momentum $u_x = \gamma\beta_{x,\text{max}} = K$ in transverse direction. This is equivalent to stating that for K approaching unity the kinetic energy of the transverse electron oscillation becomes comparable to the electron rest energy mc^2 . Since magnetic fields do no work, but merely exert Lorentz forces perpendicular to the electron velocity, an undulator field cannot increase the transverse velocity of an electron without at the same time reducing its velocity along the undulator axis. As a result, the mean electron velocity $\bar{\beta}_z = \beta_0(1 - K^2/(4\gamma^2))$ on axis (see (2.7)) is reduced. In order to be consistent with an equivalent description later in laser-electron dynamics (ch. 2.3), this effect is named the *photon drag*. The longitudinal oscillation frequency $2k_u c\beta_0$ is twice the undulator frequency, because transverse deflections in any direction reduce the on axis velocity β_z . Hence, the initial assumption of $z(t) \simeq c\beta_0 t$ does not hold anymore for large oscillation amplitudes $x(t)$, when K approaches values of unity or greater.

This leads to the distinction between the linear undulator regime $K \ll 1$, where all motions are sinusoidal, as in (2.6) and (2.9), and the so called wiggler regime for $K \gg 1$, where above equations are not valid anymore.

More specifically, the large K -parameter of a wiggler leads to a spectral and angular radiation profile that strongly differs from the monoenergetic spectrum expected for a simple harmonic os-

cillation of an electron in an undulator, as in 2.2(d). Not only does the decreased on-axis velocity $\bar{\beta}_z$ cause a redshift of the entire radiated spectrum, but due to the oscillation in $z(t)$, the electron motion becomes anharmonic. The radiation spectra arising from these anharmonic electron trajectories are broad and consist of many higher harmonics, see Fig. 2.2(e). Also, the radiation cone widens in the plane of electron oscillations. For $\gamma \gg 1$, the maximum angle of the electron with respect to its axis of propagation is given by $\tan \alpha = \beta_{x,\max}/\bar{\beta}_z \simeq K/\gamma_0$, which shows that wigglers $K \gg 1$ radiate into a larger solid angle cone than undulators with $1/\gamma_0$.

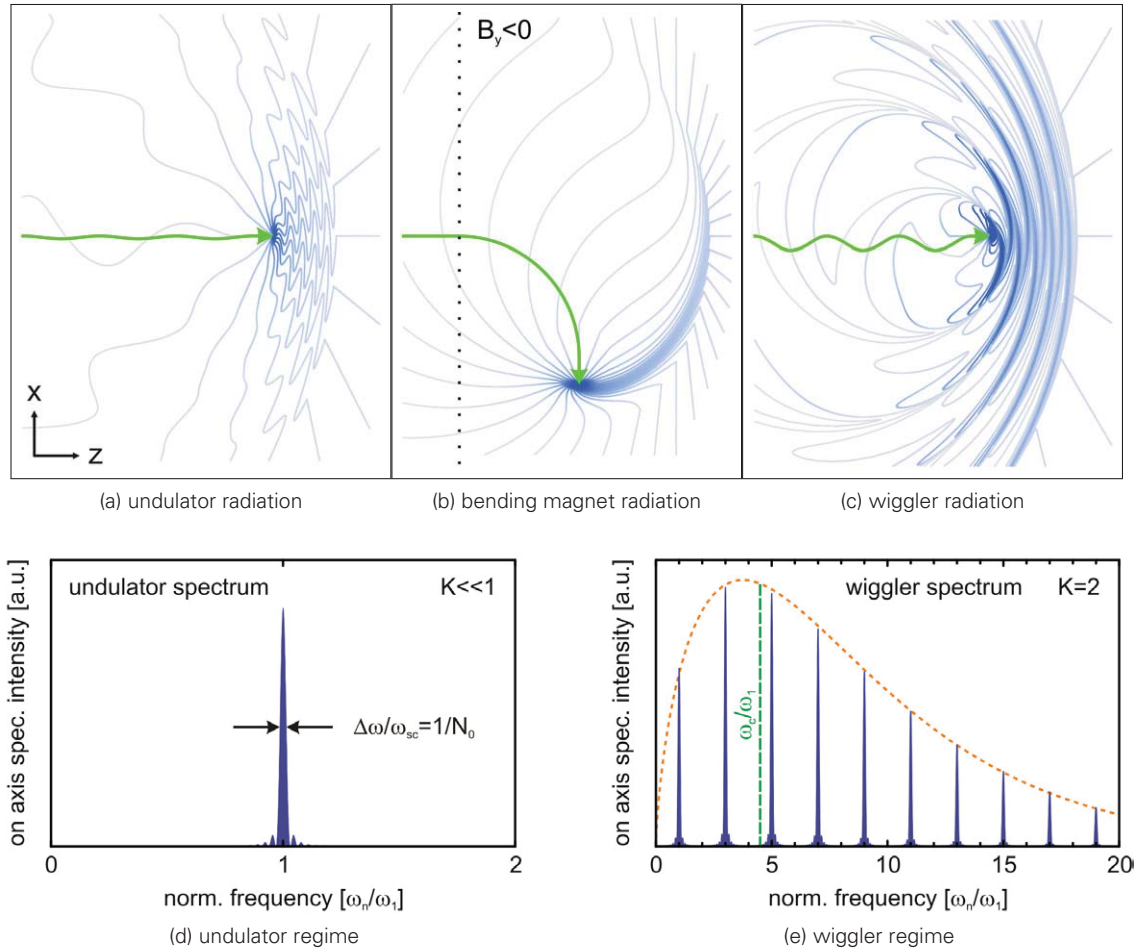


Figure 2.2: (a)-(c) compares the electric field lines of a single relativistic electron at $\gamma_0 = 2$ (green) in the near field after passing through (a) a five-period undulator ($K = 0.2$), (b) a bending magnet and (c) a wiggler ($K = 1.0$). In the undulator, the electric field lines feature sinusoidal oscillations. The bending magnet gives rise to an electromagnetic shock-front, whereas a wiggler with its large electron oscillation amplitudes acts like a series of bending magnets. (d-e) depict the resulting on-axis spectra of (d) the undulator, which radiates only at the fundamental $\omega_{sc} = \omega_0 \cdot 2\gamma_0^2$ and (e) shows the corresponding multi-harmonic spectrum for a wiggler. The red dotted curve depicts the broad bending magnet spectrum, corresponding to the same critical frequency (green) as the wiggler. Both curves are normalized to the same maximum spectral amplitude.

The resulting undulator spectrum in the far field from a single electron can be derived by integrating (2.6) and (2.7) over N_0 undulator periods, using the classical, relativistic radiation formula

from Jackson [2]

$$\frac{d^2 W}{d\omega d\Omega} = \frac{e^2}{4\pi^2 c} \left\| \int_{-\infty}^{+\infty} \frac{\mathbf{n} \times [(\mathbf{n} - \boldsymbol{\beta}(t)) \times \dot{\boldsymbol{\beta}}(t)]}{(1 - \boldsymbol{\beta}(t) \cdot \mathbf{n})^2} e^{i\omega \overbrace{(t - \mathbf{n} \cdot \mathbf{r}(t)/c)}^{t_{\text{ret}}}} dt \right\|^2. \quad (2.11)$$

Hereby, the detector is assumed to be in a direction of unit vector \mathbf{n} with respect to the electron and $\mathbf{r}(t)$ denotes the electron trajectory. In general the n^{th} harmonic has a wavelength of

$$\lambda_n = \frac{\lambda_u}{2\gamma^2 \cdot n} \left(1 + \frac{K^2}{2} + \gamma^2 \theta^2 \right), \quad (2.12)$$

and a bandwidth of $\Delta\lambda/\lambda_n = 1/(n \cdot N_0)$, where N_0 denotes the number of undulator periods. The observation angle θ is taken between the undulator axis in electron propagation direction and the direction of the observer. In the second factor $K^2/2$ is the photon drag contribution and $\gamma^2 \theta^2$ the off-axis Doppler effect. Both contributions have the effect of a red-shift in wavelength.

When integrating a more general expression [1, 3, 4] without the approximation for $z(t) \simeq c\beta_0 t$ the spectral energy distribution on axis is given by

$$\left. \frac{dW_n}{d\Omega d\omega} \right|_{\theta=0} = \frac{e^2 \gamma_0^2}{4\pi \epsilon_0 c} \cdot F_n(K) \cdot \frac{\sin^2(N_0 \pi (\omega - n\omega_1)/\omega_1)}{(\pi (\omega - n\omega_1)/\omega_1)^2}, \quad (2.13)$$

with

$$\omega_1 = \frac{2\pi c}{\lambda_u} \cdot \frac{(1 + \beta_0) \gamma_0^2}{1 + K^2/2} \quad (2.14)$$

$$F_n(K) = \frac{n^2 K^2}{(1 + K^2/2)^2} \left[J_{(n-1)/2} \left(\frac{nK^2}{4(1 + K^2/2)} \right) - J_{(n+1)/2} \left(\frac{nK^2}{4(1 + K^2/2)} \right) \right]^2, \quad (2.15)$$

where ω_1 denotes the fundamental angular frequency of the emitted radiation and $F_n(K)$, which uses Bessel functions of the first kind $J_m(x)$, comprises the relative amplitudes of the higher harmonics. From basic Fourier transform properties of periodic functions, when considering (2.11) being rescaled to retarded time $t' = t - \mathbf{n} \cdot \mathbf{r}(t)$, one can derive [1, 3, 4] that on axis, only odd harmonics ($n = 1, 3, 5 \dots$) give a contribution, while even harmonics ($n = 2, 4, 6 \dots$) only appear at off-axis angles.

When integrating over the spectrum, the on-axis intensity of scattered radiation becomes

$$\left. \frac{dW_n}{d\Omega} \right|_{\theta=0} = \int \left. \frac{dW_n}{d\Omega d\omega} \right|_{\theta=0} d\omega = \frac{e^2 \gamma_0^2 N_0 \omega_1}{4\pi \epsilon_0 c} \cdot F_n(K), \quad (2.16)$$

The total radiated energy from N_e electrons is

$$W_{\text{tot}} = \int \sum_{n=1}^{+\infty} \left. \frac{dW_n}{d\Omega d\omega} \right|_{\theta=0} d\Omega d\omega = \frac{\pi e^2 K^2 \gamma_0^2 N_e N_0}{3\epsilon_0 \lambda_u} \quad (2.17)$$

and solely for the first harmonic for $K \ll 1$ [4]

$$W_{1,\text{tot}} = \int \left. \frac{dW_1}{d\Omega d\omega} \right|_{\theta=0} d\Omega d\omega = \frac{\pi e^2 \gamma_0^2 N_e N_0}{3\epsilon_0 \lambda_u} \cdot \frac{K^2}{(1 + K^2/2)^2}. \quad (2.18)$$

Due to the angle dependence of (2.12) the combination of minimum fundamental wavelength λ_1 and the minimum bandwidth $\Delta\lambda/\lambda_1$ can only be achieved within a central cone of $\theta_{\text{cen}} = \sqrt{1 + K^2/2}/(\sqrt{N_0}\gamma_0)$. Integrating over the corresponding solid angle $\Delta\Omega = \pi(1 + K^2/2)/(N_0\gamma_0^2)$ yields

$$W_{1,\text{cen}} = \frac{\pi e^2 \gamma_0^2 N_e}{\varepsilon_0 \lambda_u} \cdot \frac{K^2}{(1 + K^2/2)^2} \cdot \left[J_0 \left(\frac{K^2}{4(1 + K^2/2)} \right) - J_1 \left(\frac{K^2}{4(1 + K^2/2)} \right) \right]^2. \quad (2.19)$$

Note that the radiated energy here is independent from the number of undulator periods N_0 . Instead, longer undulators provide smaller bandwidths $\Delta\lambda/\lambda_1 = 1/N_0$.

Although equation (2.15) already denotes the spectral amplitudes of the higher harmonics on axis, in the wiggler limit $K \gg 1$, where the number of harmonics grows as K^3 , the critical frequency

$$\omega_c = n_c \cdot \omega_1 \quad (2.20)$$

is a useful figure. The critical frequency occurs at the $n_c = \frac{3K}{4} \left(1 + \frac{K^2}{2} \right)$ harmonic and is defined such that half the radiated power is radiated at lower frequencies and the other half at higher energies.

2.2 FREE-ELECTRON LASERS

Radiation from a self-amplified spontaneous emission free-electron lasers (SASE-FEL) [5–8] is essentially undulator radiation, which is intense enough to act back on the electrons, and cause micro-bunching in an electron beam with a period matching the wavelength of the undulator radiation. Due to this micro-bunching the radiation emitted by the electrons becomes partially coherent in time and hence more intense. This amplified radiation can again act back on the electrons and further enhance the electron bunching and thus induce both temporal and spatial coherence of the radiation. By sustaining this feedback, the radiation field amplitude can grow exponentially until it eventually reaches saturation and the originally incoherent undulator radiation attains, partial temporal and full transversal coherence, and thus an enhancement in power by several orders of magnitudes. When realized at high electron energies, this process leads to much coveted, laser-like radiation properties in the X-ray part of the spectrum.

Regarding the experimental requisites, the deciding difference between undulator radiation and a SASE-type free-electron laser is the phase space density of the electron beam. Thereby, high electron density is required for a strong coupling between electrons and radiation, whereas a low beam divergence and energy spread is essential for starting and maintaining the bunching dynamics of the FEL feedback, so that an increasing fraction of electrons radiates at virtually the same frequency into the same direction and thus collectively contributes towards one spatially coherent radiation mode. In practice, this leads to daunting requirements on the desired electron beam parameters. Since the electrons are the key to FELs, any improvement in electron beam quality beyond the current state-of-the-art has a direct impact on FEL performance and the range of realizable FEL designs.

The term free-electron laser (FEL) draws a parallel to conventional optical lasers that has arisen from the quantum description of this process [9], which was developed before it was in most cases being replaced by a purely classical description [10]. This parallel becomes especially apparent in an FEL amplifier as in Fig. 2.3(a) or [6], where not the undulator radiation itself, but an external seed pulse at the resonant wavelength interacts with the electron bunch inside an undulator and results in an amplification of the seed pulse. This approach is often extended to a seeded FEL resonator as in Fig. 2.3(b), where the amplified pulse is picked up by mirrors and routed back to the undulator entrance, where it is again used as a seed pulse with another, new electron bunch. In succession, the pulse is repeatedly amplified and fed back as the seed for the consecutive pass through the undulator. Like in a laser oscillator, a mirror with a few percent transmission or a small hole couples out part of the amplified FEL radiation. So the pulse intensity grows until the losses by the outcoupling mirror equals the gain of a single pass. Compared to a laser using stimulated emission from a metastable quantum state, an FEL realizes amplification by interaction with an electron bunch in an undulator and transfers kinetic energy of the electron bunch into coherent radiation. This method has proven to be successful in providing intense, both spatially and temporally coherent pulses in the far UV. However, the extension of such resonators towards the X-ray region is increasingly difficult, since efficient mirrors with reflectivities beyond 90% and ultrashort light sources for the initial seed pulse are not available.

In contrast to such a seeded FEL, a self-amplified spontaneous emission free-electron laser (SASE-FEL) does not require an external seed, since the incoherent undulator radiation, also called spontaneous emission, is itself the seed pulse that causes the first bunching and continues to drive a feedback loop of amplified radiation giving rise to increased electron bunching, more radiation and so on – until the process saturates because maximum bunching is reached. In a SASE-FEL the issue of efficient mirrors is avoided by extending the undulator to a length that allows to achieve saturation in a single pass through an undulator. For these reasons, this type of FEL is currently the basis for all X-ray FELs in the world.

Nevertheless, the basic physics for FELs, seeded or self-amplified, is the same: For a single electron in an undulator the wavelength condition is that for each undulator period the longitudinal walk-off between the relativistic electron and the emitted radiation amounts to one radiation wavelength λ for every undulator period λ_u – otherwise the radiation would destructively interfere with itself. If now a second electron with the same velocity would be placed one radiation wavelength ahead of the first electron, the radiation coming from the first electron behind would exactly match the oscillating field that the second electron experiences from the undulator. Then the radiation of the first and the second electron would constructively interfere. So perfect coherence would be obtained if all electrons are longitudinally separated by multiples of the radiation wavelength. Electron beams from a standard accelerator source, however, are not in such a perfect initial arrangement. Instead the electrons are randomly scattered within the bunch. Going back to the single electron, reacting to some radiation field, either from electrons further behind or from an external seed pulse, the change in motion can be calculated according to the Lorentz equation

$$\frac{d}{dt}(\gamma mc\boldsymbol{\beta}) = e(\mathbf{E} + c\boldsymbol{\beta} \times \mathbf{B}) , \quad (2.21)$$

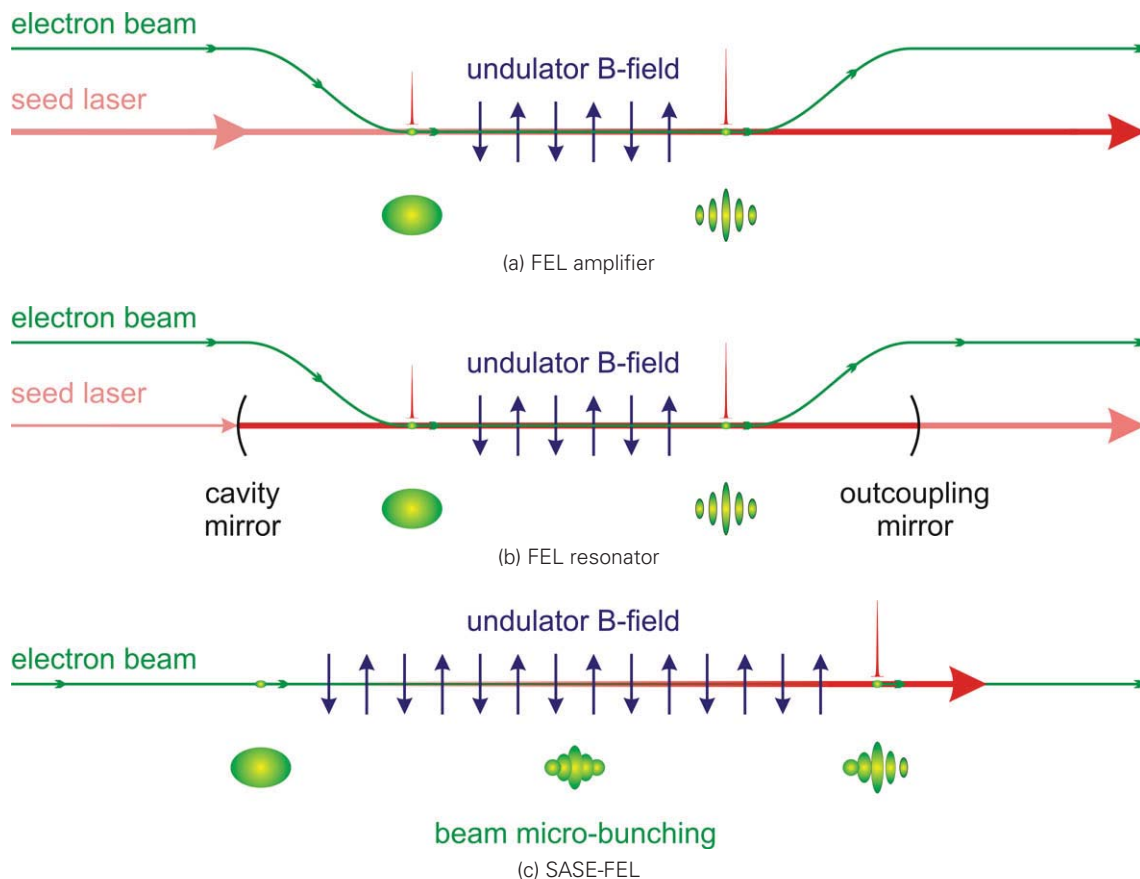


Figure 2.3: (a) In an FEL amplifier, the initial radiation field is provided by a seed laser overlapping with the electron bunch. In such a scenario, the radiation wavelength resulting from the undulator needs to be tuned close to the one of the seed laser. Within the undulator the interaction between laser field and electron beam leads to micro-bunching and a mean energy reduction in the electron bunch, so that kinetic electron energy is transferred to the laser beam. The result is an amplified laser beam. (b) Similarly, this scheme can be also realized in a seeded resonator configuration. Here, the amplified radiation from one electron bunch interacting in the undulator with the initial seed laser pulse is trapped in a cavity. Then, in subsequent passes through the undulator, the same radiation is used as its own seed for the interaction with new electron bunches and thus is amplified further. As a result, the intensity of the oscillating laser pulse increases with each pass. Part of that increase in laser energy is coupled out by a semi-transparent mirror. (c) In a SASE-FEL configuration, there exists neither an external seed laser nor an enhancement cavity. Here the seed is entirely provided by the incoherent undulator radiation itself and the entire amplification takes place in a single pass of an electron bunch through a long undulator.

which when multiplied by β yields the change in kinetic energy

$$\frac{dW_{\text{kin}}}{dt} = \frac{d(\gamma\beta)}{dt} \cdot \beta = e\mathbf{E} \cdot \beta \quad (2.22)$$

of one electron at a given velocity β . In the ultra-relativistic limit when $\beta \simeq 1$ and $|\dot{\beta}| \ll \dot{\gamma}/\gamma$ this equation simplifies to

$$\dot{\gamma} = \frac{e\mathbf{E} \cdot \beta}{m \cdot c}. \quad (2.23)$$

Equivalently in the low energy limit at $\beta \ll 1$ (2.22) becomes

$$\frac{dW_{\text{kin}}}{dt} = ec\mathbf{E} \cdot \beta. \quad (2.24)$$

The latter eq. (2.24) can be used to explain the FEL bunching mechanism in a nutshell. In the average electron rest frame both the undulator field $E_u(\omega^*t + k^*z)$ and the external radiation field $E_r(\omega^*t - k^*z)$ are counterpropagating and have the same periodicity $\omega^* = \gamma \cdot \omega_0$, so that the incident frequency is the same as the scattered frequency. One can write the total electric field and the perpendicular oscillation velocity β_{\perp} as

$$\begin{aligned} E_{\perp} &= E_{\perp,u} + E_{\perp,r} \\ \beta_{\perp} &= \beta_{\perp,u} + \beta_{\perp,r}. \end{aligned} \quad (2.25)$$

When calculating the change in electron energy according to (2.24), the term $\mathbf{E} \cdot \beta = E_{\perp} \cdot \beta_{\perp}$ oscillates with the angular frequency ω^* . This situation becomes more clear when one examines the average energy change over one optical cycle (ω^*t) and obtains the energy equation for the ponderomotive force

$$\begin{aligned} \frac{1}{ec} \left\langle \frac{dW_{\text{kin}}}{dt} \right\rangle &= \langle E_u(\omega^*t + k^*z) \cdot \beta_u(\omega^*t + k^*z) \rangle + \langle E_r(\omega^*t - k^*z) \cdot \beta_r(\omega^*t - k^*z) \rangle \\ &+ \langle E_u(\omega^*t + k^*z) \cdot \beta_r(\omega^*t - k^*z) \rangle + \langle E_r(\omega^*t - k^*z) \cdot \beta_u(\omega^*t + k^*z) \rangle \\ &= F(2k^*z) \end{aligned} \quad (2.26)$$

In the first two terms of (2.26) the same phase relation exists at all electron positions, so that the average is constant. Furthermore, this constant vanishes according to (2.21), as long as the cycle averaged energy change from the following mixed terms is much smaller compared to the electron rest energy mc^2 . For the mixed terms there is no fixed phase relation and the average depends on the respective electron position z . Since the undulator and radiation field feature both the same frequency, the ponderomotive force on the electrons has a spatial periodicity of $2k^* = 2\omega^*/c$. Therefore electrons can in an undulator, depending on their relative position in the beam z , gain or lose energy through the interaction with radiation. Due to conservation of energy in an electron beam of electron density n_e

$$n_e mc^2 \Delta W_{\text{kin}} = \frac{\Delta E_r^2}{8\pi}, \quad (2.27)$$

this leads to a decrease or increase in the radiation field energy density respectively.

In order to obtain a more quantitative picture of the working of SASE-FELs with its requirements on electron beams and limitations, it is useful to discuss a simple self-consistent SASE-FEL model in 1D. For every FEL one needs

1. modulation of the electron energy with respect to the longitudinal position by interacting with the radiation field.
2. change of the longitudinal electron positions relative to the bunch due to path length differences arising from the energy modulation.
3. coherent emission of radiation by a micro-bunched electron beam and hence growth of the radiation field amplitude. The field acts back on the electrons to increase spatial energy modulation.
4. precise synchronization of electron velocity with the undulator period to sustain the driving process of the modulation over many undulator periods.

In the following, the inertial frame of the discussion is now chosen to be the laboratory frame, so that the undulator field is the static magnetic field, which as a starting point and for mere analytical convenience is assumed to be helical instead of planar. The on-axis magnetic field of such an undulator [1] is

$$\mathbf{B} = B_0 [\cos(2\pi z/\lambda_u) \cdot \mathbf{e}_x + \sin(2\pi z/\lambda_u) \cdot \mathbf{e}_y] , \quad (2.28)$$

while the corresponding electron velocity in the undulator field is given by

$$\boldsymbol{\beta} = \frac{K}{\gamma} [\sin(2\pi z/\lambda_u) \mathbf{e}_x + \cos(2\pi z/\lambda_u) \mathbf{e}_y] + \beta_z \mathbf{e}_z . \quad (2.29)$$

Furthermore, the undulator parameter K is in the following, for sake of simplicity, chosen to be small $K \ll 1$. Derivations for larger K show basically similar physics, where the main effects are a different resonant wavelength and the inclusion of higher harmonics. Therefore, in this limit of small K the first harmonic of the undulator (2.12) is

$$\lambda = \frac{\lambda_u}{2\gamma^2} . \quad (2.30)$$

Then, as the driver of the energy modulation one assumes an electro-magnetic one-dimensional plane wave

$$\mathbf{E} = E_r [\mathbf{e}_x \cos(2\pi z/\lambda - \omega t + \Psi) + \mathbf{e}_y \sin(2\pi z/\lambda - \omega t + \Psi)] \quad (2.31)$$

with an arbitrary phase Ψ . In general this can be any component of the initial electric field of the incoherent undulator radiation, where the phase Ψ is determined by the random electron positions within the electron beam. That radiation from spontaneous undulator radiation is often also referred to as *shot noise*. Initially, many such plane wave modes with different phases Ψ and frequencies ω exist relative to one another. Only because the FEL process amplifies at one characteristic frequency ω_r , the corresponding mode is preferred and thus becomes dominant compared to all other radiation modes. In the following, only the mode which is amplified in the end is considered.

The first FEL equation in 1D features the aforementioned electron energy modulation (2.23) derived from the Lorentz equation (2.21)

$$\dot{\gamma} = \frac{e\mathbf{E} \cdot \boldsymbol{\beta}}{m \cdot c}. \quad (2.32)$$

Now, inserting the electron motion in the undulator (2.29) and the external field (2.31) into (2.32) yields

$$mc\dot{\gamma} = eE_0 \frac{K}{\gamma} \sin(\phi), \quad (2.33)$$

with the so called *ponderomotive force phase*

$$\phi = 2\pi \left(\frac{1}{\lambda} + \frac{1}{\lambda_u} \right) (c\beta_{z,0}t + z_{0,j}) - \omega t + \Psi, \quad (2.34)$$

now in the laboratory frame instead of $\phi^* = 2k^*z_{0,j} + \Psi$ in the average electron rest frame. Here the position

$$z = (c\beta_{z,0}t + z_{0,j}) \quad (2.35)$$

of the j^{th} electron in an electron bunch is parameterized by the average bunch velocity $c\beta_{z,0}t$ and the electron position $z_{0,j}$ relative to the bunch. It is immediately clear from (2.33) that for a cycle-averaged change in electron energy $\langle \dot{\gamma} \rangle_t$, which does not cancel out over a few periods of the undulator or radiation field, it is necessary to keep ϕ constant over time.

$$\dot{\phi} = 0 \quad (2.36)$$

This criterion is often dubbed the *synchronism condition* because it requires a stationary phase relation between the external radiation field and the electron oscillation in the undulator. For (2.34), it is satisfied for the radiation wavelength $\lambda_r = \lambda_u(1 - \beta_{z,0})/\beta_{z,0}$, which is nothing else but the relation for on-axis radiation in a helical undulator

$$\lambda_r = \frac{\lambda_u}{2\gamma^2} (1 + K^2) \quad \text{for } \gamma \gg 1. \quad (2.37)$$

Phrased differently, above resonance condition (2.37) says that an electron needs to phase slip backwards in the external field by one period for each oscillation in the undulator.

After the energy modulation, each electron in the bunch has a different kinetic energy, which depends on the electron's phase Ψ and thus its longitudinal position relative to the radiation field. Since the electron energies now differ slightly from the resonant energy, they slip with respect to the ponderomotive phase ϕ . For some electron j of an electron bunch consisting of N_e electrons the phase slipping velocity becomes

$$\frac{d\phi}{dt} = \frac{2\pi c}{\lambda_r} \left(\frac{\beta_z}{\beta_{z,0}} - 1 \right) \quad (2.38)$$

and denotes the second FEL equation.

If the electrons are in or close to resonance with the radiation field, the interaction leads to an energy modulation, which is sinusoidal in the longitudinal electron bunch coordinate (see (2.33) and Fig. 2.5(b)). Electrons within the phase interval $]0 + \Psi, \pi + \Psi[$ gain energy and electrons in

the phase interval $]\pi + \Psi, 2\pi + \Psi[$ are slowed down. Therefore, all electrons tend to drift towards the phase $\pi + \Psi$ and become bunched with the periodicity of the radiation field.

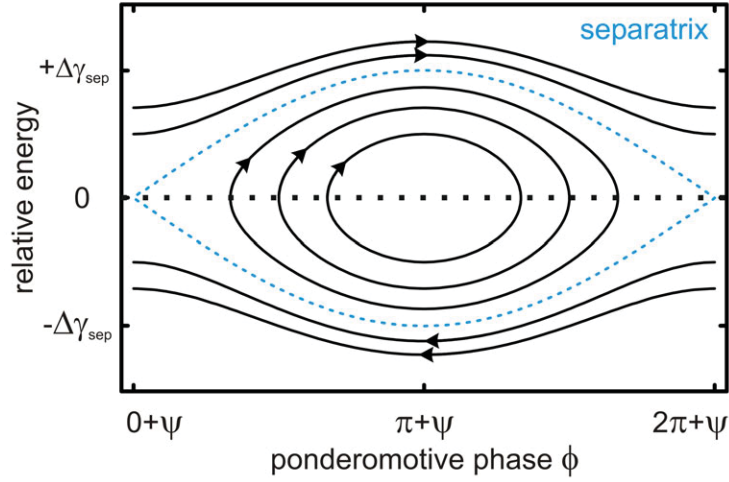


Figure 2.4: Phase-space diagram of ponderomotive phase ϕ and the electron energy relative to the resonant energy γ_0 as in (2.37), corresponding to the phase-space trajectories of electrons that individually oscillate in the ponderomotive potential of a free-electron laser. Initially, electrons are arbitrarily distributed in phase around a defined starting energy. As time passes the electrons start to either oscillate around $\pi + \Psi$ within the separatrix or, above a threshold deviation $\Delta\gamma$ in energy, drift unboundedly to higher or lower phases.

Combining (2.38) and (2.33) to a second order differential equation yields a *pendulum equation*

$$\frac{d^2\phi}{dt^2} = \frac{2\pi c}{\lambda_r} \frac{\dot{\gamma}}{\gamma_r^3} = 2ck_u \underbrace{\frac{eE_0 K}{mc\gamma_r^2}}_{\equiv \Omega^2} \sin(\phi) \quad (2.39)$$

$$\frac{d^2\phi}{dt^2} - 2ck_u\Omega^2 \sin(\phi) = 0. \quad (2.40)$$

This equation governs the phase-space trajectories of electrons, when these do not significantly change the initial radiation field. In this limit, individual electrons are seen as being isolated from all other electrons and simply react to an external field. In a SASE-FEL, where the radiation field grows by several orders of magnitudes from incoherent undulator radiation, this condition is clearly violated. However, these simple solutions give insight into the general nature of these trajectories and a first estimate on the necessary condition for electron trapping.

After introducing the quantity $\eta = (\gamma - \gamma_r)/\gamma_r$ for the relative change in electron energy compared to the resonant energy γ_r , (2.40) can be readily rephrased as a Hamiltonian

$$H(\phi, \eta) = ck_u\eta^2 + \Omega^2 \cos \phi, \quad (2.41)$$

with its canonical momenta

$$\frac{\partial H}{\partial \phi} = -\dot{\eta} \quad (2.42)$$

$$\frac{\partial H}{\partial \eta} = \dot{\phi}. \quad (2.43)$$

In Fig. 2.4, the Hamiltonian can then be used to map out the possible electron phase-space trajectories. Analogous to every other pendulum, there exists a set of trajectories which represent electrons being trapped within the ponderomotive potential and a set of unbound trajectories at large energies $|\eta|$. The curve dividing these two sets is the separatrix. According to (2.41) the largest energy deviation attained on this curve is

$$\Delta\gamma_{\text{sep}} = \sqrt{\frac{eE_0K}{mc^2k_u}}, \quad (2.44)$$

so only electrons that are within the energy interval of $[\gamma - \Delta\gamma, \gamma + \Delta\gamma]$ can become trapped in the ponderomotive potential and thus contribute to the FEL process.

Hence, if the initial electron energy is close to resonance γ_r , where the undulator field frequency is equal to the external radiation field frequency in the instantaneous rest frame of the electron, the electron is trapped inside the separatrix. In an FEL with many electrons, the initial phase distribution of electrons is arbitrary. If these electrons start from around the resonant energy with regard to the external field, the electrons start to circle around and at times reach a point, where the energy spread of all electrons has increased, but the electrons have become bunched in phase, such that these start to radiate coherently. Since the electrons continue to oscillate within the separatrix, they get out of phase again after some time.

So far, in this discussion only a single electron responding to two external fields or many electrons without mutual interaction were considered. For an FEL amplifier, which is essentially amplifying some external seed field, this analysis is valid for the so called low gain regime [5]. In an FEL starting without an initial external seed field or in a high-gain amplifier the interactions of the electrons among one another cannot be neglected anymore. In case of no initial radiation field, small density fluctuations in the electron beam provide the initial field, which acts on the electron beam and is amplified, while the density fluctuations are increased. Such a self-seeding and amplifying FEL process is the very definition of a SASE (self-amplified stimulated emission) FEL. Since such a SASE-FEL free-electron laser consists of a feed back the growth in the field depends on the existing radiation field, one expects some type of exponential growth in the time-evolution of radiation field. The strength of this growth will on the one hand depend on the strength of the undulator field and on the other hand on the density of the electron beam, which radiates and absorbs radiation. Thus, a higher electron density is expected to result in a stronger radiative coupling between the individual electrons and thus a stronger growth of the radiation field.

At some point an FEL is going to saturate. One possibility is that all electrons are in phase and thus cannot become more bunched. The other possibility is that the electrons loose so much energy due to the emitted radiation, see first term in (2.26), that they eventually fall out of resonance. Also, in this high-gain, SASE regime the electrons influence each other and thus do not follow the pendulum equation anymore. The general characteristics of Fig. 2.4 however remain the same. Electron bunching happens at the cost of an increasing energy spread and there is some finite energy width criterion which needs to be met for starting and maintaining the FEL instability.

Self-consistent SASE-FEL in 1D

In addition to the first two FEL equations describing the phase slippage (2.38) and energy modulation (2.33) it is now necessary to close the set of 1D FEL equation by including the back reaction of the oscillating electrons to the radiation field. In this way all electrons follow individually the first two FEL equations, but interact through a common radiation field.

That is done by the wave equation derived from the Maxwell equations using the vector potential $\mathbf{A}(A_x, A_y, A_z)$ and the current density $\mathbf{J}(J_x, J_y, J_z)$.

$$\left(\nabla^2 - \frac{1}{c^2} \frac{\partial^2}{\partial t^2} \right) \mathbf{A} = -\frac{4\pi}{c} \mathbf{J} \quad (2.45)$$

For the sake of simplicity we constrain ourselves to the case of small $K \ll 1$, such that the change in current density J_z in the direction of propagation becomes negligible. In addition, changes over the transverse beam and field cross section are assumed to be small, so in the following (2.45) can be reduced to a scalar equation using complex scalars for the transverse components of the vector potential $\hat{A} = A_x - iA_y$ and current density $\hat{J} = J_x - iJ_y$.

$$\left(\frac{\partial^2}{\partial z^2} - \frac{1}{c^2} \frac{\partial^2}{\partial t^2} \right) \hat{A} = -\frac{4\pi}{c} \hat{J} \quad (2.46)$$

According to $\mathbf{J} = -ecn_e\boldsymbol{\beta}$ and (2.29) for the undulator field, J_x and J_y can be written down as

$$J_x = -ec \langle n_e(\mathbf{x}) \rangle_{\lambda_r} \left\langle \frac{K}{\gamma_j} \cos(k_u z_j) \right\rangle_{\lambda_r} \quad (2.47)$$

$$J_y = -ec \langle n_e(\mathbf{x}) \rangle_{\lambda_r} \left\langle \frac{K}{\gamma_j} \sin(k_u z_j) \right\rangle_{\lambda_r} . \quad (2.48)$$

Here, both the density n_e and the velocity $\boldsymbol{\beta}$ are denoted by averaged quantities over one radiation wavelength λ_r in z , such that n_e represents a smooth number density envelope (without microbunching) over the electron beam and $\langle \beta \rangle$ the mean transverse current from the undulator oscillation. Hence, the average $\langle . . . \rangle$ is to be taken over N_e electrons $1/N_e \cdot \sum_{j=1}^{N_e} (. . .)$ within a radiation wavelength. In principle it is necessary to also include the transverse current by the radiation field. In practice however, the corresponding K-parameter $K_r = eE_r/(mc^2 k_r)$ from the radiation field is much smaller than the undulator K , so that a term for self-induced radiation damping is negligible.

The vector potential is written as

$$\hat{A} = i \frac{\alpha}{K_r} e^{ik_r(z-ct)}, \text{ with } \alpha = -E_r e^{i\Psi_r} \quad (2.49)$$

Furthermore, it is assumed that the electron bunch length L_b is much longer than the radiation wavelength $L_b \gg \lambda_r$ and the total slippage length $L_b \gg N_0 \cdot \lambda_r$, which is the longitudinal walk-off between electrons and emitted radiation over the entire N_0 undulator periods. Here, these

approximations allow to neglect the z -derivative. In reality, these conditions do not always hold. Especially, ultrashort electron bunches with durations of only a few fs violate this slowly-varying envelope approximation (SVEA). However, it is possible to formulate an analytic FEL theory in 1D, which does not rely on the SVEA [11]. In such an extended theory it turns out that such electron bunches have a shorter start-up time in an FEL and reach the exponential amplification regime faster than the long electron beams of the same electrons density.

Inserting these definitions into the scalar equation (2.46)

$$\left(\frac{\partial^2}{\partial^2 z} - \frac{1}{c^2} \frac{\partial^2}{\partial^2 t} \right) i \frac{\alpha}{k_r} e^{ik_r(z-ct)} = -4\pi n_e K \left\langle \frac{e^{-ik_u z_j} \cdot e^{-ik_r(z-ct)}}{\gamma_j} \right\rangle \cdot e^{ik_r(z-ct)}, \quad (2.50)$$

applying the derivatives to α and $e^{ik_r(z-ct)}$

$$\underbrace{\frac{i}{k_r} \left[\frac{\partial^2 \alpha}{\partial^2 z} - \frac{1}{c^2} \frac{\partial^2 \alpha}{\partial^2 t} \right]}_{\simeq 0} - 2 \left[\frac{\partial \alpha}{\partial z} + \frac{1}{c} \frac{\partial \alpha}{\partial t} \right] = -4\pi n_e K \left\langle \frac{e^{-i\phi_j}}{\gamma_j} \right\rangle, \quad (2.51)$$

as well as the slowly varying amplitude approximation

$$\frac{\partial \alpha}{\partial z} + \frac{1}{c} \frac{\partial \alpha}{\partial t} = 2\pi n_e K \left\langle \frac{e^{-i\phi_j}}{\gamma_j} \right\rangle \quad (2.52)$$

and the long electron bunch approximation yields

$$\frac{\partial \alpha}{\partial t} = 2\pi e c n_e K \left\langle \frac{e^{-i\phi_j}}{\gamma_j} \right\rangle. \quad (2.53)$$

In this derivation the slowly varying envelope approximations

$$\left| \frac{1}{k_r \alpha} \frac{\partial \alpha}{\partial z} \right| \ll 1 \quad ; \quad \left| \frac{1}{c k_r \alpha} \frac{\partial \alpha}{\partial t} \right| \ll 1 \quad (2.54)$$

allow to neglect the second order derivatives, whereas the longitudinal coordinate z is eliminated in the field equation by separating the average electron bunch movement $\langle \beta_z \rangle ct$ from changes in the temporal bunch or radiation field profile, which are both assumed to be negligibly small.

After rewriting (2.32) in terms of vector potential amplitudes and (2.38) in terms of γ instead of β , the set of closed set of FEL equations is.

$$\begin{aligned} \dot{\phi}_j &= \frac{2\pi c}{\lambda_u} \left(1 - \frac{\gamma_0^2}{\gamma_j^2} \right) && \text{(phase slipping)} \\ \dot{\gamma}_j &= -\frac{e c K}{2 m c^2 \gamma_j} [\alpha e^{i\phi_j} + c.c.] && \text{(energy modulation)} \\ \dot{\alpha} &= 2\pi e c n_e K \left\langle \frac{e^{-i\phi_j}}{\gamma_j} \right\rangle && \text{(radiation field)} \end{aligned} \quad (2.55)$$

The first two equations determine how the individual electrons move in the radiation field. If the coupling of the electrons to the external radiation field is weak $\Delta\alpha \ll \alpha$, so that α can

be considered constant, these *pendulum equations* suffice to describe the basic dynamics of the system. Up to this point the electrons are not significantly interacting with one another. If however the radiation contribution of the electrons significantly changes the external radiation field, the third equation describing the evolution of the field parametrically couples N_e electrons to one another. The phase-space picture of Fig. 2.4 is now invalid.

The term $B(t) = \langle \exp(-i\phi_j)/\gamma_j \rangle$ can be identified as a measure of micro-bunching in the electron beam. If all electrons are at the same phase and energy, the factor is unity and all electrons radiate coherently. In the other extreme the electrons are arbitrarily distributed along the axis of propagation, where the phase-average approaches zero and all electrons radiate incoherently. However, it is not exactly zero, since the finite number of electrons N_e in the beam gives rise to a statistical remainder of phase correlation on the order of $\sqrt{1/N_e}$. It is this *shot noise* from electron bunches which provides the initial seed field from incoherent undulator radiation and starts the SASE process.

The field equation and the pendulum equations are parametrically coupled by the radiation field amplitude and the bunching factor $B(t)$. Without micro-bunching the field would only grow linearly with time. The question is thus: under which conditions is a positive feedback loop established between radiation field and electron beam micro-bunching, so that the radiation amplitude becomes an exponentially growing quantity?

Extracting more on the system properties is greatly facilitated by a choice of dimensionless coordinates [5, 12, 13] that features a *universal scaling*. In these coordinates all coupling factors depending on undulator wavelength, radiation wavelength or electron energy are normalized to be part of the coordinates, so that solutions of the coupled equations only depend on initial conditions. Such a universal scaling goes beyond a mere mental exercise, since it relates free-electron lasers with very different electron energies or undulator geometries to one another and thus enables comparisons between different machines.

When rewriting the field α as a dimensionless quantity parallel to the K parameter, the radiation equation can be put into the suggestive form

$$\frac{\partial}{\partial t} K_r(t) = - \frac{4\pi}{\underbrace{\hat{\beta}_{\text{trans}}}_{=K/\gamma_0}} \underbrace{(2\omega_0)}_{\propto [t^{-1}]} (\gamma_r/\gamma_0)^2 \overbrace{\rho^3}^{\propto n_e} \left\langle \frac{e^{i\phi_j}}{\gamma_j} \right\rangle. \quad (2.56)$$

The equation already looks similar to (2.46), whereby $\hat{\beta}_{\text{trans}} = K/\gamma_0$ denotes the dimensionless transverse velocity and $(2\omega_0) = 4c\pi/\lambda_u = (\omega_r/\gamma_0^2)$ the normalized radiation frequency. The new dimensionless ρ^3 parameter collects all remaining constants and is proportional to the electron density n_e . The definition of this so called *Pierce parameter* is

$$\rho = \left(\frac{K\gamma_0^2 \Omega_p}{4\gamma_f^2 \omega_0} \right)^{2/3} \quad (2.57)$$

where the electron beam plasma frequency Ω_p in the laboratory frame is given by

$$\Omega_p = \sqrt{\frac{4\pi n_e e^2}{m_e \gamma_0^3}}. \quad (2.58)$$

The physical reasoning behind the definition of this coupling constant as a cubed quantity is separation of longitudinal and transverse dimensions. With everything else the same, it is expected that a doubling of the longitudinal electron line density, proportional to $n_e^{1/3}$ and ρ , also doubles the speed of the electron beam dynamics. Equally, doubling the transverse electron density, which is proportional to $n_e^{2/3}$ and ρ^2 , doubles the radiated field amplitude along the entire electron beam. This motivates the new time scaling

$$\tau = 2\omega_0 \rho (\gamma_r / \gamma_0)^2 t. \quad (2.59)$$

In universal coordinates, also the bunching factor $\langle \exp(i\phi_j) / \gamma_j \rangle$ needs to be normalized to the electron energy $\langle \exp(i\phi_j) / (\gamma_j / \gamma_0) \rangle$, otherwise it would vary with the average beam energy. Furthermore, in order to separate any initial electron phase drift $\dot{\phi}_0$ arising from a mismatch between the initial average electron energy γ_0 and the resonant energy γ_r , defined by the undulator geometry and the radiation frequency of the external field, the electron phases ϕ_j are redefined

$$\Psi_j = \phi_j - \dot{\phi}_0 t. \quad (2.60)$$

with respect to the initial phase slipping velocity $\dot{\phi}_0$ as in (2.38)

$$\dot{\phi}_0 = \omega_0 \left(1 - \frac{\gamma_r^2}{\gamma_0^2} \right). \quad (2.61)$$

In order to rewrite $\dot{\phi}_0 t$ in terms of rescaled time τ , one defines the initial deviation from the resonance energy γ_r as the constant detuning parameter

$$\delta = \frac{\gamma_0^2 - \gamma_r^2}{2\gamma_r^2 \rho}, \quad (2.62)$$

so that (2.60) simplifies to

$$\Psi_j = \phi_j - \delta \tau. \quad (2.63)$$

Finally, the rest of the factors in (2.56) are absorbed into the new field definition

$$A = e\alpha e^{i\delta\tau} \frac{K}{4mc^2 \gamma_r^2 k_u \rho^2} = -\exp(i(\delta\tau - \Psi_r)) \frac{K \cdot K_r}{2\rho^2}, \quad (2.64)$$

so that (2.56) takes the new form

$$\frac{\partial}{\partial \tau} A = \left\langle \frac{e^{-i\Psi_j}}{\rho \Gamma_j} \right\rangle + iA\delta, \quad (2.65)$$

where Γ_j denotes the particle energy normalized to ρ times the initial energy

$$\Gamma_j = \frac{\gamma_j}{\rho\gamma_0}. \quad (2.66)$$

This latter definition is not physically motivated by a universality requirement, but serves to make some of the later results, such as energy conservation (2.70) or the gain length (2.76) appear in a more elegant form.

In the end the simplified, dimensionless set of 1D FEL equation becomes.

$$\frac{d}{d\tau}\Psi_j = \frac{1}{2\rho}\left(1 - \frac{1}{\rho^2\Gamma_j^2}\right) \quad (2.67)$$

$$\frac{d}{d\tau}\Gamma_j = -\frac{1}{\rho}\left[\frac{A}{\Gamma_j}e^{i\Psi_j} + \text{c.c.}\right] \quad (2.68)$$

$$\frac{d}{d\tau}A = \left\langle \frac{e^{-i\Psi_j}}{\rho\Gamma_j} \right\rangle + iA\delta \quad (2.69)$$

Apart from the normalization, each of the equations has retained its direct physical meaning. With (2.68) and (2.69) a constant of motion

$$\frac{d}{d\tau}(|A|^2 + \langle \Gamma_j \rangle) = 0 \quad (2.70)$$

can be immediately found. Within this choice of coordinates that constant represents conservation of energy between the radiation field and the mean particle energy.

Even in this simplified one dimensional case above set of equations is nonlinear and has no general closed solution. For further analysis one usually invokes Liouville's theorem and simplifies this system of $(2N_e + 1)$ equations to 3 equations by using the Vlasov equation [5]. Such an approach describes the evolution of arbitrary electron beams in terms of phase space distribution functions and shows to be more suited for generalizations and lends itself to analysis in 2 or 3 dimensions. However straight forward stability analysis of small perturbations already yields some general properties of the electron-radiation dynamics. Thereby a linearized set of equations (2.67)-(2.69) around an equilibrium state is derived.

The equilibrium conditions are, zero field $A_0 = 0$, monoenergetic electrons at the resonance energy $\Gamma_{0,j} = 1/\rho$ and a spatially uniform beam without initial bunching $\langle e^{-i\Psi_j} \rangle = 0$. Then small perturbations around the equilibrium state

$$\begin{aligned} A &= A_0 + a = a \\ \Psi_j &= \Psi_{0,j} + \xi_j, \quad j = 1, 2, \dots, N_e \\ \Gamma_j &= \frac{1}{\rho}(1 + \eta_j), \quad j = 1, 2, \dots, N_e \end{aligned} \quad (2.71)$$

are defined and collective variables introduced for both particle phase and energy by performing

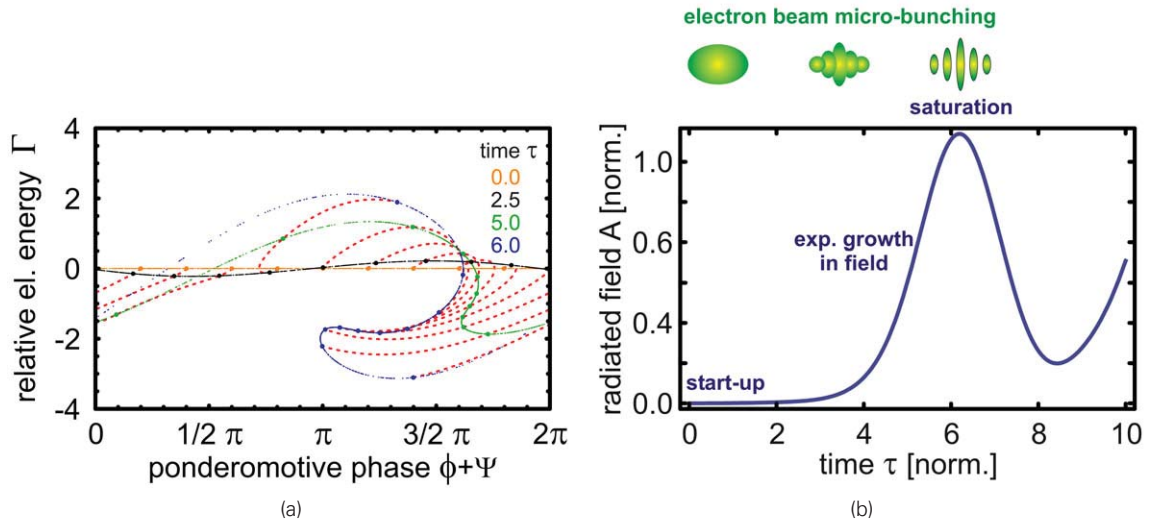


Figure 2.5: Numerical solution of (2.67)–(2.69) with 1000 electrons, $\rho = 10^{-3}$ and $\delta = 0$. (a) depicts the electron phase-space at different times. The trajectories of some selected electrons (red-dashed) shows bunching in phase. The corresponding evolution of the radiation field A amplitude shows exponential growth until it saturates at $\tau = 6$, where maximum bunching of the electrons is achieved. If the FEL feedback is sustained beyond saturation, both the radiation field amplitude, as well as the bunching of electrons reduces.

the phase-weighted average over the respective equations.

$$\begin{aligned}
 x &= \langle \xi_j e^{-i\Psi_{0,j}} \rangle \\
 y &= \frac{1}{\rho} \langle \eta_j e^{-i\Psi_{0,j}} \rangle
 \end{aligned} \tag{2.72}$$

Hereby, the phase x averaged over all electrons has only an appreciable magnitude if all electrons have a similar phase. Hence the physical meaning corresponds to a bunching factor, which has a magnitude of unity when all electrons are in the same phase. Similarly, the other collective quantity y denotes a relative energy detuning averaged over all electrons. After inserting (2.72) into (2.67)–(2.69), applying the phase-weighted average and dropping higher terms of the perturbing quantities, one arrives at

$$\begin{aligned}
 \frac{dx}{d\tau} &= y \\
 \frac{dy}{d\tau} &= -a \\
 \frac{da}{d\tau} &= -i\delta a - ix - \rho y.
 \end{aligned} \tag{2.73}$$

This linearized set of FEL equations around the starting conditions of an FEL is now analytically tractable. A radiation field of the form $a = A \propto e^{i\Lambda\tau}$ only has solutions if it satisfies the characteristic equation of (2.73).

$$\Lambda^3 - \delta\Lambda^2 + \rho\Lambda + 1 = 0 \tag{2.74}$$

This polynomial has in general one real and two complex conjugated solutions. The real parts of the solutions belong to oscillating modes and, depending on the sign, the imaginary parts to

modes that are exponentially decaying or growing in field amplitude. After a start-up regime, where all modes begin with similar amplitudes, the growing mode will eventually become the dominant mode of the system.

For electron beams at resonance $\delta = 0$ and for a small Pierce parameter $\rho \simeq 0$, the solutions to (2.74) are $\Lambda \in \{-1, \frac{1}{2} + \frac{i}{2\sqrt{3}}, \frac{1}{2} + \frac{-i}{2\sqrt{3}}\}$. Hence the growing mode is $A \propto e^{\frac{1}{2\sqrt{3}}\tau}$, or rewritten in non-normalized coordinates and for $\gamma_r \simeq \gamma_0$

$$E_r \propto e^{\frac{\sqrt{3}}{2} \cdot 2\omega_0 \rho t} \propto e^{\frac{2\pi\sqrt{3}\rho}{\lambda_u} z}. \quad (2.75)$$

Hence the characteristic distance

$$L_g = \frac{\lambda_u}{4\pi\sqrt{3}\rho}, \quad (2.76)$$

after which the radiation power ($\propto E_r^2$) has grown by a factor e^1 is known as the gain length in FEL physics.

At this point the role of ρ as a coupling parameter between electrons and radiation becomes apparent. The instability growth rate is proportional to ρ and thus shows the feedback strength of the system. By dimensional analysis this can be understood from a physical point of view. Through the plasma frequency, the Pierce parameter (2.57) is proportional to the cubic root of the electron density $n_e^{1/3}$. This shows that coherence evolves faster, when the average distance between the electrons on the z-axis is smaller and electrons have a shorter distance to the next electron to affect the bunching and hence amplification behavior.

The $\rho \propto 1/\gamma_r$ dependence in (2.57) is straight forward and traces back to (2.33) and (2.38). Physically, for a phase advance, there must be a significant slipping velocity between two electrons with different energies, when compared to the radiated wavelength $\lambda \propto 1/\gamma^2$. For electron velocities close to the speed of light, such differences in velocities can only become exceedingly small.

The $\rho \propto K^{2/3}$ dependence of the normalized undulator field amplitude can be understood by the competing influence of undulator radiation, where the radiation amplitude of one electron is $\propto K^2$ and the energy modulation as shown in (2.32), which is $\propto K$. If the amplification of the field would depend directly on the field strength present as in a $\dot{A} = \text{const.} \cdot K \cdot A$ type equation, the gain length would have to be $\propto 1/K$. For the free-electron laser however, a fraction of the radiation field is absorbed to further drive the energy modulation and hence FEL instability, so one ends up with $\rho \propto K^{2/3}$.

For more insight beyond small field perturbations, the equations (2.68) and (2.69) are useful. Linearizing (2.68) around small changes in $\gamma_j = \gamma_0 + \Delta\gamma_j$ yields

$$\frac{1}{\rho} \frac{\Delta\gamma_j}{\gamma_0} = -A[e^{i\Psi_j} + \text{c.c.}]. \quad (2.77)$$

After multiplying both sides with the complex conjugate and averaging over all electrons

$$\left\langle \frac{\Delta\gamma_j}{\gamma_0} \right\rangle = 2\rho^2 A^2, \quad (2.78)$$

and applying the energy conservation law (2.70) gives the gain-spread relation

$$\frac{1}{2\rho} \left\langle \frac{\Delta\gamma_j^2}{\gamma_0^2} \right\rangle = \left\langle \frac{\Delta\gamma_j}{\gamma_0} \right\rangle. \quad (2.79)$$

Naturally, this equation is not valid for arbitrary energy spreads. Instead it is limited by the saturation of the FEL instability. Since by energy conservation and (2.79), field amplitude growth is inextricably connected to a growth in energy spread, there will be a point in the evolution of the instability, when the energy of the individual electrons has changed so much compared to the resonance energy, that these no longer satisfy the synchronism condition $\dot{\phi} = 0$ from (2.34). As a result, a varying phase Ψ in the energy modulation equation (2.33) prevents efficient energy transfer between the electrons and the radiation field. At that point the radiation field growth stops and neither the energy spread, nor the mean energy shift increases anymore. Saturation has occurred.

By knowing there is some limiting $\Delta\gamma_{\text{limit}}$ at both sides of the resonance γ_r , one can assume at saturation a mean electron energy shift $\left\langle \frac{\Delta\gamma_j}{\gamma_0} \right\rangle = -\frac{\Delta\gamma_{\text{limit}}}{\gamma_r}$ and an energy spread $\sqrt{\left\langle \frac{\Delta\gamma_j^2}{\gamma_0^2} \right\rangle} = 2\Delta\gamma_{\text{limit}}$, covering the entire range from $-\Delta\gamma_{\text{limit}}$ to $+\Delta\gamma_{\text{limit}}$. Inserting these values into (2.79) gives

$$\left| \frac{\Delta\gamma_{\text{limit}}}{\gamma_r} \right| = \rho \quad (2.80)$$

as an estimate of the mean energy loss at saturation. This result, gives ρ a meaning as an overall energy efficiency, denoting the fraction of the electron beam kinetic energy that is converted into radiation. The total radiation field energy at saturation is therefore

$$W_{\text{sat}} = \rho\gamma_r mc^2. \quad (2.81)$$

Numerical simulations confirm this order of magnitude [6, 7], which makes this result a useful upper estimate for FEL photon yields.

The limit (2.80) combined with (2.79) also gives an upper estimate for the acceptable energy spread

$$\sqrt{\left\langle \frac{\Delta\gamma^2}{\gamma_r^2} \right\rangle} \ll 2 \cdot \rho, \quad (2.82)$$

which is the central statement, when discussing non-ideal effects. All non-ideal effects that negatively impact the performance of an FEL do directly or indirectly increase the energy spread or have an equivalent influence on the wavelength spread of the scattered radiation, which is $2 \cdot \sqrt{\langle (\Delta\lambda/\lambda_r)^2 \rangle} = \sqrt{\langle (\Delta\gamma/\gamma_r)^2 \rangle}$ for regular undulators.

These results were calculated for helical undulators and small $K \ll 1$. More detailed calculations [6, 7] that include these effects, lead to changes in resonance energy and a slightly different definition of the Pierce parameter

$$\rho = \left(\frac{f_c \cdot K\gamma_0\Omega_p}{4\gamma_r^2\omega_0} \right)^{2/3}, \quad (2.83)$$

which now includes an additional coupling parameter

$$f_c = \frac{J_0(\chi) - J_1(\chi)}{\sqrt{2}} \text{ with } \chi = \frac{K^2/2}{2(1 + K^2/2)}. \quad (2.84)$$

The resonance wavelength λ_r is the same as the undulator radiation wavelength and now also includes the respective nonlinear terms.

$$\lambda_r = \frac{\lambda_u}{2\gamma^2} \left(1 + \frac{K^2}{2}\right) \quad (2.85)$$

Note that for planar undulators, the nonlinear factor is $(1 + K^2/2)$, which is different from the $(1+K^2)$ of helical undulators. The physical reason is that the photon drag, axially slowing down the electrons, is a constant in a helical undulator (modulus of transverse field amplitude is constant), whereas it oscillates in a planar undulator, which leads to the factor 1/2 average.

To have a more straightforward connection to experimental electron bunch parameters, it is often customary to write the electron number density $n_0 = I_p/(2\pi\sigma_b^2 \cdot e)$ of the Pierce parameter in terms of RMS electron bunch diameter σ_b and an on-axis peak current I_p .

$$\rho = \frac{1}{2\gamma_r} \left(\frac{I_p}{I_A} \cdot \left(\frac{f_c \cdot K \lambda_u}{2\pi\sigma_b} \right)^2 \right)^{1/3} \quad (2.86)$$

There are several ways to improve FEL performance – i.e. optimize electron number density, undulator period or undulator strength.

In conventional accelerators, which is already a mature and proven technology, improvements in phase space density and hence electron number density are rather small and incremental. But the small scale of laser-wakefield accelerated electron bunches could make a huge difference here, since the electron bunch duration is expected to be significantly shorter than 100 fs, eventually even down to below 10 fs, as well as have normalized emittances that can be on the order of $\epsilon_{n,\text{trans}} = 0.1 \pi \text{ mm mrad}$, which leads to proportionally smaller electron bunch foci. In an rough and optimistic estimate, (2.86) suggests that the combined effect of one order of magnitude improvement in all three spatial electron bunch coordinates $\rho \propto n_e^{-1/3}$, could lead to FELs that are by one order of magnitude more efficient.

Changing the undulator period λ_u , while keeping the resonance wavelength and the undulator strength K constant is always connected to a simultaneous change of the resonance electron energy $\lambda_u \propto \gamma_r^2$. Therefore the FEL efficiency scaling $\rho \propto \lambda_u^{1/6}$ is quite weak, whereas the gain length scales almost linearly $L_g \propto \lambda_u^{5/6}$. This means shorter undulator periods with smaller electron energies would lead to more compact FELs. In reality this is difficult to realize by magnetic undulators. The undulator parameter K , which is a measure for the oscillation amplitude of the electron is also proportional to the undulator period. Therefore maintaining a sizable K at shorter undulator periods, means that the magnetic field B_0 on the undulator axis needs to increase proportionally. Therefore small undulator structures are with sizable K are increasingly difficult to realize for small undulator periods. In addition resistive field effects, i.e. interaction of the electron bunch with the undulator wall, interferes with FEL operation.

Optical undulators on the other hand, which are basically focused high-power laser beams that collide head-on with the electrons, have high fields and effective sub-micron undulator periods of half the laser wavelength.

2.3 HIGH-POWER LASERS

High-power lasers existing today provide laser beams of intensities $I_0 = 10^{18} - 10^{21} \text{ W/cm}^2$. The corresponding electric fields of $3 \times 10^{10} - 3 \times 10^{12} \text{ V/cm}$ far exceed atomic fields, such as the $5 \times 10^9 \text{ V/cm}$ of the first Bohr orbit in Hydrogen. As a result, the leading front of these laser pulses is enough to fully or partially ionize all matter and create a plasma. Two especially important properties of high-power lasers are relativistic intensities and strong ponderomotive forces.

In non-relativistic calculations an electron oscillating with frequency ω in an electro-magnetic plane wave $\mathbf{E} = E_0 \sin(\omega t - kz) \mathbf{e}_x$ attains in direction of the electric field a maximum quiver velocity of $v_q = eE_0/m_0\omega$. As soon as the quiver velocity approaches the speed of light, the dynamics change dramatically since in the Lorentz equation

$$\frac{d}{dt}(\gamma m \dot{\mathbf{x}}) = -e(\mathbf{E} + \mathbf{v} \times \mathbf{B}) \quad (2.87)$$

the $\mathbf{v} \times \mathbf{B}$ -term and a γ -factor greater than one become relevant and at higher intensities even dominating. Hence for the following discussion it is useful to define the dimensionless laser strength parameter

$$a_0 = \frac{eE_0}{m_0 c \omega} \quad (2.88)$$

$$\simeq 0.85 \times 10^{-9} \lambda_0 [\mu\text{m}] I_0^{1/2} [\text{W/cm}^2], \quad (2.89)$$

which is proportional to the electric field and characterizes the transition from sub-relativistic $a_0 \ll 1$ to relativistic $a_0 \geq 1$ quiver velocities.

One central example of this transition is the electron motion within an intense plane wave. The physics has been described in detail in [14, 15], so here only the result is presented. An electron, initially at rest, oscillates in a laser field, which propagates in the z-direction and is linearly polarized in y. The resulting solution

$$\begin{aligned} k \cdot y(t) &= a_0 \sin \phi(t) \\ k \cdot z(t) &= \frac{a_0^2}{4} \cdot \left[\phi(t) + \frac{1}{2} \cos 2\phi(t) \right] \\ \phi(t) &= \omega t - kz(t) \end{aligned} \quad (2.90)$$

is implicit, since the phase $\phi(t)$ contains a $z(t)$ dependence. However, it is clear that in longitudinal direction the field oscillates with twice the frequency in the transverse y-direction. In

addition, the longitudinal oscillation amplitude scales with a_0^2 , so this oscillation becomes dominant at high laser intensities. This becomes especially apparent, when one transforms (2.90) to the average rest frame of the electron

$$16z(\phi)^2 = \gamma(\phi)^2(a_0^2/(1 + a_0^2/2) - \gamma(\phi)^2), \quad (2.91)$$

where the electron trajectory for $a_0 \geq 1$, as shown in Fig. 2.6, increasingly turns into an 8-figure.

One important consequence of the longitudinal motion is that in the presence of an electromagnetic wave an electron without initial transverse momentum, immediately starts to drift by an average momentum $p_{\text{drift}} = mc \cdot a_0^2/4$ – a phenomenon also known as the “photon drag”. Since in the laboratory frame of reference, the electron is moving close to the speed of light, addition of velocities is not symmetric with regard to the direction of acceleration. Hence the cycle-averaged net velocity from the longitudinally, oscillatory motion is not zero anymore. Instead, the cycle averaged velocity of the electron is reduced.

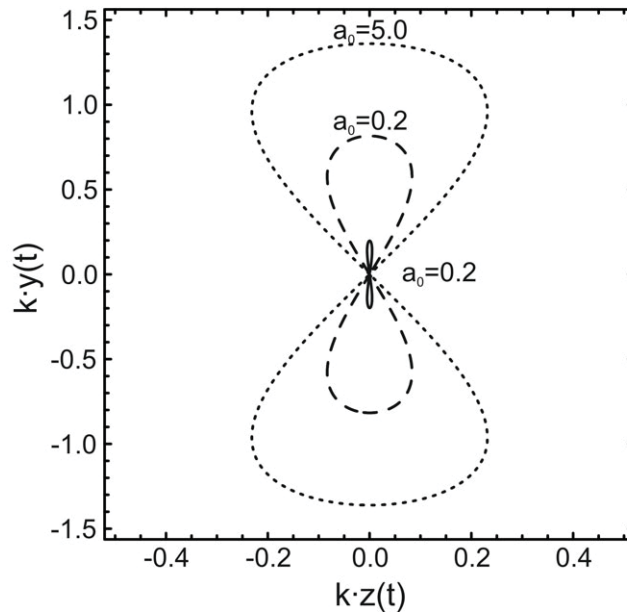


Figure 2.6: Figure-8 motion of an electron in its average rest frame in a linearly polarized EM plane wave of laser strength a_0 .

Quite different from that drift momentum, which is gone as soon as the laser field is gone, is the momentum gained by the ponderomotive force. Here a laser beam with a transverse variation in its electric field is required, such as the Gaussian-like beam profile of a focused laser. An electron oscillating in the center of that laser beam has a larger oscillation amplitude than off-center where the laser intensity is lower. Therefore an electron starting at the center is displaced to either side within half a laser-period. Since the electron is now in a region of less field strength, the opposite field of the second half of the laser period has a weaker amplitude and the electron does not return to the beam center after the full laser period. The electron has experienced a cycle-averaged net force towards a region of smaller electric fields.

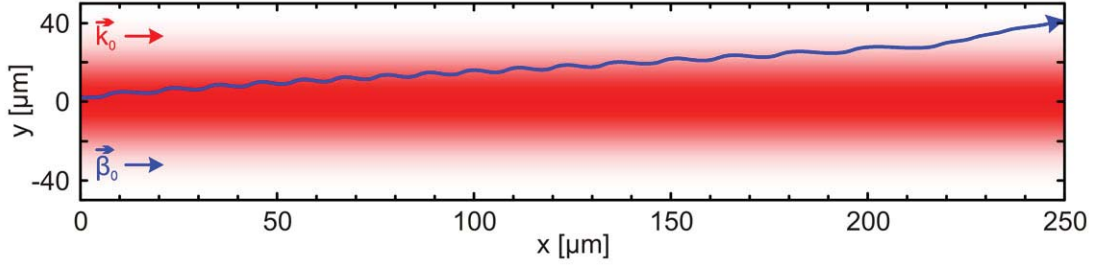


Figure 2.7: An electron oscillates in a laser beam of finite diameter. Due to its radially varying intensity, the electron tends to move away from the region of maximum laser intensity. The corresponding cycle-averaged change in momentum is called *ponderomotive force*. (transverse Gauss profile with $a_0 = 0.25$ at 800 nm and $\gamma_0 = 10$ electron)

According to [14] the ponderomotive force is described by

$$\mathbf{F}_p = \frac{d\bar{\mathbf{p}}}{dt} = -mc^2 \nabla \overline{\gamma_f}, \text{ with } \gamma_f = \sqrt{1 + \frac{\bar{\mathbf{p}}^2}{m^2 c^2} + \frac{a_0^2}{2}} \quad (2.92)$$

in its fully relativistic form. Hereby the overlined quantities represent averages over the respective optical cycles, filtering out the fast oscillation. At sub-relativistic intensities ($a_0 \ll 1$) the ponderomotive force

$$\mathbf{F}_p = \frac{d\bar{\mathbf{p}}}{dt} = -\frac{mc^2}{4} \nabla (\overline{a_0^2}) \quad (2.93)$$

is proportional to the intensity gradient, whereas in the ultra-relativistic limit $a_0^2/2 \gg (1 + \bar{\mathbf{p}}^2/(m^2 c^2))$, the force

$$\mathbf{F}_p = \frac{d\bar{\mathbf{p}}}{dt} = -\frac{mc^2}{\sqrt{2}} \nabla |\overline{a_0}| \quad (2.94)$$

becomes proportional to the modulus of the field gradient.

2.4 THOMSON SCATTERING RADIATION

In the classical Thomson backscattering picture [15–18] relativistic electrons are driven by the electric field of a laser pulse to an oscillatory motion similar to the situation in a magnetic undulator. As a consequence, the oscillating electrons emit Doppler-upshifted radiation of narrow bandwidth into a relativistically contracted solid angle cone in the laboratory frame. For highly relativistic electrons ($\beta_0 \simeq 1$) the wavelength λ_{sc} of the scattered light scales as

$$\lambda_{sc} = \frac{\lambda_0}{n \cdot 2\gamma_0^2 \cdot (1 - \beta_0 \cos \phi)} \cdot (1 + a_0^2/2 + \gamma_0^2 \theta^2), \quad (2.95)$$

where λ_0 denotes the laser wavelength, n the harmonic number and ϕ the angle between the electron beam and the incoming light, i.e. $(1 - \beta_0 \cos \phi) = 2$ for counterpropagating beams at $\phi = 180^\circ$. For values of a_0 approaching unity, the $\mathbf{v} \times \mathbf{B}$ term of the Lorentz force starts to alter interaction dynamics, thus entering the nonlinear Thomson regime [19–21]. According to (2.95) one observes an intensity dependent shift to longer wavelengths.

Most experiments aiming for X-ray radiation from Thomson scattering sources, use a “head-on” geometry, in which laser and electrons are counter propagating ($\phi = 180^\circ$), since this yields the highest photon energy. Side-scattering on the other hand has attracted interest, because of its tunability in the resulting wavelength and the ability to produce ultrashort pulses [22] through a different overlap between lasers and electrons.

Due to the short wavelength of the incoming laser light as compared to the situation in an undulator, X-ray energies of the scattered light can already be reached with relatively moderate electron energies as depicted in Fig. 2.8. Note that as a purely classical theory, Thomson scattering always assumes that the scattered photon energy in the electron rest frame is much smaller than the electron rest energy mc^2 . For larger photon energies, the quantum recoil of the electron becomes relevant and the physics has to be described by quantum theory. The result is Compton scattering with first-order cross sections relating to the Klein-Nishina formula [23–25]. Here the Compton scattering cross section is a function of electron energy and generally becomes lower. However, the classical Thomson theory is valid for most practical scenarios, since relativistic electron beams at $1 \mu\text{m}$ laser wavelength do not reach the Compton limit $\hbar\omega_{sc} \geq \gamma mc^2$ in the first harmonic until electron energies of $\simeq 50 \text{ GeV}$.

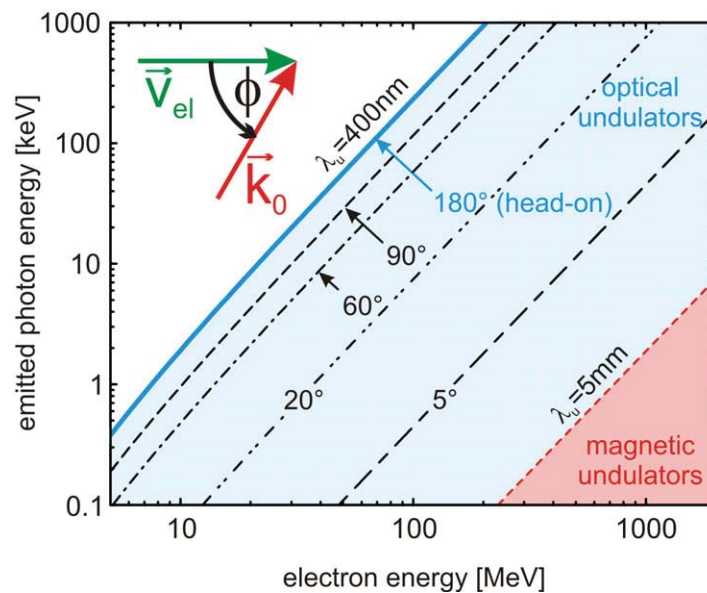


Figure 2.8: Scattered undulator energies with respect to electron energies for various scattering angles ϕ between laser and electrons.

Equivalence of Thomson scattering to undulator radiation

It has to be emphasized that undulator radiation is very similar to Thomson scattering. This becomes especially apparent if one transforms the static magnetic field of an undulator into the average rest frame of the electron $\beta_{\text{avg}} = \beta_0 \mathbf{e}_z$. According to the Lorentz-transform [2] the fields

are

$$\mathbf{E}' = \gamma(\mathbf{E} + \boldsymbol{\beta} \times \mathbf{B} \cdot c) - \frac{\gamma^2}{\gamma + 1} \boldsymbol{\beta}(\boldsymbol{\beta} \cdot \mathbf{E}) \cdot c \quad (2.96)$$

$$\mathbf{B}' = \gamma(\mathbf{B} - \boldsymbol{\beta} \times \mathbf{E}/c) - \frac{\gamma^2}{\gamma + 1} \boldsymbol{\beta}(\boldsymbol{\beta} \cdot \mathbf{B})/c. \quad (2.97)$$

Inserting (2.4) yields

$$\mathbf{E}' = -\gamma c \beta B_y(y, z') \cdot \mathbf{e}_z \quad (2.98)$$

$$\mathbf{B}' = \gamma B_y(y, z') \cdot \mathbf{e}_y \quad (2.99)$$

$$\mathbf{E}' \stackrel{\gamma \gg 1}{\Rightarrow} -\mathbf{e}_z \times \mathbf{B}'/c, \quad (2.100)$$

which for highly relativistic electrons corresponds to the field of a counter propagating wave. The only difference is within the incident frequency, such that the Lorentz transform of the static B-field

$$\cos(k_u z) \rightarrow \cos(k_u \gamma(z - ct)) \quad (2.101)$$

has half the frequency compared to the Thomson case

$$\cos(k_u(z - ct)) \rightarrow \cos(k_u 2\gamma(z - ct)). \quad (2.102)$$

Since in the ultrarelativistic limit $\gamma \gg 1$ the undulator field is equivalent to an electromagnetic plane wave, the resonant conditions of linearly polarized Thomson scattering

$$\lambda_r = \frac{\lambda_0}{2\gamma_0^2(1 - \beta_0 \cos \phi)} \left(1 + \frac{a_0^2}{2} + \gamma^2 \theta^2 \right) \quad (2.103)$$

can be compared to linearly polarized undulator radiation

$$\lambda_r = \frac{\lambda_u}{2\gamma_0^2} \left(1 + \frac{K^2}{2} + \gamma^2 \theta^2 \right), \quad (2.104)$$

so it becomes apparent that also the normalized undulator parameter K is equivalent to the normalized laser strength parameter a_0 .

This finding is well known [26] and has the primary advantage that knowledge from Thomson/Compton scattering can be reused for undulator radiation and vice versa. For example all the yield equations (2.13) to (2.18) from undulator radiation essentially remain the same when performing the substitutions

$$\lambda_0/(1 - \beta_0 \cos \phi) \leftrightarrow \lambda_u \quad (2.105)$$

$$a_0 \leftrightarrow K. \quad (2.106)$$

For linear Thomson scattering at laser amplitudes $a_0 \ll 1$ and a given accepted bandwidth $\Delta\omega_{sc}/\omega_{sc}$, one can quickly estimate the total photon yield into the full solid angle following Esaray *et al.* [16]

$$N_{\text{phot}} = 2\pi\alpha_f N_0 N_b a_0^2 (\Delta\omega_{\text{sc}}/\omega_{\text{sc}}). \quad (2.107)$$

Here, $\alpha_f = 1/137$ is the fine structure constant, N_0 the number of laser oscillation periods during the interaction and N_b the number of electrons within the bunch. In the classical description, when $\hbar\omega_{\text{sc}} \ll (\gamma - 1)mc^2$, the Thomson cross-section is constant and the total yield from a scattering event proportional to the laser intensity. The duration of the scattered pulse amounts to

$$\tau_{\text{tot}} = \tau_{\text{bunch}} + \frac{\tau_{\text{laser}}}{2(1 - \beta_0 \cos \phi) \cdot \gamma_0^2}. \quad (2.108)$$

Nonlinear Thomson scattering

Nonlinear Thomson scattering is quite complex in both angular and spectral structure. A thorough account on the details can be found under [16–18, 20, 21, 27]. Here, only a brief overview shall be given.

The transition from a sinusoidal oscillation to the figure-8 electron motion at large laser field strengths a_0 close to or exceeding unity, leads to the emergence of higher harmonics. In a qualitative picture the circular motion of the “fat eight” can be compared with bending magnet radiation, where the electrons are deflected on a circular trajectory with radius R . Since the narrow angular $\sim 1/\gamma$ search light pattern changes direction due to the circular trajectory, the radiation reaching the observer in the far field originates from a short arc of length $\delta l \sim 2R/\gamma$. After dividing by c and accounting for the $1/2\gamma^2$ relativistic time contraction, the time duration of the radiation flash originating from a single electron is $\Delta t \sim R/c\gamma^3$. Using general Fourier transform arguments, the typical large spectral width of the spectrum can be obtained.

$$\Delta\omega \sim \frac{2\pi}{\Delta t} \sim \frac{2\pi\gamma^3}{c \cdot R} \quad (2.109)$$

In contrast to a single bending magnet a laser pulse or equivalently an undulator features $2 \cdot N_0$ bending radii, so there are distinct frequencies, where the contributions from the single bends constructively interfere and thus give rise to many higher harmonics instead of a continuous spectral distribution.

Going through a more thorough analysis of the bending behavior of (optical) wigglers with respect to a_0 and γ gives

$$\lambda_c = \frac{\lambda_0}{3\gamma^2 a_0}, \text{ for } a_0 \gg 1 \quad (2.110)$$

as the critical wavelength λ_c , defining that one-half of the scattered laser power is radiated at shorter wavelengths and the other half at longer wavelengths.

In the high intensity limit $a_0 \gg 1$ the scattered spectrum of a linear polarized laser pulse becomes so densely populated by harmonics, so that it can be considered as a quasi-continuum. In addition the opening angle in the plane of polarization increases to $\sim a_0/\gamma$.

The total scattering power efficiency P_s/P_0 remains independent of the laser intensity even in

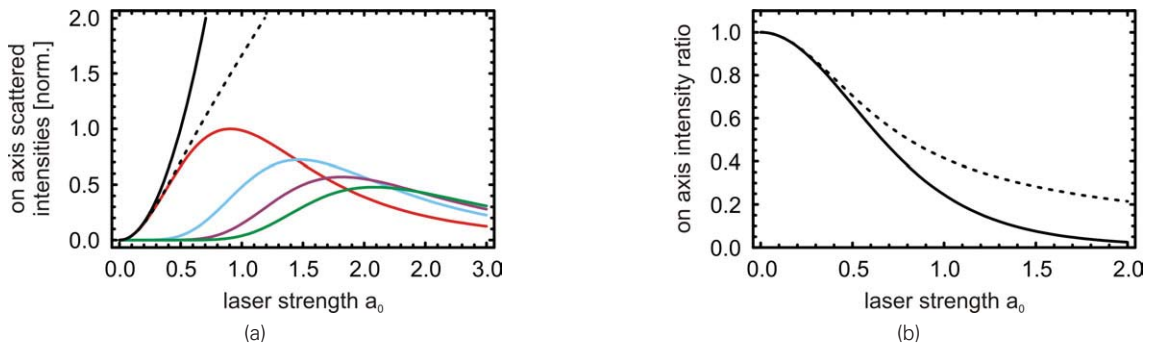


Figure 2.9: (a) On axis scattering intensities for the first harmonics normalized to the maximum intensity of the first harmonic (b) Comparison of on axis scattering intensities of the first harmonic (solid line) compared to a scaling $\propto a_0^2 \propto I_0$. The dashed line denotes the intensity sum of all harmonics. Both (a) and (b) show that the on axis intensity efficiency decreases at higher laser intensities. The reason is a distribution of scattered energy over more higher harmonics, a broadening of the cone angle and also harmonics that radiate off-axis (even harmonics).

the nonlinear Thomson regime. Note that this does not hold true for the number of photons, as the critical frequency increases proportional to a_0 .

Differences between magnetic and optical undulators

Although the fundamental physics is essentially the same, there are general differences when considering experimental realization and non-ideal effects. For undulators it is relatively easy to engineer the magnetic fields such, that these feature a constant field amplitude over the entire undulator. This makes it possible to operate wigglers at a well-defined undulator parameter $K > 1$, which remains the same for each shot. One distinct disadvantage of undulators is that they are large. Typical undulator periods are usually on a **cm** scale and in practice cannot be scaled below a couple **mm** [28, 29], so undulators are usually meter long. The main reason is that the undulator parameter K is proportional to the undulator period λ_u , so that increasing magnetic fields and smaller undulator gaps are required to sustain a sizable K -value. Resistive field effects, i.e. interaction of the electrons with the undulator walls [30–33], lead to non-ideal effects, which significantly impact FEL performance.

On first sight, the use of lasers as optical undulators seems to be ideal for a new generation of synchrotron light sources. The undulator period here is half the laser wavelength, which is 3-4 orders of magnitudes lower than in magnetic undulators and with modern lasers the maximum field can easily exceed laser strengths of $a_0 \simeq 1$. In addition, laser beams do not require a material structure near the electron beam and have the advantage that they in principle do not require tweaking of each individual field oscillation to satisfy some B-integrals, because laser beams are electro-magnetic waves by definition. In addition to that, laser technology provides more flexibility in terms of transverse field profiles. Especially in combination with laser wakefield acceleration, it has furthered the vision of a compact and all-optical synchrotron sources, which does not require any large scale facilities.

However, two major issues are so far limiting the use of lasers as optical undulators, especially in FEL technology. For one, in contrast to undulators, which can be arbitrarily long, optical wigglers are limited in length due to the finite Rayleigh length $Z_0 = \pi w_0^2 / \lambda_0$, with w_0 being the laser spot size. Waveguide techniques are not possible, since material waveguides are quickly ionized by the laser. Also setting up several laser beams, one behind the other, is problematic in collinear geometries, because each focus requires different placement of the focusing optics. Therefore, it is often attempted to trade shorter undulator lengths by higher laser intensities, which is the reason why such laser beams are often dubbed optical *wigglers* instead of optical *undulators*.

Secondly, going to higher laser strength parameters $a_0 \geq 1$ is much less straightforward than going to higher undulator parameters $K \geq 1$. Usually, laser pulses have some Gaussian-type beam profile, both transversally and longitudinally. Therefore the laser strength parameter varies over the pulse from zero to its maximum value a_0 . Specifically for nonlinear Thomson scattering, the result of varying intensities over the entire laser pulse is a spectral broadening of the scattered radiation according to (2.95), where $\lambda_r \propto (1 + a_0^2/2)^{-1}$. Especially for high-power lasers, where optics based on absorption or transmission are problematic because of high intensities, it is technically extremely challenging to design laser pulses with a transversally flat, temporally rectangular beam profile and small shot to shot fluctuation. An additional problem are shot-to-shot fluctuations in laser intensity.

Another significant difference between magnetic and optical undulators is the different shape of the transverse profile. Magnetic undulators have a parabolic transverse magnetic field profile (2.3) with the minimum field being on axis and increasing fields towards the poles. This leads to a transversal trapping of electrons that propagate off-axis. These electrons oscillate with about the betatron frequency $\omega_\beta \approx (\gamma/K)k_u c$ around the central axis [34], so that on average the electron beam remains focused over an extended length.

For laser beams the equivalent of this effect is the ponderomotive force (2.92). In Gaussian laser beams however, the effect tends to expel electrons along intensity gradients out of the center, so that transverse trapping does not occur here. Basically, this potential problem can be avoided by either working with laser intensities that are too low for the ponderomotive force to become relevant or by tailoring the intensity gradients by using non-Gaussian, transverse laser beam profiles, such as flat tops or even concave profiles. Note however, as interaction distances between lasers and electrons are usually by orders of magnitudes shorter than meter long undulators, so that the focusing requirements of electron beams are equally less strict.

2.5 ELECTRON ACCELERATION BY LASER WAKEFIELDS

Conventional accelerator technology is limited in its maximum fields by the material breakdown fields of the accelerator structures, which are on the order of 50 – 150 MV/m [35, 36]. Therefore, the idea of making electron acceleration more efficient and compact in size by using the enormous fields from high-power lasers is tempting.

However, direct acceleration of an electron beam by a laser field alone is not straightfor-

ward, since in vacuum an electron cannot gain net acceleration from electro-magnetic plane waves [37, 38]. The reason is that such a plane wave laser-pulse overtaking an electron would accelerate the electron with rising laser intensity through the axial ponderomotive force $F_{p,z} \simeq -(m_0 c^2 / \gamma) (\partial / \partial z) a^2 / 2$, but then decelerate it again by the same amount when the laser intensity decreases again. Hence, direct laser acceleration concepts need to break this symmetry between acceleration and deceleration by limiting the interaction either in time or in space, which can be done by focusing geometries, gas media, ionization or nonlinear interactions [14, 39]. Although such methods have been experimentally demonstrated [40, 41], electron acceleration directly by the laser field does not scale easily beyond several **MeV** electron energy. Hereby, a fundamental limitation is the length scale of the laser wavelength λ_0 , which is on the order of one μm and thus smaller than typical electron bunch dimensions. Since the final electron momentum is phase-sensitive with respect to the initial phase-space position of the individual electrons with respect to the laser field, this prevents uniform acceleration of all electrons and hence collimated, monoenergetic electron beams.

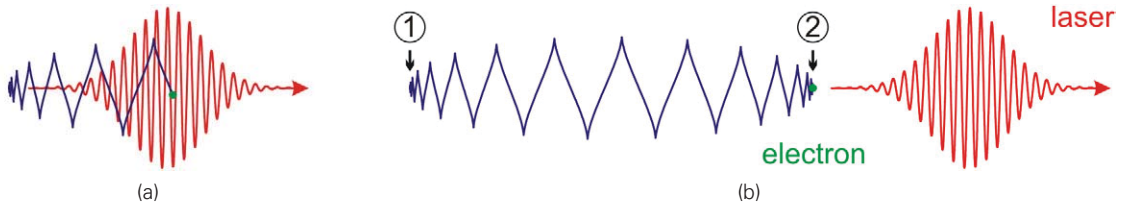


Figure 2.10: (a) An 800 nm, 25 fs linearly polarized laser pulse with a peak intensity corresponding to $a_0 = 5$ overtakes an electron, which is initially at rest. During interaction the electron acquires relativistic velocities, but after interaction (b), the electron has transferred its energy back to the laser and is again at rest.

This is different for laser-wakefield acceleration, which was first proposed 1979 by Tajima and Dawson [42] and first realized in 1995 [43]. Here, the acceleration takes place within a plasma, which can naturally sustain high electric fields because it is already completely ionized and hence cannot undergo material breakdown anymore. In contrast to direct laser acceleration, the laser is used here to create a cavity structure in the plasma, which then provides the electric field for electron acceleration. This basic acceleration scheme is depicted in Fig. 2.11. An ultrashort laser pulse propagates in a plasma and resonantly excites a charge-density wave, which travels with a phase velocity v_p equal to the group velocity of the driving laser pulse

$$v_g = c(1 - \omega_p^2 / \omega_0^2)^{1/2} = v_p \lesssim c \quad (2.111)$$

in the plasma. Here,

$$\omega_p = (e^2 n_e / \epsilon_0 m_e)^{1/2} \quad (2.112)$$

denotes the plasma frequency, which determines the typical eigenfrequency and thus the time scale of the plasma to respond to external fields. The basic wave excitation mechanism relies on the transverse intensity gradient of the laser pulse, which leads to the ponderomotive force pushing away plasma electrons perpendicular to the laser direction of propagation. This in turn reduces the electron density behind the laser pulse as shown in Fig. 2.11, whereas plasma ions due to their large mass $m_p \gg m_e$ remain largely unaffected. The result is a separation of charges and a restoring force on the displaced electrons by the positive space-charge of the immobile

ion background remaining on axis. Subsequently, this electron displacement leads to transverse charge-density oscillation forming the wakefield behind the laser. The scale of this plasma wave is determined by its plasma wavelength

$$\lambda_p = 2\pi v_p / \omega_p \simeq 2\pi c (e^2 n_e / \epsilon_0 m)^{-1/2} \lambda_p [\mu\text{m}] \simeq 3.3 \times 10^{10} / \sqrt{n_e [\text{cm}^{-3}]}, \quad (2.113)$$

and thus the initial plasma electron density n_e . In experiment, such plasmas have electron densities typically in the range of $n_e = 10^{18} - 10^{19} \text{ cm}^{-3}$. For optimal resonant excitation of a plasma wave driven by the laser ponderomotive force, it is the time-scale of the laser pulse duration τ_0 and not the laser period $2\pi c / \omega_0$ which needs to match the plasma period $\tau_p = \lambda_p / c$.

The result is a charge-density wave, comoving with the laser pulse, which features strong transversal and longitudinal electric fields between negatively charged regions with a surplus of electrons and positively charged regions with a deficit of electrons compared to the ionic background of the plasma. These longitudinal electric fields within a wakefield can become so large that they can be exploited for electron acceleration.

Hence, the next (crucial) step is electron injection into this plasma-generated cavity to begin acceleration. Hereby, injected electrons can originate from the plasma itself or some external source.

Since the accelerated electrons become faster than the plasma wave this acceleration can only last until the electrons outrun the plasma wave and start to decelerate when reaching a wake region with reversed field polarity. Then the electrons have reached the dephasing limit. For that reason a LWFA plasma should ideally end before the accelerated electrons reach the dephasing length.

The characteristic magnitude of the maximum electric field amplitude of an electrostatic plasma wave traveling near the speed of light can readily be estimated from Poisson's equation

$$\nabla \cdot \mathbf{E} = e / \epsilon_0 (n_b - \delta n_e), \quad (2.114)$$

where δn_e denotes the electron density perturbation with respect to the initial electron density n_e and n_b the quasistatic ion background density $n_b = n_e$. The electric field of a plasma wave in a laser-wakefield accelerator in the linear regime $|\delta n / n_e| \ll 1$ is assumed to have the form $E_z = E_{\text{max}} \sin[\omega_p(z/v_p - t)]$ with $v_p \simeq c$. Inserting this longitudinal electrostatic wave into Poisson's equation and using the difference $(n_e - \delta n_e)$ between the ion background density n_e and assuming that the electron density fluctuation δn_e cannot exceed n_e in a linear oscillation yields $(\omega_p / c) E_{\text{max}} = e / \epsilon_0 n_e$. Hence the maximum field that can sustain a linear plasma wave is

$$E_{\text{max}} = cm_e \omega_p / e$$

$$E_{\text{max}} [V/m] \simeq 96 \sqrt{n_e [\text{cm}^{-3}]}. \quad (2.115)$$

This limit is commonly called the cold nonrelativistic wave breaking limit. A more detailed calculation that accounts for nonlinear, periodic plasma waves using the nonlinear relativistic, cold fluid

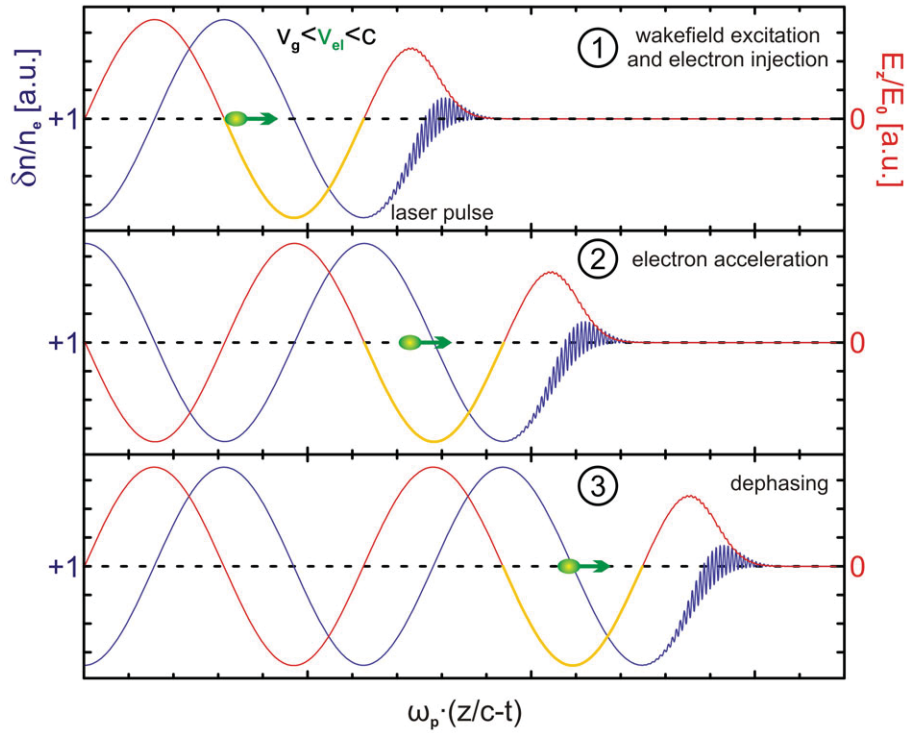


Figure 2.11: (1-3) shows the plasma electron density modulation $\delta n/n_e$ of a laser wakefield along the direction of propagation at different times during the interaction. (1) An intense, ultrashort laser pulse in an underdense plasma excites a charge density wave. Being driven by the laser pulse, this wave takes the form of a wake and travels with the same group velocity v_g as the laser. Through the inhomogeneous electron density modulation, this wakefield provides strong longitudinal fields E_z , which in the linear regime can reach up to the wavebreaking field amplitude E_{max} . Electrons are injected into the part of the wake with accelerating field $E_z < 0$ (yellow). This can happen by self-injection in the plasma wave, when large wake amplitudes cause partial wavebreaking or by some other externally controlled process, which either relocates plasma electrons into the accelerating field or provides an entire pre-accelerated electron bunch from outside the plasma. (2) The injected electrons are accelerated in the longitudinal wakefield and become faster than both the plasma wave and the laser pulse ($v_g < c$). (3) Electron acceleration continues as long as the driving laser pulse is present and until the fast electron outrun the wakefield after the dephasing length L_d and enter a region with reversed electric field E_z , which leads to deceleration.

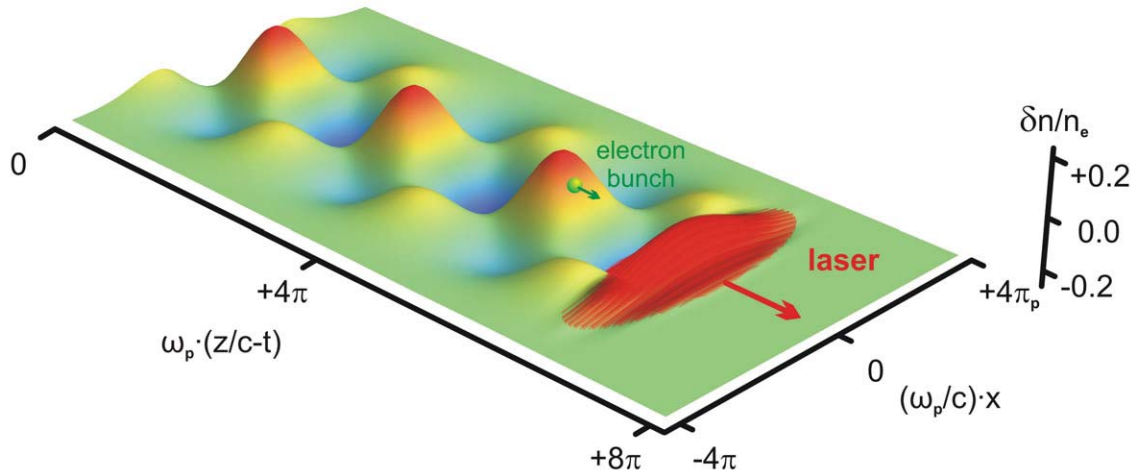


Figure 2.12: 2D cross-section of a laser (red) driving a wakefield according to (2.117). The laser ponderomotive force expels plasma electrons off-axis, until the restoring force from the ion background pulls the electrons back on-axis and leads to the transverse oscillation in electron density that give rise to the longitudinal wakefield structure consisting of several density “buckets” into which injected electron bunches can be accelerated.

equations [44] yields

$$E_{\text{WB}} = \sqrt{2}(\gamma_p - 1)^{1/2} E_{\text{max}}, \text{ with } \gamma_p = \left(1 - \frac{v_p^2}{c^2}\right)^{-1/2}. \quad (2.116)$$

Although there exists no analytic solution of the 3D problem at relativistic laser intensities $a_0 > 1$, it is instructive to consider 3D solutions of the cold fluid equations [14, 39, 45–47] for linear wakefields and non-relativistic laser intensities $a_0^2 \ll 1$, where electron density perturbations are assumed to be small $|\delta n/n_e| \ll 1$. For such density perturbations one arrives at

$$\delta n/n_e = (c^2/\omega_p) \int_0^t dt' \sin[\omega_p(t-t')] \nabla^2 a^2(\mathbf{r}, t')/2, \quad (2.117)$$

while the corresponding electric field is denoted by

$$\mathbf{E}/E_{\text{max}} = -c \int_0^t dt' \sin[\omega_p(t-t')] \nabla a^2(\mathbf{r}, t')/2. \quad (2.118)$$

Although these equations are non-relativistic at small intensities, they show that, for large amplitude charge density waves close to the wavebreaking limit E_{max} , fields close to or exceeding $a_0 \geq 1$ are required.

Thus the plasma wave breaks when the laser pulse drives the plasma wave field amplitude beyond this limit. According to above derivation and (2.117)-(2.118), one needs a $\delta n/n_e \simeq 1$ and thus a strong laser field $a_0 \geq 1$ to obtain wave breaking and subsequent self-injection of electrons into the plasma wake.

Between two oppositely charged regions the longitudinal electric field can be in excess of **TV/m**. The acceleration mechanism is that electrons, which are by some means injected into this region, can be “surfing” on this plasma wave and get accelerated to energies much higher than the plasma electrons.

One important quantity in laser wakefield accelerators is the dephasing length. It is defined as the length a relativistic electron $\beta \simeq 1$ must travel before it has phase-slipped by half a plasma wavelength with respect to plasma wave propagating at the phase velocity v_p .

$$(1 - v_p/c)L_d = \lambda_p/2 \quad (2.119)$$

$$L_d \simeq \gamma_p^2 \lambda_p, \text{ for } \gamma_p = \left(1 - \frac{v_p^2}{c^2}\right)^{-1/2} \simeq \omega_0/\omega_p \gg 1 \quad (2.120)$$

So after injection into the accelerating field behind the maximum electron density of the wakefield (see Fig. 2.11) and subsequent acceleration over a dephasing length on the order of L_d , the electrons outrun the wakefield and start to become decelerated by the wakefield region with reversed field polarity. This length can then be used to make rough estimates on the performance and geometry of such a LWFA.

In addition to maintaining a stable acceleration structure, injecting the electrons into this acceleration cavity is a critical issue. In most experiments available at the moment, self-injection is used. That means the intensity of the driving laser is chosen to be high enough, such that the wave partially breaks at the maximum electron density behind the first “bucket” and thus injects these electrons into the acceleration gradient near the maximum electron density. The big advantage of this mechanism is, that it is easy to realize once enough laser intensity is available without requiring additional experimental means. On the other hand, wavebreaking is by definition a highly nonlinear process, which makes control of its properties and hence the properties of the electron beam challenging.

In some experiments injection is controlled by optical means. It was demonstrated that a standing wave from two additional laser pulses can be used to inject background electrons into the acceleration cavity. These methods have the advantage of an increased degree of control on position and time of the injection, but have the difficulty that laser pulses are at most comparable, but not significantly smaller than the wakefield in which they inject electrons.

External injection of electrons from a conventional electron gun or another wakefield accelerator potentially allow for complete control on the electron beam properties that are to be injected. However, due to the tremendous technical difficulties of injecting an electron bunch at the right time into the small dimensions of a wakefield this scheme has not been demonstrated in experiment yet. Since electrons from conventional accelerators are significantly longer than the dimensions of the wakefield, the current line of research is to inject a slow electron bunch in front of the laser, which overtakes the bunch, such that it successively gets trapped, spatially compressed in the wakefield and accelerated to higher energies.

Bubble acceleration

A novel regime of laser wakefield acceleration, now known as the “bubble regime”, was proposed by Pukhov and Meyer-ter-Vehn on the basis of PIC simulations [48] and in 2004 experimentally demonstrated by several groups [49–51]. It was predicted that short ($\tau \leq c/\lambda_p$) and intense ($a_0 > 4$) laser pulses could produce quasi-monoenergetic electrons of several tens to hundreds of MeV. Here the driving laser is so intense that the excited plasma wave immediately breaks, so only the first “wave bucket” remains.

In contrast to the case of linear or mildly nonlinear plasma waves there is no hope to describe the plasma physics with a standard fluid model [52]. This becomes evident when one considers the effect of the laser ponderomotive force in the plasma. In the beam center the laser intensity in bubble regime is by definition so strong, that all electrons are expelled in transverse directions, leaving behind the ionic background. At the outer edges of the laser the electrons barely move, forming a thin sheath around the bubble. This total cavitation of a region cannot be modeled by laminar flow anymore, where the plasma merely becomes more or less dense, particles trajectories do not cross and the mean velocity in a small volume is close to the velocity of individual electrons. Instead, the electron flow now has crossing particle trajectories, so that within one small volume there exist several distinct electron velocity distributions which cannot be represented anymore by a velocity average. Due to these kinetic effects, the detailed calculations of bubble acceleration quickly become computationally expensive. Currently, these are modeled by two and three dimensional particle-in-cell codes [14, 53–56] like OSIRIS or ILLUMINATION. Using these tools, it is possible to test simplified models and scalings.

One can show [57, 58] that in the ultra-relativistic limit of $a_0 \gg 1$ there exists a similarity parameter

$$S = \frac{n_e}{a_0 n_c}, \quad (2.121)$$

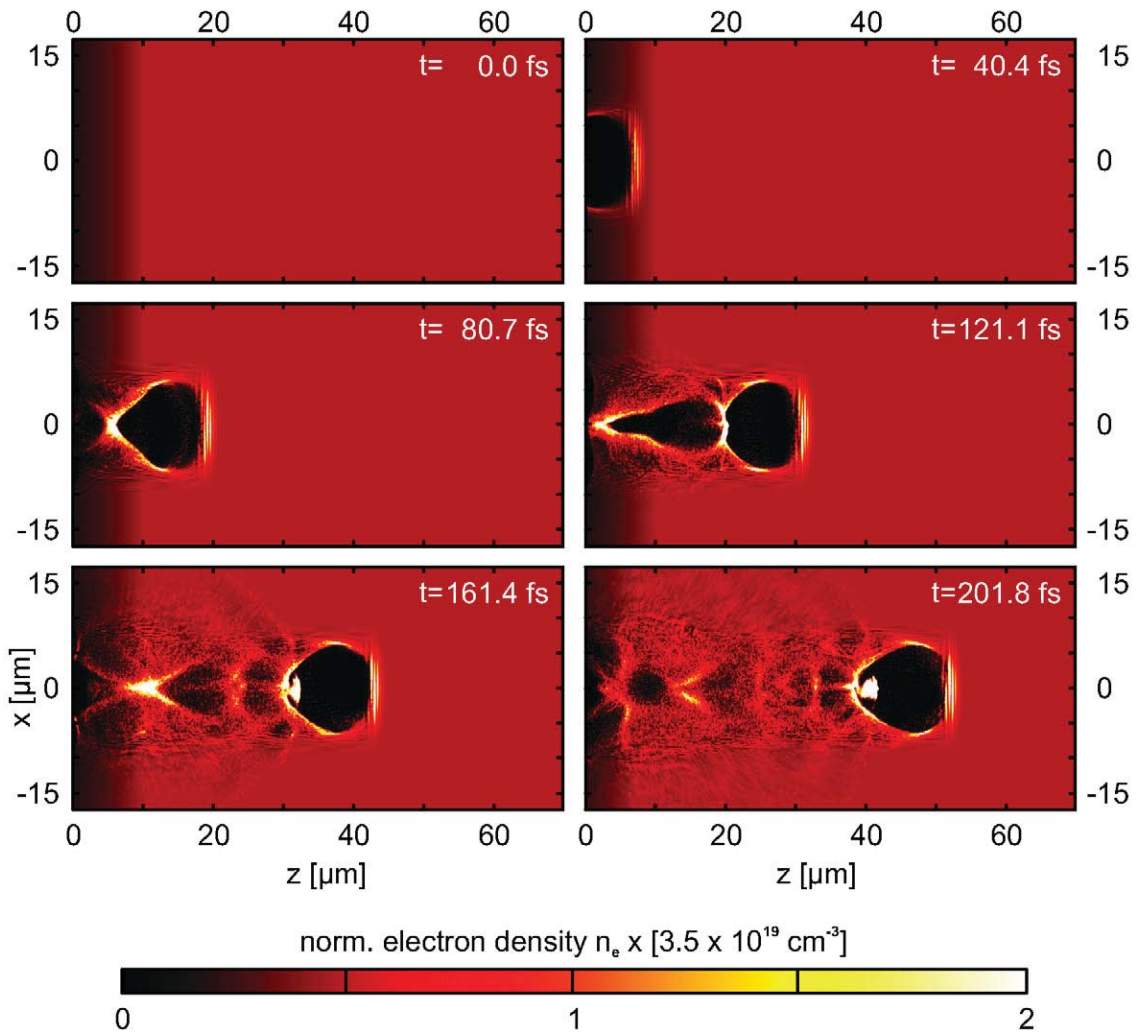
which relates a range of physical plasma densities and laser intensities to one another. As long as the similarity parameter S and the laser wavelength remain constant, the plasma physics remains similar and can thus be described in the scaled coordinates

$$\hat{t} = S^{1/2} \omega_0 t, \quad \hat{\mathbf{r}} = S^{1/2} k_0 \mathbf{r}, \quad \hat{\mathbf{p}} = \mathbf{p}/mca_0, \quad (2.122)$$

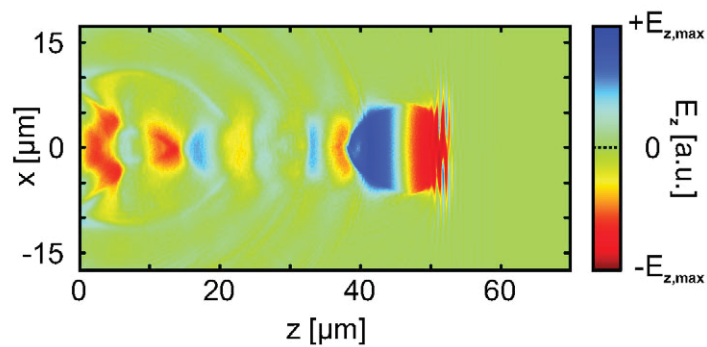
$$\hat{\mathbf{A}} = \frac{e\mathbf{A}}{mc^2 a_0}, \quad \hat{\mathbf{E}} = \frac{S^{-1/2} \mathbf{E}}{mc^2 k_0 a_0}, \quad \hat{\mathbf{B}} = \frac{S^{-1/2} \mathbf{B}}{mc^2 k_0 a_0}. \quad (2.123)$$

Space and time remain the same, whereas the fields and momenta scale proportional to the laser field a_0 . Although, this scaling is valid mainly for ultra-relativistic intensities $a_0 \gtrsim 20$, it proves already useful at much lower intensities $2 < a_0 < 20$, where one can already estimate the outcome of experiments at different plasma densities n_e and laser intensities.

For entering the bubble regime it is important that the laser pulse duration is on the order of $\lambda_p = 2\pi v_g/\omega_p$ or shorter. If the laser pulse is longer than the plasma cavity, then also portions of the laser pulse other than the rising flank interact strongly with denser plasma regions outside the bubble, thus altering pulse shape and spectrum. However, this is not a strict limit to bubble acceleration, since such *self-phase-modulation* can lead to a shortening of the laser pulse, so that the laser duration condition becomes fulfilled in that process and a bubble can form. In practice



(a) electron density during bubble acceleration



(b) E_z -field within a bubble

Figure 2.13: 3D-PIC simulation of laser-wakefield acceleration in the bubble regime with an 800 nm, 5 fs laser pulse and a 5 μm focal spot at $n_e = 1.8 \times 10^{19} \text{ cm}^{-3}$ electron density – calculated with ILLUMINATION. (a) depicts a cross-section of the plasma electron density along the laser direction at selected times. These stills show the lasers entering the plasma, bubble formation, electron self-injection at $t = 120 \text{ fs}$ and subsequent acceleration of an ultrashort electron bunch inside the bubble. (b) features the cross section of (a) at $t = 201.8 \text{ fs}$ but shows the z -component of the electric field in a color scaling, which is linear around zero, but saturates at large fields. The representation emphasizes the symmetric structure of the accelerating field gradient.

this self-modulated regime [59] is so far experimentally the most common scenario of bubble acceleration.

A similar condition also holds in the transverse dimension for the laser spot size

$$w_0 \omega_p / c \simeq R_b \omega_p / c \simeq 2 \sqrt{a_0}, \quad (2.124)$$

where the laser spot size must be matched to the bubble radius R_b , which in turn depends on the laser strength a_0 . According to the self-similarity scaling (2.123), above eq. (2.124) follows a square root dependency. The validity of this scaling, including the factor of two, is not analytically derived in any strict sense, but gleaned from PIC-simulations [52, 60]. If on the one hand the laser spot size is too small, the laser is not stably self-guided in the plasma. If on the other hand, the laser spot size is too large, the thickness of dense electron sheath surrounding the bubble increases, thus decreasing the field within the bubble and due to the thus lower electron density impeding self-injection. In the following, this relation is assumed to be valid in all following scalings of bubble acceleration.

The dephasing length in the bubble regime is

$$L_d = \frac{4}{3} \left(\frac{\omega_0}{\omega_p} \right)^3 \sqrt{a_0} \frac{c}{\omega_0} \quad (2.125)$$

and follows a derivation similar to the one for (2.120), while the depletion length

$$L_{\text{depl}} \simeq \left(\frac{\omega_0}{\omega_p} \right)^2 c \tau_0. \quad (2.126)$$

is determined by the rate at which the laser pulse is etched back by the interaction with the initial electron density at the rising laser pulse front. Laser pulses could in principle be much shorter than the plasma wavelength λ_p and still form a bubble, but in this limit the laser pulse contains less energy and is depleted after a much shorter distance.

The maximum energy gain in a bubble can be approximated from the average electric field and the dephasing length L_d initial electron density $n_e \propto \omega_p^2$

$$E_0 \simeq \frac{2}{3} m c^2 \left(\frac{\omega_0}{\omega_p} \right)^2 a_0. \quad (2.127)$$

The maximum number of electrons which can be accelerated to this energy can be estimated by balancing the total beam energy $N_b \cdot E_0$ with the total field energy in the bubble. The underlying assumption is that the field is generated by the electron sheath around the bubble. If now electrons inside the bubble gain energy, this amounts to an energy loss to the kinetic energy of the electron sheath. As soon as this energy transfer becomes comparable to the total bubble field energy this leads to a significant change of the bubble shape and fields. That effect is called *beam-loading* and the maximum number of electrons that can be trapped in the bubble resulting

from such an energy balance argument [52, 60]

$$N_b \simeq \frac{4}{30} \frac{mc^2}{e^2} \cdot w_0 a_0 \quad (2.128)$$

$$\simeq \frac{4\pi}{30} n_e R_b^3 \quad (2.129)$$

is a useful indicator for its relevance in a given scenario. It is found to either scale with the square root of laser intensity or with the normalized volume of the bubble.

Experimental state of the Art and Beam Properties

With bubble acceleration it was for the first time possible to produce electron spectra that show monoenergetic features. Typically, these electron bunches produced energies in the range of tens to hundreds of **MeV**. By extending the laser interaction distance through guiding of the laser pulse through plasma channels in capillaries, laser wakefield acceleration to energies of about 1 **GeV** was demonstrated. The charge goes up to 100 **pC** and the energy spread is at the percent level.

These laser wakefield accelerated beams are especially interesting for two main reasons – accelerator size and electron beam properties. First, the dimensions of laser wakefield accelerators are on a scale of **mm** and **cm** rather than several tens of meters to kilometers in conventional accelerators that require large structures. This advantage essentially lowers overall costs of infrastructure of both construction and maintenance by several orders of magnitudes, so a particle accelerator effectively becomes a table-top device for university-scale laboratories. In fact, most of the laboratory space is required by the high-power laser and the radiation shielding. Whereas particle accelerator have initial costs in the ballpark range of hundreds of million Euros, the most expensive equipment for a LWFA is the high-power laser, which costs including infrastructure only several million Euros.

Secondly, compared to other electron sources, LWFA electron beams are unique with respect to their ultrashort electron pulse duration, as the electron bunch length is estimated to be shorter than half the bubble length, i.e. the length of the accelerating part of the wakefield. Comparison with (2.124) and (2.113) suggests durations shorter than the plasma period, which for plasma densities of 10^{19} cm^{-3} would be shorter than 35 **fs**. 3D Particle-in-Cell (PIC) simulations suggest that these bunch durations could become even shorter than 10 **fs** [54]. In addition these beams are intrinsically synchronized with the laser beam and have a small source size, which is generally comparable to the laser focal spot size (see (2.124) and Fig. 2.13). Quantitatively, experimental estimates based on measured electron energy, divergence and an assumed initial electron bunch diameter in the bubble, which according to PIC simulations is smaller than the laser focus (see Fig. 2.13 and [48, 54, 61]), suggest that transverse emittances can be as small as $\simeq 0.1 \pi \text{ mm mrad}$, which is about an order of magnitude lower than from conventionally accelerated electron beams.

All this makes LWFA beams hugely attractive as a basis for driving a synchrotron light source in the hard X-ray range for pump-probe type of experiments. Again, such a setup could be compact

enough to fit into a university laboratory.

This has dramatic consequences for the overall electron phase space density, which is often also called the beam peak spectral brightness or peak brilliance

$$B_{\text{el}} = \frac{N_e}{\tau_{\text{beam}} \epsilon_{\text{norm,trans}}^2 [\pi \text{ mm mrad}] (10^3 \cdot \Delta E/E_0)}. \quad (2.130)$$

Here N_e is the total electron number, $\Delta E/E_0$ the relative energy spread and τ_{beam} the electron pulse duration. This quantity is mostly used to compare *photon* sources, such as X-ray beams from third generation synchrotrons or free-electron lasers. The higher the number, the higher in principle the phase space resolution for experiments. Since phase space volume is a conserved quantity under linear transformation (Liouville's theorem [62, 63]), this number is also a useful indicator on the tradeoffs between the parameters of the photon source.

Since the brightness of synchrotron sources depends on the original electron beam brightness, it is useful to compare the beam LWFA brightness to conventional beams. Although the relative energy spread of laser-accelerated beams is still one order of magnitude higher than in conventional beams (10^{-2} compared to 10^{-3}), the improvements in spatial and temporal properties in LWFA electrons improve the beam brightness by two orders of magnitudes.

Outlook on Laser wakefield-acceleration

For laser-accelerated electrons the critical tasks at hand are further increases in the maximum electron energy, realization of staging, serious improvements in the shot-to-shot stability of electron beams and decrease the relative energy spread. Towards these goals there exists a number of promising approaches.

First, shorter lasers with laser pulse durations comparable to the plasma period $\tau < 30 \text{ fs}$ and below could immediately drive a "bubble" type plasma wave, without first undergoing self-modulation until the laser pulse has become short enough to drive the wake. This has the advantage of a longer effective acceleration length and less nonlinear self-phase modulation, which through its nonlinearity introduces shot-to-shot-fluctuations.

Secondly, higher energies can be obtained, by increasing the interaction region of a focused laser within the plasma up to the dephasing length. Within gas jets relativistically, self-focused plasma channels can only sustain **mm** distances. Hence, plasma waveguides are used for enhancing the laser pulse guiding distance. The concept of using gas-filled capillary waveguides [64] have proven to be successful up to the **GeV** level. An alternative concept are optically, preformed plasma channels [65, 66], where the diameter of the guided mode can be significantly smaller $< 10 \mu\text{m}$ than in capillaries and thus realize higher intensities and smaller electron source sizes.

Furthermore, gas targets should be more homogeneous to obtain more even plasma densities in the propagation direction. This has been realized by [67, 68] in a capillary setup with two gas inlets and little gas flow in between. The resulting plasma conditions have proven to be homogeneous enough to reproduce similar monoenergetic electrons at each shot. In addition

the capillary setup is used as a plasma waveguide, that enables longer acceleration distances than in a gas jet.

Also, the electron injection process can be improved. In most experiments the electrons are self-injected by plasma wavebreaking above a threshold laser intensity of $a_0 > 4$ [52, 54], which is a highly-nonlinear regime susceptible to small changes in initial conditions. To avoid these nonlinearities, one approach is to optically trigger the plasma wave breaking. By an additional pair of counter-propagating laser pulses select time and space, where electrons from the plasma wave in the combined focus are injected into and trapped in the acceleration cavity of the plasma wave. With this technique monoenergetic electrons with tunable electron energies have been generated [69].

Instead of externally triggering plasma wavebreaking another strategy is to employ smooth gradients as obtained by gas jets to quickly decrease the density, such that a plasma wave breaks and thus self-injects electrons. In contrast to self-injection at high intensities the point of injection can be spatially controlled by the electron density and depends to a much lesser extend on the complex interplay between intense laser pulses and plasma wave. A first experimental demonstration can be found at [70, 71]

An other promising approach is external injection of electrons into the wakefield. Here, a low energy electron bunch is created with an electron gun and is subsequently injected into the laser plasma wakefield and accelerated to high energies. For electron bunches that are longer than a plasma wavelength, the idea is to inject a low energy electron bunch in front of the laser pulse, which overtakes it, such that all of the electrons are trapped by the wakefield behind and thus accelerated [72, 73]. This could become possible with externally injected electron beams in small-amplitude, non-wavebreaking wakefields in a laser beam guiding setup such as a capillary. Since this approach requires an electron gun and electron focusing system to be combined and synchronized with a laser wakefield accelerator, it is technically challenging. However, of all injection techniques, this potentially yields the most control over electron beam properties, such as the energy spread.

3 ULTRASHORT ELECTRON BUNCHES FROM LASER WAKEFIELD-ACCELERATION

Ultrashort electron bunch durations are one of the key properties for brilliant radiation sources. This is especially true for laser-wakefield driven SASE-FELs, which require high electron peak currents in the **kA** range and thus electron bunch durations significantly below **100 fs**, shorter than those achieved by conventional accelerators, and charges beyond **10 pC**. Here, the main question does not yet concern a practicable undulator setup or a sizable photon yield, but asks whether LWFA electron bunches are short enough for FEL lasing. Since a small FEL parameter ρ also leads to an even stricter condition on energy spread (2.82), a long electron bunch duration would effectively undermine the entire concept of a table-top FEL using laser-wakefield acceleration. Previous experimental efforts [1, 2] were limited in resolution to **100 fs** and hence were unable to answer this question. Therefore, it is not fully understood how these short electron pulses from LWFA evolve during and after they leave the plasma and whether their duration stays short. Finally, measuring the temporal structure of such electron bunches is of great importance also from an engineering point of view: If LWFA electrons are to be tailored for specific applications, it is necessary to be able to measure the bunch duration before the latter can be subject to optimization.

According to theory (ch. 2.5), one expects that the electron bunch length $c\tau_e < R_b$ is smaller than the bubble radius R_b , since a longer electron bunch would not spatially fit anymore into the accelerating gradient of the wakefield. In that case electrons at the front and back of the bunch would be accelerated to largely different energies, because the front electrons are decelerated in the front half of the bubble, where the field is reversed, while the electrons at the back are still being accelerated. For a standard bubble, with matched beam spot sizes, homogeneous plasma density, regular laser pulse and no beam-loading, the bubble radius according to (2.124) is $R_b = \lambda_p \cdot \sqrt{a_0}/\pi$. Considering a minimum laser intensity of $a_0 \simeq 4$ to achieve self-injection in the bubble regime this corresponds to a bubble radius of $R_b \simeq 0.6\lambda_p$. Hence for typical electron

densities of about $\sim 10^{19} \text{ cm}^{-3}$ this agrees with bunch durations of 35 fs and lower.

However the plasma wavelength estimate for the bubble diameter is not absolute, since beam loading can substantially alter the length of a bubble. A bunch with a trapezoidal longitudinal charge profile can elongate the bunch duration, while maintaining a low energy spread [3]. Precisely this beam loading is intrinsically linked to the dynamics of the electron injection and is highly nonlinear for self-injection [3–6] and thus very sensitive to the initial plasma and laser conditions. In 3D-PIC simulations, one discerns brief injection of a dense electron bunch, which terminates the injection process by its own space-charge and continuous injection of electrons until the entire bubble is loaded from back to front.

Even the argument that electrons, which are later measured to have the same energy, should have been injected at the same time and the same spatial region can fail, as there exist several plasma processes [7, 8] that are strong enough to excite betatron oscillations within different parts of the electron bunch. As these oscillation amplitudes can be on the order of microns, this potentially leads to different propagation distances within the bunch, so that even electrons of similar energy become spatially separated, even if these were originally injected as a short bunch.

From a theoretical perspective, present 3D-PIC simulations have mainly investigated the formation of the plasma wakefields, as well as subsequent electron injection and acceleration. The simulation were for reasons of limited computing power often terminated, when the electrons were still in the middle of the plasma. Especially 3D simulations with realistic parameters, such as diameters of more than 10 μm or laser durations of several 10 fs are computationally expensive, since small grid spacings are required to obtain reasonably accurate results over several mm propagation distances. Also the simulations usually assume uniform plasma densities or smooth density gradients as initial conditions, which is not necessarily the case for real gas jets in experiment. Therefore the influence of realistic gas perturbations on the electron bunch and the transition from plasma to vacuum, where the plasma density drops and the plasma bubble subsides, is not fully understood.

From an experimental perspective, all experiments in the bubble regime have consistently shown that small changes in the percent range in plasma density or laser pulse shape and intensity substantially alter beam energy, charge, divergence and pointing, so that one would expect the same for the electron bunch duration. Hence, there is yet no experimental evidence and so far no theoretical investigation assuming realistic conditions which confirm the assumption of ultrashort, monoenergetic electrons from LWFA.

The main challenges of ultrashort electron bunch duration measurements are potential durations being shorter than the drive laser pulse, the lack of shot-to-shot stability and the harsh environments of the plasma. Electronic measuring techniques, such as integrating current transformers (ICT) immediately fail at the sub-ps time scales and thus can only be used to measure the charge. Therefore an optically driven technique is required. However, the short time scale makes even direct approaches with laser pulses probing or scattering of the electron bunch difficult, since the spatial and temporal dimensions of the laser are larger than the electron beam. The lack of shot-to-shot stability currently prevents multi-shot or scanning techniques, while the plasma conditions place more strict requirements on a measurable signal-to-noise ratio.

Here, the duration of quasi-monoenergetic, laser-wakefield accelerated bunches is measured for the first time and is shown to be indeed shorter than the laser pulse duration. In a single-shot, electro-optic (EO) experiment, two electron distributions, accelerated by the 10 TW, 45 fs ASTRA laser pulse are clearly distinguished. By analyzing coherent transition radiation (CTR) from a thin aluminum tape target following the plasma region, a long electron pulse trailing a short bunch of quasi-monoenergetic electrons could be observed. When this data is combined with additional knowledge gleaned from the electron energy spectrum and the geometry of the CTR source, this allows to partially overcome the resolution limit set by a transverse-optical phonon resonance of the EO crystal and infer an electron bunch duration below 38 fs (FWHM).

3.1 BASICS OF TRANSITION RADIATION

Transition radiation is a relativistic boundary effect which occurs when an electron passes suddenly from one dielectric medium to another [9–12]. Qualitatively, the electrons in the beam repel the electrons in the medium the beam passes by, which causes time-varying radial currents in metals or polarization waves in dielectrics and thus radiation due to accelerated charges. In the bulk material all these radiation contributions vanish, either by absorption in the material or destructive interference. As long as the phase velocity of the radiation is not the same as the velocity of the relativistic electron exciting the radiation, the phase-average in the bulk leads to destructive interference – otherwise, there would be Čerenkov radiation. So for every plane wave excited at one position in the bulk there exists another plane-wave, which has the opposite phase. However, when the index of refraction changes rapidly, like at the interface to another medium this symmetry is broken and radiation near the surface does not interfere destructively. From a step-like interface between an ideal conductor and vacuum, a single electron emits radiation according to the Ginzburg-Frank formula [9, 13]

$$\frac{d^2 W_e}{d\omega d\Omega} = \frac{r_e m_e c}{\pi^2} \frac{\beta^2 \sin^2 \theta}{(1 - \beta^2 \cos^2 \theta)^2}, \quad (3.1)$$

where $r_e = e^2/(4\pi\epsilon_0 mc^2)$ denotes the classical electron radius and θ the direction of observation with respect to the electron direction of propagation. According to (3.1) and $\gamma_0 \gg 1$ the resulting transition radiation (TR) vanishes on axis $\theta = 0$, reaches its maximum at $\theta \simeq 1/\gamma_0$ and quickly reduces for larger angles (see Fig. 3.1(a)). The radiation energy distribution is axially symmetric and as depicted in Fig. 3.1(b) the radiation is linearly polarized within the plane spanned by the axis of the electron trajectory and the respective observation vector, such that the entire transition radiation beam can be described as being radially polarized.

Note that in (3.1) there is no frequency dependence, which is obviously unphysical and arises from the assumption of an ideal semi-infinite conducting plane. In reality however, the dielectric coefficient ϵ of the metal is finite and a function of frequency.

To illustrate this point, consider a finite metal target as depicted in Fig. 3.1(b). In the laboratory frame the Coulomb field of the relativistic electron passing through the foil is compressed to almost a disc with an opening angle of $1/\gamma$ and the field is directed nearly perpendicular to the direction of propagation. Therefore the metal electrons close to the passing electron experience

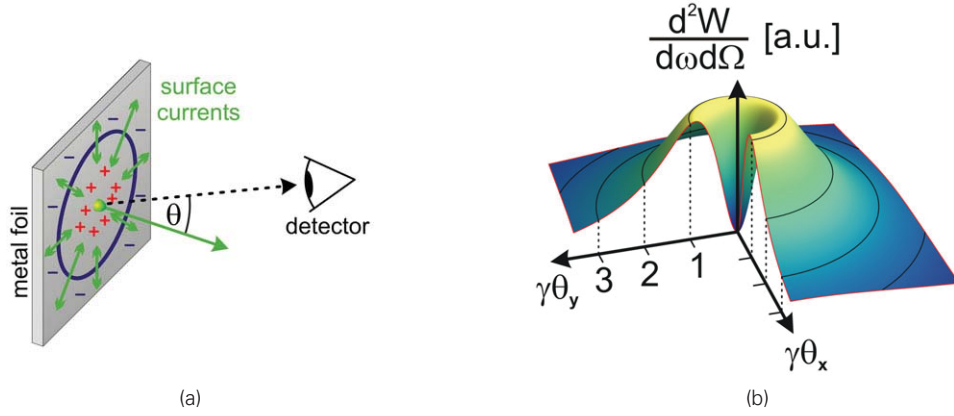


Figure 3.1: (a) An electron passing through a metal foil generates radial surface currents by its Coulomb force. (b) features the resulting radiation angular profile of the TR spectral intensity.

a much faster displacement kick from the relativistic electron than those metal electrons that are further away. This explains the frequency independence of the TR far field spectrum in (3.1) and why for any finite radiator target there always exists a long wavelength cutoff.

At the other end of the spectrum, when the radiated frequencies approach the metal plasma frequency, the radiating material becomes transparent. Then the step-like transition in the dielectric coefficient at the metal-vacuum interface vanishes and thus stops to radiate. However, the TR frequencies ω discussed here are far below the optical range and thus much smaller than the cutoff frequency $\omega_c = \gamma_0 \omega_p$. So in the following the assumption of an ideal conducting metal foil is assumed to be valid.

If not only one electron, but an entire electron bunch with N_e electrons crosses the metal-vacuum interface, one has to account for the superposition of all resulting fields. Thus, at wavelengths much longer than the bunch dimensions, the electric fields arising from the TR of the individual electrons have negligible differences in phase and add up coherently. Therefore the spectral energy of coherent transition radiation (CTR)

$$\frac{d^2 W_{\text{CTR}}}{d\omega d\Omega} = N_e^2 \cdot \frac{d^2 W_e}{d\omega d\Omega} \quad (3.2)$$

scales with the square of the number of electrons. On the other side, at wavelengths that are much smaller than the bunch dimensions, the resulting fields cover all phase differences and hence the fields add up incoherently, so the spectral energy of incoherent transition radiation (ITR)

$$\frac{d^2 W_{\text{ITR}}}{d\omega d\Omega} = N_e \cdot \frac{d^2 W_e}{d\omega d\Omega} \quad (3.3)$$

scales linear with electron number. The electric field in the time domain and the far field is according to [14]

$$\mathbf{E}(\mathbf{x}, \omega) = -\frac{2eN_e}{cR} \langle \mathcal{E}(\theta, u) D(\omega, u, \theta, \rho) F(\omega, u, \theta) \rangle_u e^{ikR} \mathbf{e}_\perp. \quad (3.4)$$

Here R is the distance between the interaction region and the point of observation \mathbf{x} , θ the observation angle with respect to the electron direction of propagation and $u = p/mc^2 = \beta\gamma$ the

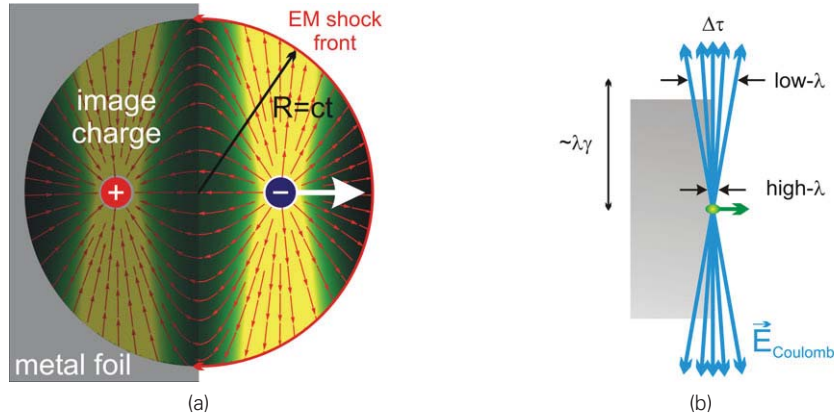


Figure 3.2: (a) In the time-domain, transition radiation can be seen as the generation of an electron and an image charge pair at the metal-vacuum interface. Since the emerging electric fields can only propagate with the speed of light and have to end at the metal surface, this leads to an electromagnetic shock front, which explains the broad spectra of transition radiation. The peaked forward radiation arises from the longitudinally contracted EM fields of the relativistic electrons propagating close to the EM shock front at the respective radius $\beta \cdot R$. Due to same highly contracted Coulomb field of the electron, there exists no field and thus no TR emission into the forward direction. (b) The long wavelength cut-off of TR at a finite radiator originates from long wavelength surface currents being generated at a distance b from the electrons $\lambda \sim c\Delta t \propto b\gamma_0/c\beta_0$.

normalized electron momentum. The field amplitude analogue of eq. (3.1) is denoted by

$$\mathcal{E}(\theta, u) = \frac{u\sqrt{1+u^2}\sin\theta}{1+u^2\sin^2\theta}, \quad (3.5)$$

and the other two quantities $D(\omega, u, \theta, \rho)$ and $F(\omega, u, \theta)$ are the diffraction and electron bunch form factor respectively. The diffraction factor

$$D(k, u, \theta, \rho) = D(b, u\sin\theta) = 1 - J_0(bu\sin\theta) \left[bK_1(b) + \frac{b^2}{2}K_0(b) \right] - \frac{b^2}{2}K_0(b)J_2(bu\sin\theta), \quad (3.6)$$

$$\text{with } b = k\rho/u \quad (3.7)$$

describes the effect of a finite transverse boundary with a radius ρ , i.e. a circular metal disc rather than an infinitely large foil. It is derived by applying Kirchhoff diffraction theory [15] to the incident fields [16]. Since the self-field of the relativistic electrons extends transversally a distance $\gamma\lambda$, diffraction radiation becomes relevant for small frequencies, where this distance exceeds the transverse size ρ of the radiating foil. This is expressed with the scaling parameter b in eq. (3.7). Diffraction effects can be neglected, when $D(k, u, \theta, \rho)$ is close to unity for all angles θ within the TR radiation cone.

The spatial form factor describes the degree of coherent transition radiation that is emitted by some electron bunch at a given frequency ω , where full coherence is $F = 1$. $F(\omega, u, \theta)$ contains all information on the electron bunch structure and is defined as

$$F = \frac{1}{g(u)} \int d^2\mathbf{r}_\perp e^{-i\mathbf{k}_\perp \cdot \mathbf{r}_\perp} \int dz e^{-iz\omega/v} f(\mathbf{r}, u) \quad (3.8)$$

where $g(u)$ denotes the momentum distribution and $f(\mathbf{r}, u)$ the electron beam distribution including both momentum and spatial properties. For electron bunches with uncorrelated, Gaussian distributions,

$$f(\mathbf{r}, u) = g(u) \cdot \frac{1}{(2\pi)^{3/2} \sigma_r^2 \sigma_z} e^{-\frac{r^2}{2\sigma_r^2} - \frac{z^2}{2\sigma_z^2}} \quad (3.9)$$

where σ_r and σ_z are the root mean square (RMS) bunch diameter and length respectively. According to eq. (3.8) one arrives at a form factor of

$$F_G = e^{-(\omega\sigma_z/c)^2/2 - (\omega\sigma_r \sin \theta/c)^2/2}, \quad (3.10)$$

which is equal to one for short $\sigma_z/c \ll \omega$ electron bunches with small transverse extent $\sin \theta \cdot \sigma_r/c \ll \omega$. These two conditions determine the degree of longitudinal (temporal) and transverse coherence respectively. The far-field electric field of CTR in the time-domain is then derived by a Fourier transform of (3.4)

$$\mathbf{E}(\mathbf{x}, t) = -\frac{eN}{\pi R} \mathbf{e}_\perp \int dk \langle \mathcal{E}(\theta, u) D(\omega, u, \theta, \rho) F(\omega, u, \theta) \rangle_u e^{-ik(ct-R)}, \quad (3.11)$$

which with (3.10) and (3.11) simplifies to

$$\mathbf{E}(\mathbf{x}, t) = -\frac{2eN}{\pi R} \mathbf{e}_\perp \left\langle \mathcal{E}(\theta, u) \int_0^\infty dk \cos(k(ct-R)) \times D(k\rho/u, u \sin \theta) \exp\left(-\frac{(k\sigma_z)^2}{2\beta^2}\right) \right\rangle_u. \quad (3.12)$$

Although it is necessary to include diffraction effects for arriving at a bipolar electric field that fulfills the Maxwell equations, the limit of no diffraction $D = 1$, where the electric field in (3.12) becomes

$$\mathbf{E}(\mathbf{x}, t) \propto \exp\left[-\frac{\beta^2(ct-R)^2}{2\sigma_z^2}\right], \quad (3.13)$$

is useful to illustrate that the electric field from CTR is a single period pulse with a duration σ_z/c resembling the duration of the electron bunch. This is the physical basis of time-domain measurements of the electron bunch duration and is used in the following to determine the electron bunch duration. The challenge is to measure this field in experiment in a way that preserves enough of the spectral amplitude and phase information to be able to reconstruct the original electric field duration.

3.2 ELECTRO-OPTICAL EXPERIMENT FOR MEASURING THE ELECTRON BUNCH DURATION

Electro-optic method

On a time scale longer than several tens of fs, the frequency of a single CTR pulse is in the THz range, which is in the far infrared and thus makes direct measurements, both in the time-domain and the spectral domain, difficult. Hence a well-known strategy in accelerator physics is to use another physical process to map the electric field to the optical part of the spectrum, where sensitive and ultrafast diagnostics are available. Especially electro-optic crystals that rely

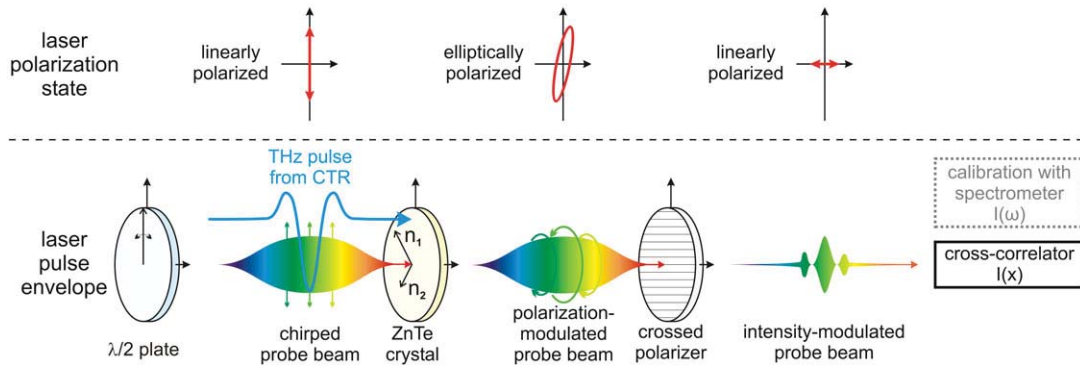


Figure 3.3: A chirped probe (CP) beam is sent through a zinc telluride (ZnTe) crystal. Parallel to the probe beam the CTR pulse (blue), which is in the THz frequency range, is sent through. Due to the Pockels effect the polarization of the CP is rotated. This rotated portion of the laser beam is subsequently transmitted through the crossed-polarizer. Thus the CTR field is imprinted as a modulation on the CP beam. This beam can then be analyzed in a spectrometer or for higher resolution in a cross-correlator.

on the Pockels effect have proven to be a successful technique [17, 18]. The basic working principle is depicted in Fig. 3.3, where a chirped laser pulse longer than the electron bunch is transmitted through a thin electro-optical crystal. Normally, when no external fields are present, the laser pulse is transmitted unaltered. A static field however changes the optical properties of the crystal, such that it becomes a wave plate, which retards the laser polarization components with respect to each other and thus introduces an elliptical polarization, see Fig. 3.4. The phase delay

$$\Gamma = \frac{\omega_0 d_{\text{cryst}}}{c} (n_1 - n_2) = \frac{2\pi d_{\text{cryst}}}{\lambda_0} n_0^3 r_{14} E_\alpha \quad (3.14)$$

corresponds to the difference in the indices of refraction $n_1 - n_2$ of the two principal crystal axes and is proportional to the static electric field strength E_α applied to the crystal. The nonlinear efficiency coefficient r_{14} and the isotropic optical index of refraction n_0 denote the material properties of the used crystal.

In this experiment the external field is provided by the “quasi-static” CTR field, that is focused along with the laser beam. In passing it should be noted, that the Lorentz-contracted Coulomb field of the electron bunch as shown in 3.1(b) is also a good signature for the electron bunch duration that could be used in an electro-optic setup [19], however the vicinity of a plasma and an intense laser makes signal discrimination for LWFA electrons prohibitively difficult, so that transition radiation at a foil is used to spatially separate the diagnostics from harsh measurement conditions near the plasma and ensure that the THz radiation comes from transition radiation and not from within the plasma.

This change in polarization can then be filtered by polarization optics. The crossed polarizer behind the crystal blocks the sections of the chirped probe beam with unaltered polarization, while perpendicular polarization components

$$E_{L,\perp} = \frac{1}{\sqrt{2}} (\cos \Gamma - 1) \cdot E_L \quad (3.15)$$

from the elliptically polarized beam E_L are transmitted. In this way, the polarization modulation,

arising from the CTR and hence the electron bunch itself, is imprinted onto the CP beam envelope, which then is detected by cross-correlation diagnostics [17].

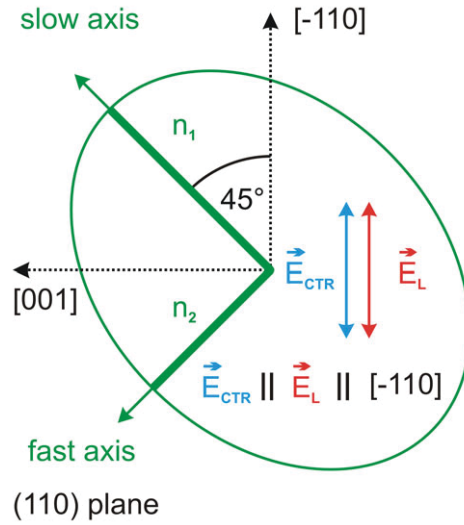


Figure 3.4: The refractive index ellipsoid projected onto the (110) plane of a ZnTe crystal. For maximum difference in the indices of refraction, the electric field vector \mathbf{E}_{CTR} encloses a 45° angle with the $[-110]$ axis of the crystal. The laser field \mathbf{E}_{CTR} is parallel to \mathbf{E}_L . Both the quasi-static electric field \mathbf{E}_{CTR} from coherent transition radiation and the laser propagate normal to the $[001]$ direction and (110) plane.

Electro-optic setup

The experimental setup is depicted in Fig. 3.5. The main part of the ASTRA laser pulse (45 fs, 500 mJ) is used to accelerate electrons in a supersonic gas jet similar to that of [20]. Using transverse interferometry, the electron density is measured (see Fig. 3.6(b)) to be $1.5 \times 10^{19} \text{ cm}^{-3}$, which corresponds to a plasma period of 30 fs. The electron spectrum is recorded using image plates and a magnetic spectrometer, while the charge is measured by an integrating current transformer (ICT).

An aluminum tape of 50 μm thickness is installed 5 mm behind the gas jet and acts as a source of coherent transition radiation (CTR). In addition, the tape blocks intense THz radiation from other sources such as the plasma wakefield accelerator [21], from linear mode conversion [22] and CTR from the plasma-vacuum transition [1]. The CTR emitted from the tape is collimated and focused into a 200 μm thick ZnTe crystal ($\langle 110 \rangle$ orientation, supplied by Ingcrys laser systems) using a pair of off-axis parabolas (OAPs), the first of which is equipped with a central hole (1 cm dia.) to transmit the electrons and the drive laser beam. A Teflon filter placed between the OAPs additionally blocks scattered laser light. 1 mJ of the ASTRA pulse is split off, negatively chirped to 5 ps duration in a Treacy-type grating arrangement and focused through the ZnTe crystal. The EO crystal material was chosen for its high nonlinear coefficient and the thickness of 200 μm to minimize signal-probe group velocity walk off. Because the diffraction limited beam ($w_0 = 100 \mu\text{m}$) is offset by $d = 600 \mu\text{m}$ from the radially polarized CTR focus, the THz field polarization within the probe beam can be assumed to be linear. The transient birefringence induced in the crystal by the THz pulse via the electro-optic Pockels effect rotates the polarization of the chirped

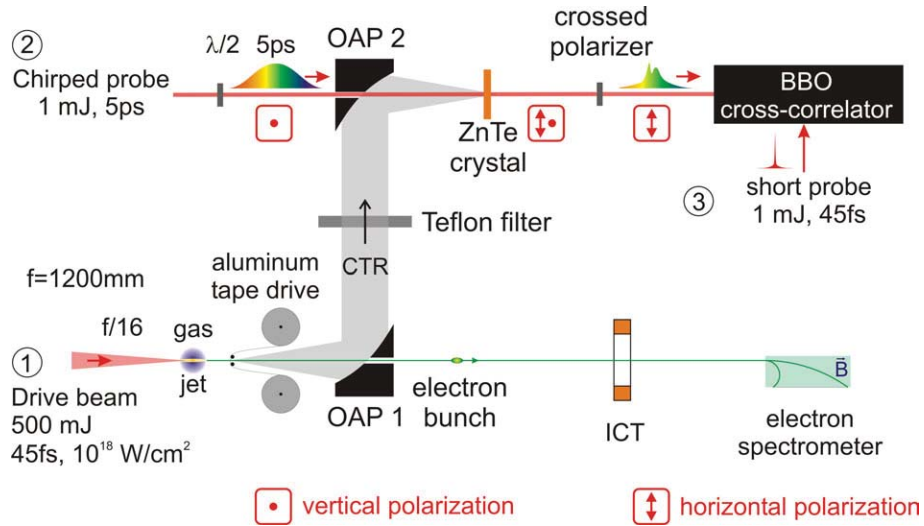


Figure 3.5: Laser-accelerated electrons generate coherent transition radiation (CTR) at an aluminum tape target. The CTR is imaged by two off-axis parabolas ($f_1 = 125 \text{ mm}$ and $f_2 = 250 \text{ mm}$) into an electro-optical ZnTe crystal, which rotates the polarization of a chirped probe (CP) beam in the time-domain. This modulation of the CP is analyzed in a cross-correlator.

probe (CP) beam. The resulting change in polarization encodes an intensity modulation onto the CP after passing through a crossed polarizer. The temporal evolution of this intensity modulation – and thus the temporal structure of the CTR pulse – is then probed directly by another 1 mJ , 45 fs part of the ASTRA laser pulse in a cross-correlator, similar to that in [17, 23].

Since the probe beam is chirped, it is in principle possible to use a simple spectrometer to measure the envelope modulation in the spectrometer. However there are some severe constraints that limit the resolution of such a diagnostic, as there exists a time-bandwidth relationship between the bandwidth of the chirp and the minimum bunch length that can be resolved [24]. For bipolar THz signals one can derive a measure for the shortest resolvable pulse length $\tau_{\min} = \sqrt{\tau_{\text{chirp}} \cdot \tau_0}$, where τ_{chirp} and τ_0 are the CP and non-stretched laser pulse duration respectively. As τ_{\min} in this experiment was on the order of 500 fs , the spectrometer was mainly used as a first diagnostic to find the EO signal and optimize the experiment for maximum signals. The maximum resolution of the cross-correlator on the other hand is given by the laser pulse length of the reference pulse, which here is on the order of 45 fs .

3.3 LIMITATIONS IN RESOLUTION

For the analysis of the experimental data the electron beam is assumed to consist of a low-emittance ultra-short electron bunch followed, after a time $\Delta\tau$, by a divergent tail of low energy electrons with a temperature T_e and duration τ_{long} . This assumption is motivated by simulations of the highly nonlinear broken-wave regime [25] and is experimentally supported by simultaneously recorded electron spectra, such as the one shown in Fig. 3.6(a). The spectrum suggests that one part of the 30 pC electron beam is accelerated to an energy of 40 MeV , with an RMS energy spread of 7 MeV , while the rest of the beam, the low energy part, exhibits an exponential

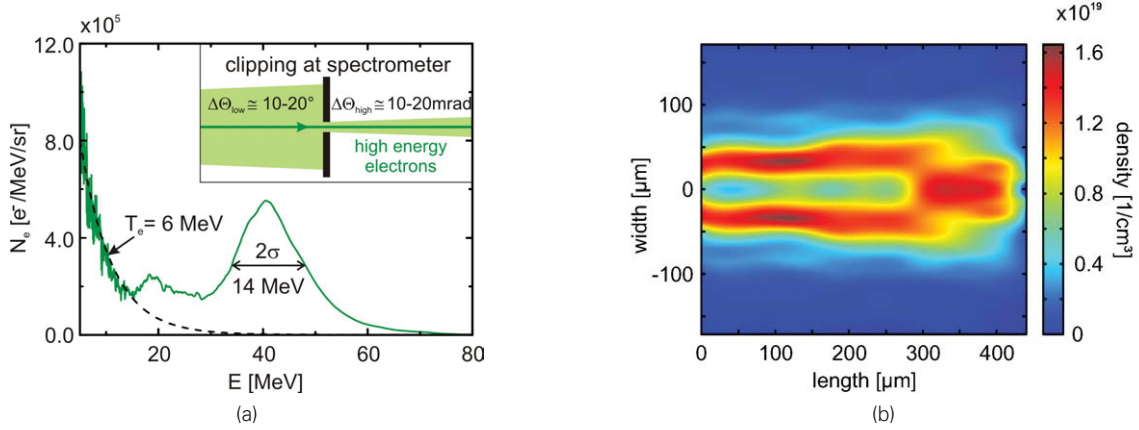


Figure 3.6: (a) A typical electron spectrum as recorded with the pulse duration measurement. Due to clipping at the spectrometer aperture, the number of low-energy electrons (dashed line) reaching the spectrometer is reduced by more than an order of magnitude. (b) shows the electron density n_e of the plasma channel, measured by transverse interferometry, in which the index of refraction was probed using spatial-fringe analysis. Since only one direction could be probed in the experiment, rotational symmetry is assumed in the electron density reconstruction.

spectrum with $T_e = 6 \text{ MeV}$. The existence of two temporally separated electron populations is confirmed by the doubly peaked cross-correlator intensity trace as shown in Fig. 3.8(B2) and were only measured when monoenergetic features were present in the electron spectrum.

The ZnTe crystal has a transverse optical phonon resonance at 5.3 THz , which limits the intrinsic resolution to $\simeq 180 \text{ fs}$. To understand how to overcome this limit consider a Gaussian-type CTR pulse much shorter than the temporal resolution limit. In the spectral domain, as shown in Fig. 3.7, this is equivalent to a Gaussian spectrum centered around zero frequency [14, 19, 26], which reaches far beyond the observable ZnTe frequency window. Inside that window, it displays a nearly constant spectral amplitude. However, different pulse durations can still be differentiated by their spectral amplitude at the cutoff frequency. Thus, the ratio of the spectral energy at high frequencies and the total radiated energy is a sensitive indicator of electron bunch duration variations. To detect them, one makes use of the sharp, 3-fold increase in the ZnTe index of refraction between 4 and 5 THz close to the resonance. This increase delays and attenuates the high frequency components, which in the time-domain appear as damped field oscillations trailing the main pulse as in the blue curve in Fig. 3.8(B1).

This effect of trailing field oscillations in the measured signal can be shown by assuming an ideal THz pulse (3.13) without diffraction effects and using it as input for the ZnTe crystal. In such a scenario all other effects which can limit the transmitted spectrum of the THz pulse are being neglected. At some depth z_d into the ZnTe crystal, the effective electric field responsible for the phase delay from birefringence is

$$E^{\text{eff}}(t, z_d) = \mathcal{F}^{-1} \left[\mathcal{F}[E_{\text{CTR}}(t)] \cdot A_{\text{trans}}(f) \cdot \exp \left(i \frac{2\pi f}{c} n(f) z_d - \frac{2\pi f}{c} \kappa(f) z_d \right) \cdot r_{41}(f) \right],$$

with $A_{\text{trans}} = \frac{2}{n(f) + i\kappa(f) + 1}$. (3.16)

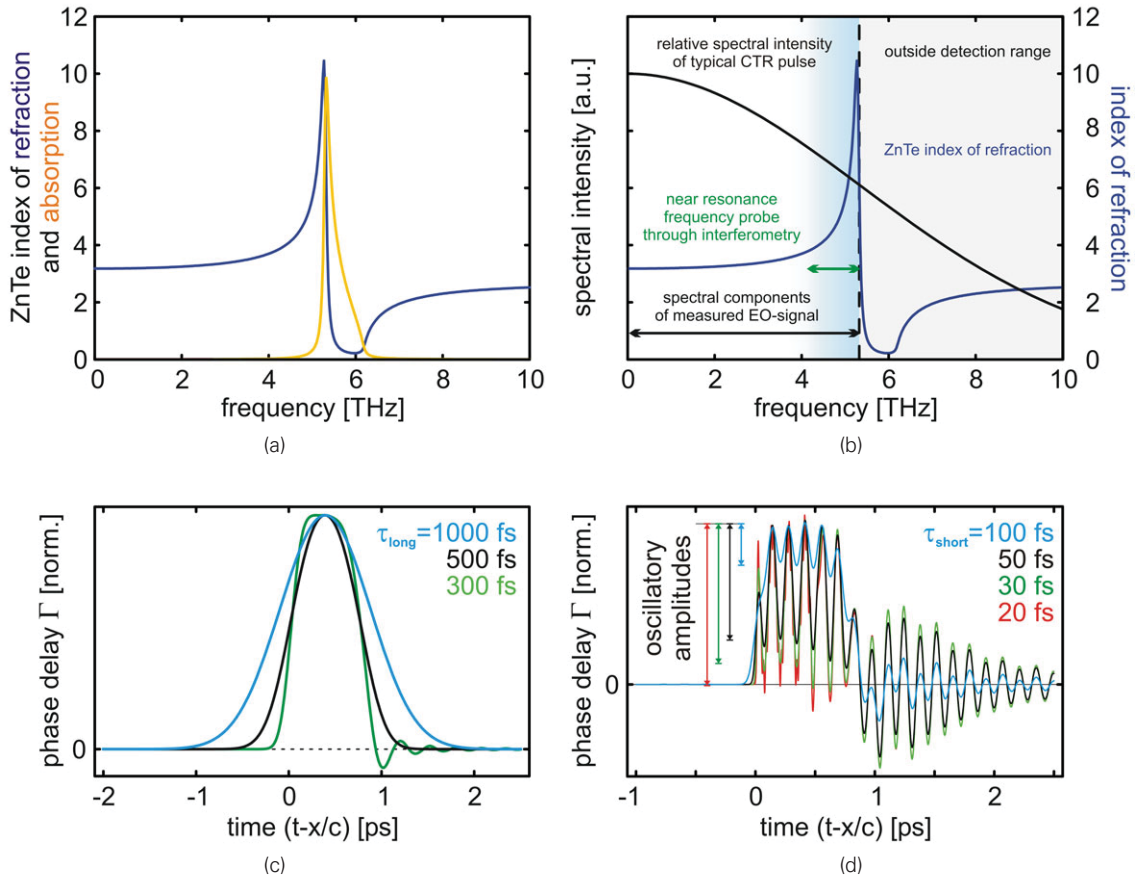


Figure 3.7: (a) depicts the index of refraction $n(\nu)$ (red) and absorption $\kappa(\nu)$ of ZnTe in the THz range. It features a transverse optical resonance at 5.3 THz. (b) shows the CTR spectrum of an ideal, ultrashort CTR pulse. In the experiment, high frequencies above 6 THz are attenuated, due to the Teflon filter and the focusing geometry. The strong change in the index of refraction near the ZnTe resonance gives rise to strong delays for this spectral amplitude, which can be measured. (c) depicts the ZnTe birefringent phase delay $\Gamma(t)$ in a laser beam, when above-resolution signals with $\tau > 5.3 \text{ THz}^{-1}$ according to (3.13) are used. Both pulse shape and width can be distinguished. (d) For below-resolution signals with $\tau < 5.3 \text{ THz}^{-1}$ this distinction does not exist anymore. The spectral amplitude near resonance shows as an oscillation in the signal, which becomes larger for shorter CTR pulses.

Hereby, the original CTR field E_{CTR} has been Fourier transformed $E_{\text{CTR}}(f) = \mathcal{F}[E_{\text{CTR}}(t)]$ to the frequency-domain, where it is weighted by the transmissivity of the crystal front surface $A_{\text{trans}}(f)$, the absorption $\kappa(f)$ and the phase delay due to the ZnTe index of refraction $n(f)$, as well as the electro-optic coefficient $r_{41}(f)$. After back transformation into the time domain (3.14) can be obtained, by convolving $E^{\text{eff}}(t, z_d)$ and the stretched laser pulse propagating at the group velocity v_g along the entire crystal.

$$\Gamma(t) = \int_0^{d_{\text{cryst}}} \frac{2\pi}{\lambda_0} n_0^3 E_{L,0}(t) \cdot E^{\text{eff}}(z_d/v_g + t, z_d) dz_d \quad (3.17)$$

The result is the relative phase delay $\Gamma(t)$ between ordinary and extraordinary polarisation of the probe laser. For long THz pulses of 1000 fs, 500 fs and 300 fs as shown in Fig. 3.7(c), both the shape and pulse duration are reasonably preserved. For CTR pulse durations below 100 fs as

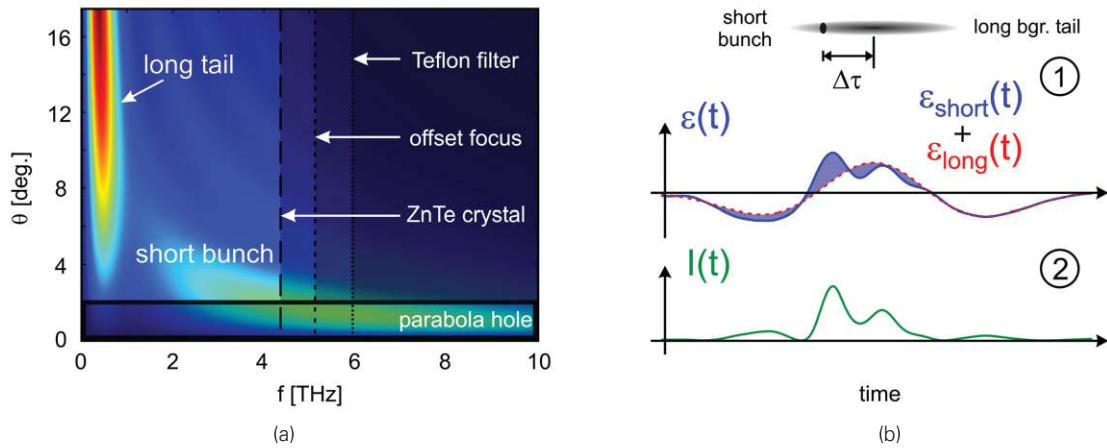


Figure 3.8: (a) The angular-spectral intensity of coherent transition radiation (CTR) from a short electron bunch ($\tau_{\text{short}} = 32 \text{ fs}$) followed after a time $\Delta\tau = 356 \text{ fs}$ by a long, low-energy electron background ($\tau_{\text{long}} = 712 \text{ fs}$) is constrained by several filter functions (arrows illustrate respective cutoff frequencies), affecting the overall time resolution. (b) In the time domain the CTR field is a superposition of the low-energy electrons (red curve) trailing in the wake of an ultrashort, sub-resolution electron bunch (1). The resulting interference (green curve) is measured as an intensity trace in the cross-correlator and includes effects of polarization optics (2).

depicted in Fig. 3.7(d), the resulting signal does not follow anymore the original pulse shape, but features oscillations trailing the first peak. While the oscillation period is largely determined by the position of the TO resonance in ZnTe, the relative oscillation amplitudes depends on the field near the resonance. This leads to shorter CTR pulses featuring more pronounced oscillations, because they have larger spectral amplitudes near resonance. Note that neither diffraction, focusing nor the transmission through a Teflon filter are considered in this example and that these alter the overall spectral envelope and thus lead to different signals. However, the spectral sensitivity near the ZnTe resonance and the corresponding oscillation amplitude for short THz signals generated by short electron bunches can be expected to be preserved in the experimental data.

From Fig. 3.7(c) it can be seen that signals beyond 200 fs above the resolution limit of the crystal resonance are not heavily distorted. The fact that long above resolution signals can be directly measured can be exploited to separate the signal contribution of THz signals from very long and extremely short electron distributions. By using the long background field $\epsilon_{\text{long}}(t) > \epsilon_{\text{short}}(t)$ as a bias for the electric field $\epsilon_{\text{short}}(t)$, this background defines a zero-field reference for the short THz field and thus preserves the latter's sign information in the cross-correlator intensity trace $I(t)$ (see green curve in Fig. 3.8(B2)). For the same reason the measurement is also robust against small polarization imperfections within the diagnostic system, which affect the entire signal, but not the field amplitudes of the short pulse with respect to the reference background.

If the ultrashort THz signal would be fully transmitted, one could hardly distinguish these oscillations from signals generated by background electrons. Thus the mutual contrast of the THz signals from the long and short electron bunch has been enhanced by using the central hole in the parabola as an angular filter, thereby selectively reducing the intensity of the reflected ultrashort THz fields from the high electron energy contribution ($\theta \simeq 1/\gamma$). The idea behind

the analysis is a time-domain interferometry (TDI) approach to separate the superposed signal from the measurement into its constituent CTR fields by distinguishing the different time scales. Hence, one has a long, above-resolution background field $\epsilon_{\text{long}}(t)$ (red curve in Fig. 3.8(B1)), which is easy to characterize and a short, sub-resolution field of the ultrashort electron bunch $\epsilon_{\text{short}}(t)$ that now modifies a known background.

3.4 AB-INITIO TRANSITION RADIATION MODELING OF THE EXPERIMENT

The modeling of the physics in the experiment consists of

- Electric fields of coherent transition radiation (CTR) according to measurements from the electron spectrometer.
- Propagation and focusing of the CTR wavefield in the ZnTe crystal.
- Propagation of laser and CTR beam within the crystal.
- Changes of the CP polarization state.

The general approach of this start-to-end model connecting all the above steps, is that an initial CTR field is decomposed in an angular spectrum modeled by a sum of plane waves, which are subsequently propagated through the experiment and as such can easily be computed using Fourier optics techniques [27], which solve the Fresnel-diffraction integral. This analysis included the broad CTR spectrum, as well as two independent polarizations for the radially polarized beam. Naturally the duration of the ultrashort and the long electron bunch, as well as their temporal delay are unknown in the beginning and are determined later when comparing the calculations with the measured cross-correlator data.

For the detailed modeling of the transition radiation of the electrons after the Al foil diffraction effects as in eq. (3.6) and (3.12) have to be taken into account because the closely spaced tape holders behind the foil define a finite emission region with an effective size of 2 mm. If electron spectra were recorded for a given shot, they were taken as the basis for the modeling of the long and short electron distributions. Using a fitting procedure the spectrum was separated into an exponential, low-energy part and a quasi-monoenergetic feature at higher energies, see Fig. 3.6(a).

The simulated far-field distribution was propagated using Fourier optic techniques [27] through a model of the THz refocusing optics, including the holes in the OAPs and the Teflon filter, to the ZnTe crystal. Hereby, the mirror holes were modeled as light blocking apertures on the mirror and the Teflon filter according to a measured transmission spectrum. For the focusing the full radially polarized THz beam and the 100 μm diameter CP focus, which is displaced by 600 μm from the THz pulse axis, was taken into account. This offset introduces another high-frequency cut-off, since high frequencies are focused to a spot too tight to interact with the off-center CP

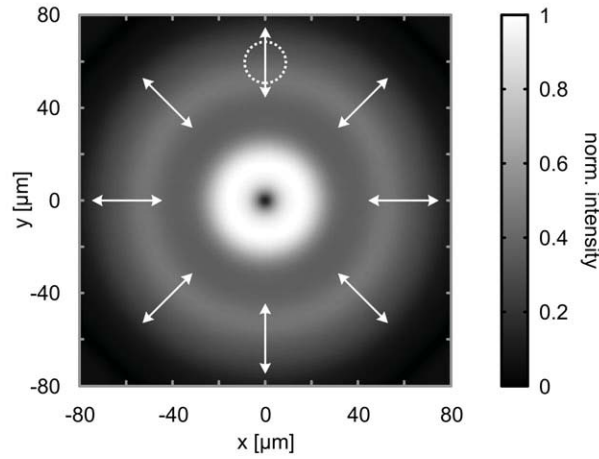


Figure 3.9: Relative CTR intensity as calculated at the ZnTe crystal surface. The dotted circle depicts the focal spot position and size of the CP beam. The $60\ \mu\text{m}$ offset with respect to the central axis was chosen to ensure a near-uniform polarization of the CTR field within the probe beam.

beam. The result is a spatio-temporal field distribution at the focus in the ZnTe crystal. The corresponding intensity distribution on the crystal and the position of the probe beam is shown in Fig. 3.9.

In the following modeling step, the THz pulse and the CP are both tracked as a superposition of plane waves through the ZnTe crystal [19, 26] according to its index of refraction and absorption properties. The result is a spatially resolved, relative phase delay $\Gamma(\mathbf{r}_\perp, t)$ between the ordinary and the extraordinary polarization component of the CP probe beam.

The transmission of the CP through the crossed polarizer, carrying the temporal information $\Gamma(\mathbf{r}_\perp, t)$, is modeled using the Jones matrix formalism [28, 29]. The final optical pulse intensity measured after the crossed-polarizer by the cross-correlator is then given by the square of the CP electric field, averaged over the CP beam diameter.

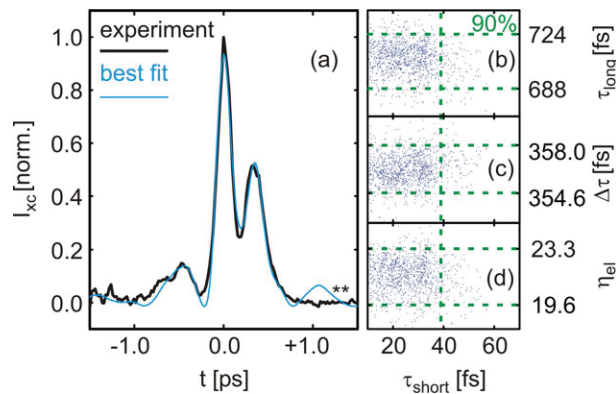


Figure 3.10: (a) The model of two electron distributions is fitted to the measured cross-correlator intensity trace determining the short pulse duration with a best fit at $\tau_{\text{short}} = 32\ \text{fs}$ (FWHM), the temporal offset $\Delta\tau = 356\ \text{fs}$ and the long electron background duration $\tau_{\text{long}} = 712\ \text{fs}$ (FWHM). (b-d) depicts error margins at the 90%-level of τ_{short} , τ_{long} , $\Delta\tau$ and η_{el} . The blue dots represent fits to random variations of the best fit. (**) This deviation is consistent with a non-Gaussian, low energy tail at later times, which does not affect the short pulse duration measurement.

3.5 ERROR ANALYSIS USING MONTE-CARLO METHODS

The measured cross-correlator intensity trace (black curve in Fig. 3.10(a)) of the sample shot from Fig. 3.6 is then fitted to the model with the main parameters being τ_{short} , τ_{long} , $\Delta\tau$ and the number ratio η_{el} of the two electron populations. It remains to examine the stability and thus error margins of the fitted parameters under small variations of the measured data from experimental uncertainties, such as the shot-to-shot deviations of the laser probe pulse profile. Due to the single shot nature of the experiment, which prevents a controllable reproduction of the same electron bunch, a Monte-Carlo approach was adopted for the error analysis.

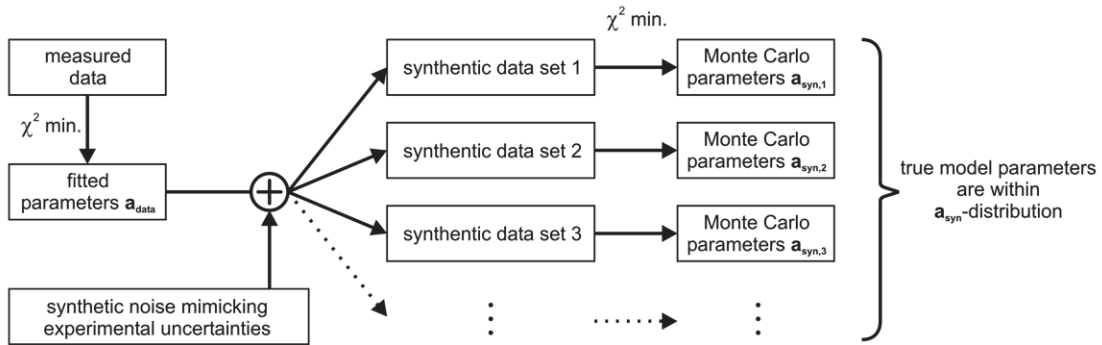


Figure 3.11: The measured signal is used to derive a best fit, characterized by the parameter vector \mathbf{a}_{data} . Furthermore analysis of the diagnostic including statistics over null shots yields the uncertainty of the measured result. Then, many different synthetic data sets are generated by adding random noise, which is statistically weighted to correspond to the measurement errors. Then each of these synthetic data sets is fitted to a new set of fitting parameters $\mathbf{a}_{\text{syn},i}$. The true set of parameters \mathbf{a}_{data} according to the model lies within the resulting distribution of all $\mathbf{a}_{\text{syn},i}$.

As depicted in Fig. 3.11, the starting point is the actual single-shot data from which a best fit according to the assumed model is computed. Then a statistically representative number of synthetic data sets is produced by adding pseudo-randomly generated noise to the best fit. However, this computer-generated noise is not arbitrary, but needs to reflect the shot-to-shot variations in the diagnostics from other sources than the electron bunch. For that reason 19 calibration measurements without accelerated electron beams were analyzed to characterize the typical shot-to-shot fluctuations as RMS values for each pixel along the cross-correlator time axis. These RMS-values then form the basis for the synthetic noise mimicking repeated measurements with an identical electron beam. For each of the synthetic data sets a new best fit is performed, thus resulting in distributions of fitting parameters (see Fig. 3.10(b-d)), where each fit is marked by a blue dot. The statistical deviations within this set of fitting parameters then determines the error margins.

The model fits were based on a minimum χ^2 , which was obtained by a nonlinear fit using a Pattern Search algorithm [30]. The algorithm was chosen for this analysis, since compared to other common optimization methods, such as Levenberg-Marquardt, simulated annealing or genetic algorithms, implementation tests have shown a considerable faster convergence speed and stable optimizations results with negligible dependence on the randomly chosen starting values. These properties of the algorithm were essential for calculating model fits to a statistically

large number of over 1000 synthetic data sets. The final error margins for the parameters τ_{short} , τ_{long} , $\Delta\tau$ and the number ratio η_{el} were determined by a 90% confidence criterion, stating that 90% of all repeated measurements lie within this interval.

In addition to the physics arguments, the quality of the assumed model is statistically supported in Fig. 3.12 by a “goodness-of-fit” test, which shows that the residual deviation between fit and measured data reasonably follows a normal distribution and that there are no systematic deviations left that are not accounted by the model. Furthermore, this is an indicator that the measured data does not provide significantly more insights, that could be obtained if a more detailed model would be assumed.

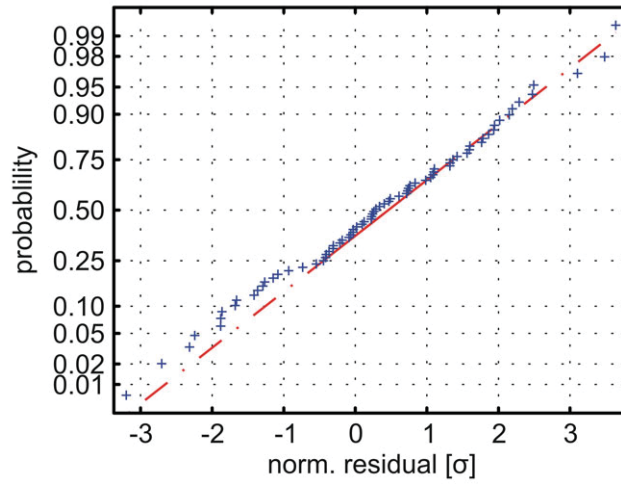


Figure 3.12: The normal probability plot graphically compares the distribution of the residuals between fit and data to a Gaussian distribution (red line). On the horizontal axis the residual value is normalized to the measured shot-to-shot RMS fluctuation. The vertical axis quantifies the probability of the occurring deviations.

3.6 MEASURED ELECTRON BUNCH DURATIONS

For the shot in Fig. 3.10 a best fit has been determined at $\tau_{\text{short}} = 32 \text{ fs}$ (FWHM) with 90% of all Monte Carlo scenarios below 38 fs (FWHM). Fig.3.10(b-d) illustrates error margins of $\tau_{\text{long}} = 712^{+12}_{-24} \text{ fs}$ and $\Delta\tau = 356^{+1.5}_{-1.8} \text{ fs}$. The relative uncertainties due to the small misalignment in polarization optics $\Delta\phi_{\text{pol}}$, the electron number ratio η_{el} and the CP to CTR offset d are 14.0%, 8.7% and 3.0% respectively.

Typical background electron durations τ_{long} from various shots were determined to be in a range of 450-800 fs with delays $\Delta\tau$ of 300-450 fs behind the respective ultrashort electron bunches. These delays and bunch durations (several 100 fs) are in good agreement with the time-of-flight dispersion of the low-energy electrons as they propagate over a distance of 5 mm to the Al foil.

A selected set of four shots with corresponding short electron bunch durations and the respective fits is displayed in Fig. 3.13. For shot (1) and (2) (red) electron spectra could be used for

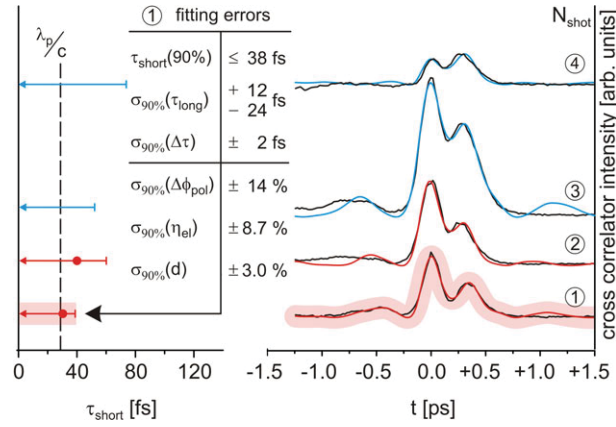


Figure 3.13: Left: Bunch duration measurements of several shots including all error contributions. Right: Corresponding measured cross-correlator traces (black) with best fits (colored). For the calculation of the red curves a measured electron spectrum was available. The best fit electron bunch duration of shot no. 1 (highlighted) is **32 fs** and thus comparable to the measured plasma period $\lambda_p/c = 30$ fs (dashed line).

detailed modeling [14]. Although the electron spectrometer was not in operation for shots (3) and (4) (blue), considerable information can be retrieved based on spectra comparable to (1) and (2) combined with assuming varying energies of their monoenergetic peaks. However, due to this uncertainty in shot (3) and (4) no best fit could be obtained for the short bunch duration τ_{short} .

Shot (1), corresponding to Fig. 3.10, has a 90% upper limit at **38 fs** and a best fit at **32 fs**, which suggests an electron bunch duration comparable to or shorter than the plasma period $\lambda_p/c = 30$ fs. While the best fit value is slightly above the pulse duration expected by PIC simulations [31], it has to be pointed out that no lower limit can be given and that effects such as beam loading [3] can lead to a substantial elongation with respect to ideal case PIC scenarios with durations well below half the plasma period.

In summary, these are the first experimental results showing that laser-plasma wakefield accelerated electrons are in fact shorter than the drive laser pulse duration, even after exiting the plasma. The upper limit of the electron bunch duration at a laser pulse duration of **45 fs** was found to be **38 fs** (FWHM), which is comparable to the plasma period. This result paves the way towards future ultrashort x-ray sources of high-brilliance, such as ultrafast Thomson-scattering [32, 33] or, in a more long-term perspective, a laboratory-scaled SASE FEL [34], for which ultrashort electron pulses with high peak currents in the **kA** range are essential. These developments might make compact, brilliant X-ray beams for applications available in mid-sized university labs.

3.7 COMPLEMENTARY APPROACHES: SPECTROSCOPIC DETERMINATION OF THE BUNCH DURATION

The bunch duration measurement presented here shows that electron bunch durations ≤ 33 fs are shorter than the laser duration **45 fs** and are comparable to the plasma period **30 fs**. For future application this is significant in two main aspects: the duration was measured outside

of the plasma where it can actually be used for applications and this duration is shorter than most electron accelerators, which is essential for the vision of all table-top SASE-FELs based on laser-wakefield accelerated electrons.

However, the resolution limits of the electro-optical crystal made possible only a determination of an upper limit for the duration. So the question remains: what are the shortest electron bunch durations achievable by LWFA? The answer to that question would not only be important for designing future radiation sources or be a valuable parameter for optimizing laser wakefield accelerators. Knowing a precise bunch duration would in combination with wakefield imaging methods [35] yield unique insights into the temporal structure of LWFA processes.

To illustrate this point, Fig. 3.14 shows the an electron spectrum recorded at the undulator experiment at the JETI laser. The properties of the 13 pC electron bunch at 45 MeV energy were exceptional in the experiment. The divergence was 3.7 mrad and the energy width 0.7–0.8 MeV. The on-axis energy width is an upper limit value because it has reached the energy resolution of the electron spectrometer. In the tail of the electron bunch an oscillation over two oscillation shows in the energy-angle-plane in Fig. 3.14(inset). One now can assume that these electrons were injected in the same region, but later into the wakefield, so that these electrons have less time for acceleration and hence achieve lower final energies. This also leads to electrons having different positions in the wake behind the head of the electron bunch, such that there is a monotonic relationship between longitudinal position and energy – the electrons in the front gain higher energies than those trailing behind. The spectrum depicts an oscillation in energy with a period in the range 6–9 MeV, which immediately raises the question on the physical origin of that situation. The most likely candidates are either relatively slow betatron oscillations [36], where a transversally, deflected electron bunch oscillates with $\omega_b \sim \omega_p/\sqrt{2\gamma}$, driven by space-charge forces, around the positively charged center of the plasma bubble – or a resonant interaction between the electron pulse and a trailing part of the laser pulse [37], acting like a driven oscillator and leads to a microstructure with a period comparable to the laser wavelength λ_0 . Measuring the precise time scale of the bunch duration could establish a relationship between time and energy and thus decide, which process causes the observed angle-oscillations.

In principle there is still room to improve the measurement technique presented in the last chapter, especially by using a GaP crystal instead of a ZnTe crystal for better electro-optic resolution. However, with almost an order of magnitude lower nonlinear efficiency (see [19]), this would at best only double the resolution down to about 15 fs detection limit, which is still not enough to detect sub-10 fs laser pulses. Therefore a different diagnostic is required.

For a new diagnostic it is a good idea to change the perspective from a time-domain to a frequency-domain measurement. Instead of determining the pulse duration of the CTR and hence the electron bunch duration Δt one can also seek the position in the spectrum $\nu_{\text{TR}} = 1/\Delta t$, where the spectral intensity changes from coherent to incoherent transition radiation. For shorter electron bunches this becomes easier because the transition from coherence to incoherence occurs at shorter wavelengths, which are not in the far infrared anymore, but in the middle and near infrared, where sensitive detectors are available. Thus, the measurement reduces to taking the spectrum of the transition radiation of an ultrashort pulse.

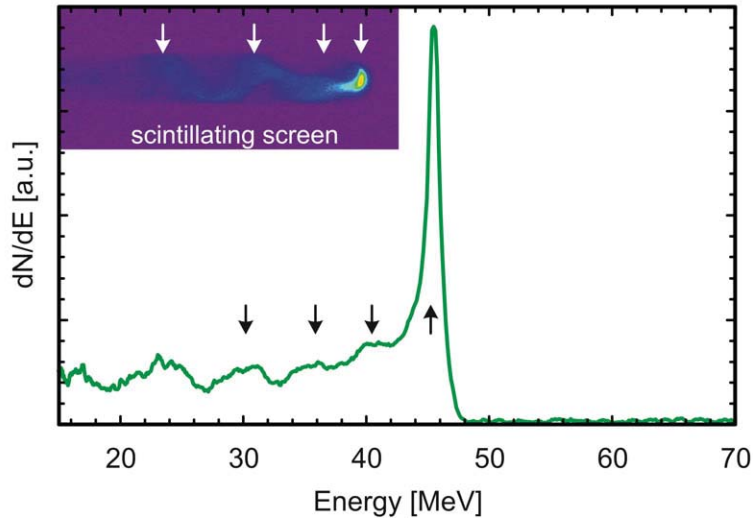


Figure 3.14: Electron spectrum of a LWFA electron bunch (13 pC charge and 3.7 mrad divergence for the main peak) at the JETI laser in the undulator experiment (see later in this chapter). The electron was angular-averaged over the data from the scintillating screen (inset). The scintillating screen image (inset) depicts the raw data (only X-rays removed) with the horizontal axis being related to the electron energy and the vertical axis to the angle. The electron beam tail features an oscillation in angle. The arrows indicate matching energies for interesting deflections between the scintillating screen image and the angle-integrated electron spectrum. The period of the oscillation in angular deflection is $\sim 6 - 9$ MeV.

This becomes more clear in an overview of the different regimes of transition radiation (see Fig. 3.15) below the plasma frequency ω_p of the metal foil radiator. At long wavelengths, the transverse extent of the fields $\gamma\lambda \gg \rho$ exceeds the radius of the metal foil and thus intensity is lost due to diffraction. On the other end at large frequencies of $\omega \geq \gamma\omega_p$ beyond optical frequencies, the radiator material stops acting like an ideal conductor. As a result the discontinuity in dielectric coefficients at the metal-vacuum interface vanishes and transition radiation is strongly suppressed.

In between these extremes, defined by the material and size of the radiator, the transition spectral intensity of a single electron (3.1) is independent of frequency and thus quasi-constant. Therefore the TR spectrum of the electron beam is entirely governed by its longitudinal and transverse coherence properties. Specifically, there is a steep transition from coherent to incoherent radiation, when the emitted wavelength becomes comparable to the bunch length $\lambda \simeq c\tau_{\text{bunch}}$. Thus the measurement of the electron bunch duration is reducible to the recording of broad frequency spectra, which makes transition radiation in the frequency-domain well-suited for single-shot type of experiments. The spectral position of the edge in spectrum intensity indicates the electron bunch duration.

In contrast to measurement in the time-domain, where in principle durations can be measured to arbitrarily long durations, in the frequency-domain there is both a lower and an upper limit for the detectable bunch duration as spectrometers have a finite frequency range. Since one knows from the time-duration measurement of the last chapter that the bunch duration is shorter than $\simeq 30$ fs, the corresponding target spectral range around $\lambda = c/30 \text{ fs} = 9 \mu\text{m}$ has to be in the mid-infrared.

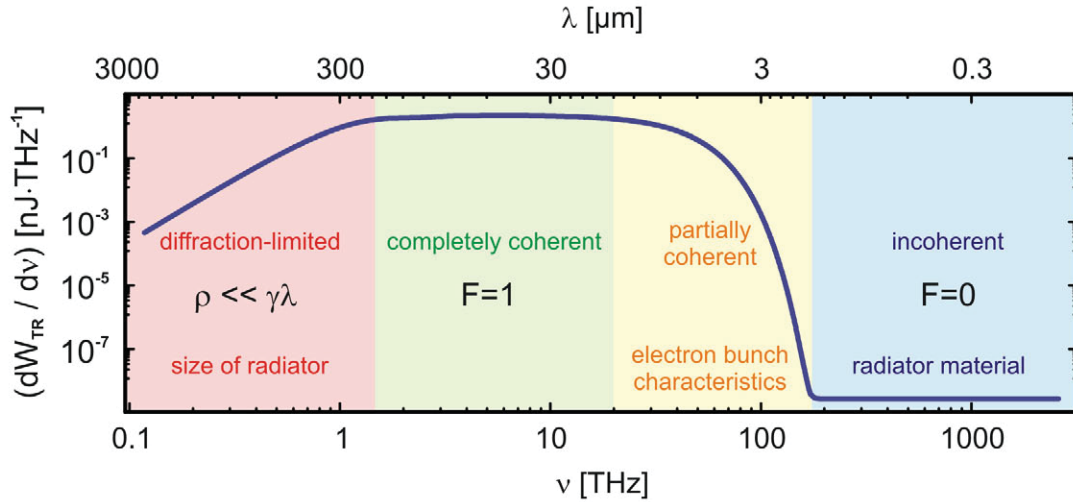


Figure 3.15: Overview on a typical transition radiation spectrum of an electron bunch: The general spectral shape is governed by both the transverse extent of the radiator and the spatial dimensions of the electron bunch. Towards longer wavelengths, the foil radius ρ eventually becomes small enough $\rho \ll \gamma\lambda$ for the geometry of the radiator surface to act as an aperture, so that diffraction reduces the spectral intensity. Towards shorter wavelengths, diffraction effects become negligible and the finite electron bunch dimensions emerge as the dominant influence on spectral intensity. Below some minimum wavelength, the transition radiation generated from individual, spatially separated electrons, stops to interfere constructively. Since transition radiation is primarily radiated into the direction of the electron trajectories, this loss in coherency and spectral intensity is determined by the longitudinal bunch density and hence electron bunch duration.

However, there is also a possible problem with the high temporal-resolution from spectral measurements. A coherent to incoherent transition can belong to a density modulation within the electron bunch, so it is possible to observe the characteristic size of this modulation at an intensity decline at high frequencies and potentially mistake it for the (longer) bunch duration. For that reason it is mandatory in frequency-domain based bunch duration measurements to verify that the degree of coherency in radiation towards longer wavelengths does not decline, as a decline is a tell-tale sign for a beam modulation. In principle this check has to be extended up to wavelengths where time-domain measurements can confirm that there are no other, longer, super-structures involved. This issue is important, because the average electron density of an electron beam, which is so central to the performance of an FEL, remains the same with or without internal substructure. According to PIC simulations, such micro-structures can arise in LWFA accelerated beams by resonant interaction of the electron bunch with parts of the laser beam [37]. Experimentally, modulations in LWFA beams were observed by transition radiation in the visible spectrum.

Transition radiation in frequency domain

The theoretical description for the TR spectral intensities in the far field can be readily inferred from the electric fields by Fourier transforms and Parseval's theorem. Following [13, 14, 19] the spectral energy distribution for a rotationally symmetric electron beam passing through an ideally

conducting and circular interface of radius ρ is

$$\frac{d^2 W}{d\omega d\Omega} = \frac{d^2 W_{\text{TR}}}{d\omega d\Omega} + \frac{d^2 W_{\text{CTR}}}{d\omega d\Omega} \quad (3.18)$$

$$= \frac{e^2}{4\pi^3 \epsilon_0 c} (N_e \cdot |\langle \mathcal{E}D \rangle|^2 + N_e^2 \cdot |\langle \mathcal{E}DF \rangle|^2), \quad (3.19)$$

where N_e , \mathcal{E} , D and F correspond to the familiar definitions of the number of electrons, the radiation field amplitude (3.5), the diffraction factor (3.6) and the electron form factor (3.8).

The form factor depends on the normalized momentum distribution $g(u)$, with $u = p/mc = \beta\gamma$ and the position-momentum distribution $f(\mathbf{r}, u)$ and can for uncorrelated longitudinal and transverse distributions be separated as $F = F_{\perp} F_{\parallel}$. For Gaussian electron beams with small divergences $\psi \ll 1$, the longitudinal

$$F_{\parallel} = \exp[-(\omega\sigma_z/v)^2/2] \quad (3.20)$$

and the transverse form factor component become

$$F_{\perp} = \exp[-(\omega\sigma_r \sin \theta/c)^2/2]. \quad (3.21)$$

From equations (3.19) to (3.21) it is apparent that the spectral dependence with respect to ω arises entirely from the form factor and that the form factor becomes unity as long as the electron bunch length σ_z remains short $\omega \cdot (\sigma_z/c) \ll 1$ and satisfies the significantly weaker transverse coherence condition on the electron bunch radius $\sigma_r \sin \theta \ll \sigma_z$. The observation angle θ is taken with respect to the central axis, normal to the radiator foil, and maximum TR intensities are reached at $\sim 1/\gamma$. Therefore the transition from coherent to incoherent transition radiation in the spectrum is the central indicator on the electron bunch length and hence duration.

In Fig. 3.16, the spectrum integrated over the fully solid angle was calculated for an LWFA type electron beam with 200 MeV energy and 20 pC charge. The electron density profile was assumed to be Gaussian with a bunch duration of 10 fs (FWHM) and a bunch diameter of 20 μm (FWHM) when exiting the foil. While Fig. 3.16(a) is in ω -coordinates and thus compares to Fig 3.15 and its different TR regimes, the version in Fig. 3.16(b) is rescaled to wavelengths λ and a linear spectral intensity axis to reflect more closely the situation of an experiment, where spectrometers linearly disperse light with respect to wavelengths.

This can be contrasted by another calculation, which additionally includes a density modulation with period 1 μm ($\sigma_{\Delta} = 2 \mu\text{m}$). Substituting the following model for the longitudinal charge distribution

$$f(\mathbf{r}, u) = g(u) \cdot f_{\perp,G}(r) f_{\parallel,G}(z) \cdot \frac{2}{1 + \exp\left(-\frac{8\pi^2\sigma_z^2}{\sigma_{\Delta}^2}\right)} \cos^2[2\pi z/\sigma_{\Delta}] \quad (3.22)$$

and calculating the longitudinal form factor according to eq. (3.8) yields an additional peak in the spectrum Fig. 3.17. Note, that this is not a mere redistribution of energy within a spectral distribution, but that the total radiated energy increases. In a wavelength based spectrum it shows that the additional peak does, due to the general λ^{-2} intensity scaling, dominate the rest of the spectrum in spectral intensity. The spectral feature on the right in 3.17(b), which contains the information on the electron bunch duration is by one order of magnitude smaller than the CTR

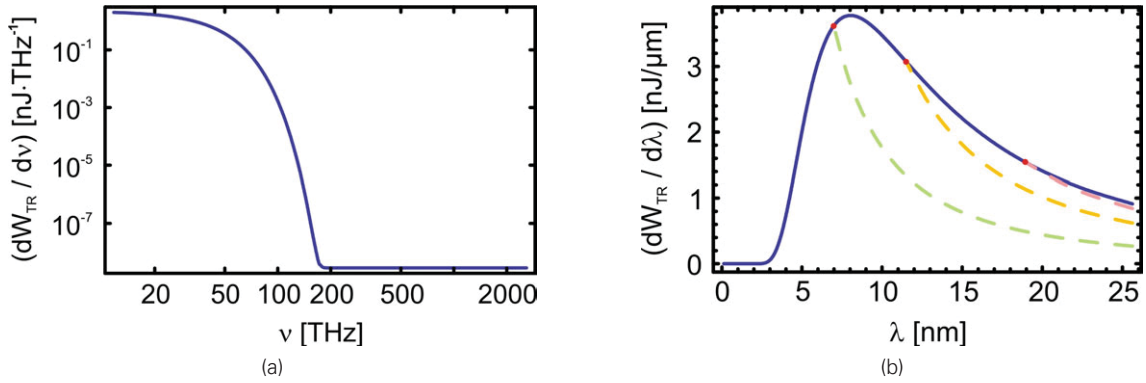


Figure 3.16: (a) Calculated TR spectrum of a 200 MeV, 20 pC, beam of a Gaussian charge density profile with 10 fs (FWHM) bunch duration and 20 μm (FWHM) diameter. (b) shows the corresponding spectrum over wavelengths λ , as observed in experiments. The dashed lines depict a graphical λ^{-2} -scaling extending from some selected reference amplitudes towards higher wavelengths. If the radiated spectrum lies above the dashed line (green and orange), the degree of coherency of CTR is increased. If the scaling closely follows the radiation line (pink), the change in coherency is small.

of the density modulation. As a consequence, even weak electron density modulations at short time scales can lead to appreciable spectral amplitudes, such that the dynamic range of the detection system has to span at least two orders of magnitude in order to resolve and quantify even small amplitude features at longer wavelengths to discriminate the global bunch structure from eventual modulations. A strict criterion (within the uncertainties in measurement) of the largest bunch structure is, that coherence does not decrease towards longer wavelengths. Graphically, this corresponds to a monotonically rising spectral intensity towards smaller frequencies in a frequency based graph, or in a wavelength based graph the requirement, that λ^{-2} curves starting from each data point on the curve must be smaller or equal than all other data points at longer wavelengths respectively. For the density modulation in Fig. 3.17 these conditions are clearly violated.

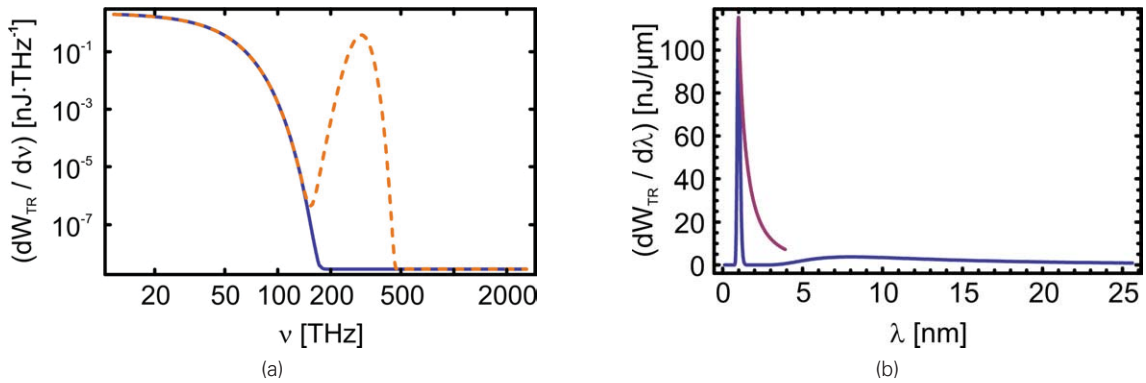


Figure 3.17: (a) CTR ω -spectrum of a micro-bunched beam (dashed) compared to the beam without a sub-bunch structure. (b) CTR λ -spectrum of a microbunched electron beam (blue) with an “isocoherency” line (violet) at the peak depicting the sub-bunch character of the feature.

Several conclusions can be drawn from these theoretical considerations for future experiments:

- For LWFA electron bunches, the spectral intensities are on the order of $\text{nJ}/\mu\text{m}$, which points out rather high demands on detector sensitivity.
- Beside checking for steep CTR to ITR edges, it is necessary to confirm that the degree of coherency increases towards longer wavelengths, in order to show that the peak originates from the electron bunch length and not some small scale electron density fluctuations.
- As micro structures in the beam can lead to large spectral amplitudes, the detection systems need to cover a dynamic range of at least two orders of magnitudes to detect small deviations at longer wavelengths with reasonable error margins.

3.8 SYNCHROTRON RADIATION FROM LASER-WAKEFIELD ACCELERATED ELECTRONS

Since laser-accelerated electrons are indeed ultrashort, they have one of the essential properties for a potential free-electron laser on table-top. However from practical point of view it is necessary to not only measure the electron beam properties, but have enough control over the electrons to combine them in another step with classical insertion devices, such as undulators, and actually use the electrons as a light source. In the proof of principle experiment shown here [38–40], a laser was used to accelerate quasi-monoenergetic electrons in a gas jet plasma by laser-wakefield acceleration in the bubble regime up to energies of approximately 85 MeV , which then were passed through an undulator, generating undulator radiation in the optical spectral range. This makes it the first production of synchrotron light from laser-wakefield accelerated electrons. The properties of the undulator radiation, such as intensity, wavelength and higher harmonics are confirmed by comparing measured, single-shot spectra of the synchrotron radiation to the theoretical expectations derived from the measured electron spectra.

The experiment was carried out at the Jena high-intensity titanium:sapphire laser JETI, that delivers pulses at 800 nm with 85 fs duration and 430 mJ pulse energy on target. The laser ionizes a Helium gas jet and in the plasma accelerates by laser-wakefield acceleration a monoenergetic electron bunch, which after exiting the plasma passes through an undulator, where it undergoes a wiggling motion due to the magnetic field and radiates primarily at infrared or optical frequencies. This radiation is then detected with an optical spectrometer. The electron beam energy spectrum is diagnosed by an electron spectrometer and the beam profile is imaged by two retractable scintillating screens before and after the undulator. All parts of the setup were aligned along one axis and were located, except for the optical spectrometer, in vacuum.

The laser pulses are focused by an $F/6$, 30° off-axis parabolic (OAP) mirror to a slightly elliptical focus with an average diameter of $11 \mu\text{m}$ (FWHM) and a peak intensity of $5 \times 10^{18} \text{ W/cm}^2$, corresponding to a normalized vector potential of $a_0 = 1.5$. The pulsed, supersonic Helium gas-jet from a 2 mm nozzle features a super-Gaussian density profile and is positioned such that the laser reaches the focus at the steep density upramp (the outer edge) of the gas jet. The peak gas density in the interaction region reaches $2 \times 10^{19} \text{ cm}^{-3}$. Due to the high intensity of the laser

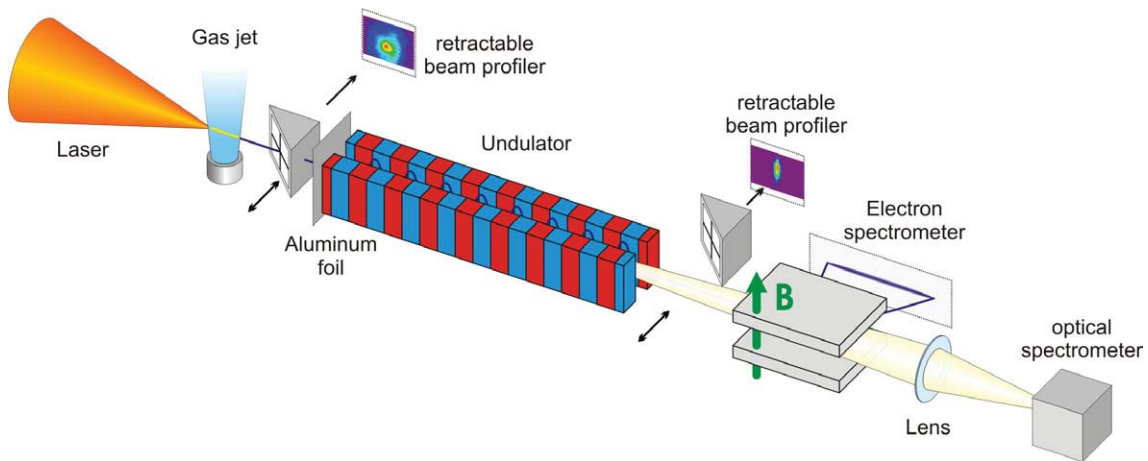


Figure 3.18: The main laser is focused by an off-axis parabola mirror into a supersonic gas jet, where it accelerates electrons through Laser-wakefield acceleration to several tens of **MeV**. These electrons then pass through an undulator and generate undulator radiation at optical wavelengths. Both undulator radiation and electrons are then simultaneously analyzed in an electron and optical spectrometer. In order to avoid background signals in the spectrometers, a $15\ \mu\text{m}$ thin Aluminum foil at the undulator entrance blocks laser light and radiation from the plasma. Two retractable scintillating screens are used for analysis of the electron beam profile and alignment of beams through the undulator to the diagnostics.

the gas is fully ionized and the laser undergoes ponderomotive and relativistic self-focusing and propagates within a self-generated plasma channel. At the selected laser and plasma parameters, the laser pulse experiences a strong longitudinal self-modulation, which shortens the pulse and steepens the plasma wake [41]. By wave breaking, electrons are self-injected into the wake and efficiently accelerated via the *bubble regime* to energies on the order of 50–100 **MeV** [41].

For online diagnostic and optimization of laser and gas jet the self-emission and the scattered laser light from the plasma channel were recorded for every shot in a side view perpendicular to the laser direction of propagation. The intense laser fundamental was blocked by a 400 **nm** bandpass filter. Both channel length and emission characteristic were subject to significant shot-to-shot fluctuations, thus indicating strong nonlinearities of the interaction. Typical channels, as the one shown in Fig. 3.19(a), are about 1 **mm** in length.

For electron beam pointing and steering, as well as divergence measurements and beam quality assessments, two retractable scintillating screens (Konica KR) were installed, one before and one after the undulator (see Fig. 3.18). The electron beam profiles measured 30 **cm** behind the gas jet in front of the undulator, as the one depicted in Fig. 3.19(b), include almost always a largely divergent fraction, while well-collimated beams with divergences below 10 **mrاد** appear often – i.e. in 70% of all shots.

The accelerated electrons displayed large shot-to-shot fluctuations in beam pointing and divergence, that originate from the highly nonlinear processes in the plasma, where small changes in plasma density or the laser beam lead to large changes in the resulting electron beam characteristics. As depicted in Fig. 3.19(c), the beams show a large on average divergence of 30 **mrاد**, while well-collimated beams typically had divergences in the range of 3-7 **mrاد** that for some selected shots such as in Fig. 3.19(b) were as small as 1 **mrاد**. The pointing variation of these

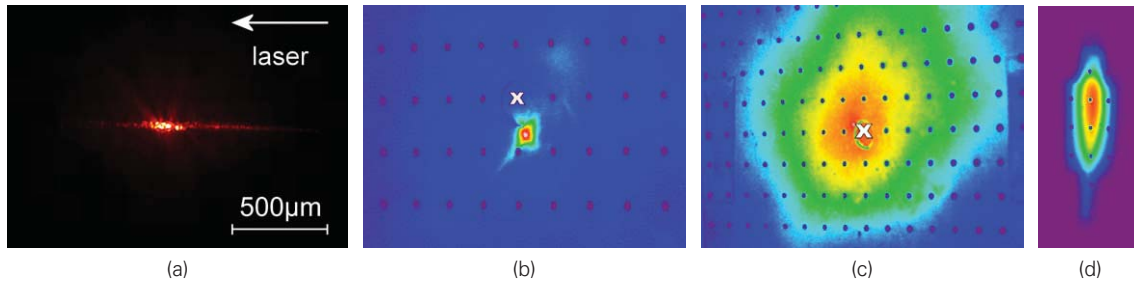


Figure 3.19: (a) depicts a self-emission sideview on the plasma channel with the 800 nm laser light being blocked by a 400 nm band pass filter. (b) shows the transverse electron beam profile of well-collimated electrons close to the undulator axis on the scintillating screen 30 cm behind the gas jet. The screen grid features a 5 mm spacing. (c) shows the same situation, averaged over 50 consecutive shots, and thus displays the large variance in both electron beam pointing and divergence. The x in (b) and (c) marks the central axis respectively. (d) features an average over 46 shots of the electron beam profiler at the undulator exit. It shows the focusing effect in the direction parallel to the undulator field, such that on a 5 mm grid the average electron deviation from the z-axis in x-direction is 2 mm. The edges in the beam arrive from the undulator braces.

collimated beams was as large as 60 mrad. Hence only a few shots were close enough to the axis ≤ 3.5 mrad to pass through the undulator to the electron spectrometer. Hence to increase this fraction, the mean direction (averaged over several tens of electron profiles) of the electrons was optimized by adjusting the laser incidence position on the off-axis parabola by using two steering mirrors before the parabola. It has to be noted, that optimal steering conditions were not obtained for laser beams geometrically centered on the parabola. Instead, imperfections of laser profile and parabola coating lead to an optimal incidence position, which was off-axis and changed the focusing axis by several degrees. After optimizing average electron beam pointing, the probability of a well-collimated beam to pass through the undulator was about one in a hundred shots. The second beam monitor behind the undulator was then used for verification of electron beam transmission through the undulator before performing measurements with the electron spectrometer.

The electron spectrometer was based on permanent magnets inside an iron yoke. The input aperture of the spectrometer was 2 cm, however the effective electron acceptance angle was limited to 7.2 mrad by the 10 mm wide undulator exit. The magnetic field strength was 720 mT, extending 20 cm in length and 10 cm in width with a gap of 2 cm. For single shot online diagnostic of the deflected electrons a scintillating screen (Konica KR) in combination with a CCD camera was used. The detectable energy range was 14 to 85 MeV. The energy to position calibration and the dispersion properties were provided by particle tracking simulation (GPT) that used as input the measured 3D magnetic field including fringe fields [42]. For an absolute charge calibration of the electron spectrometer scintillating screen, imaging plates (BAS-MS2025 by Fujifilm) were used. Such imaging plates have the advantage of a large dynamical range, a highly linear response and are well characterized [43]. In the end, the lowest spectrally dispersed charge, which could be detected by the electron spectrometer was approximately 0.5 pC/MeV. The characteristics of the electron spectra were also subject to shot-to-shot variations showing a random mixture of exponentially-shaped spectra and monoenergetic spikes (see Fig. 3.20(a)). Such spectra with monoenergetic features were measured in 25% of all shots. The narrowband peak energies varied between 20 and 70 MeV with a maximum in the range of 40-45 MeV. The charge of such

peaks was typically between 10 and 20 pC, mostly below 40 pC.

The undulator design is a Halbach-Hybrid [44]. It is built from permanent magnets with a period of $\lambda_u = 2 \text{ cm}$ and a total length of 1 m (50 periods). The gap between the magnets was set to 1 cm, with a maximum magnetic field on axis of 330 mT, so the undulator parameter $K = 0.6$. The distance from the gas nozzle was about 40 cm. In order to protect the magnets from off-axis electrons, a 1 cm thick, 1 cm diameter lead aperture was placed in front of the undulator. In experiment, transmission of the electrons could be characterized by averaging over multiple shots as depicted in Fig. 3.19(d), which clearly demonstrates the focusing effect of the undulator that arises from the magnetic field gradient along the x-axis and deflects off-axis electrons towards the central axis. The focal length is highly dependent on the electron energy and initial divergence, but as an estimate it can be compared to half the length of a betatron oscillation $\lambda_\beta \approx (\gamma/K)\lambda_u$ [45]. Therefore typical focal lengths of that undulator well exceed the undulator length for electron energies larger than 30 MeV. The slight deviation of 4 mrad in the y-direction in Fig. 3.19(d) has to be attributed to the mean steering direction of the electrons.

The optical detection system had two main challenges. It had to image radiation from along the entire 1 m long undulator axis and had to be sensitive enough to detect even small photon fluxes. Secondly, it should image a wide spectral range in a single shot. The undulator radiation was collected and focused into the entrance plane of a symmetrical Czerny-Turner spectrometer. A thermoelectrically cooled 16-bit CCD camera (Andor DO-420 BN) was used as a detector. The spectral range was set to 560 – 990 nm and the wavelength calibration was performed using a Hg-vapor lamp. The entire system consisting of imaging optics, spectrometer and CCD was calibrated to absolute photon numbers using a He-Ne-Laser and manufacturer information on the CCD spectral quantum efficiency and the spectrometer grating efficiency. In order to screen the spectrometer against direct exposure from laser or plasma light a 15 μm aluminium foil was placed in front of the undulator. Since the light source extends along the entire undulator length of 1 m and can cover a spectral range from 560 – 990 nm, a short focal lens was setup for a high depth of focus, such that it images the middle of the undulator onto the spectrometer entrance slit. Measurements with a HeNe laser have determined that on average more than 90% of the light is captured along the undulator length and that the acceptance angle is 2 mrad. Raytracing simulations of the optical system with extended light sources of wavelengths over the entire spectral range yield similar results and confirm an acceptance angle of 2 mrad (FWHM).

Fig. 3.20 shows three single shots with electron spectra in (a) and the corresponding measured optical spectrum. The gray lines in depict the energy range in which undulator radiation is expected to be detectable by the optical spectrometer. The red electron spectrum, peaked at 64 MeV lies within said energy range with little contributions at lower energies. The corresponding radiation spectrum in Fig. 3.20(b) has a pronounced peak which agrees well with the wavelength as expected from undulator radiation according to (2.12) in chapter 2.1

$$\lambda_r = \frac{\lambda_u}{2\gamma^2} (1 + K^2/2). \quad (3.23)$$

The green electron spectrum is intense and broadband, which attains a local maximum somewhere around 67 MeV and falls off beyond 70 MeV. This drop in the electron distribution is also mirrored in the corresponding photon spectrum, which is also broadband and falls off towards

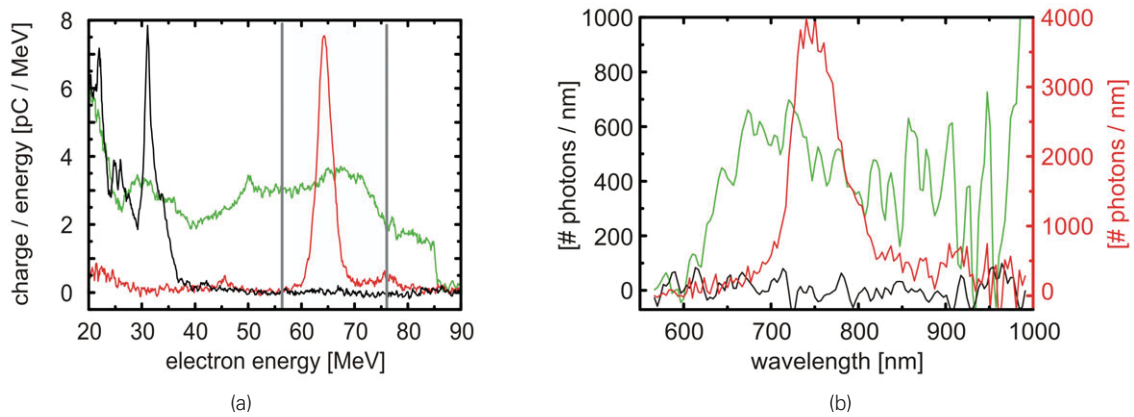


Figure 3.20: In three selected shots, measured electron spectra (a) are compared to their corresponding optical spectra (b). The grey window in (a) shows the energy region, for which first harmonic undulator radiation is detectable in the optical spectrum. The red spectrum **64 MeV** falls within that window and shows also as a peaked spectrum in the optical spectrum. The black spectrum, peaked at **32 MeV**, shows the expected null result, while the broad green spectrum is also broad in the optical spectrum. The right-hand-side ordinate in (b) belongs to the red spectrum.

smaller wavelengths. The black electron spectrum features a peak at **32 MeV**, which in terms of charge is comparable to the red spectrum, but has no electrons within the target energy range. Therefore the undulator radiation is expected to be around $3\ \mu\text{m}$, which is clearly outside of the optical spectrometer detection range. This confirmed by the black spectrum in Fig. 3.20(b), which shows no signal.

A more detailed analysis was carried out with the help of calculations according to undulator theory as in ch. 2.1 and [44, 46]. Here, the measured electron spectrum was taken as input to account for the charge contribution at each energy. The radiation power amplitude $d^2W/d\omega d\Omega$ was calculated and integrated up to the acceptance angle of the detection system at **2 mrad** FWHM. Fig. 3.21(a) shows again the shot, which is displayed red in Fig. 3.20(a). The electron spectrum (inset) is peaked at **64 MeV**, has an energy width of **3.4 MeV** (FWHM), features a divergence of **3.8 mrad** (FWHM) and contains a charge of **30 pC**. The measured optical spectrum (red) is peaked at **740 nm** and has a bandwidth of the **55 nm**. Within this bandwidth the total photon number is 2.8×10^5 . The simulated spectrum (green) shows excellent agreement with the measured optical spectrum. The slight offset in the peak energy lies within the uncertainty of absolute energy calibration of the electron spectrometer, due to electrons arriving at the entrance aperture at slight position offsets with respect to the central axis. Spectral width and photon numbers are in perfect agreement.

Pairs of electron and optical spectra with quasi-monoenergetic features were recorded for a number of shots. The correlation between the electron peak energies and the peak optical wavelength is depicted in Fig. 3.20(b) and compared to the fundamental and second harmonic according to the undulator equation (3.23). For each shot within the energy range **55-75 MeV** and with a sufficiently high spectral charge density larger than **1 pC/MeV**, the optical spectrum has shown radiation, which corresponds well to the wavelength expected by undulator radiation. Apart from this group of spectra, there were also shots with quasi-monoenergetic peaks with

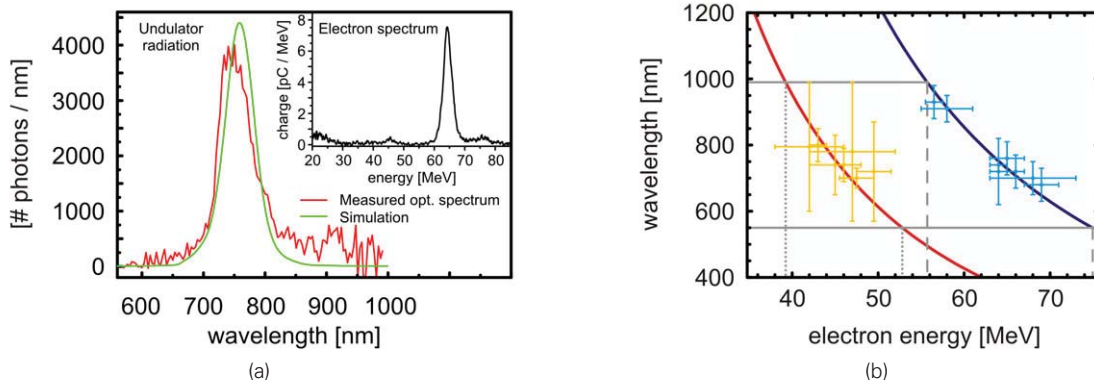


Figure 3.21: (a) The main plot depicts one of the measured optical spectra (red) in absolute calibration. The simulated optical spectrum (green) is calculated on the basis of the corresponding electron energy spectrum of the same shot (inset). The good agreement between the curves confirms the presence of undulator radiation, as well as the consistency of the diagnostics. (b) Peak electron energies from measured electron spectra are plotted against the peaks in the corresponding optical spectra. The bars do not denote error bars, but denote the actual widths in the respective spectra. The solid blue and red line depict the theoretical undulator wavelengths in the first and second harmonic with respect to electron energy. The experimental results show good agreement with theory and thus confirm that the detected radiation is undulator radiation.

spectral charge densities exceeding 7 pC/MeV in the range $40\text{-}50 \text{ MeV}$ that have shown very weak radiation at signal-to-noise levels $S/N < 2$, which can be explained by the second harmonic of the undulator radiation ($n = 2$). The weak radiation signature is consistent with theoretical estimates for the actual undulator parameter $K = 0.6$ and the acceptance angle 2 mrad , which indicates a spectral intensity ratio between first and second harmonic of about 10:1. It must be emphasized that all measured pairs of spectra agreed well with undulator radiation and that there were no optical spectra without the corresponding electron spectrum and vice versa.

Other possible sources of light are excluded either by the experimental setup or by the measured data. Laser light, plasma self-emission or transition radiation from the plasma-vacuum boundary is blocked by the aluminium foil in front of the undulator. Also, tiny leakages in the foil would have been easy to detect, as the comparably narrowband laser radiation 800 nm constitutes the largest fraction of the light. The only other credible source of radiation is transition radiation originating from the backside of the light blocking foil. However, this radiation is out of focus for the lens, which images the light onto the spectrometer entrance slit. In addition transition radiation does not contribute on axis, but instead consists of radially polarized light emitted into a cone with maximum intensity at $1/\gamma$, so the polarization dependent gratings and the angular distribution make it even more difficult for transition radiation to reach the CCD. Furthermore, if there was a signal it would be very broadband and would only very weakly depend on the electron energy. Such a background was not observed and it can be concluded, that the measured radiation spectra were indeed from undulator radiation.

The achieved peak brilliance of the undulator source can be estimated through the measured spectral properties of both electrons and photons in Fig.3.21, as well as the assumption of a source size of $3 \text{ }\mu\text{m}$ and 10 fs electron bunch duration after acceleration, which according to the

measured laser spot size and gas density were gleaned from scaling laws. Being a mere proof-of-concept, the resulting brilliance of $6.5 \times 10^{16} \text{ mm}^{-1} \text{ mrad}^{-2} \text{ s}^{-1}$ [0.1 %BW] is far below most laser pulse sources in the visible (see eq. (2.1)). However, if these numbers are scaled up to the X-ray range by going to 1 GeV LWFA electron energies [47] and by using an improved undulator design ($\lambda_u = 1.5 \text{ cm}$, $K = 1.0$, 200 periods [48]), one could obtain 220,000 photons in the first harmonic at an energy of 420 eV within a 0.1 mrad solid angle cone and a peak brilliance of $2.5 \times 10^{24} \text{ mm}^{-1} \text{ mrad}^{-2} \text{ s}^{-1}$ [0.1 %BW] [38]. According to Fig. 1.3, such a peak brilliance would be comparable to those of existing synchrotron sources. This makes it possible to realize ultra-short, brilliant light sources in the X-ray regime on the compact scale of a university laboratory.

4 THOMSON SCATTERING – LASERS AS OPTICAL UNDULATORS

With magnetic undulator structures as shown in the previous chapter, bright X-ray beams driven by present laser-wakefield accelerated electrons of up to 1 GeV [1] can scale up to photon energies of about 1.9 keV using undulator periods as small as $\lambda_u \simeq 5$ mm. Beyond that the undulator technology is limited in field by the materials used for permanent magnets or superconducting electro-magnets. [2]. It is for this reason, that Thomson scattering, the all-optical analogue of undulator radiation with half the laser wavelength as the equivalent undulator period, becomes attractive in the search for bright light sources of increasingly higher photon energies. For a 800 nm Ti:Sa laser, a GeV-electron beam leads to a photon energy of 24 MeV. Two major advantages make especially the combination of LWFA acceleration and Thomson scattering very interesting as an X-ray source. For one Thomson scattering and LWFA acceleration can be driven by the same laser system, which makes beam synchronization trivial, when compared to synchronizing a conventionally accelerated electron beam and a laser beam to sub-ps precision. Secondly, since neither a long electron accelerator, nor massive undulators are required, these techniques are very compact with respect to infrastructure requirements. The largest part of such a facility is the laser itself, so that the entire setup only requires the room of a university laboratory.

In this chapter, the tools for realistic simulations of Thomson spectra are presented and applied in describing two different Thomson source designs. One that aims for a high average photon flux and one whose purpose is a high peak photon flux. Here, a special emphasis is put on the limitations from non-ideal effects, not only for pointing out bottlenecks in performance, but also to lie the foundation of the next chapter, which attempts a solution to these limitations.

4.1 NUMERICAL MODELING OF THOMSON SCATTERING

Since the expected scattered photon energies in the electron frame of reference are much smaller than the electron rest energy $\hbar\omega/\gamma \ll m_e c^2$ the physics of Thomson scattering can be accurately described by classical electrodynamics as the radiation of accelerated charges. According to [3] the scattered, spectral intensity in the far field into the solid angle $d\Omega$ of a single electron is

$$\frac{d^2 I}{d\omega d\Omega} = \frac{e^2}{4\pi^2 c} \left| \int_{-\infty}^{+\infty} \frac{\mathbf{n} \times [(\mathbf{n} - \boldsymbol{\beta}) \times \dot{\boldsymbol{\beta}}]}{(1 - \boldsymbol{\beta} \cdot \mathbf{n})^2} e^{i\omega(t - \mathbf{n} \cdot \mathbf{r}(t)/c)} dt \right|^2. \quad (4.1)$$

The far field approximation is valid because the interaction takes place in a volume with dimensions much smaller than the distance to the observer, so the radiation source can be approximated as a point source.

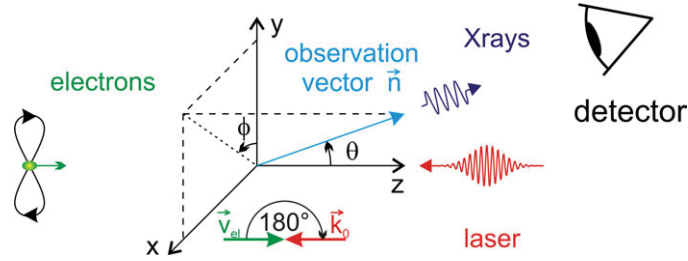


Figure 4.1: Thomson scattering geometry

The normalized velocity $\boldsymbol{\beta}(t)$ and acceleration $\dot{\boldsymbol{\beta}}(t)$ of the electron is given by the electron trajectory and \mathbf{n} denotes the direction of observation. In practice (4.1) is a bounded integral, because the integrand contributes only when there is a finite acceleration $\dot{\boldsymbol{\beta}}(t)$. If multiple electrons are considered, a sum over the respective radiation amplitudes has to be performed within the vector norm brackets to account for relative phase delays between em-waves from different electrons. Similarly the effect of polarization filters \mathbf{P} has to be taken into account before evaluating the norm.

$$\frac{d^2 I}{d\omega d\Omega} = \frac{e^2}{4\pi^2 c} \left| \mathbf{P} \cdot \sum_j \int_{-\infty}^{+\infty} \frac{\mathbf{n} \times [(\mathbf{n} - \boldsymbol{\beta}_j) \times \dot{\boldsymbol{\beta}}_j]}{(1 - \boldsymbol{\beta}_j \cdot \mathbf{n})^2} e^{i\omega(t - \mathbf{n} \cdot \mathbf{r}_j(t)/c)} dt \right|^2 \quad (4.2)$$

For $\mathbf{P} = (1, 1, 1)$, no filter is in place, whereas $\mathbf{P} = (0, 1, 0)$ corresponds to a polarizer that lets the y -polarization pass through. In order to calculate realistic photon numbers by Thomson scattering, one has not only to calculate the electron trajectories of a statistical ensemble within an external laser field that varies in space and time, but also to sum up the energy contributions over all relevant frequencies and full solid angle. In fact, the complete problem of calculating absolute photon numbers from a given set of electron trajectories is a 9-dimensional integral in nature – 6-dim for electron phase space, 2-dimensions for the solid angle and 1-dim for the required energy bandwidth. As a result (4.2) would have to be calculated many times over, thus increasing computational cost. However, the task can be considerably simplified by reformulating the problem, such that it can be efficiently solved by fast Fourier transform (FFT) algorithms.

The exponent in (4.2) looks very similar to $e^{i\omega t}$, thus suggesting a Fast Fourier transform algorithm for speedy computation. However, this is complicated by the additional term $-\mathbf{n}\cdot\mathbf{r}(t)/c$, which denotes the change to retarded time $t_{\text{ret}} = t - \mathbf{n}\cdot\mathbf{r}(t)/c$ and thus accounts for the resulting wave fronts to start at different positions and times. These relative shifts in phase are essential for modeling the relativistic frequency shifts such as $4\gamma^2$ dependency for Thomson scattering. In order to change the integral from time coordinates $t \rightarrow t_{\text{ret}}$, it is necessary to transform all electron trajectory coordinates $\beta_j(t)$ and $\dot{\beta}_j(t)$ to retarded times.

Since the electrons cannot move faster than the speed of light, it is possible to assign a monotonously increasing retarded time t_{ret} along each electron trajectory. By oversampling of the electron trajectory in t with regard to the typical oscillation period, it is possible by interpolation techniques, such as assuming cubic splines, to obtain equidistant points in t_{ret} .

On a more technical note the numerical stability of the fraction in (4.2), where the difference in the denominator becomes exceedingly small, especially for high electron energies, can be improved by using normalized momentum $(\gamma\beta)(t)$ and $\gamma(t)$ instead of velocity coordinates $\beta(t)$. Together, with above transformation to retarded times, one arrives at

$$\frac{d^2 n_{\text{phot}}}{d\omega d\Omega} = \frac{e^2/(\hbar\omega)}{4\pi^2 c} \left| \mathbf{P} \cdot \underbrace{\int_{-\infty}^{+\infty} \sum_j^N \left(\frac{\gamma\mathbf{n} \times [(\gamma\mathbf{n} - \gamma\beta_j) \times \gamma\dot{\beta}_j]}{(\gamma - \mathbf{n}\cdot\gamma\beta_j)^3} \right) \cdot e^{i\omega t_{\text{ret}}} dt_{\text{ret}}}_{\text{Fourier-Transform}} \right|^2. \quad (4.3)$$

Equation (4.3) is meant to sum over all N electron trajectories, however calculating a large number of electron trajectories is computationally expensive. Hence in simulations only a statistical ensemble of N_{sim} electrons is tracked. Two issues complicate the matter: First, the high sensitivity of (4.3) with regard to phase $i\omega t_{\text{ret}}$ requires a high number of electrons ($> 10^6$) to be tracked in order to obtain a reasonable phase average and thus a "smooth" spectrum without random spikes due to poor statistics. Secondly, tracking N_{sim} simulated electrons to obtain trajectories over \mathbf{ps} -time scales at time increments as small as tens of attoseconds creates large data sets, which quickly exceed the main memory of current computers.

As for $\gamma \gg 1$ the resulting X-ray wavelengths are much smaller than the electron bunch which is at minimum micrometers in size. Also, the resulting radiation in the scenarios considered here is too weak to drive an FEL-type instability. Therefore, the resulting radiation can safely be assumed to be incoherent. That simplifies (4.3), because eliminating the spectral phase average by exchanging the sum and norm leads to the fully coherent result $((d^2 n_{\text{phot}})/(d\omega d\Omega) \propto N^2)$, which by dividing by N becomes the required, fully incoherent result $(d^2 n_{\text{phot}})/(d\omega d\Omega) \propto N$.

After rewriting $N = \frac{Q/e}{N_{\text{sim}}^2} \cdot \left(\sum_j^{N_{\text{sim}}} 1 \right)^2$ in terms of N_{sim} and bunch charge Q , equation (4.3) becomes

$$\frac{d^2 n_{\text{phot, incoh}}}{d\omega d\Omega} = \frac{Q/e}{N_{\text{sim}}^2} \cdot \frac{e^2/(\hbar\omega)}{4\pi^2 c} \left(\mathbf{P} \cdot \int_{t_{\text{ret}}(t_{\text{start}})}^{t_{\text{ret}}(t_{\text{end}})} \sum_j^{N_{\text{sim}}} \left(\frac{\gamma\mathbf{n} \times [(\gamma\mathbf{n} - \gamma\beta_j) \times \gamma\dot{\beta}_j]}{(\gamma - \mathbf{n}\cdot\gamma\beta_j)^3} \right) \cdot e^{i\omega t_{\text{ret}}} dt_{\text{ret}} \right)^2. \quad (4.4)$$

This expression reduces the number of simulated electrons required for a statistically representative ensemble of electrons by several orders of magnitudes and is used as the basis for the "**CL**assical **RA**diation Calculator" (CLARA) code, developed to calculate radiation spectra from a set of electron trajectories. The aforementioned memory issue is dealt by partitioning the interaction time into a number of slices, as shown in Fig. 4.2. For each time window a separate spectrum is calculated, which corresponds to the kind of spectrum seen by a streak camera behind a spectrometer. Since everything is incoherent and spectral intensity directly adds up, the total spectrum is obtained by summing up all slice-spectra.

$$\frac{d^2 n_{\text{phot, incoh}}}{d\omega d\Omega} = \sum_i^{N_{\text{slices}}} \left(\frac{d^2 n_{\text{phot, incoh}}(i \cdot T_{\text{slice}} \rightarrow (i+1) \cdot T_{\text{slice}})}{d\omega d\Omega} \right) \quad (4.5)$$

Since the approximation (4.5) is an effective reduction in spectral resolution, each time window has to be long enough to resolve the smallest spectral features expected by the examined physical system. In practice, this approximation is also useful, for it allows to neglect electrons in time slices, where those do not radiate.

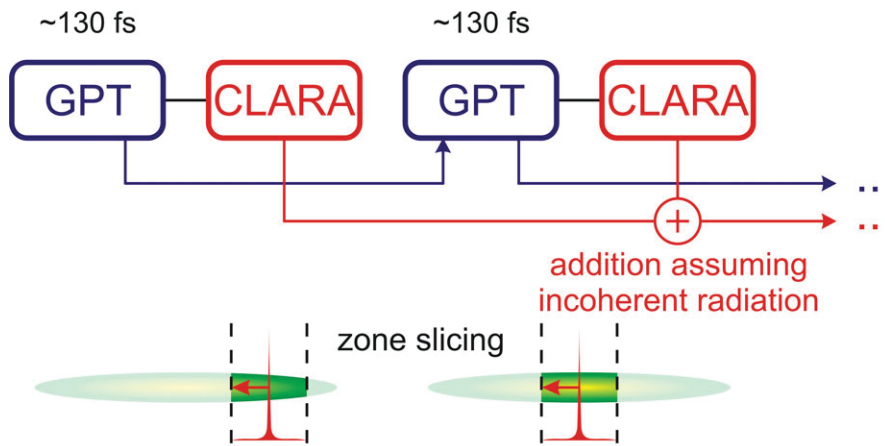


Figure 4.2: Calculations for picosecond long electron pulses are made computationally viable by restricting spectral calculations to the portions of the electron bunch (slicing) that interact with the laser pulse.

Since CLARA requires electron trajectories as input, it is designed to interface with an external particle tracker code, that models the interaction of lasers with electrons and outputs respective trajectories. Here that task is handled by the commercial GPT (General Particle Tracer) [4]. Support of laser beams has been added to the GPT framework by specifying the analytic expressions for the electromagnetic laser fields in paraxial approximation. The model of the laser consists of a Gaussian beam (spatially as well as temporally) with the correct focusing geometry. The evolution of the bunches included space-charge effects by GPT's 3D grid-based method working in the electron frame of reference [5, 6]. The electron traces are recorded at a temporal resolution of λ_{80} to account for higher harmonics. That intermediate result is then processed by CLARA. As described above, CLARA solves the Liénard-Wiechert potentials by computing eqs. 4.4 and 4.5 through a transformation to retarded times and subsequent calculation of the spectra using an FFT-based algorithm. The code was benchmarked against analytic solutions of radiation problems [7, 8] and slower representations of the same algorithm in Mathematica [9]. The accuracy

of the results can be said to be within 5%. An overview on the code architecture is depicted in Fig. 4.3.

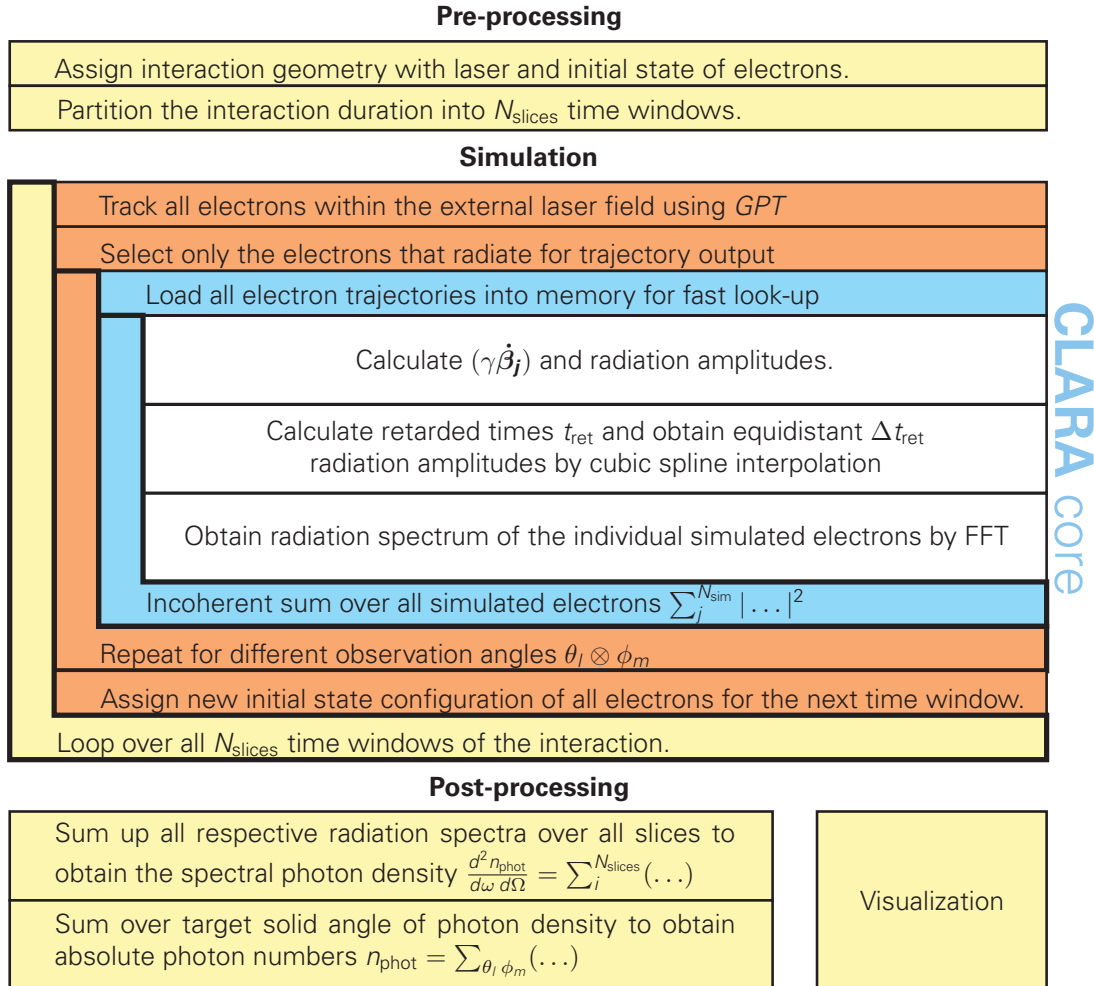
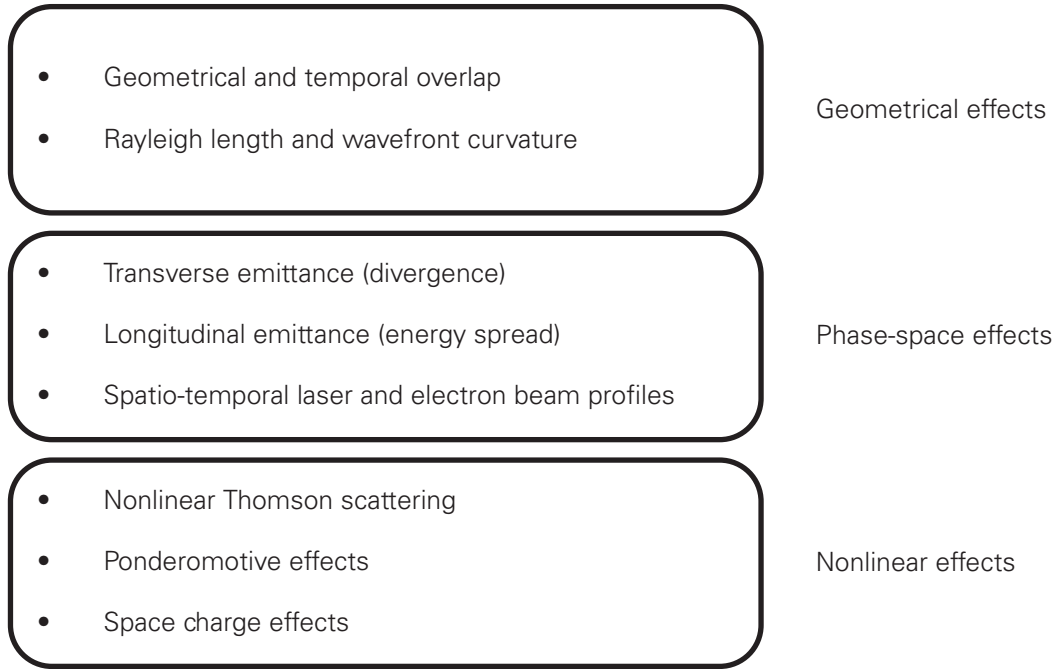


Figure 4.3: Code architecture of CLARA interfacing with GPT. The core of CLARA (blue-white) is realized in *C++*. The particle tracking routines (red) are realized within GPT, while pre-processing and post-processing (yellow) is implemented by scripting languages.

CLARA is capable of modeling Thomson scattering in complex electron and laser beam scenarios with relativistic intensities and simulation durations at tens of ps. The optimizations with respect to speed and memory facilitate parameter scan investigations, covering the full solid angle. In contrast to cross-section based codes, such as *Geant4* [10, 11], it also takes into account the phase of the laser field, which especially at nonlinear laser field strengths $a_0 \geq 1$ becomes relevant and leads to effects, such as substructures in the resulting radiation spectra as depicted in Fig. 4.4(d) below.

4.2 NON-IDEAL EFFECTS

Non-ideal effects are unwanted side effects that diminish the photon yield, broaden the spectrum or lead to the excitation of higher harmonics. Most prominently the non-ideal behavior arises from the chosen experimental geometry, the phase-space of both laser and electrons, as well as a range of nonlinear effects such as space-charge blow up, ponderomotive effects from the laser and the nonlinear Thomson regime.



For designing Thomson scattering experiments it is necessary to minimize the relevant non-ideal effects. According to (2.95)

$$\lambda_{sc} = \frac{\lambda_0}{n \cdot 2\gamma_0^2 \cdot (1 - \beta_0 \cos \phi)} \cdot (1 + a_0^2/2 + \gamma_0^2 \theta^2), \quad (4.6)$$

the scattered bandwidth is affected by variations in electron energy, direction of electron propagation and laser intensity. For the yield in eq. (2.107)

$$N_{\text{phot}} = 2\pi\alpha_f N_0 N_b a_0^2 (\Delta\omega_{sc}/\omega_{sc}). \quad (4.7)$$

one has to consider the conditions for optimal overlap between laser and electron pulses, as well as the energy efficiency of the desired harmonic (eq. (2.13)) in comparison to all the other harmonics. It is straightforward that low transverse and longitudinal emittances of electron pulses determine divergence, energy spread and therefore the radiated bandwidth into a given angle. However the goal of keeping the laser strength $a_0 \ll 1$ in favor of increasing the interaction distance L_{int} is less clear. According to Fig. 2.2(b) it seems reasonable to choose an $a_0 > 1$ in order to maximize the on axis yield of for example the 5th harmonic and achieve higher scattered photon energies in comparison to the fundamental mode. At this point it is very instructive to

look at one of the more pronounced nonideal effects at higher laser intensities ($a_0 \geq 1$) - the rich substructure of the Thomson spectra caused by realistic temporal laser profiles.

Fig. 4.4(a)-(e) show numerical results obtained from the particle tracker GPT combined with the radiation code CLARA. Angular resolved spectral distributions of Thomson backscattering demonstrate scenarios with various temporal laser profiles and maximum intensities. Here, three laser-electron models are being distinguished: The ideal model considers an electron bunch with zero emittance and an ideally collimated laser beam with rectangular temporal profile and transversally flat intensity distribution. The Gauss model only differs by assuming a Gaussian temporal envelope in which the laser field amplitude rises from zero to a maximum field and then declines again. The realistic model shows a scenario with parameters as they can be obtained at the ELBE facility at the HZDR using the DRACO laser. They include not only the full focusing geometry generating an overlap with a transversally Gaussian beam, but also ponderomotive effects, as well as electron space-charge and transverse and longitudinal emittance. For this example a 250 fs electron bunch with $\gamma = 25$ and realistic emittances of $\epsilon_{n,\text{trans}} = 2.5 \pi \text{ mm mrad}$ and $\epsilon_{\text{long,norm}} = 40 \pi \text{ keV ps}$ was considered. The electron bunch diameter with 50 μm was assumed to be large to minimize electron divergence ($\simeq 7 \text{ mrad}$), but also small enough so the required intensity on the target corresponding to a laser strength $a_0 = 1.5$ can successfully be delivered to the focal area by the DRACO laser.

While at $a_0 = 0.1$ the ideal and the realistic scenario vary only weakly in spectral shape, the situation radically changes for laser strengths $a_0 \geq 1$. In Fig. 4.4(c) the ideal case depicts a multitude of harmonics with only the odd harmonics radiating on axis. According to the energy normalization, one can see how the nonlinearity has decreased the respective photon energies by about a factor of 2. In the Gauss scenario of Fig. 4.4(d) it becomes apparent that the laser strength parameter changes within the interaction thus shifting the scattering energy according to eq. (4.6). The first harmonic is most instructive, as here it is clearly visible how at low intensities ($a_0 \ll 1$) the scattering energy starts off at $\omega_{\text{sc}}/(4\gamma_0 \cdot \omega_0) = 1$, then decreases with each successive oscillation, until the maximum laser field $a_0 = 1.5$ at $\omega_{\text{sc}}/(4\gamma_0 \cdot \omega_0) = 0.5$ is reached. After that the fields declines again and the spectrum shifts back to $\omega_{\text{sc}}/(4\gamma_0 \cdot \omega_0) = 1$. The higher harmonics partly overlap. The third harmonic goes from 1.5 to 3, while the fifth extends from 2.5 to 5. These spectral features make it plain that the full temporal field information of the laser pulse is contained within such a spectrum. However a realistic simulation with ELBE type electron bunches Fig. 4.4(e) shows that the substructure is almost completely washed out by non-ideal effects. The main reason for this behavior lies in the transverse Gaussian intensity distribution of the focus, which creates a superposition of a whole range of substructured spectra from low intensities at the outskirts of the laser beam up to the center where the peak laser strength interacts with the electrons. By this superposition the spectral oscillations from the laser are averaged out and the overall spectrum resembles a broadened spectrum of a lower mean laser strength. Other less pronounced non-ideal effects come from the divergence and the ponderomotive potential. According to eq. (4.6) electron divergences of $\theta \simeq 5.5 \text{ mrad}$ increase the bandwidth by up to $\gamma^2 \theta^2 \simeq 2\%$. To improve that situation and preserve such an interesting signature one would have to resort to laser-accelerated electron bunches that have the advantage of smaller bunch diameters and significantly lower transverse emittances on the order of $\epsilon_{n,\text{trans}} = 0.1 \pi \text{ mm mrad}$. Such a configuration would enable spectral signatures that are more comparable to Fig. 4.4(d), because a flat intensity distribution is easier to realize across smaller cross-sections.

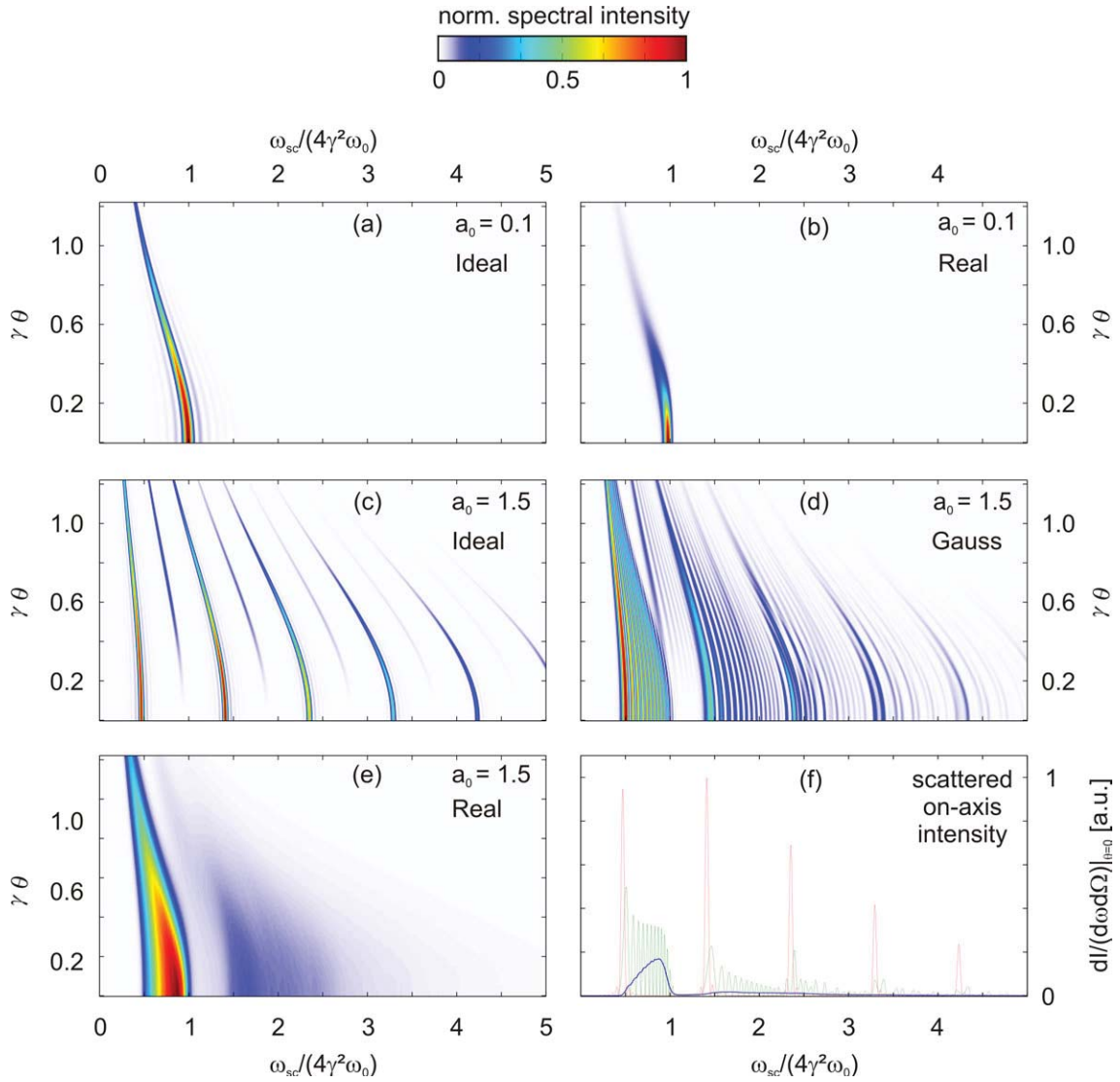


Figure 4.4: (a)-(e) show angular resolved spectral energy distributions for a range of Thomson backscattering scenarios featuring various laser strengths a_0 i.e. laser intensities and temporal laser profiles. There are three different models for laser and electrons: an ideal scenario contains a zero emittance electron bunch and a spatially flat laser profile with a rectangular temporal pulse shape; the Gauss scenario adds a Gaussian envelope to the temporal laser profile and the Real model depicts a full treatment of ELBE type electron beam parameters with finite electron emittances, complete focusing geometry and the influence ponderomotive and space-charge effects. The scale is normalized to the maximum value for each plot. In (f) the relative spectral intensities of the three scenarios at $a_0 = 1.5$ are compared on axis $\gamma\theta = 0$.

Hence for optimization of yield and bandwidth in a Thomson experiment one will prefer to keep the laser intensity low on target ($a_0 \leq 1$) and instead increase the interaction distance L_{int} to the extent allowed by the laser Rayleigh length.

According to eq. (4.6) the scattered bandwidth is affected by variations in electron energy, direction of electron propagation and the laser intensity. Varying γ_0 and θ immediately leads to the two conditions

$$\frac{\Delta E/E}{\gamma_0^2 \Delta \theta^2} < 1/2 BW \quad (4.8)$$

$$\frac{\gamma_0^2 \Delta \theta^2}{1 + a_0^2/2} < BW. \quad (4.9)$$

Note that the energy bandwidth $\Delta E/E$ has to be half the desired radiation bandwidth. With the normalized transverse and longitudinal emittances eq. (4.9) can be transformed into conditions for the electron bunch diameter d_{bunch} , as well as for the electron bunch duration τ_{bunch} .

$$d_{\text{bunch}} \geq \frac{(4 \log 2) \epsilon_{\text{trans},n}}{\sqrt{BW \cdot (1 + a_0^2/2)}} \quad (4.10)$$

$$\tau_{\text{bunch}} \geq \frac{(8 \log 2) \cdot \epsilon_{\text{long},n}}{\gamma_0 \cdot \Delta E}. \quad (4.11)$$

The factor $(8 \log 2)$ in front of the RMS emittances takes into account that all other parameters are normally given at FWHM. In addition to the emittance constraints spatial overlap is established by matching $w_0 \simeq d_{\text{bunch}}$ depending on the exact transverse electron distribution and divergence during interaction. For good temporal overlap the interaction range $L_{\text{int}} = (\tau_{\text{laser}} + \tau_{\text{bunch}}) \cdot c/2$ must lie within the Rayleigh length $Z_0 = \frac{\pi w_0^2}{\lambda}$. The list of geometrical constraints is completed by the laser wavefront curvature due to focusing, which leads to an additional half-angle divergence of magnitude $\Delta \theta = 2\pi \cdot d_{\text{bunch}}/2/R(L_{\text{int}}/2)$ with $R(z) = z + Z_0^2/z$ denoting the curvature radius of a laser wavefront at a distance z from the focus. Combined with eq. (4.9) one arrives at

$$\frac{\gamma_0^2}{1 + a_0^2/2} \left(\frac{\pi d_{\text{bunch}}}{L_{\text{int}}/2 + Z_0^2/(2L_{\text{int}})} \right)^2 \leq BW. \quad (4.12)$$

The laser pulse length has to be long enough to have its natural bandwidth meet the BW limits $\lambda_0/(c \cdot \tau_{\text{laser}}) \leq BW$.

The nonlinearity constraints due to the scattering process itself, ponderomotive broadening and charge blowup complete the picture. For small laser strengths $a_0 \ll 1$ the scattered yield is $\propto a_0^2$, but as a_0 approaches unity scattered intensity is increasingly diverted into higher harmonics (Fig. 2.9) thus decreasing the effective scattering efficiency. For the yield of the fundamental it is therefore more efficient to stay below a certain intensity threshold (for example $a_0 = 0.148$ with 5% of the energy going into higher Harmonics) and increase the interaction distance to the full extent allowed by the Rayleigh range. If scattering efficiency is not the main issue, for instance if laser intensity is cheap, one can further increase the intensity until the scattering intensity reaches the maximum of a given harmonic. At higher intensities the electron bunch is subject to ponderomotive forces by the laser. Thereby the exact nature depends on the intensity gradients of the laser pulse. However, an upper limit for the change in kinetic energy ΔE due to this effect

can be derived from the ponderomotive potential of the laser $\Delta E = mc^2 a_0^2/4$. The above set of constraints is summarized in Table 4.1.

trans. emittance (divergence)	$d_{\text{bunch}} \geq \frac{(4 \log 2) \epsilon_{\text{trans},n}}{\sqrt{BW \cdot (1 + a_0^2/2)}}$ $(\gamma_0^2 \Delta \theta^2)/(1 + a_0^2/2) \leq BW$
long. emittance (energy spread)	$\tau_{\text{bunch}} \geq \frac{(8 \log 2) \cdot \epsilon_{\text{long},n}}{\gamma_0 \cdot \Delta E}$ $2 \Delta E/E < BW$
temporal overlap (Rayleigh length)	$L_{\text{int}} \leq Z_0$ $L_{\text{int}} = (\tau_{\text{laser}} + \tau_{\text{bunch}}) \cdot c/2$ $Z_0 = \pi W_0^2/\lambda_0$
natural bandwidth	$\lambda_0/(c \cdot \tau_{\text{laser}}) \leq BW$
ponderomotive broadening	$a_0 \leq \sqrt{4 \Delta E/mc^2}$
eff. decrease due to nonlinearity	$a_0 = 0.148$ (5% efficiency degradation) $a_0 = 0.76$ (maximum scattered intensity)
laser curvature	$\frac{\gamma_0^2}{1 + a_0^2/2} \left(\frac{\pi d_{\text{bunch}}}{L_{\text{int}}/2 + Z_0^2/(2L_{\text{int}})} \right)^2 \leq BW$

Table 4.1: Constraints for backscattering geometries due to non-ideal effects. A maximum accepted on-axis bandwidth $BW = \Delta\omega_{\text{sc}}/\omega_{\text{sc}}$ for the scattered radiation is assumed. The emittances are normalized RMS values, while the rest is taken at FWHM.

4.3 HIGH-REPETITION THOMSON SOURCES FOR HIGH AVERAGE PHOTON YIELDS

Generally, for the application of X-ray beams by Thomson scattering, high photon numbers are crucial for imaging, in order to cover large phase spaces at high spatial and temporal resolution, for material processing, for investigation of small cross-section reactions or simply for overcoming an unfavorably large background signal. Hence, the goal in designing an Thomson X-ray source is in most cases to maximize the number of photons from given experimental constraints to desired X-ray beam properties. Before going into detail, it is useful to state an important distinction: For many applications, the temporal structure of the X-ray beam is less important than the average photon flux, whereas for other applications such as pump-probe type of diagnostics the peak-photon flux is essential. This has major consequences on the required technology, as well as on physics and strategy of source optimization. In spite of being useful in both areas, conventionally accelerated electrons profit from being available at much higher repetition-rates, while the strength of laser-wake field accelerated electrons lies in the high beam quality and its intrinsic synchronization to a laser system. In the following, first the ambitious example of future EUV Lithography at 13.5 nm is used to illustrate design and capabilities of high average flux Thomson sources. This has the advantage of highlighting the limits of the state-of-the-art, while other interesting applications, such as phase-contrast imaging, are similar in design, but due to less demanding flux requirements are easier to realize. In the second step, the view is then extended

towards Thomson sources with maximum peak photon flux, where many photons are in a single X-ray pulse.

Source Requirements for EUV Lithography

According to the International Technological Roadmap for Semiconductors (ITRS) [12] printable patterns of 32 nm half-pitch are required by the semiconductors industry by 2017. In order to achieve this, the use of extreme ultraviolet lithography (10-20 nm) is envisioned [13]. The realization of such a process depends on a radiation source that has to meet the challenging task of delivering 0.7 W average EUV power on the die [14]. Additional restrictions have to be taken into account, that arise due to the limited reflectivity and bandwidth of available optics for EUV wafer scanners (silicon-molybdenum mirrors). The semiconductor industry therefore aims for an EUV source with target specifications of 100-150 W average power at 13.5 nm, which roughly corresponds to 1×10^{19} photons/s and a viable bandwidth of 2% [14, 15].

Discharge produced plasmas or laser plasmas from tin, Lithium or Xenon targets could eventually meet these criteria [14]. However, all these processes generate relevant amounts of debris that finds its way to the collector optics, reducing its life time. Changing expensive optics more than a couple of times per year remains a serious impediment for industrial application. An idea to solve this problem lies in going to a radiation process that is intrinsically debris-free and scales well up to the required parameters. A free-electron laser (FEL) seems to be of special interest, since it could deliver kW of EUV power in a stable vacuum environment [16]. The downside is the large size of such a facility of several tens of meters, which also needs heavy radiation shielding and thus leads to high costs associated with the infrastructure.

A Thomson source is debris-free, but much more compact. Also a laser wavelength on the order of μm together with electron energies of only a couple of MeV, that can easily be obtained by room sized electron accelerators, are sufficient to tune to the desired EUV wavelength. However, as Thomson backscattering is in contrast to an FEL usually an incoherent process, the question of optimum yield and technical feasibility becomes a critical issue.

The properties of the required source are primarily determined by the 0.7 W of power that are needed on die level [14] for economic operation of the lithography process and the optics required for the beam transport in an EUV scanner. Due to strong absorption of EUV radiation in all materials, there are no lenses available. Therefore one resorts to highly reflective multi-layer mirrors made of alternating layers of molybdenum and silicon. The reflectivity of such a mirror is on the order of 66% with a bandwidth of almost 5% around 13.5 nm [14, 15]. Considering that a scanner needs about 11 multilayer reflections one arrives at target specifications for a potential source [14, 15], such as an average power exceeding 100-150 W at 13.5 nm, which roughly corresponds to 1×10^{19} photons/s and a viable bandwidth of 2%.

Potential candidates for next generation lithography [14, 15] are compared by the CW power they can deliver to the 1 mm x 1 mm x 1 mm intermediate focus of a projector. Those numbers are calculated for a source that radiates over the full solid angle and thus requires an efficient optical collection system.

The fact that Thomson backscattered EUV radiation is confined to a small cone of a few degree, makes collimation and beam transport considerably easier compared to radiation from laser or discharge produced plasmas, where emission is largely isotropic. Quantitatively, the product of source size and collection angle (etendue) drops by more than two orders of magnitude. Hence, the Thomson source length may be a lot longer than 1 mm and also the collection optics of the scanner could be simplified to less mirrors, which directly lowers the power requirements of EUV lithography, because less power is lost in the optics.

Considering that only 0.7 W of EUV power are needed on the die itself [14], a simplification of this imaging system to 4 mirrors due to the small source divergence would mean a new power requirement of $0.7 \text{ W}/(0.66)^4 = 3.7 \text{ W}$. The bandwidth requirement of 2% also eases slightly by a factor of $\simeq 1.65$. However, for the sake of direct comparison with other systems, the following simulations assume the strict 2% bandwidth limit defined by an 11-mirror scanner.

When examining head-on collision between laser beam and electrons, there are mainly ten parameters to define. These consist of electron bunch parameters, such as energy, charge, bunch length, bunch diameter, longitudinal and transverse emittance, as well as the laser parameters wavelength, pulse energy, pulse length and spot size. For the present analysis the strategy is to first calculate with the help of CLARA, how many photons one can obtain by Thomson scattering under an optimized setup, when assuming realistic laser pulses and electron bunches including all non-ideal effects. It is then possible to discuss, whether the required EUV optical power output is currently achievable through scaling towards higher repetition rates, higher bunch charges or higher laser pulse energies through power enhancement cavities.

The laser wavelength is determined by currently available technology, i.e. diode-based laser systems at about 1.06 μm , which are in principle able to provide ps-long pulses at high repetition rates on the order of MHz with a pulse energy of about 1 mJ [17, 18], corresponding to an average optical power in the kW-range. For easy scaling and for evaluating space-charge effects, an initial scenario with 1 nC of electron bunch charge is assumed. The electron energy, as determined by the laser wavelength and the target wavelength 13.5 nm is 1.76 MeV and thus can be provided by a dedicated electron gun system. The normalized transverse and longitudinal emittance $\epsilon_{n,\text{trans}} = 2.5 \pi \text{ mm mrad}$ and $\epsilon_{\text{long,norm}} = 40 \pi \text{ keV ps}$ are assumed to be similar to the ELBE facility at the HZDR when using the new SRF gun [19, 20]. Additionally, an optimistic scenario in which these emittances are decreased by a factor of 4 is also considered. An overview on these basic parameters can be found in Table 4.2.

λ	1.06 μm
laser pulse energy [mJ]	1.0
γ	4.43
energy[MeV]	1.76
maximum ΔE [MeV]	0.0227
required bandwidth (BW) [%]	2.0
required energy spread	$\Delta\gamma/\gamma = BW/2 = 0.01$
charge[nC]	1.0
norm. trans. emittance [$\pi \text{ mm mrad}$]	2.5 (0.625)
norm. long. emittance [$\pi \text{ keV ps}$]	50 (12.5)

Table 4.2: Overview on the general parameters for an EUV Thomson source.

Spatial and Temporal Overlap

Optimal spatial overlap is realized when the laser waist size w_0 equals the minimum electron bunch diameter d_{bunch} . Since the transverse spatial distributions here are assumed to be Gaussian, any substantial mismatch between the electron number and laser intensity distributions decreases either the total number of scattered photons or scattering electrons. Therefore, all following scenarios assume equal laser spot and electron bunch diameters.

In order to maintain temporal overlap, the interaction between laser and electrons has to take place within the Rayleigh range (Table 4.1), while on the other hand the electron bunch has to be long enough to avoid a large energy spread due to the finite longitudinal emittance. This situation is further complicated by the presence of high space-charge [21–23] which for **nC**-beams at can increase both the energy spread or the beam divergence. Thus the impact of space-charge on the photon yield is similar to a large longitudinal emittance alone.

In Fig. 4.5 and 4.6, the scattered on-axis intensity within the 2%-bandwidth is depicted for two different longitudinal emittances ($\epsilon_{n,\text{long}} = 50 \pi \text{ keV ps}$ and $12.5 \pi \text{ keV ps}$), as well as three bunch charge scenarios (1 **nC**, 250 **pC** and 75 **pC**). The yield of the 250 **pC** and 75 **pC** bunch charge scenarios was multiplied by 4 and 16 respectively, so that the efficiency of a 1 **nC** Thomson source can be directly compared to a 250 **pC** source with four times the laser repetition rate. In all scenarios the on-axis yield slowly saturates due to a decreasing influence of both bunch charge and longitudinal emittance as the bunch becomes longer. While for the $50 \pi \text{ keV ps}$ case in Fig. 4.5 the yield reduction is determined still to a large degree by longitudinal emittance, space-charge becomes the dominant influence in Fig. 4.6. Hence, for the performance of an EUV Thomson source a small longitudinal emittance is less of a critical issue. In order to minimize space-charge effects at 1.8 **MeV**, a 1 **nC**-beam needs to be close to a bunch length of 10 **ps** – or exceed it – before the space-charge-induced spectral broadening becomes significantly smaller than 2%. In the following a bunch length of $\tau_{\text{bunch}} = 15 \text{ ps}$ is assumed.

The laser pulse length has rather weak constraints, for it can be shorter or longer than the electron bunch without affecting the scattering yield. It merely has to be long enough to guarantee the laser bandwidth fulfills the bandwidth goal of 2% ($\tau_{\text{laser}} > 60 \text{ fs}$) and the laser pulse has to be short enough for the interaction to happen within the Rayleigh range ($\tau_{\text{laser}} < 80 \text{ ps}$ for $w_0 = 65 \mu\text{m}$). For these reasons the pulse length of 15 **ps** is chosen mainly for convenience and is otherwise a free parameter.

Optimal interaction diameter

For optimizing the photon yield of Thomson sources, the diameter of the interaction region is a crucial parameter. Decreasing both electron and laser diameters while maintaining the total energy of the laser leads to a higher intensity per electron – without having to invest in more laser photons. Thus, the total yield is inversely proportional to the square of the laser waist size. Therefore the important question is: How small can the laser waist size and the electron

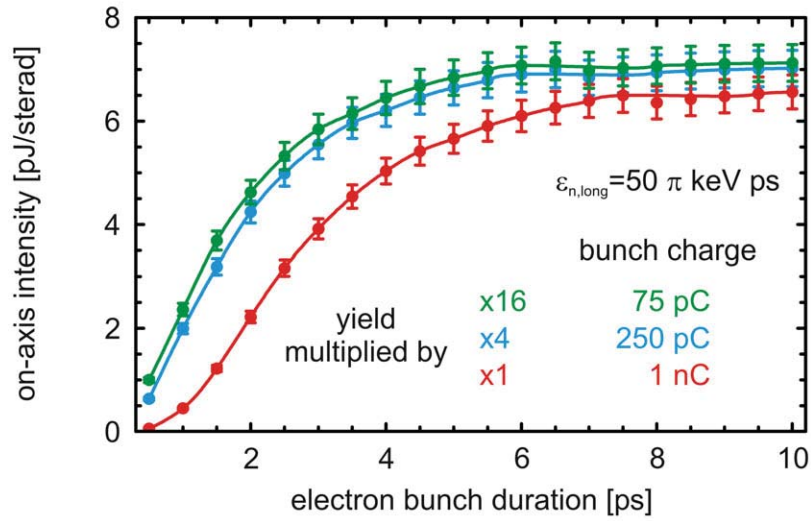


Figure 4.5: For the temporal overlap the electron bunch duration τ_{bunch} is varied. For each laser scenario there is one parameter scan with a longitudinal emittance of $\epsilon_{n,\text{long}} = 50 \pi \text{ keV ps}$ for bunch charges of 75, 250 and 1000 pC. The interaction diameter $d_{\text{bunch}} = 65 \mu\text{m}$ was suitably chosen in hindsight to match later parameter optimizations. In general, an increase in EUV photon yield until saturation at longer electron bunches is observed.

bunch diameter be made before non-ideal effects mainly from transverse emittance take over and decrease the bandwidth-limited yield?

For the radiated on-axis intensities, such an optimization is depicted in Fig. 4.7. Here one finds the highest intensity at $w_0 = d_{\text{bunch}} = 50.0 \mu\text{m}$ for ELBE-like beams and $w_0 = d_{\text{bunch}} = 15.0 \mu\text{m}$ for the optimistic scenario featuring a four times smaller emittance.

As word of warning, while on-axis scans are often a good way of analyzing the presence of non-ideal effects and can give a first estimate on the optimal parameters of a Thomson source without having to calculate various observation angles, this strategy fails here. At low electron energies, the absolute electron divergence can well be in the range of several degrees, so one cannot neglect the shift in on-axis scattered wavelength

$$\lambda_{\text{sc}} = \frac{\lambda_0}{2\gamma^2(1 - \beta_0 \cos \Phi)} \simeq \frac{\lambda_0}{4\gamma^2 \left(1 - \frac{\Delta\Phi^2}{4}\right)}, \text{ with } \Phi = \pi + \Delta\Phi \quad (4.13)$$

due to the laser side-scattering at electrons traveling at an off-axis angle. For that reason, electrons have different scattered intensities in their respective direction of propagation. Therefore it is necessary to optimize the yield over the full radiation cone and calculate total bandwidth-limited photon numbers that can be used for a potential EUV lithography application.

Generally the solid angle has to be scanned in both azimuthal and polar angles. However, the scenario is rotationally symmetric with respect to the electron density and laser intensity distributions, such that only the spectra in azimuthal observation angles need to be calculated. The following photon numbers are numerically integrated by assuming rotational symmetry in ϕ .

The main result is depicted in Fig. 4.8 and shows the total bandwidth-limited EUV photon

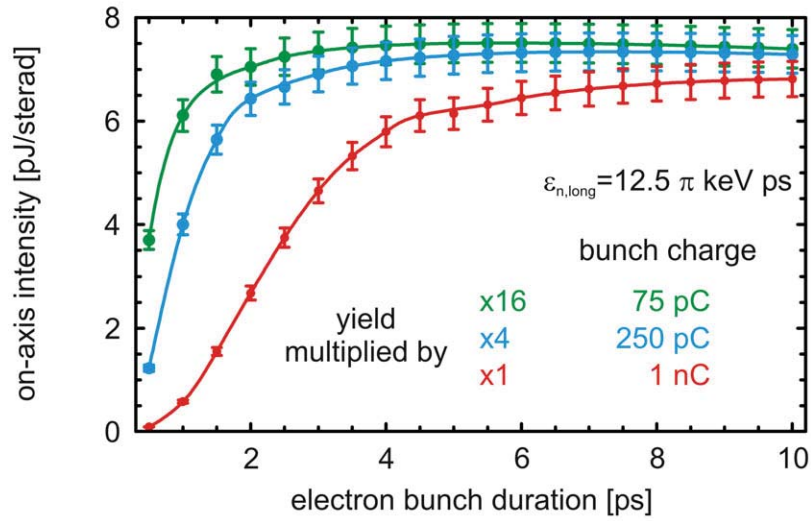


Figure 4.6: For the temporal overlap the electron bunch duration τ_{bunch} is varied. For each laser scenario there is one parameter scan with a longitudinal emittance of $\epsilon_{n,\text{long}} = 12.5 \pi \text{ keV ps}$ for bunch charges of 75, 250 and 1000 pC. Compared to Fig. 4.5, the relative effect of space-charge compared to the lower longitudinal emittance is more pronounced.

numbers from a mJ laser beam scattering at a nC electron bunch at various interaction diameters. The inset of Fig. 4.8 depicts the radiation cone of the optimum setting for the 65 μm scenario with its rotational symmetry. At large interaction diameters the laser photon density around each electron is small, thus decreasing the scattering efficiency. Towards very small interaction diameters, the scattering efficiency and thus the total photon yield is high, but the finite electron beam emittance leads to a large divergence angle at small interaction diameters. Therefore, a large fraction of the side-scattered photons is Doppler-shifted outside of the target 2% photon bandwidth. In between these two extremes one achieves an optimal bandwidth-limited photon yield.

In actual numbers (see Fig. 4.8), one expects an optimal yield of 400 photons/(mJ nC) at $w_0 = d_{\text{bunch}} = 135 \mu\text{m}$ for ELBE-type electron beams and 1300 photons/(mJ nC) at $w_0 = d_{\text{bunch}} = 65 \mu\text{m}$ for transversally and longitudinally improved emittances.

In Fig. 4.9 the angular profiles of the diameters of 25 μm , 60 μm and 195 μm are shown. In all cases the relevant radiation is constrained by the 2% bandwidth goal and thus covers only about 2/10 of the $1/\gamma$ -cone, which is little more than 2.5° .

Scaling towards EUV lithography

By knowing which laser energy to photon number efficiency to expect, it has become straightforward to calculate the requirements of a full scale EUV source for lithography. The remaining options to achieve a high photon flux in the range of 1×10^{17} - 1×10^{19} photons/s are increasing the laser pulse energy, the repetition rate and last but not least, the electron bunch charge. The actual EUV photon flux is then determined by available technology.

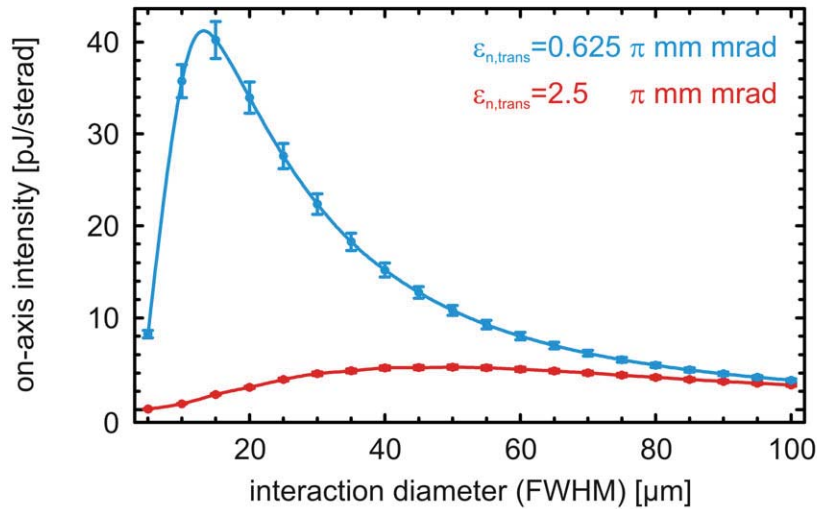


Figure 4.7: The on-axis yield is optimized by simultaneously varying the electron bunch diameter d_{bunch} and the laser waist size w_0 , while keeping spatial overlap $w_0 = d_{\text{bunch}}$ and the pulse energy. The parameter scan is shown for a transverse emittance of $\epsilon_{n,\text{trans}} = 2.5 \pi \text{ mm mrad}$ and an optimistic setting of $\epsilon_{n,\text{long}} = 0.625 \pi \text{ mm mrad}$.

On the electron accelerator side, repetition rates can be in the GHz range, whereas laser oscillators operate in the **MHz** range. Since only a tiny fraction of all laser photons is used for scattering, it is useful to recycle the laser pulses by building a resonator cavity around the interaction area. According to the Q-factor of the resonator, a defined amount of laser pumping power can achieve a Q times higher EUV photon yield without increasing the thermal load in the laser amplifiers. A similar argument can be also made for the electron pulses, so an energy-recovering linac would substantially lower power consumption. However, the main bottleneck of current linacs with regard to Thomson scattering is the maximum charge per electron bunch.

Each interaction of the laser beam with an electron bunch within a (laser) resonator as depicted in Fig. 4.10 means that by reflection at the end mirrors one has losses. In order to keep the energy loss per backscattered photon low it is essential to maximize the charge of the bunch. Three basic photo-injector technologies are available. There are DC photo-injectors, normal conducting photo-injectors and superconducting photo-injectors. The first two technologies are mature proven technologies, the latter combines the best of both worlds, efficiency of DC-guns and performance of RF-guns. Due to the EUV requirements, high-average currents exceeding 1 A become necessary and thus only superconducting guns remain an efficient option. A review on this topic can be found at [24]. Another idea [25–27], conceptionally still at the beginning, is the generation of secondary electrons in a diamond slab directly behind the photoelectron gun. In such a microns-thin diamond slab, each electron of the original beam excites through inelastic scattering many electrons in the diamond from the valence into the conduction band, which then in 1-10 ps thermalize by phonons towards the lowest conduction band. With the help of an external electric field, these electrons drift to the diamond surface, where these are field-emitted into the vacuum, forming a new secondary electron bunch for subsequent acceleration. Such an electron bunch can have 1-2 orders of magnitudes more electrons than the original bunch. Its electron temperature tends towards the lattice temperature of the diamond slab. Using such an

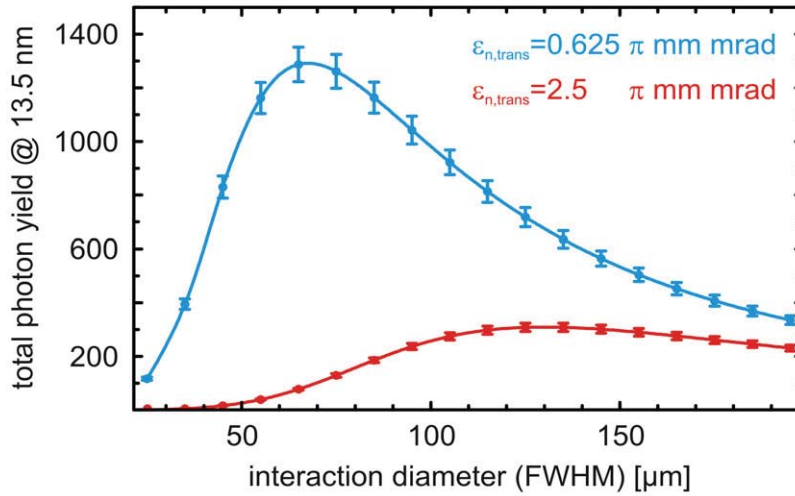


Figure 4.8: Main optimization result shows total EUV photon scattering yields at 13.5 nm with respect to the common interaction diameter of both electron and laser beam $w_0 = d_{\text{bunch}}$.

approach, the e-RHIC aims for 16 nC bunches at 28.15 MHz corresponding to an average current of 450 mA [24].

For the driving laser system, diode-pumped fiber lasers using solid core photonic crystal fibers (PCF) are especially suitable for ps-pulse, high-repetition rate systems with high average power. These lasers have favorable thermo-optical properties and feature wall-plug efficiencies beyond 50%. The tremendous advance on this field in recent years led to the experimental realization of 1 mJ, 1 ps lasers at 1 MHz [17, 18, 28, 29].

For pulsed lasers, power enhancement resonators routinely feature enhancements on the order of 10^2 . Additionally, for stacking continuous wave (CW) laser beams in Fabry-Perot cavities there exists a lot of experience in various fields such as in gravitational wave astronomy, so that these techniques could be successfully demonstrated for ultrashort laser pulses [30, 31].

With regard to a potential EUV source for lithography, a fairly optimistic stance is taken with respect to available and near-future technological capabilities. For one the calculated result of 1300 photons/(mJ nC) assumes an excellent electron gun emittance of $\epsilon_{n,\text{trans}} = 0.6 \pi \text{ mm mrad}$. Then a laser system with 25 MHz repetition rate and a pulse energy of 1 mJ is considered, which probably would be an efficient 25 kW diode pumped fibre laser that is currently just beyond technological realization as a single laser system, but which could be arranged by using several lasers in parallel. Furthermore a 0.5 A superconducting RF-gun accelerating 20 nC bunches at the laser repetition rate is envisioned. Finally, an enhancing resonator cavity with a power enhancement factor of 10,000 [31] recycles the laser power. This scenario would lead to an EUV source with $10^4 \cdot 25 \text{ MHz} \cdot 1 \text{ mJ} \cdot 20 \text{ nC} \cdot 1.3 \times 10^3 \text{ photons/(mJ nC)} = 6.5 \times 10^{15} \text{ photons/s}$ or 0.1 W. In terms of EUV yield for lithography this is by 2–3 orders of magnitudes short.

Depending on the scenario, photon yields on the order of 1300 photons/(mJ nC) at a bandwidth of 2% at 13.5 nm can be obtained by Thomson backscattering. These numbers include non-ideal effects. Depending on the normalized transverse emittance, electron bunches should

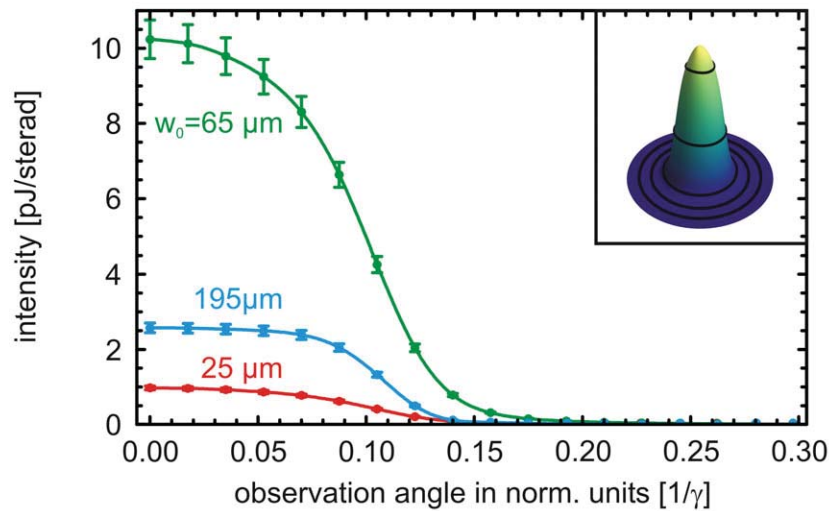


Figure 4.9: Angular profile of the peak positions of Fig. 4.8. The solid lines correspond to ELBE-like emittances of $\epsilon_{n,trans} = 2.5 \pi \text{ mm mrad}$ and the dashed lines to emittances improved by a factor of 4. (Inset) Displays the rotational symmetry of the calculated angular profile cone. Any deviation from symmetry is smaller than 1%.

feature spot sizes in a range of (50-150 μm) and exceed 10 ps in duration. Towards higher photon yields, a high bunch charge per shot and an efficient power-enhancement resonator has priority before repetition frequency because this keeps energy losses down. With foreseeable technology, an average power on the order of several tenth of Watts at 13.5 nm and 2% bandwidth seems to be within the range of possibilities. To the desired specs stated by semiconductor industry there is still a gap of more than two orders of magnitudes. However, considering that on the die level only a power of 0.7 W is needed and that Thomson radiation has a divergence of 4° and below, an eventual simplification of the EUV collector system from 11 to 4 mirrors could lower the photon number requirement and increase the maximal bandwidth acceptance to bridge the aforementioned performance gap and bring an application within reach.

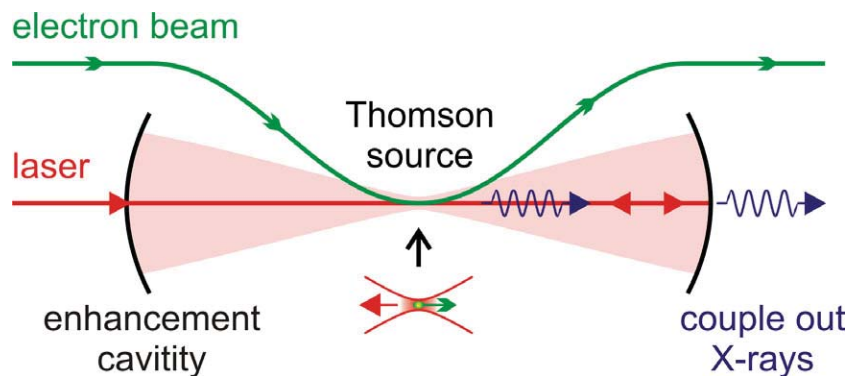


Figure 4.10: Laser resonator as power-enhancement cavity for high-average yield Thomson sources.

For further improvements in photon yield other than merely scaling up laser or electron sources, one needs to increase the efficiency of the scattering process itself. Since the Thomson cross section is fixed, the only option left is coherent light emission. In practice this is equivalent

to aiming for a free-electron laser (FEL) type process that causes micro-bunching in the electron beam and thus coherent radiation.

4.4 SINGLE-SHOT THOMSON SOURCES WITH ELBE AND LASER-WAKEFIELD ACCELERATED BEAMS

Thomson sources are very promising for pump-probe experiments, as these can deliver hard X-rays ($> 10 \text{ keV}$) at small bandwidth in a **fs** to **ps** time frame. Especially due to the short laser wavelength, Thomson sources quickly exceed the photon energies available in conventional synchrotron and FELs. Potential experiments are time-resolved $K\alpha$ -spectroscopy of high-Z materials, X-ray backlighting of optically overdense plasmas from solids, as well as nuclear physics at **MeV** photon energies. In such pump-probe type of experiments, a high number of photons per shot is crucial.

The main difference compared to a high-repetition Thomson sources is that the objective is to get as many X-ray photons as possible into a single, short X-ray pulse (*high peak brilliance*) rather than a high photon yield spread over many pulses (*high average spectral brightness*). Therefore maximum energy efficiency or scalability towards high repetition rates is less important.

The electron source can be both a conventional linear accelerator or a laser-wakefield accelerator (LWFA). Whereas LWFA electrons are of little use for high-repetition Thomson sources, because the technical challenges of providing laser pulse energies on the Joule level and a well controlled gas target for each shot currently prevent LWFA from achieving repetition rates beyond tens of **Hz**. However, when aiming for high-photon numbers per pulse, the ultrashort electron bunch duration and the small emittance of LWFA are key advantages over conventional accelerators. On another, more practical note, using LWFA electrons for Thomson scattering is desirable, since a single CPA laser system can be used for both the Thomson source and the ultrashort pump beam driving the LWFA electron beam. Hence, a sophisticated beam synchronization between two different lasers or an additional beam stretcher-compressor system for the same laser is not necessary.

The required laser systems are by definition low-repetition laser systems, providing intense laser pulses (**TW** to **PW**) with high pulse energies. In addition to the constraints from geometry, electron bunch emittance and space-charge, these laser pulse intensities become high enough, for nonlinear Thomson scattering effects, such as spectral shifting, spectral broadening and the generation of higher harmonics, to come into effect.

Due to the strong relativistic length contraction $\propto 1/(4\gamma^2)$, the resulting X-ray pulse duration [see eq. (2.108)]

$$\tau_{\text{xray}} = \tau_{\text{bunch}} + \frac{\tau_{\text{laser}}}{2(1 - \beta \cos \phi) \cdot \gamma^2} . \quad (4.14)$$

is primarily determined by the electron bunch duration τ_{bunch} and only weakly related to the initial laser pulse duration τ_{laser} . Therefore, one possible way around high laser pulse intensities is to increase the laser duration in exchange for lowering the laser intensity. However, for low-emittance

electron beams there exists, as for high-repetition Thomson sources, an optimal interaction diameter at a small laser spot size w_0 on the order of μm . As a result, the maximum usable laser pulse duration is restricted by a short Rayleigh length $Z_0 = \pi w_0^2 / \lambda_0$ corresponding to a few **ps**. Therefore trading laser intensity to laser pulse duration to avoid the nonlinear Thomson regime is only of limited applicability.

The following analysis highlights what is possible for head-on Thomson scattering in terms of single shot photon yields with both conventionally accelerated and laser-wakefield accelerated electrons using existing high-power lasers. As a reference for applications, the X-ray photon yields, for a range of X-ray bandwidths down to 5% is shown. Note, that in this chapter, the minimum X-Ray bandwidth is still constrained by the laser bandwidth. In the next chapter this limitation is going to be lifted.

The laser beam assumed for the Thomson source corresponds to the DRACO laser system (4 J per pulse, 25 fs, 800 nm). To avoid the nonlinear Thomson backscattering regime, the beam is recompressed to merely 1 ps, such that the laser strength parameter $a_0 \ll 1.0$ remains below unity. The transform-limited bandwidth of the laser and thus the minimum bandwidth of the Thomson source driven by the DRACO laser is 4.7%. To retain a higher degree of generality, the scenarios were calculated for the smaller bandwidth of a transform-limited 1 ps, so the results remain applicable for other lasers with shorter bandwidths than DRACO. The bandwidth of the respective laser then determines the applicable spectral resolution limit.

For the electrons two different electron beams are compared: A conventionally accelerated electron beam (ELBE-beam) with a normalized transverse emittance of $\epsilon_{\text{trans,rms}} = 2.5 \pi \text{ mm mrad}$ at 40 MeV as in the high-repetition rate scenario and a laser-accelerated electron beam at 1 GeV with low emittance $\epsilon_{\text{trans,rms}} = 0.1 \pi \text{ mm mrad}$, see also Table 4.3.

Many of the results are given in terms photon densities with respect to photon energy and solid angle. This has the benefit of giving quick access to absolute photon numbers as these are often used for designing experiments with X-rays, and in contrast to the radiation energy the number of photons is invariant with respect to electron energy. Therefore it is easy to generalize the results for other scenarios at different electron energies. However, using a scale of scattered energy as in Fig. 4.4 and Fig. 4.11-4.13(f) has the advantage of showing what relative proportions of the laser pulse energy go into which part of the scattered spectrum. Angular-resolved spectra as shown in Fig. 4.11(a),(b),(d) are averaged over all polar angles, weighted with respect to the azimuthal observation angle according to the integration factor $\sin \theta$ in spherical coordinates. In addition the spectra are normalized to photon energies, such that summing up the photon density over some specified diagram area immediately results in the respective photon yield.

For each the ELBE and the LWFA scenario, angular-resolved spectra are shown for several interaction diameters. Due to the finite electron bunch emittance, the electron bunch divergence increases towards smaller interaction diameters and leads to spectral broadening through the off-axis Doppler effect. Since this broadening happens in the angular coordinate only, the sharp edge at the maximum scattered photon energy is maintained, see Fig. 4.11(d). Physically, this is equivalent to affirming that the maximum electron energy is always scattered into the respective direction of propagation.

The reason, why this edge blurs at small interaction diameters is solely an intensity-related phenomena from nonlinear Thomson scattering. According to theory in chapter 2, the scattered photon energy decreases with the factor $(1 + a_0^2/2)^{-1}$, where $a_0 \propto \sqrt{I_0} \propto w_0$. Since the temporal laser pulse profile is Gaussian, rather than a rectangular pulse, the photon redshift arising from the “photon drag” in (2.90) is zero at the beginning of the laser pulse, reaches the maximum in the middle and afterwards decreases to zero again. This range of different maximum photon energies causes the blurred, intensity-broadened edge on the energy scale of the spectrum.

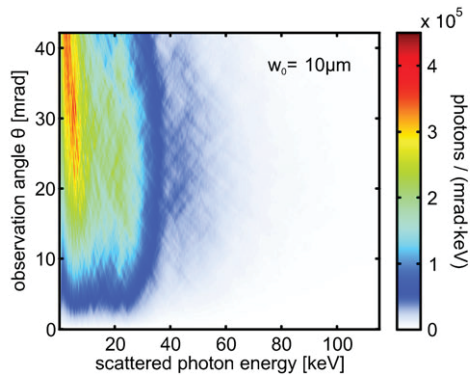
Depending on the electron bunch emittance, the other telltale sign of nonlinear Thomson scattering being higher harmonics, is not always distinguishable from emittance or pulse-profile related broadening. While for $\epsilon_{n,trans} = 2.5 \pi \text{ mm mrad}$ and $\epsilon_{n,trans} = 0.1 \pi \text{ mm mrad}$, the second and the third harmonics are visible, this is not possible in the emittance dominated scenario $\epsilon_{n,trans} = 10 \pi \text{ mm mrad}$, where most of the spectral features are gone.

Summing up the photon density or correspondingly the spectral intensity over the full calculated solid angle yields Fig. 4.11-4.13(e) and (f). From the photon number figures 4.11-4.13(e) it is evident that due to the linear $\hbar\omega$ -energy dependency, there exist sizable quantities of low energy photons, that can even exceed the main photon peak as depicted in Fig. 4.13(e). For this reason and for an unambiguous definition the maximum in the spectral intensity spectra Fig. 4.11-4.13(e) is chosen as the reference central X-ray energy around which photon numbers at various bandwidths are to be determined.

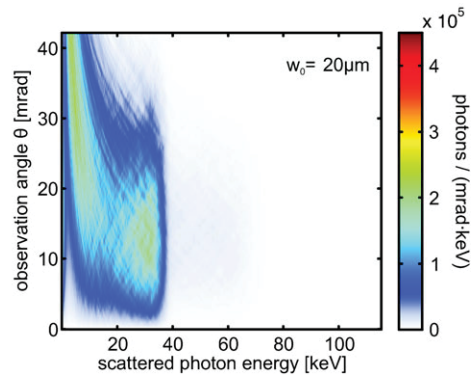
Parallel to Fig. 4.8, the diameter dependency on the total photon numbers at various bandwidths is shown in Fig. 4.11-4.13(g) and (h). Since X-ray focusing optics require the radiation to be constrained within a defined solid angle [32] the use of an aperture of 5 mrad half-angle or 40% the $1/\gamma$ cone was assumed in Fig. 4.11(h) and 4.12(h). For better comparison the aperture in the LWFA case, see Fig. 4.13(h), was chosen accordingly to be $200 \mu\text{rad}$ half-angle.

The results in Fig. 4.12(h) and Fig. 4.13(h) show, that for realistic beam parameters, the expected photon yields are in a range of 3×10^7 (5%) to 2.7×10^8 (total) for 1 nC ELBE-beams and 1×10^7 (5%) to 2.6×10^8 (total) for 0.1 nC laser-accelerated electrons. In contrast to the low-intensity, high-repetition case, the number of photons per bunch charge at 5% bandwidth scales only weakly with a reduced emittance. Due to this intensity-dependent nonlinearity and despite the smaller phase space volume occupied by the low-emittance electrons, small photon energy bandwidths become increasingly difficult, thus identifying the laser intensity as a major bottleneck in single-shot Thomson scattering.

As soon as the electron transverse emittance is good enough for smaller and thus more efficient interaction diameters, the depth of focus becomes shorter than a mm . This in turn requires high-quality electron beams and laser pulses that are both shorter than one ps and temporally synchronized with respect to each other. Whereas these requirements can be met by high-end conventional electron beams and in particular by LWFA electrons, the deciding limitation arises from high laser intensities ($a_0 \simeq 1$). When aiming for high photon yields at small bandwidths, these intensities cannot be avoided in head-on Thomson scattering without sacrificing either spatio-temporal overlap or the small interaction diameter, hence lowering the number of scattered X-ray photons per incident laser energy.



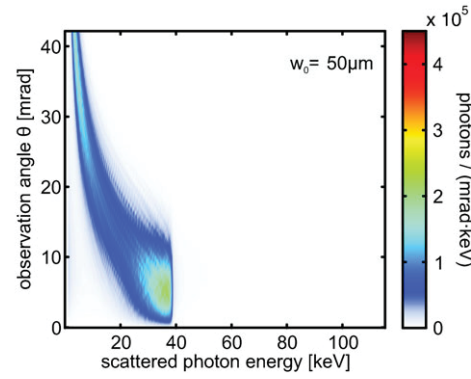
(a) photon density at $w_0 = 10 \mu\text{m}$



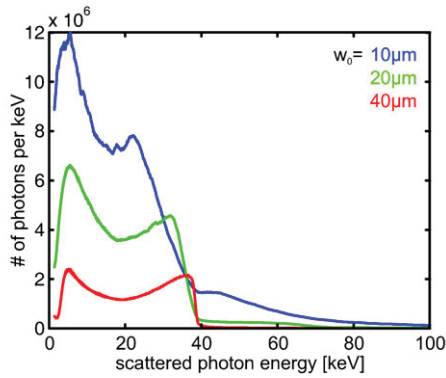
(b) photon density at $w_0 = 20 \mu\text{m}$

λ_0	800 nm
γ_0	79.3
Energy[MeV]	40
1 st Harmonic	
photon energy [keV]	39
Charge[nC]	1.0
Laser pulse	
energy [J]	4.0
$\varepsilon_{\text{trans,rms}}$ [π mm mrad]	10.0
$\varepsilon_{\text{long,rms}}$ [π keV ps]	50

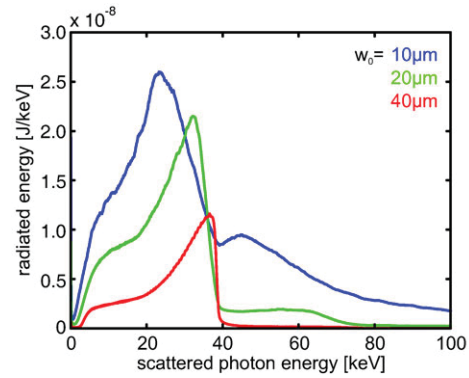
(c) ELBE beam parameters



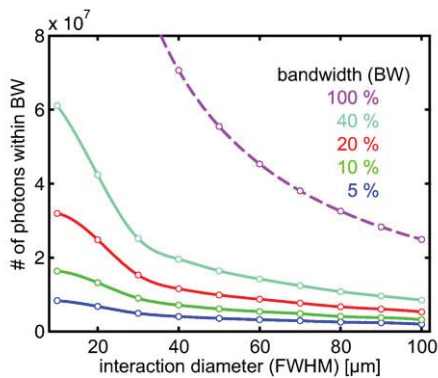
(d) photon density at $w_0 = 50 \mu\text{m}$



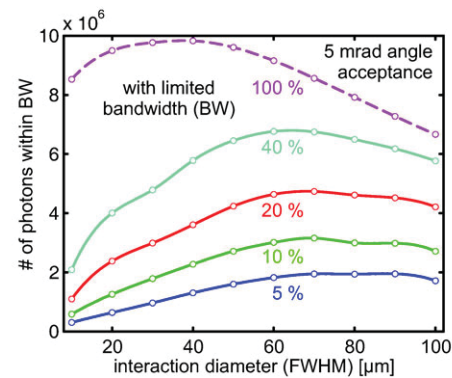
(e) total photon yields for varying w_0



(f) total scattered energy for varying w_0

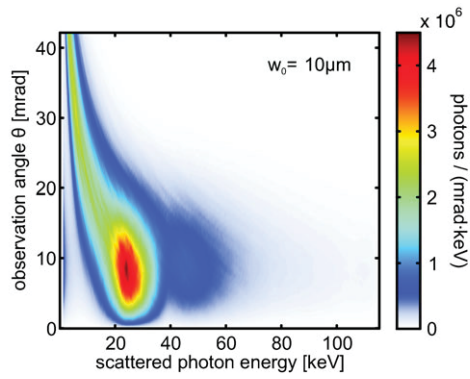


(g) bandwidth limited photon yields

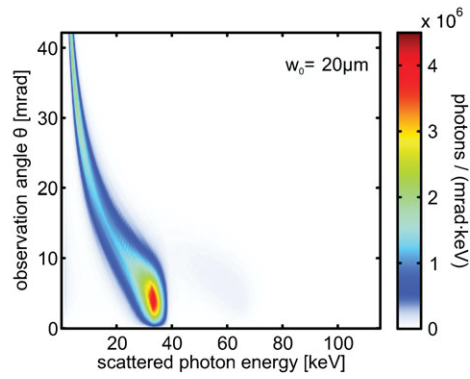


(h) bandwidth and acceptance angle yields
 $\theta < 5 \text{ mrad} \approx 0.4 \cdot 1/\gamma_0$ photon yields

Figure 4.11: CLARA simulation results for Thomson scattering at $\varepsilon_{\text{trans,rms}} = 10 \pi$ mm mrad ELBE electrons.



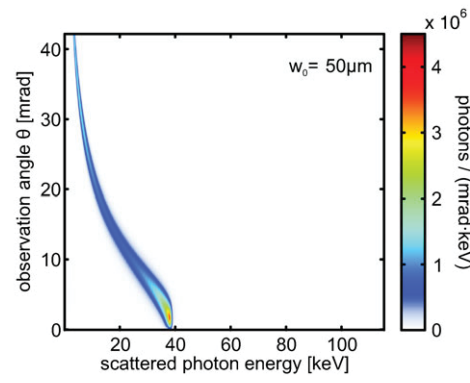
(a) photon density at $w_0 = 10 \mu\text{m}$



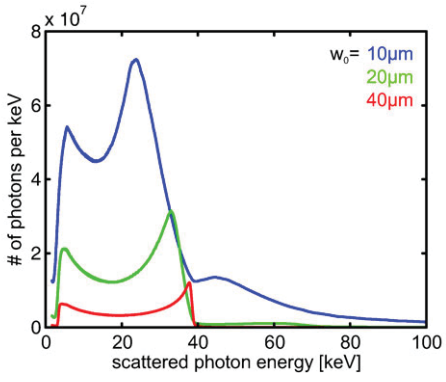
(b) photon density at $w_0 = 20 \mu\text{m}$

λ_0	800 nm
γ_0	79.3
Energy[MeV]	40
1 st Harmonic	
photon energy [keV]	39
Charge[nC]	1.0
Laser pulse	
energy [J]	4.0
$\epsilon_{\text{trans,rms}}$ [π mm mrad]	2.5
$\epsilon_{\text{long,rms}}$ [π keV ps]	50

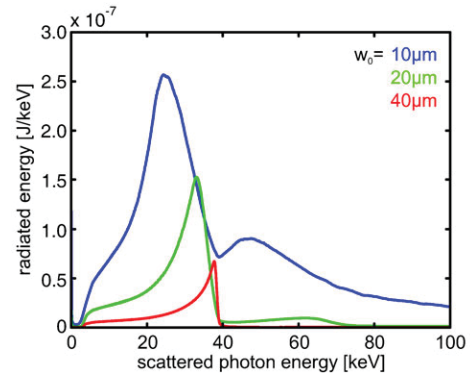
(c) ELBE beam parameters



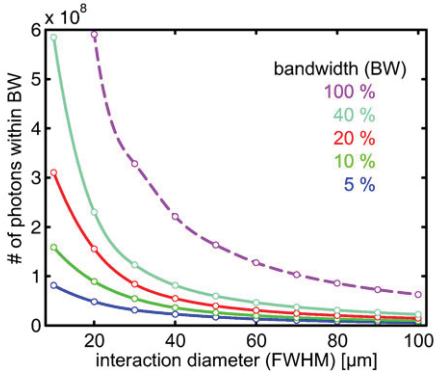
(d) photon density at $w_0 = 50 \mu\text{m}$



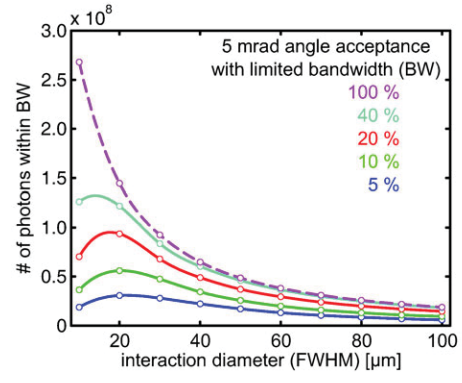
(e) total photon yields for varying w_0



(f) total scattered energy for varying w_0



(g) bandwidth limited photon yields



(h) bandwidth and acceptance angle limited photon yields $\theta < 5 \text{ mrad} \approx 0.4 \cdot 1/\gamma_0$

Figure 4.12: CLARA simulation results for Thomson scattering at $\epsilon_{\text{trans,rms}} = 2.5 \pi$ mm mrad ELBE electrons.

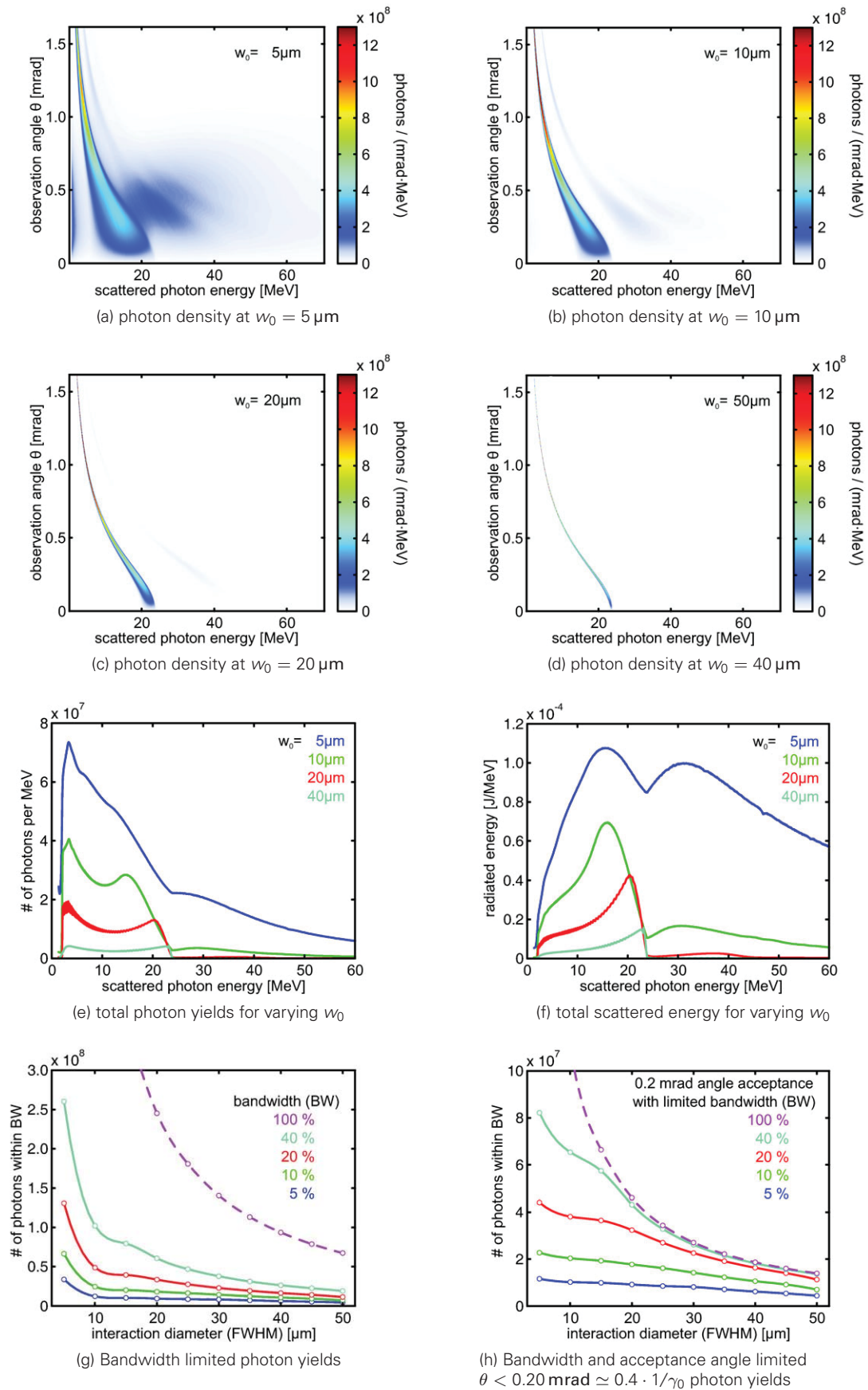


Figure 4.13: CLARA simulation results for Thomson scattering at low-emittance ($\epsilon_{\text{trans,rms}} = 0.1 \pi \text{ mm mrad}$) LWFA pulses

λ_0	800 nm
Laser pulse energy [J]	4.0
γ_0	1958
Energy[MeV]	1000
1 st Harmonic photon energy [MeV]	23.8
Charge[nC]	0.1
$\varepsilon_{\text{trans,rms}}$ [π mm mrad]	0.1
$\Delta\gamma/\gamma_0$	0.01
τ_{el} [fs]	30

Table 4.3: Laser and electron beam parameters for Thomson scattering at laser-wakefield accelerated (LWFA) electrons.

In conclusion, it can be stated, that present laser and electron beams can provide ultrashort, monochromatic X-ray pulses with beyond 10^7 photons per pulse at 5% bandwidth, which is of great interest for a broad range of experiments and applications. However, the low emittance of LWFA electrons cannot be fully exploited in head-on Thomson scattering with regard to its potential photon yield. In addition, the minimum bandwidth of the X-ray spectrum is ultimately constrained by the transform-limited bandwidth of an ultrashort laser pulse.

As a consequence, if orders of magnitudes more photons in a single X-ray pulse at smaller bandwidths are desired, difficulties in scaling up the photon yield make it inevitable to abandon the present head-on Thomson approach. Therefore, the following chapter will take a more general view on Thomson scattering and detail a novel experimental geometry that has the potential to overcome all these limitations.

5 SCALABLE OPTICAL UNDULATORS WITH TRAVELING-WAVE THOMSON SCATTERING

In the previous chapters it has been shown that laser wakefield-accelerated electrons are ultrashort, monoenergetic and originate from a small source volume (ch. 3), so that undulator or Thomson scattering techniques can be used to generate brilliant radiation pulses of the same ultrashort duration (2.108).

However, currently achievable photon numbers of $10^6 - 10^7$ per pulse are still too few for many experiments. In pump-probe experiments, which look at transient atomic or nuclear states, the cross-sections can easily become small, narrow in energy or a nonlinear transition requires a minimum photon flux. In single-shot imaging techniques at high-resolution, the detector needs to be illuminated by many photons in every pixel, channel or resolvable area to provide a high signal-to-noise ratio. The same is important in warm dense matter experiments, where bremsstrahlung and other radiation processes in the plasma provide a high radiation background, which has to be overcome by a probe in the same spectral range.

Therefore, scaling up these numbers is one major question and the starting point here. More precisely, the question is whether it is possible to increase photon yields on a per shot basis rather than by increasing the repetition rate of the source. Otherwise the main advantage of ultrashort light pulses, that all photons arrive at a target in a single event, is rendered irrelevant.

The high densities within small beam diameters achieved by such laser-accelerated electron beams suggest that laser foci can be reduced accordingly in size to increase the photon scattering efficiency of laser beams for Thomson scattering. However, optical focusing limits the interaction region to the Rayleigh length $Z_0 = \pi w_0^2 / \lambda_0$, which is typically on the order of **mm** or below. So

with decreasing laser spot sizes the limited interaction length starts to counteract these efficiency gains and becomes the most limiting factor in scaling up the photon yield in head-on (180°) Thomson scattering geometries.

Naturally, this calls for a waveguide approach to prevent laser beam diffraction. However, a waveguide would need to withstand high laser intensities far beyond typical ionization threshold intensities around 10^{14}W/cm^2 of condensed matter and keep both laser and electron beam unchanged. For these reasons, classic glass fibers or dielectric waveguide structures [1] cannot work. In principle, the ionization problem could be solved by using a plasma waveguide [2–4], except that both the electron beam and the intense laser create wakefields. As in a laser-wakefield accelerator, those strongly modulate energy and spectrum of both electron and laser beam. However, this defeats the purpose of controlling electron acceleration and the scattering interaction independently of one another and prevents direct scaling of the photon yield.

In this chapter, a novel traveling-wave Thomson scattering (TWTS) scheme is introduced [5], that does not rely on pulse guiding and efficiently converts high-intensity laser pulses into X-ray photons. It is shown how this can be realized in a side-scattering geometry at arbitrary interaction angles, in which ultrashort laser pulses with defined pulse-front tilts are used to maintain continuous overlap between electrons and the laser beam over **cm** to **m** distances. One of the main challenge towards experimental implementation is going to be increasing laser pulse durations resulting from pulse propagation with a tilted pulse-front. Those become significant for large interaction angles $\gtrsim 10^\circ$, but can be compensated using varied-line spacing (VLS) gratings. Here, the spatio-temporal dispersion requirements on the laser pulse are derived and it is demonstrated how a ray-tracing approach can be utilized to optimize experimental setups for a range of interaction angles. This new flexibility in side-scattering angles allows for tuning the scattered radiation over the entire spectral range from EUV to hard X-rays at **keV** and **MeV** energies, even for electron sources of constant energy.

Compared to head-on scattering geometries the longer interaction distances of the TWTS design increase X-ray photon yields by several orders of magnitude. Using the 1D-FEL scaling from chapter 2, it is shown that for small interaction angles these photon yields can be so high that the radiation reaction could be used to efficiently drive an FEL instability. In order to better exhibit both potential advantages and disadvantages of a TWTS-FELs, the differences in physics compared to standard FELs are highlighted.

5.1 PHOTON YIELD LIMITATIONS IN HEAD-ON THOMSON SCATTERING GEOMETRIES

In principle, the photon yield (2.107)

$$N_{\text{phot}} = 2\pi\alpha_f N_0 N_b a_0^2 (\Delta\omega_{\text{sc}}/\omega_{\text{sc}}) \quad (5.1)$$

of a Thomson source can be linearly scaled up by either increasing the incident laser intensity $I_0 \propto a_0^2$ or the number of oscillation periods N_0 through a longer laser pulse duration at same

intensity. However, both approaches have limits.

The intensity can only be increased until the electron oscillation becomes relativistic and the $\mathbf{v} \times \mathbf{B}$ -term of the Lorentz-force (2.87) noticeably alters the electron dynamics. Then the nonlinear Thomson scattering regime is reached and the scattered laser energy spreads out over multiple higher harmonics [6, 7]. In addition, intensity related redshifts and broadening, arising from the $a_0^2/2$ term in (2.95)

$$\omega_{\text{sc}} = n\omega_0 \cdot \frac{2\gamma_0^2(1 - \beta_0 \cos \phi)}{1 + a_0^2/2 + \gamma_0^2\theta^2}, \quad (5.2)$$

further deteriorate the resulting Thomson spectrum (see Fig. 4.11–4.13). Thus for efficient scattering into the first harmonic it is essential to avoid the nonlinear regime and keep the laser strength parameter below unity $a_0 \ll 1$, which corresponds to an intensity $I_0 \ll 10^{18} \text{ W/cm}^2$ for an 800 nm beam. In comparison, existing laser facilities feature focal intensities up to the 10^{21} W/cm^2 range, which is already orders of magnitudes beyond this nonlinearity limit.

Alternatively, the laser energy W_0 can be distributed at reduced intensities over longer laser pulses and hence longer interaction distances L_{int} . That however, is limited by the Rayleigh length $Z_0 = \pi w_0^2/\lambda_0$, which determines the length of the focal region and thus the maximum interaction distance L_{int} . Longer laser pulses defocus before they have the chance to interact with the electrons. Especially for electron bunches with small diameters this becomes a severe restriction. For example, a laser beam with a waist size matched to the 4 μm diameter of a laser-plasma wakefield-accelerated electron bunch features a Rayleigh length of mere 63 μm , which suggests laser pulses should become no longer than 210 fs.

Certainly, the Rayleigh length Z_0 could be increased by using a different focal geometry with a larger laser waist size w_0 . But this also requires an increase in laser energy $W_0 \propto \sqrt{w_0}$ just for the option to use longer laser pulses. All that leads to a poor spatial overlap between a large laser waist and a smaller electron bunch, so large parts of the laser pulse do not participate in the interaction and are thus wasted. Accordingly, when both Rayleigh and nonlinear intensity limit are reached for a given electron diameter, any further increase in the scattered photon yield N_{phot} becomes prohibitively expensive. In order to increase the yield by one order of magnitude, one now needs two orders of magnitude more in laser pulse energy

$$N_{\text{phot}} \propto W_0^2. \quad (5.3)$$

Hence it is clear that in a traditional head-on scattering geometry a small interaction diameter is mutually exclusive to a long interaction length defined by the laser pulse duration, which makes the head-on approach by design exceedingly inefficient for low-emittance, high-charge electron bunches and ultrashort, high-power lasers. So the question arises: is it possible to resolve these two conflicting goals?

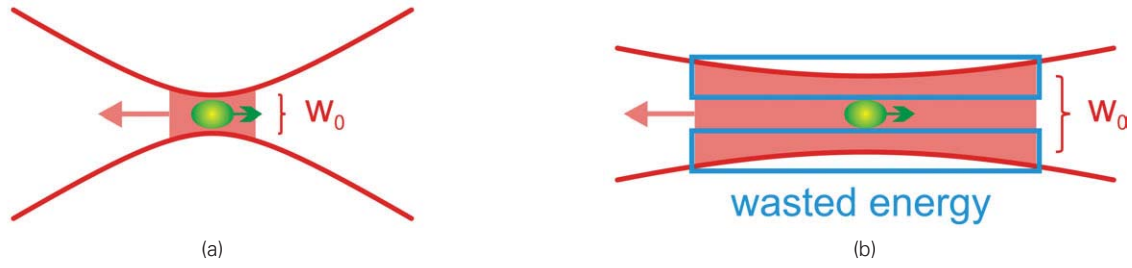


Figure 5.1: (a) depicts the largest interaction volume, for which head-on Thomson scattering works without losing energy either to poor overlap or nonlinear Thomson scattering. In such a scenario the electron beam is focused to the minimum, emittance-limited diameter determined by the desired radiation bandwidth. The counter propagating laser has an intensity just below the nonlinearity threshold at $a_0 = \simeq 0.2$, overlaps tightly with the electron beam and fills the entire Rayleigh length Z_0 . Higher intensities lead to nonlinear Thomson scattering and longer laser pulses give rise to defocusing during the interaction. (b) features the overlap, when the Rayleigh length is increased. Since such an increase can only be realized through a larger focal spot size, parts of the laser beam do not interact with the electrons anymore. Increasing the electron bunch size could only improve overlap, but not intensity, interaction duration or the resulting photon yield. This laser energy is thus wasted.

5.2 TRAVELING-WAVE THOMSON SCATTERING

In order to overcome the Rayleigh limit a beam setup in which the electrons do not leave the focal region of the laser becomes necessary. That is possible with cylindrical optics, where the laser is focused – in one direction only – to a focal line. If now the electrons travel along that line as in Fig. 5.4(a), they remain in the focal region over the entire laser beam width d_{beam} .

This implies that a side-scattering geometry [8] with some interaction angle $0^\circ < \phi < 180^\circ$ has to be used (see Fig. 5.4(b)). However, that also leads to laser and electrons propagating in separate, non-collinear directions, so in these scenarios spatial overlap usually is lost after relatively short distances that are comparable to the beam dimensions. One solution to this problem is tilting the laser pulse-front by some angle α with the purpose that despite of beam propagation there always exists a region of overlap with the electrons (see Fig. 5.4(c)).

Such a pulse-front tilt α can be derived by simple geometrical arguments. Fig. 5.2 shows the laser to be incident on the electrons at an arbitrary angle ϕ . In the laboratory frame, the electron bunch moves with $v_{\parallel} = \beta_0 c \cdot \cos \phi$ in direction of the laser propagation and, perpendicular to that, with $v_{\perp} = \beta_0 c \cdot \sin \phi$ along the phase front; β_0 denotes the ratio $v_{\text{el}}/c = \sqrt{1 - 1/\gamma_0^2}$. Because the laser itself propagates with the speed of light, the phase slipping velocity of the electrons is $v_{\text{slip}} = c - v_{\parallel} = c \cdot (1 - \beta_0 \cos \phi)$. The ratio v_{slip} to v_{\perp} now determines the angle

$$\alpha = \arctan \left(\frac{v_{\text{slip}}}{v_{\perp}} \right) = \arctan \left(\frac{1 - \beta_0 \cos \phi}{\beta_0 \sin \phi} \right) \stackrel{\gamma_0 \gg 1}{\simeq} \phi/2, \quad (5.4)$$

by which the laser field envelope has to follow up the electrons for these to remain stationary with respect to the temporal laser field envelope. According to Fig. 5.3, the tilting angle relation (5.4) quickly converges towards $\alpha = \phi/2$ for $\gamma_0 \gg 1$. In the following this approximation is always assumed to be fulfilled. However note, that β_0 in (5.4) identifies an arbitrary speed of the

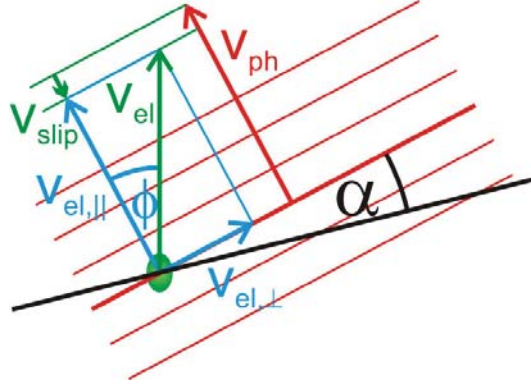


Figure 5.2: An electron bunch propagates at an incidence angle ϕ through a laser pulse and thus experiences a phase slipping velocity v_{slip} . For the electron bunch to remain stationary with regard to the laser envelope centerline, the laser pulse front needs to be tilted by $\alpha = \arctan(v_{\text{slip}}/v_{\perp}) \simeq \phi/2$ (black line).

interaction zone, similar to a moving spotlight cast by distant flashlight, and not a propagation speed of light. Therefore, it should be kept in mind that other, sub-luminal or super-luminal velocities β_0 can become interesting for alternative targets (ch. 5.8). Note that the pulse-front tilt only alters the envelope, but not the wave fronts, which determine the frequency of the scattered light. In other words, the pulse-front tilt introduces a spatially dependent group velocity delay, which shifts the laser envelope with respect to the carrier phase. As a result of the electrons being stationary with respect to the temporal field envelope, their motion in the laboratory frame is determined by the laser carrier frequency ω_0 divided by the geometric factor $(1 - \beta_0 \cos \phi)$ arising from phase slippage.

In Fig. 5.4(d) the entire Thomson scattering scheme is summarized in one graph, where it depicts the laser and electron beam positions at three different times (1-3) — at beginning, middle and end of the scattering interaction. The combination of the three different geometries is shown: the focusing line along the electron trajectory, the side-scattering with interaction angle ϕ and pulse-front tilted by an angle α . Furthermore, the figure illustrates how in the course of the interaction, the entire laser beam slides across the electron bunch, so all parts of the laser interact with the electrons. In this sense the electrons and thus the resulting X-ray pulse are continuously pumped by the laser as both travel along the laser line focus. These distinctive features are summarized by the name *traveling-wave Thomson scattering* (TWTS).

In order to calculate the minimum laser duration τ_{min} required for full spatial overlap, an ellipsoidal geometry of the electron bunch is assumed and its semi-axes are $c \tau_{\text{beam}}/2$ and $d_{\text{beam}}/2$. Therefore, the tilted laser pulse fronts at angle $\phi/2$ as in eq. (5.4) must be long enough to be at minimum tangent to the electron bunch ellipse. Hence one arrives at a minimum laser duration,

$$\tau_{\text{min}} \geq d_{\text{beam}}/c \cdot \left(1 + \frac{(c \tau_{\text{beam}} d_{\text{beam}})^2 - (c \tau_{\text{beam}})^4}{(c \tau_{\text{beam}})^4 + d_{\text{beam}}^4 \tan^2(\phi/2)} \right)^{-1/2}. \quad (5.5)$$

For the number of oscillations N_0 experienced by the electrons, the effective interaction distance $d_{\text{beam}}/\sin \phi$ has to be divided by the effective laser wavelength $\lambda_0/(1 - \beta_0 \cos \phi)$.

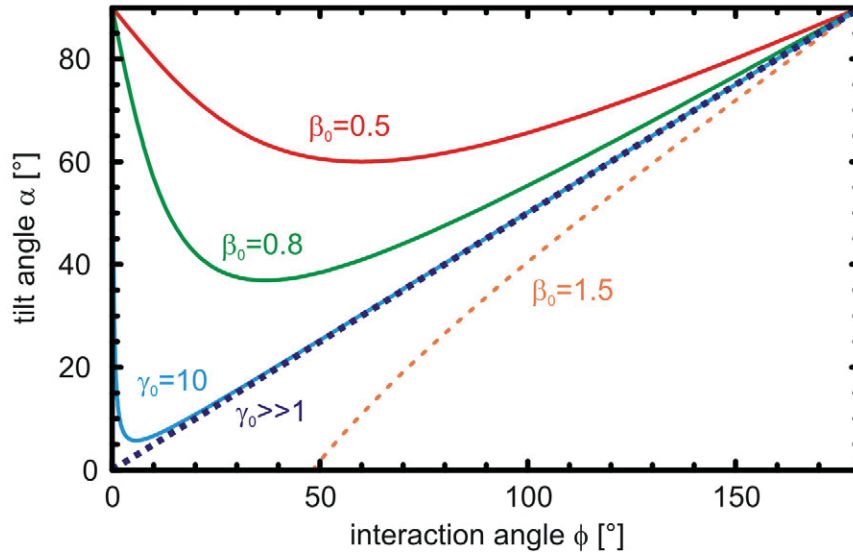


Figure 5.3: Tilt angle α with respect to the interaction angle ϕ according to eq. (5.4). The different curves correspond to various bunch velocities β_0 , where the diagonal curve denotes the limit for $\gamma_0 \gg 1$.

$$N_0 = \frac{d_{\text{beam}}}{\lambda_0} \cdot \frac{1 - \beta_0 \cos \phi}{\sin \phi} \simeq \frac{d_{\text{beam}}}{\lambda_0} \tan(\phi/2). \quad (5.6)$$

The advantages of traveling-wave Thomson scattering (TWTS) come at the cost of additional optics introducing a large pulse-front tilt. In the following the means for realizing such a pulse-front tilt using reflective gratings are described in more detail and it is shown what kind of difficulties are to be expected.

5.3 EXPERIMENTAL APPROACHES AND CONSTRAINTS

Two methods for pulse-front tilt (PFT) generation as depicted in Fig. 5.5 are known: PFT by angular dispersion [9–11] and PFT by a combination of a spatial chirp and group delay dispersion [12]. However, the requirement for ultrashort pulses within the region of the line focus excludes the second possibility because a minimized spatial chirp is desired in the interaction region. Otherwise, the electrons would experience a spatially separated spectrum and thus a frequency chirp, which would broaden the bandwidth of the scattered radiation. In addition, the efficiency of the interaction would be affected by the intensity drop due to the laser pulse being elongated by spatial dispersion. Hence the pulse-front tilt

$$\begin{aligned} PFT \equiv \tan \alpha &= \omega_0 \left. \frac{d\theta_{\text{out}}}{d\Omega} \right|_{\Omega=\omega_0} \\ &\equiv \frac{\partial(c\Delta t_{\text{out}})}{\partial x_{\text{out}}} \end{aligned} \quad (5.7)$$

has to be realized by angular dispersion. Here, α , ω_0 and θ_{out} represent the pulse-front tilt angle, the central angular laser frequency and the deflection angle compared to the central ray passing

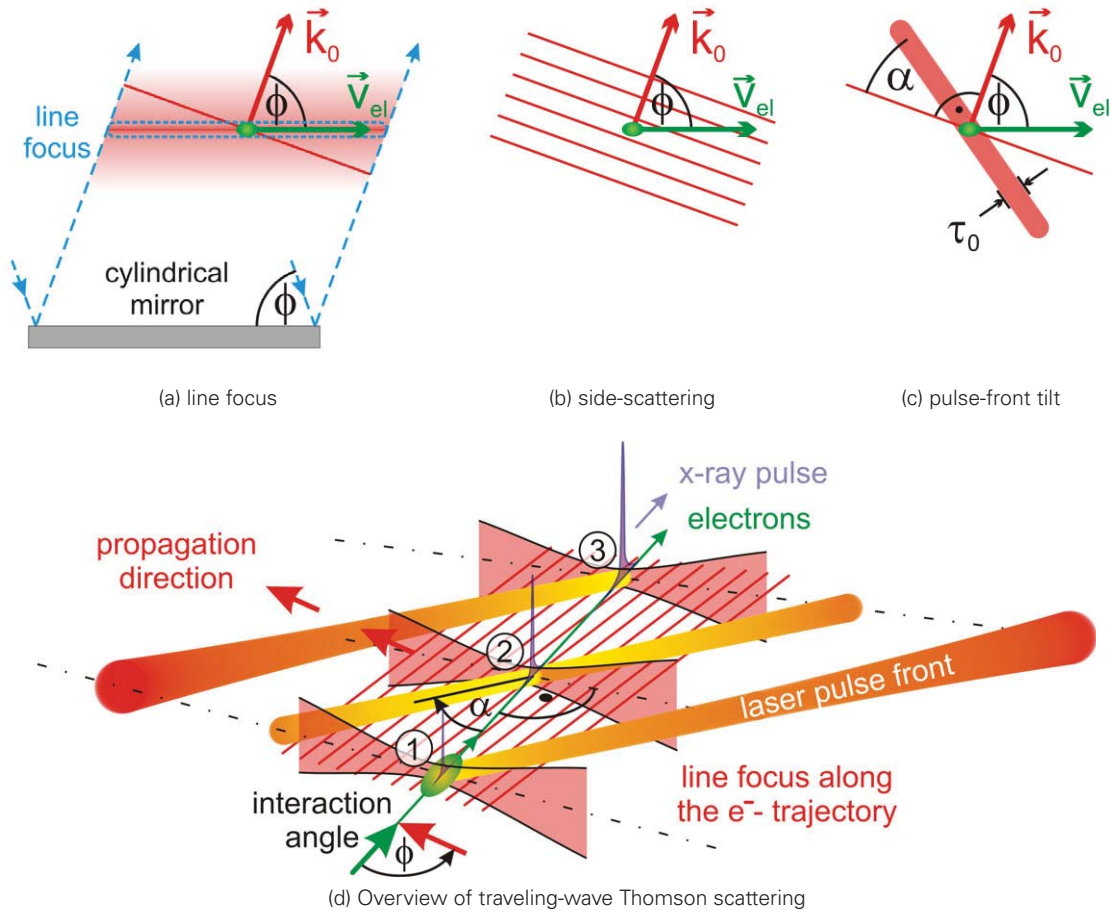


Figure 5.4: In traveling-wave Thomson scattering (TWTS) the laser is (a) focused with a cylindrical mirror to a line focus along the electron trajectory. (b) This leads to a side-scattering geometry with ϕ being the enclosing angle between laser pulse and electron bunch. (c) In order to maintain continuous overlap during the interaction the laser pulse envelope must be tilted by $\phi/2$ to compensate for the different propagation directions. (d) shows an overview of the TWTS scheme that combines above design principles in one graph and depicts the laser pulse envelope at the beginning, middle and end of the interaction (1-3). The result is a comoving interaction region in which scattered X-ray radiation can accumulate over propagation distances that are much longer than the laser Rayleigh length.

through the dispersive element respectively. The second definition of the pulse-front tilt (5.7) arises from a ray-picture. In a group of rays after a dispersion element, the pulse front tilt defines the distance by which an off-axis ray with distance x_{out} to a central ray is advanced or delayed with respect to that central ray.

Reflective gratings are ideal for this purpose as they can introduce large linear angular chirps

$$\left. \frac{d\theta_{\text{out}}}{d\Omega} \right|_{\Omega=\omega_0} = \frac{\sin \psi_{\text{out}} - \sin \psi_{\text{in}}}{\omega_0 \cdot \cos \psi_{\text{out}}} \quad (5.8)$$

$$\tan \alpha = \frac{\sin \psi_{\text{out}} - \sin \psi_{\text{in}}}{\cos \psi_{\text{out}}} \quad (5.9)$$

without having issues with higher order dispersion. One grating can easily introduce the required pulse-front tilt. However, complications arise through the requirement of zero spatial dispersion

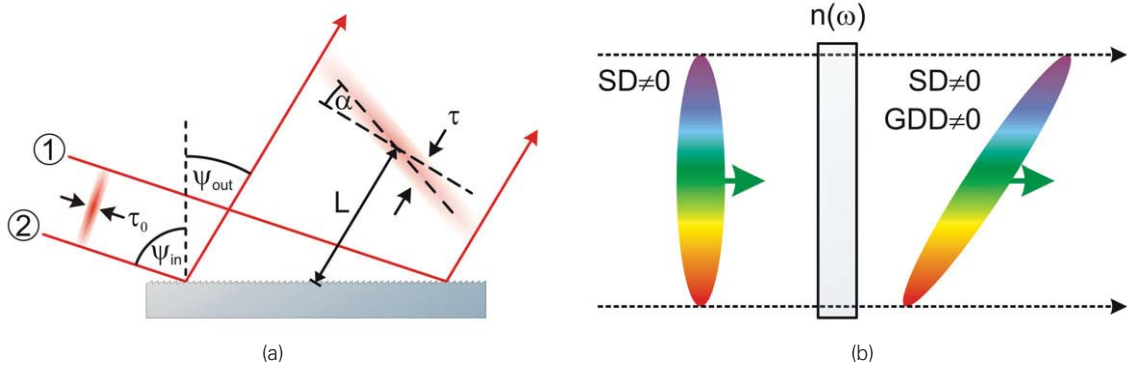


Figure 5.5: (a) A diffraction-limited laser pulse of duration τ_0 is incident on a grating. Since the propagation distance of beam (1) is longer than the distance of beam (2), there exists a pulse-front tilt α . The angular dispersion – different angles Ψ_{out} for varying frequencies – introduced by the grating leads over the subsequent propagation distance L to both spatial dispersion and pulse elongation through group delay dispersion. (b) depicts a laser pulse with spatially dispersed spectrum $SD \neq 0$, which by passing through a dispersive medium is delayed as a function of frequency according to the index of refraction $n(\omega)$ and thus results in a pulse-front tilt. That tilting mechanism is complementary to (a).

within the interaction region. The angular dispersion (AD)

$$\begin{aligned}
 AD &\equiv 2\pi \left. \frac{d\theta_{\text{out}}}{d\Omega} \right|_{\Omega=\omega_0} \\
 &\equiv \frac{\partial\theta_{\text{out}}}{\partial\Delta\nu}
 \end{aligned} \tag{5.10}$$

introduced by the grating is responsible for a growing spatial dispersion (SD)

$$SD \equiv \frac{\partial x_{\text{out}}}{\partial\Delta\nu} \tag{5.11}$$

which after some propagation distance then gives rise to a temporal broadening of the beam by both a spectral walk-off, reducing the local frequency bandwidth. Likewise, angular dispersion with subsequent beam propagation gives leads to group delay dispersion (GDD)

$$GDD \equiv \frac{\partial\Delta t_{\text{out}}}{\partial\Delta\nu} \tag{5.12}$$

because the individual spectral components propagate into different directions [13]. In the following the spectral walk-off can be neglected $(2 \tan \alpha / \tau_0 \omega_0) \cdot L \ll d_{\text{beam}}$ as the beam diameters considered here are in the centimeter range. That is different for the GDD, which broadens a tilted beam as it propagates off the plane of ideal temporal compression. According to [13], the laser pulse duration τ of collimated, transform-limited beams that are tilted by an angle α changes with propagation distance L as given by

$$\tau^2 = \tau_0^2 \left(1 + \frac{L^2 \lambda_0^2 \tan^4 \alpha}{\pi^2 (c\tau_0)^4} \right). \tag{5.13}$$

Note that this equation is valid only in the limit of geometrical optics, which requires the

Rayleigh length Z_0 to be much longer than any propagation distance L in the optical setup. Here, this condition is easily fulfilled, since the waist size of a collimated 800 nm laser beam is on the order of $w_0 \simeq 10$ cm, which corresponds to a Rayleigh length of $Z_0 \simeq 40$ km.

Small tilt angles

As the second term of (5.13) is proportional to $\tan^4(\alpha)$, laser pulse elongation due to the pulse-front tilt $\alpha = \phi/2$ becomes negligible for small scattering angles $\phi \lesssim 10^\circ$, when laser and electron beams are almost collinear. Such a small-angle limit is a good starting point for relatively simple experimental setups as in Fig. 5.6, because those can ignore propagation-induced effects from angular dispersion and thus need only one standard grating. In addition, the resulting scattered wavelengths $\lambda_{sc} \simeq \lambda_0/(2\gamma_0^2(1 - \beta_0 \cos \phi))$ are much longer compared to a colliding geometry and the interaction distance $L_{int} = d_{beam}/\sin \phi$, due to the small angle, quickly scales up into the meter range. Compared to magnetic undulators, setups exploiting this small-angle limit provide optical undulators with effective undulator periods $\lambda_{eff} = \lambda_0/(1 - \beta_0 \cos \phi)$ that are 1-2 orders of magnitudes smaller and correspondingly feature greater photon energies as shown in Fig. 2.8.

For a geometry as shown in Fig. 5.6 an upper limit can be found for the propagation length $L \leq 2f_{cyl}/\sin \phi$ from grating to interaction region with f_{cyl} denoting the focal distance of the cylindrical mirror. With a pulse-front tilt of $\alpha = \phi/2$ and (5.13), one arrives at the pulse duration τ for small angles ϕ

$$\tau = \tau_0 \sqrt{1 + \left(\frac{f_{cyl} \lambda_0 \phi}{2\pi (c\tau_0)^2} \right)^2}. \quad (5.14)$$

This scaling improves when an additional pair of gratings preceding the setup is used to pre-compensate spatial and group delay dispersion emerging between the last grating and the line focus. Then the relevant distance for dispersion is set by the laser propagation distance during interaction, $d_{beam}/\tan \phi$. As a consequence, eq. (5.14) becomes

$$\tau = \tau_0 \sqrt{1 + \left(\frac{d_{beam} \lambda_0 \phi}{4\pi (c\tau_0)^2} \right)^2}. \quad (5.15)$$

and scales with the laser diameter d_{beam} instead of the focal distance f_{cyl} .

It should be noted that the appeal of such small-angle arrangements becomes apparent when the Pierce parameter ρ

$$\rho = \frac{1}{2\gamma_0} \left(\frac{I_p}{I_A} \left(\frac{\lambda_u a_0}{2\sqrt{2}\pi\sigma_b} \right)^2 \right)^{1/3} \quad (5.16)$$

is calculated, which defines the efficiency of an FEL [14, 15]. In (5.16) I_p denotes the electron peak current, $I_A = 4\pi\epsilon_0 m_0 c^3/e = 17.0$ kA the Alfvén current, σ_b the RMS electron bunch diameter and λ_u is the effective optical undulator period $\lambda_{eff} = \lambda_0/(1 - \beta_0 \cos \phi)$. For conditions achievable by conventional, small-scale linear accelerators and high-power lasers around 100 fs, for ρ one typically arrives within a range of $10^{-4} - 10^{-3}$, which is comparable to existing facilities [16–19]. The discussion of such a TWTS-FEL as an X-ray source with its potential and requirements is postponed until later in ch. 5.7.

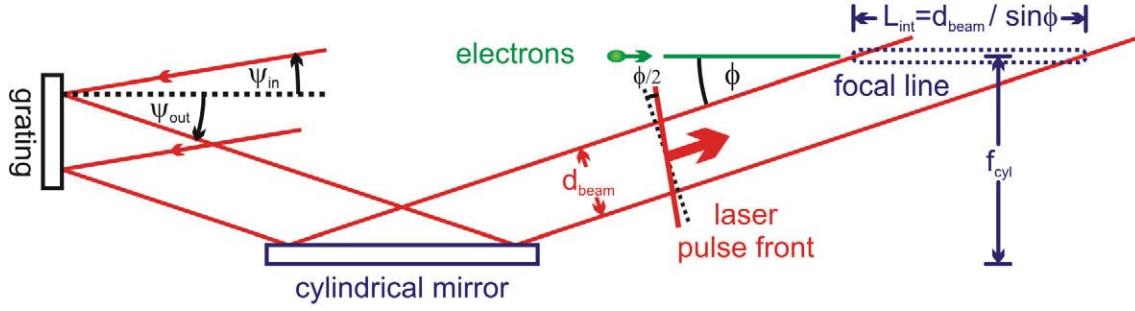


Figure 5.6: Setup for small interaction angles ϕ , where the propagation-induced laser pulse elongation is negligibly small. First, a single grating introduces the pulse-front tilt $\phi/2$ corresponding to the interaction angle ϕ . Then a cylindrical mirror focuses to a line focus, where the tilted laser slides across the electrons, thus generating X-rays at a photon energy of $W_\gamma = \hbar\omega_0 \cdot 2(1 - \beta \cos \phi)\gamma^2$.

Large tilt angles

Since the aforementioned small-angle scheme results in photon energies much smaller than in head-on scattering geometries, a method to compensate for the spatial dispersion at larger angles ϕ becomes essential. As known from grating compressors, a pair of gratings in principle can accomplish that. However, this is not enough, because here the laser pulse propagates non-negligible distances $\Delta L > \frac{\pi(c\tau_0)^2}{\lambda_0 \tan^2 \alpha}$, see eq. (5.13), while interacting with the electrons. The group delay dispersion and the spatial dispersion of the laser must be zero, not only at one point in time, but along the entire interaction distance to prevent efficiency losses from laser pulse elongation and frequency chirp in the scattered radiation. It turns out that such a situation cannot be arranged with standard grating optics. The reason for this lies in its almost linear transformation properties with respect to the set of possible optical path length differences in wave optics or correspondingly the ray bundles in geometric optics. When optics are used, where two arbitrary rays with relative position, angle, time and frequency properties can always be related to one another by a linear transformation, one can describe the system in a first-order theory. For example, this means that two parallel rays of the same wavelength remain parallel after hitting a plane, standard grating. Therefore, if the desired properties of an optical system cannot be defined by linear transforms, it follows that this system cannot be realized using (locally) linear optics such as mirrors, lenses and plane, standard gratings. For illustration of the problem encountered here, consider one electron bunch overlapping with a tilted laser pulse. In a first-order theory one has

$$SD(x) = \Delta L(x) \cdot AD, \quad (5.17)$$

where $SD(x)$ denotes the spatial and AD the constant angular dispersion. The x -coordinate is the transverse position deviation from the center beam in Fig. 5.8. Although in the context presented here $x = x_{\text{out}}$, this convention refers to the laser beam properties around the interaction region and not to a particular choice of preceding optics. Precompensation of the spatial dispersion by an additional grating pair sets $SD(0) = 0$ for $\Delta L(0) = 0$. Now as the electrons move in x along the laser pulse front, the laser continues to propagate another distance $\Delta L(x)$, so the spatial dispersion $SD(x)$ is not zero anymore. The only way to compensate for that is to modify the spatial dispersion in advance, so it also becomes a function of x . But this means $SD'(x) = (\partial^2 x_{\text{out}} / \partial \Delta \nu \partial x_{\text{in}})|_{x=x_{\text{out}}} \neq 0$ and thus one cannot operate anymore in the framework of a first-order

theory and require optics that feature non-negligible higher order derivatives in x .

It is useful to formulate the necessary TWTS conditions on laser beam dispersion independent of specific optics. Thereby the basic design principle of TWTS is kept in mind: Only at the current electron bunch position and nowhere else, good overlap and a high quality laser beam is required. First, the spatial dispersion condition can be stated with the help of Fig. 5.7. The change in spatial dispersion $SD(x, t) = \partial x_{\text{out}}/\partial \Delta\nu$ along the electron trajectory $x_{el}(t)$ and hence across the laser beam diameter

$$SD(x, t)|_{x=x_{el}(t)} \equiv SD(x_{el}(t), 0) - AD(x_{el}(t)) \cdot \Delta L(x) \ll \frac{\pi c \tau_0^2}{\tan \phi/2} \quad (5.18)$$

$$\Delta L(x) = (\tan(\pi/2 - \phi) + \tan \phi/2) \cdot x \quad (\text{Minimize spatial dispersion})$$

needs to counterbalance the spatial dispersion gained by the beam propagation distance $\Delta L(x)$ to the line of interaction. According to Fig. 5.7 this propagation distance $\Delta L(x)$ is defined by the difference in slopes of electron bunch trajectory and laser pulse-front tilt with respect to the wave front. The limit on the right hand side of (5.18) derives from the temporal walk-off (5.14) generated by the angular dispersion (5.17).

Then, the required pulse-front tilt $PFT(x) = c \cdot (\partial \Delta t(x)/\partial x)$ from (5.4) needs to be constant across the entire laser pulse width, so the pulse front does not bend.

$$c \cdot \Delta t(x) - x \cdot \tan \phi/2 \ll c \tau_0 \quad (\text{Minimize pulse-front bending}) \quad (5.19)$$

Finally, the temporal laser profile should not change, thus the group velocity delay has to be kept smaller than the transform-limited pulse duration

$$GDD(x, t)|_{x=x_{el}(t)} \Delta\nu_0 = \frac{\partial \Delta t_{\text{out}}(x, t)}{\partial \Delta\nu}|_{x=x_{el}(t)} \Delta\nu_0 \ll \tau_0 \quad (\text{Optimal pulse compression}), \quad (5.20)$$

along the entire electron bunch trajectory $x_{el}(t)$. For general non-Gaussian temporal profiles, as well as nonlinearly chirped pulses, above eq. (5.20) can be expressed [9] as

$$\left\langle \left(\frac{\Delta\nu}{2\pi} GDD(x, t, \Delta\nu)|_{x=x_{el}(t)} \right)^2 \right\rangle_{\Delta\nu} \ll \tau_{0,\text{rms}}^2. \quad (5.21)$$

The proposed setup in Fig. 5.8 is similar to the small-angle case in Fig. 5.6, but includes spatial dispersion (SD) and group delay dispersion (GDD) precompensation. For the first order dispersion of the beam from the grating to the interaction region this is achieved by some additional grating combination at the beginning of the setup. Such SD and GDD compensation is standard technology and is extensively used in the stretchers and compressors of chirped pulse amplification (CPA) lasers.

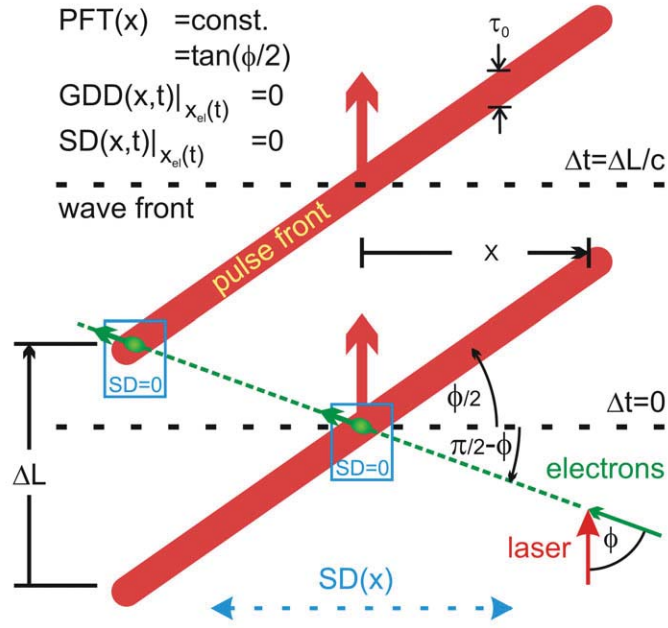


Figure 5.7: During propagation of a tilted laser pulse over a distance ΔL , spatial dispersion (SD) and group delay dispersion (GDD) change due to angular dispersion. In order to maintain best laser pulse compression and thus efficient overlap with the electrons, both SD and GDD need to be zero along the electron trajectory. This requires the spatial dispersion $SD(x)$ to vary linearly across the transverse laser pulse coordinate at any fixed point in time.

However, the goal is to have zero SD and GDD, not only at one instant of laser beam propagation, but reasonably small SD and GDD at the current electron positions along the entire interaction distance. Hence, higher order dispersion compensation to satisfy the conditions (5.18), (5.19) and (5.20) is required. In the setup (Fig. 5.8) this is accomplished by changing the last grating to a VLS grating with a quadratic line-spacing chirp (see Appendix A). In this way, an additional angular dispersion

$$AD(x_{in}) = AD_0 + SD_0 C_1 \cdot x_{in}, \quad (5.22)$$

which varies linearly across the laser beam diameter, is realized, such that the linear spatial dispersion condition (5.18) is fulfilled in the line focus after the final propagation distance $L_0 = \overline{ABC}$.

Considering that the spatio-temporal beam imaging properties of a VLS grating are by definition nonlinear, setup designs and their limitations can quickly become difficult to assess. Thus a theoretical description for modeling laser beam dispersion to higher orders is essential for designing efficient large angle scattering geometries that provide high X-ray energies. Moreover it should be emphasized here, that these techniques of tailoring the laser beam to alternative interaction volumes using VLS gratings are rather general and are also applicable for other areas in laser-matter interactions (see ch. 5.8), since the target does not need to be an electron beam, but can be anything that moves close to the speed of light.

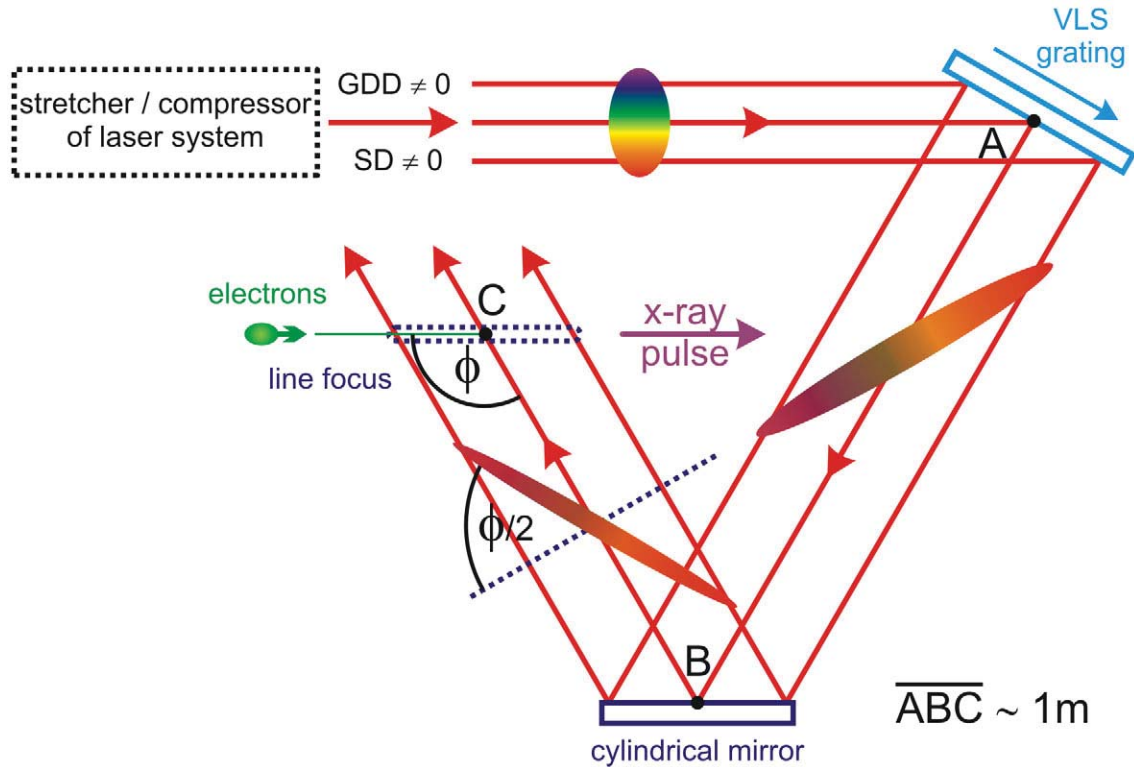


Figure 5.8: A CPA laser system provides a stretched laser pulse with spatial dispersion. The last grating (**A**) introduces the required pulse-front tilt $\phi/2$. The corresponding angular dispersion introduced by the grating subsequently compresses the laser pulse until best compression and zero spatial dispersion is reached in the line focus of the setup. The grating has a varied line-spacing (VLS) such that zero spatial dispersion is reached not only at one instant in time, but spatially along the entire line focus.

5.4 THEORETICAL TOOLS FOR DESIGNING VLS GRATINGS

To begin with, it is useful to reduce the problem to plane waves in two dimensions, which is possible because the cylindrical mirror focuses only in one dimension, which is perpendicular to the plane of projection in Fig. 5.4(a). Thus the wavefront curvature parallel to the interaction plane, that is spanned by the laser and electron beam directions, can be neglected. Considering that all the gratings introduce dispersion in the same way for each plane parallel to the interaction plane, it is a good approximation to evaluate only the interaction plane. Hence, the laser pulse can be modeled in 2D using a ray-tracing approach.

The most comprehensive treatment for the first order behavior of an optical system was given by Kostenbauder [20] and utilizes 4×4 "ray-pulse" matrices to model the laser beam coordinates (position x , angle θ , time delay Δt and frequency shift $\Delta\nu$), relative to a central ray. This formalism is adopted in order to define the first order properties of the grating-based setup in Fig. 5.8 and to satisfy the constraints on AD, GDD and SD for the central ray and its close vicinity at $x = 0$. In a next step, this linear solution is analytically extended to higher orders for off-axis rays $x \neq 0$. At that point it is possible to describe the required line-spacing function of the grating as a second order correction to a linear ray transfer operator. Beyond this second order analysis, numerical calculations up to the 4th order are performed over a range of interaction

angles ϕ . With the help of these numerical calculations, optimal angles and grating parameters are determined by minimizing dispersion according to (5.18)-(5.20) in an optimization approach. For one, this constitutes a numerical test on the range of validity of the analytical approximation – especially of the analytical grating chirp. But even more important, it provides physical insight on the useful range of a VLS grating with regard to interaction angles ϕ and maximum achievable interaction lengths. For the technical details on the Kostenbauder formalism and its extension, the reader is referred to the Appendix A and the discussion here is continued with the linear case.

The requirement of a $\phi/2$ pulse-front tilt defines the first order grating properties. Thus the grating equation combined with (5.9) simplifies to

$$\psi_{\text{in}} = \arcsin(\cos \psi_{\text{out}}(\tan \psi_{\text{out}} - \tan \phi/2)), \quad (5.23)$$

with the grating period d_0

$$d_0 = \lambda_0 / (\sin \psi_{\text{out}} - \sin \psi_{\text{in}}). \quad (5.24)$$

The stretcher-compressor combination of a CPA laser at the beginning of the setup has to ensure in first order zero GDD and SD at the final focus, so together with (5.23) the first order precompensation for spatial dispersion and group delay dispersion has to be

$$SD_0 = \frac{\partial x_{\text{out}}}{\partial \Delta\nu} = \frac{L_0 \lambda_0 \tan \phi/2}{c \cdot \cos \psi_{\text{out}}} \sqrt{\cos(\phi - \psi_{\text{out}}) \cos \psi_{\text{out}} / \cos^2 \phi/2} \quad (5.25)$$

and

$$GDD_0 = \frac{\partial \Delta t}{\partial \Delta\nu} = \frac{L_0 \lambda_0}{c^2} \tan^2 \phi/2. \quad (5.26)$$

According to (5.23) and (5.25) the angle ψ_{out} is constrained by

$$-\pi/2 + \phi < \psi_{\text{out}} < \pi/2 + \phi. \quad (5.27)$$

Up to this point, everything in the design could be obtained using the Kostenbauder formalism or any other first order theory. As a correction to these first order constraints, now a varying grating period featuring a quadratic dependency

$$d(s) = d_0 + b_g \lambda_0 s^2, \quad (5.28)$$

along its surface coordinate is introduced.

By extending the Kostenbauder formalism to higher orders in x as shown in Appendix A, the spatial, angular and temporal ray displacement components $x_{\text{out}}(x_{\text{in}}, \Delta\nu)$, $\theta_{\text{out}}(x_{\text{in}}, \Delta\nu)$ and $\Delta t_{\text{out}}(x_{\text{in}}, \Delta\nu)$ are obtained for above setup. Thus, the spatial dispersion $\partial x_{\text{out}}(x_{\text{in}}, \Delta\nu) / \partial \Delta\nu$ in the interaction region after a distance L_0 can be calculated to higher orders in the transverse beam coordinate x_{in} . As a result the condition (5.18), using (5.17), (5.22), (5.25) and (5.23), can be

rewritten as

$$\frac{SD(x_{in}, 0)}{x_{out}(x_{in})} = AD(x_{in}) \cdot (\tan(\pi/2 - \phi) + \tan(\phi/2))$$

$$-\frac{2\lambda_0 b_g L_0^2 \tan^3 \phi/2}{c \cdot \cos \psi_{out}} = \frac{\lambda_0}{c} \tan \phi/2 \cdot (\tan(\pi/2 - \phi) + \tan(\phi/2)) + \mathcal{O}(x, \Delta\nu),$$

so when neglecting higher order dispersion, this condition is satisfied for quadratic line-spacing chirps

$$b_g = -\frac{\cos \psi_{out} \cdot (\tan(\pi/2 - \phi) + \tan \phi/2)}{2L_0^2 \tan^2 \phi/2}. \quad (5.29)$$

Note, that above quadratic VLS profile in (5.28) is a useful parametrization, but it is not necessarily the best solution with regard to higher order dispersion. Ideally one would optimize for a whole range or even arbitrary grating period functions to achieve better results with less dispersion. However, such a general approach is rather technical and distracts from the main point, which is how traveling-wave Thomson scattering can experimentally be realized. Therefore, for the sake of simplicity, the following analysis focuses exclusively on a second order polynomial as the VLS grating function.

The only remaining degrees of freedom in this setup are now the length L_0 between the VLS grating and the line focus and the outgoing angle ψ_{out} . Over that remaining parameter space, the dispersion conditions (5.18) to (5.20) are calculated and subsequently minimized. For accuracy reasons higher order terms up to the third order in x are included. The optimizations below are performed numerically on a computer using a combination of a global optimization algorithm (Differential Evolution [21]), followed by a local optimization technique.

5.5 INTERACTION DISTANCES USING VLS GRATINGS – CALCULATION RESULTS

For a discussion of the optimization results, the local laser pulse duration τ/τ_0 along the line focus is of special interest. It is calculated from the frequency dependence of the remaining GDD after optimization (see eq. (5.21)) and is normalized to the transform-limited laser pulse duration τ_0 . If this local pulse duration τ/τ_0 is significantly larger than unity, it indicates a chirped pulse and can be interpreted as the stretch factor by which the laser is elongated. Such an elongated pulse leads to a less efficient overlap with the electrons. Moreover, it can also broaden the scattered spectrum, because the carrier frequency of a chirped beam varies across the electron bunch. Physically, this is the result of higher order dispersion from the VLS grating that becomes significant further away from the central laser beam axis and critical for the broad spectra of ultrashort laser pulses. Therefore, this quantity is an indicator for the limits on the available interaction length L_{int} of a given large angle TWTS design.

As an example, Fig. 5.9 (a) and (b) show the results for some typical scenario of a 30 fs and

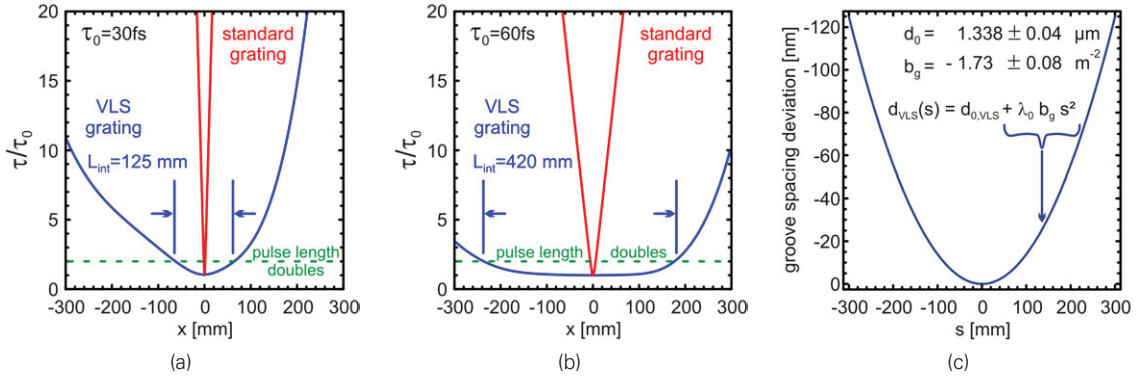


Figure 5.9: For a scattering angle $\phi = 60^\circ$, (a) shows the local pulse elongation τ/τ_0 of a 30 fs laser pulse (blue) in comparison to the corresponding scenario using standard gratings (red), (b) is the same as (a), except that a 60 fs laser pulse is used. (c) depicts the nm-scale deviation in the line-spacing profile $d(s)$ of a typical VLS grating compared to the corresponding standard grating.

60 fs laser pulse at 800 nm and an interaction angle of $\phi = 60^\circ$ at a fixed VLS grating to line focus separation of $L_0 = \overline{ABC} = 1 \text{ m}$. Additionally, these results are compared to the corresponding scenario, using a standard grating (red line) instead of a VLS grating (blue line). The influence of propagating laser pulses with pulse-front tilt on the pulse duration was calculated according to (5.13), where $L = (\tan(\pi/2 - \phi) + \tan \phi/2) \cdot x$ denotes the displacement from the plane of maximum beam compression. In that case best pulse compression (red line) is only maintained for a couple of mm around the beam center, so outside that region the intensity loss due to temporal pulse broadening quickly approaches one order of magnitude. In contrast, the beams in the VLS grating setup remain at good compression (blue line) over a laser beam diameter of 125 and 420 mm. This enables effective Thomson scattering over an interaction distance of many times the Rayleigh length. The VLS grating function required for such a setup (Fig. 5.9(c)) shows an overall variation in the groove spacing, which is well below the central grating period d_0 and thus technologically viable.

Such optimal configurations at the same fixed grating to focus separation distance $L_0 = \overline{ABC} = 1 \text{ m}$ can be found for a whole range of interaction angles ϕ . As an indicator for the limits of this setup due to the higher order dispersion terms in x and ν , Fig. 5.10(a) depicts the maximum interaction distances L_{int} over which the local pulse duration remains below $\tau/\tau_0 = 2$, i.e. does not double (blue lines). This again is compared to scenarios with standard gratings (red lines) instead of the VLS gratings. The limitations at very small or large angles ϕ are explained by the geometry. According to (5.18) the required slope in the spatial dispersion is proportional to $\tan \phi/2 \cdot (\tan(\pi/2 - \phi) + \tan \phi/2)$ and becomes infinite for $\phi \rightarrow 180^\circ$. Hence, towards larger angles ϕ increasingly higher SD chirps become necessary and higher order effects noticeable. A similar argument applies for the small-angle limit $\phi \rightarrow 0^\circ$, where a small but precise compensation is required, so that in between these two extremes, the usable interaction distance attains a maximum.

Thus for VLS gratings it is found that dispersion precompensation becomes more difficult towards larger angles ϕ which in practice defines an upper limit for ϕ . This upper limit depends on the laser pulse duration (5.13), the interaction length L_{int} over which good dispersion compen-

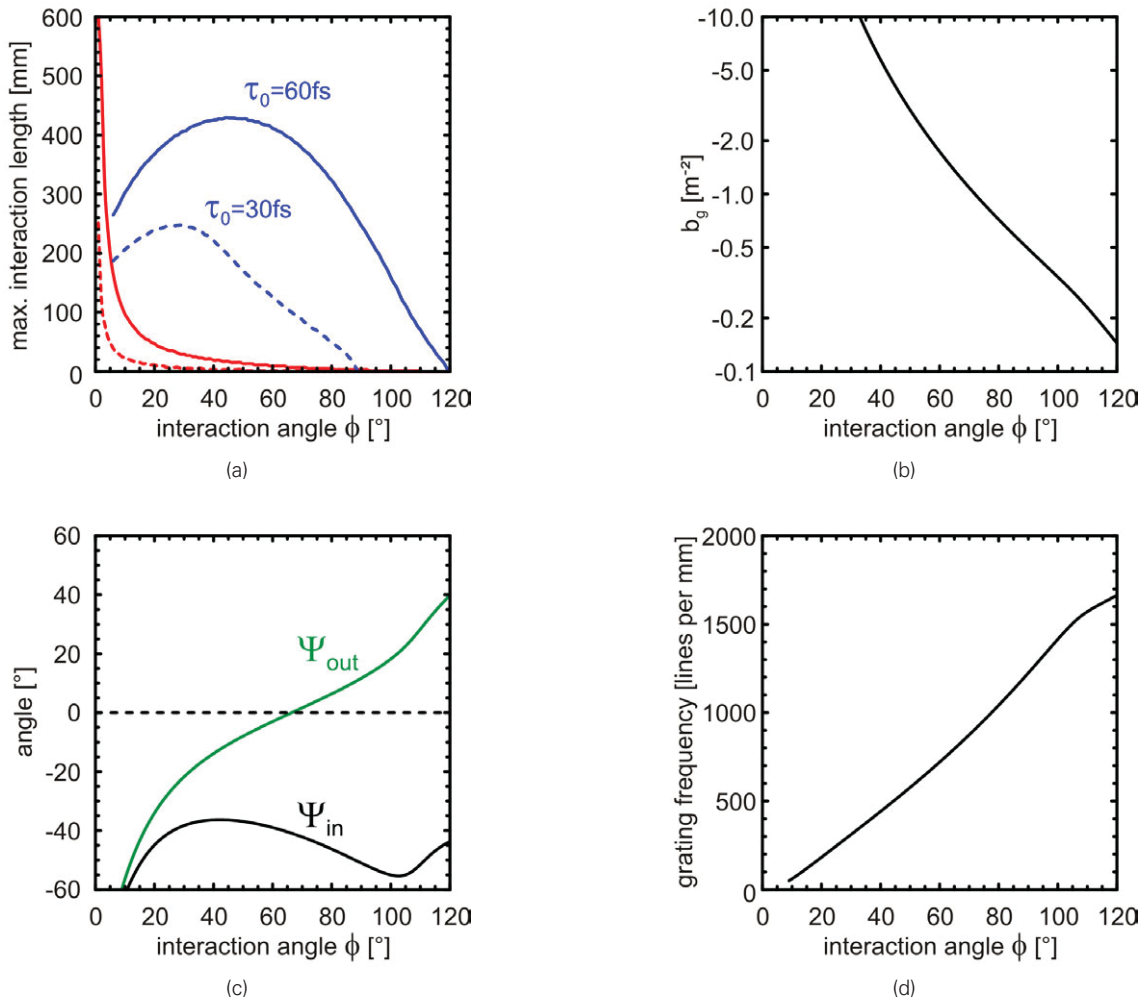


Figure 5.10: (a) depicts the maximum interaction distances with respect to the interaction angle ϕ , for 60 fs (solid) and 30 fs (dashed) pulses in a VLS grating setup (blue) as in Fig. 5.8 compared to using standard gratings (red). In (b)-(d) the corresponding optimized parameters are shown: (b) the normalized quadratic chirp of the VLS grating, (c) incident and output angles, and (d) the central grating frequency of the VLS grating. In all calculations, a laser wavelength of 800 nm has been assumed.

sation is required in the application, as well as the VLS grating function and the optical setup. For standard gratings however it is again confirmed that these perform well towards very small angles ϕ and hence complement the VLS gratings at large angles.

Another important measure for the quality of the setup is the local pulse front displacement, which quantifies the difference between the desired straight pulse front and a curved one. Such non-ideal pulse fronts are an unwanted side effect that arise from the higher order nonlinearities of VLS gratings. If that displacement $\Delta\tau/\tau_0$ becomes larger than the local laser pulse duration τ/τ_0 , overlap is lost. For a setup configuration with a 60 fs laser pulse at 60° one arrives at a maximum overlapping distance of 20 mm, as depicted in Fig. 5.11 (red). Though this is still longer than the interaction distances achievable by standard gratings, it is considerably smaller than the interaction distances possible according to Fig. 5.10. However, this can be compensated by modified setups or VLS grating functions. For example two VLS gratings can be used: the first

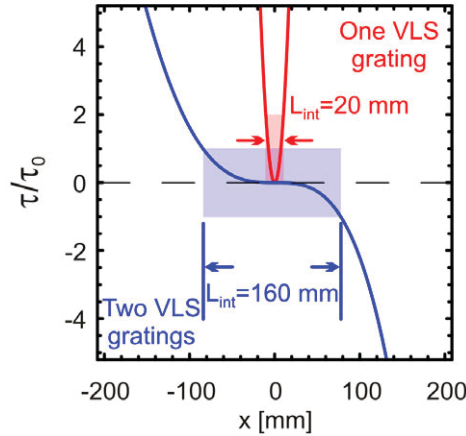


Figure 5.11: Local pulse front deviation of a 60 fs laser pulse at $\phi = 60^\circ$ in a setup with a single quadratic VLS grating (red) and an improved setup using an additional quadratic VLS grating (blue) to reduce the bending of the pulse front.

grating to precompensate a quadratic shift in pulse front as shown by the red curve in Fig. 5.11, and the second grating to apply the remaining compensation in SD. If such an additional VLS grating with a well-adjusted, quadratic line-spacing chirp replaces the last compressor grating in the setup discussed here, the quadratic deviation of the pulse-front tilt can be removed and a much longer overlapping distance of 160 mm is obtained, see Fig. 5.11 (blue line).

It should be stressed that these optimizations belong to one specific setup type using VLS gratings with a quadratic chirp. These results change significantly, when non-polynomial VLS functions or different optical setups are being used. Since the optimization conditions (5.18) to (5.20) become increasingly stringent for shorter laser pulses or interaction angles beyond $\phi = 120^\circ$, more specialized solutions for controlling higher order dispersion warrant further investigations.

5.6 SCALING FOR INCOHERENT TWTS SOURCES

In the previous section, it was discussed how traveling-wave Thomson scattering (TWTS) can be realized in experiment. The question arises: how does it compare to head-on scattering and what kind of lasers profit most of that scheme? Generally, basic properties remain similar to head-on Thomson scattering, so the resulting X-ray pulses still have durations corresponding to the copropagating electron bunches $\tau_{\text{xrays}} \simeq \tau_{\text{bunch}}$. Also the natural bandwidth, i.e. the monochromaticity, continues to be determined by the number of laser oscillation periods

$$\Delta\omega_{sc}/\omega_{sc} = 1/N_0 = \frac{\lambda_0}{d_{\text{beam}} \sin \phi \tan \phi/2}, \quad (5.30)$$

seen by the electrons. The resulting photon energy scales with the scattering angle $\propto (1 - \beta_0 \cos \phi)$, thus allowing for a large degree of tunability from EUV to hard X-ray radiation, even for electron sources that operate at a fixed energy. However, the main advantage of TWTS with regard to head-on scenarios is that it allows to increase the photon numbers per pulse by several orders of magnitudes without entering the nonlinear Thomson regime.

Since in head-on focal geometries today's high-power lasers easily exceed the nonlinearity threshold

$$I_{0,\max}[\text{W/cm}^2] = 1.37 \times 10^{18} \left(\frac{a_{0,\max}}{\lambda_0[\mu\text{m}]} \right)^2 \quad \text{with } a_{0,\max} \simeq 0.2 \ll 1. \quad (5.31)$$

Currently discussed designs plan to use high-repetition systems in both laser system and electron sources. Here, each laser pulse has a low intensity, but is matched to a small electron beam diameter for good efficiency. The added yield over many shots then gives rise to substantial X-ray photon fluxes. For such designs high-repetition laser systems in the **MHz** range with **kW** of average power from fiber based laser systems [22, 23], in combination with laser enhancement cavities [24], and high-average current linacs are envisioned. Yet, important applications such as pump-probe studies or single molecule imaging, require high photon numbers in a single short X-ray pulse rather than a high flux spread over many pulses.

In the following two high-repetition rate systems are compared to a TWTS using a high-power laser. All these systems feature the same average laser power of **200 W**. For the electrons, ELBE parameters (**1 nC**, **40 MeV**, $\epsilon_{\text{norm,rms}} = 2\pi\text{mm mrad}$, $\tau_{\text{bunch}} < 150\text{ fs}$) using the new SRC-Injector [25] are assumed.

The minimum laser waist size $w_{0,\min}$ has to match the bunch diameter of the focused electron beam, which according to the angle term $\gamma^2\theta^2$ in (5.2) is determined by a divergence and hence emittance criterion

$$w_{0,\min} = 2\epsilon_{\text{norm,rms}} / \sqrt{\Delta\omega_{\text{sc}}/\omega_{\text{sc}}}, \quad (5.32)$$

where $\Delta\omega_{\text{sc}}/\omega_{\text{sc}}$ denotes the bandwidth design goal of the scattered radiation.

The first high-repetition laser is an ytterbium-doped fiber CPA system at **1 MHz** repetition rate [22, 23]. The second laser is a **kHz**-system based on Yb:YAG, which at **200 mJ** per pulse is already a challenge with respect to the current state-of-the-art [26]. In contrast to the **MHz**-system the intensities reached are close to the nonlinear intensity limit.

In the TWTS scenario a petawatt class, diode-pumped laser (**200 J**, **150 fs**, **1 μm** , **> 1 Hz**) as planned for the HZDR [27, 28] is used. Note that the long pulse duration of **150 fs** here considerably simplifies GDD, SD and pulse front compensation compared to the **30 fs** and **60 fs** pulses discussed above. Therefore, large angles exceeding $\phi = 90^\circ$, hence higher X-ray energies (5.2), and longer interaction lengths L_{int} become experimentally feasible. In fact, the maximum interaction distance in this example is not limited by the TWTS scattering geometry, but by the electron divergence, which determines the characteristic distance

$$L_{\max} = w_{0,\min}^2 \cdot \frac{\gamma_0}{2\epsilon_{\text{norm,rms}}}, \quad (5.33)$$

after which the electrons leave the laser focus. As a consequence, the laser waist size of the line focus has to be increased until the effective interaction length L_{\max} is long enough to achieve a focal intensity

$$I_{0,\text{TWTS}} = \frac{W_0}{\pi/4 \cdot d_{\text{beam}} w_0 \tau_0} \leq I_{0,\max} \quad (5.34)$$

below the nonlinear intensity limit $I_{0,\max}$. The final photon yields are estimated for $\Delta\omega_{\text{sc}}/\omega_{\text{sc}} = 5\%$ scattered bandwidth using (5.1), where for TWTS the number of oscillations N_0 along the

	MHz head-on ($\phi = 180^\circ$)	kHz head-on ($\phi = 180^\circ$)	PW-TWTS ($\phi = 120^\circ$)	PW-TWTS ($\phi = 120^\circ$)
repetition rate [Hz]	10^6	10^3	1	1
λ_0 [μm]	1	0.5	1	1
w_0 [μm]	18	18	62	17
τ [ps]	1	1	0.15	150
I_0 [W/cm ²]	7.9×10^{13}	7.9×10^{16}	5.5×10^{16}	5.7×10^{16}
W_0 [mJ]	0.2	200	200×10^3	200×10^3
avg. laser power [W]	200	200	200	200
L_{int} [mm]	0.3	1.5	57.6	200
$\hbar\omega_{\text{sc}}$ [keV]	31	62	23	3500
$N_{\text{phot},5\%}$ per pulse	2.5×10^5	1.2×10^8	4.9×10^{10}	3.4×10^{10}

Table 5.1: (Col. 1-3) Comparison of TWTS per shot photon yields with high-repetition laser systems in head-on geometry. The laser systems of photon yield scaling ($\Delta\omega_{\text{sc}}/\omega_{\text{sc}} = 5\%$) using the planned petawatt laser at the HZDR (200 J, 150 fs, 1 μm) and ELBE electrons (1 nC, 40 MeV, $\epsilon_{\text{norm,rms}} = 2.0 \pi \text{ mm mrad}$, $\tau_{\text{bunch}} = 100 \text{ fs}$). (Col. 4) Example of photon yield scaling ($\Delta\omega_{\text{sc}}/\omega_{\text{sc}} = 5\%$) with the planned petawatt laser at the HZDR (200 J, 150 fs, 1 μm) and laser wakefield-accelerated electrons (0.2 nC, 500 MeV, $\epsilon_{\text{norm,rms}} = 0.1 \pi \text{ mm mrad}$).

interaction length is given by

$$N_0 = \frac{L_{\text{int}}}{\lambda_0} \cdot \sin \phi \tan \phi / 2. \quad (5.35)$$

As a result, the TWTS yield $N_{\text{phot},5\%}$ of 4.9×10^{10} photons per shot from ELBE electrons (see Table 5.1) exceeds the ones from the high-repetition laser systems by more than two orders of magnitudes respectively.

As suggested by (5.32) to (5.35), the combination of TWTS and laser wakefield-accelerated laser-wakefield accelerated (LWFA) electrons is especially promising. With transverse emittances as low as $\epsilon_{\text{norm,rms}} = 0.1 \pi \text{ mm mrad}$ and electron energies up to the 1 GeV [2] range, long interaction distances at small diameters (see eq. (5.33) and (5.34)) and thus high photon yields are possible. In addition, such a setup profits of an easy synchronization when using the same laser. Especially for laser wakefield-accelerated electrons it is not straightforward to change the resulting energy. Hence the scalability of the resulting X-ray energy with respect to the angle ϕ facilitates tuning the energy of optimized electron sources that operate in a limited energy region. Since LWFA electrons are not available at high-repetition rates, a high flux cannot be obtained by aforementioned high-repetition designs (ch. 4.3), but by TWTS that also works at low repetition rates. As shown in Table 5.1 X-rays in the MeV range with photon yields over 10^{10} photons at an electron bunch charge of 200 pC can be achieved. The small source size on the order of μm and the ultrashort time scale of tens of fs [29] make this an X-ray source (see Fig. 1.3) with a brilliance on the order of $10^{26} - 10^{27} \text{ mm}^{-1} \text{ mrad}^{-2} \text{ s}^{-1}$ [0.1 %BW].

5.7 TRAVELING-WAVE THOMSON SCATTERING FEL

A major incentive for small-angle scattering setups as shown in Fig. 5.6 in ch. 5.3 is the prospect of realizing interaction lengths which are long enough for an FEL instability to develop. Inserting typical laser and electron parameters, achievable by small, conventional accelerators and current high-power lasers into

$$\rho = \frac{1}{2\gamma_0} \left(\frac{I_p}{I_A} \left(\frac{\lambda_u a_0}{2\sqrt{2}\pi\sigma_b} \right)^2 \right)^{1/3}, \text{ with } \lambda_u = \lambda_0/(1 - \beta_0 \cos \phi) \quad (5.36)$$

yields an FEL parameter ρ in a range of $10^{-4} - 10^{-3}$, which corresponds to power gain lengths $L_{\text{gain}} = \frac{\lambda_u}{4\pi\sqrt{3}\rho}$ on the order of **cm**, while the available interaction distance can be on a meter scale. Since the effective undulator periods of the scenario are in the sub-**mm** to **mm** range, FEL radiation in the XUV to X-ray region is possible in a much more compact setup and at lower electron energies compared to existing FEL systems. As summarized in Table 5.2, the main advantage of a TWTS based SASE-FEL would be its small scale in the sub-**mm** to meter range. With lower electron energies, as used for FELBE (IR-FEL resonator), XUV (13 **nm**) to X-ray wavelengths (1 **Å**) could be achieved, which up to now are the domain of large facilities such as FLASH and LCLS. An important prerequisite for TWTS-FEL operation are low-emittance electrons below $\epsilon_{n,\text{trans}} = 1 \pi \text{ mm mrad}$, which arise from the small interaction angle ϕ and are discussed later in this chapter (eq. (5.60)). Thus LWFA electrons with 100 **pC** charge and 10 **fs** duration are assumed in this example.

In contrast to earlier proposals of optical FELs [30, 31], the other distinct advantage of TWTS-based, optical undulators is that it is not limited by the Rayleigh length, but instead can in principle be arbitrarily long. This is crucial, because with TWTS it is possible to trade longer interaction lengths for smaller intensities in the FEL design without sacrificing peak field strength. Note, that a low laser strength parameter $a_0 \ll 1$ keeps the scattering process firmly in the linear regime. Hence, varying laser envelope amplitudes have largely reduced effect on the nonlinear shift of the resonant FEL frequency (5.2), which from an experimental perspective makes the process significantly more robust and less dependent on specific laser intensity profiles.

Furthermore, as an optical undulator, TWTS takes place in vacuum, so that the driving field is not bound to any material structure near the electron beam. Especially resistive feedback effects [32, 33], such as wall-wakefields, where the electron beam interacts with the undulator structure and thus limits the minimum gap size in magnetic undulators, do not exist in optical undulators.

Since the effective undulator period is $\lambda_u = \lambda_0/(1 - \beta_0 \cos \phi)$, all major operational parameters of a TWTS-FEL fundamentally depend on what interaction angle ϕ between laser and electrons is being used. Thus, this added flexibility in ϕ leads to new scalings. First of all, ϕ naturally affects the resonant wavelength

$$\lambda_{\text{sc}} = \frac{\lambda_0}{2\gamma_0^2(1 - \beta_0 \cos \phi)} \stackrel{1/\gamma_0 \ll \phi \ll 1}{\approx} \frac{\lambda_0}{\gamma^2 \phi^2}, \quad (5.37)$$

and together with the laser beam diameter d_{beam} the length of the line focus (see Fig. 5.4(a)) and

thus the maximum interaction distance

$$L_{\text{int}} = \frac{d_{\text{beam}}}{\sin \phi} \stackrel{\phi \ll 1}{\simeq} \frac{d_{\text{beam}}}{\phi}. \quad (5.38)$$

For a given laser system with an on-axis intensity according to (5.34) and laser strength a_0 (2.89) and the angle dependent λ_u the FEL parameter scales as

$$\rho = \frac{1}{2\gamma_0} \left(\frac{I_p}{I_A} \left(\frac{\lambda_u a_0}{2\sqrt{2}\pi\sigma_b} \right)^2 \right)^{1/3} \stackrel{\phi \ll 1}{\propto} \gamma_0^{-1} \phi^{-4/3}. \quad (5.39)$$

Note that for small ϕ the role of γ_0 and ϕ are similar in both (5.37) and (5.39). The gain length

$$L_{\text{gain}} = \frac{\lambda_0}{(1 - \beta_0 \cos \phi) \cdot 4\pi\sqrt{3}\rho} \stackrel{\phi \ll 1}{\propto} \gamma_0^{-1} \phi^{-10/3} \quad (5.40)$$

on the other hand has more than an inverse cubic dependence on ϕ , which in practice is more of a feature, rather than a problem, because it allows a TWTS-FEL to be scaled in its length dimension from several **mm** to **m** without negatively impacting the FEL parameter.

However, for scaling towards an X-ray SASE FEL it is not only necessary to adjust the resonant wavelength and maximize the FEL parameter. One also needs to consider the overall energy output of an FEL, given by the saturation energy

$$W_{\text{sat}} \simeq \gamma_0 m c^2 \cdot \rho = m c^2 \cdot \left(\frac{I_p}{I_A} \left(\frac{\lambda_u a_0}{2\sqrt{2}\pi\sigma_b} \right)^2 \right)^{1/3} \propto \phi^{-4/3} \quad (5.41)$$

of the resulting X-ray pulse. Since (5.41) depends on ϕ instead of γ_0 , it now becomes apparent that the FEL resonant condition (5.2) is preferably fulfilled by high electron energies γ_0 and small scattering angles ϕ . Combining modern high-power lasers with the ongoing progress in the quality of laser wakefield electrons [34, 35] achieving low-emittance and high peak-current electron bunches at high energies with small energy spreads, this could lead to compact all-optical SASE-FELs.

Differences of TWTS- compared to conventional FEL

Aside from the much smaller undulator period of an optical undulator, TWTS has additional differences compared to conventional FELs. These differences mainly arise from the laser beam being incident from a non-collinear angle ϕ and hence lead to new questions on potential geometry effects with regard to transversal coherence or the SASE amplification process. Furthermore, the question of tolerances with respect to the initial laser and electron beam requirements, such as intensity or emittance, needs to be investigated in a broader context.

In principle relativistic electrons all radiate into a narrow $1/\gamma_0$ -cone. If these electrons radiate coherently the superposition of that radiation forms according to Huygens's principle a plane wave, which in conventional undulators is parallel to the mean electron direction of propagation. In TWTS however the incident laser wave comes at an angle and thus defines a varying phase

Parameter	FELBE ^a	TWTS	TWTS	FLASH ^b
FEL type	IR Resonator	XUV-SASE	XRAY-SASE	XUV-SASE
peak current [kA]	0.11	10.0	10.0	2.5
electron energy [MeV]	34	100	500	1000
bunch length (FWHM) [fs]	1648	10	10	393
und. period [mm]	27.3	1.0	0.2	27.3
K	0.7	0.1	0.1	1.2
wavelength [nm]	5000	13.0	0.1	13.0
Pierce parameter	4.0×10^{-4}	1.4×10^{-3}	1.0×10^{-4}	9.8×10^{-4}
gain length [m]	3.1	0.032	0.091	1.28
interaction length [m]	1.86	0.65	2.0	27
peak photon power [MW]	1.54	1.4×10^3	4.8×10^2	2.5×10^3

^aHelmholtz-Zentrum Dresden-Rossendorf (HZDR)

^bDESY

Table 5.2: Compares a potential TWTS based FEL with existing facilities. The TWTS scenarios are all based on laser wakefield-accelerated electrons with 10 fs duration, 100 pC of charge, 20 μm RMS beam diameter and a normalized transverse emittance $\epsilon_{n,\text{trans}} = 0.1 \pi \text{ mm mrad}$. The interaction angles ϕ for the XUV and X-ray TWTS-SASE scenarios at a laser wavelength $\lambda = 1.0 \mu\text{m}$ are 2.6° and 5.9° respectively.

across the beam cross-section. The resulting coherent superposition leads to a plane wave that does not propagate in direction of the electrons, but at an angle ϕ_{sc} . Due to relativity this angle is contracted compared to the incident angle ϕ . In Fig. 5.12(a) the incident laser beam is shown with a phase difference between (1) and (2) across the beam. The resulting angle ϕ_{sc} can be determined by taking into account the Lorentz invariance of phase, so in the plane wave of the resulting radiation (1) and (2) have the same phase difference. In addition the resulting wavelength in the forward direction is known to scale according to (5.2) as $(1 + \gamma_0^2 \theta^2)(2\gamma_0^2 (1 - \beta_0 \cos \phi))$, where θ denotes the observation angle. Therefore the distance along the phase gradient contracts by the same factor and hence the coherently scattered angle ϕ_{sc} becomes

$$\begin{aligned} \sin \phi_{\text{sc}} &\simeq \frac{(1 + \gamma_0^2 \phi_{\text{sc}}^2)}{2\gamma_0^2 (1 - \cos \phi)} \cdot \sin \phi \\ \tan \phi_{\text{sc}} &= \frac{\sin \phi_{\text{sc}}}{\cos \phi_{\text{sc}}} = \frac{1 + \gamma_0^2 \phi_{\text{sc}}^2}{2\gamma_0^2 (1 - \cos \phi)} \cdot \frac{\sin \phi}{\cos \phi_{\text{sc}}} \end{aligned} \quad (5.42)$$

For $\gamma \gg 1$ eq. (5.42) has simple solutions.

$$\phi_{\text{sc}} = \begin{cases} \phi & \text{for } \phi < \frac{1}{\gamma_0} , \\ \frac{1}{\gamma_0 \cdot \phi} & \text{for } \phi > \frac{1}{\gamma_0} \text{ and } \phi \ll 1, \\ \arctan \left(\frac{\sin \phi}{2\gamma_0^2 (1 - \beta_0 \cos \phi)} \right) & \text{for } \phi \gg \frac{1}{\gamma_0} . \end{cases} \quad (5.43)$$

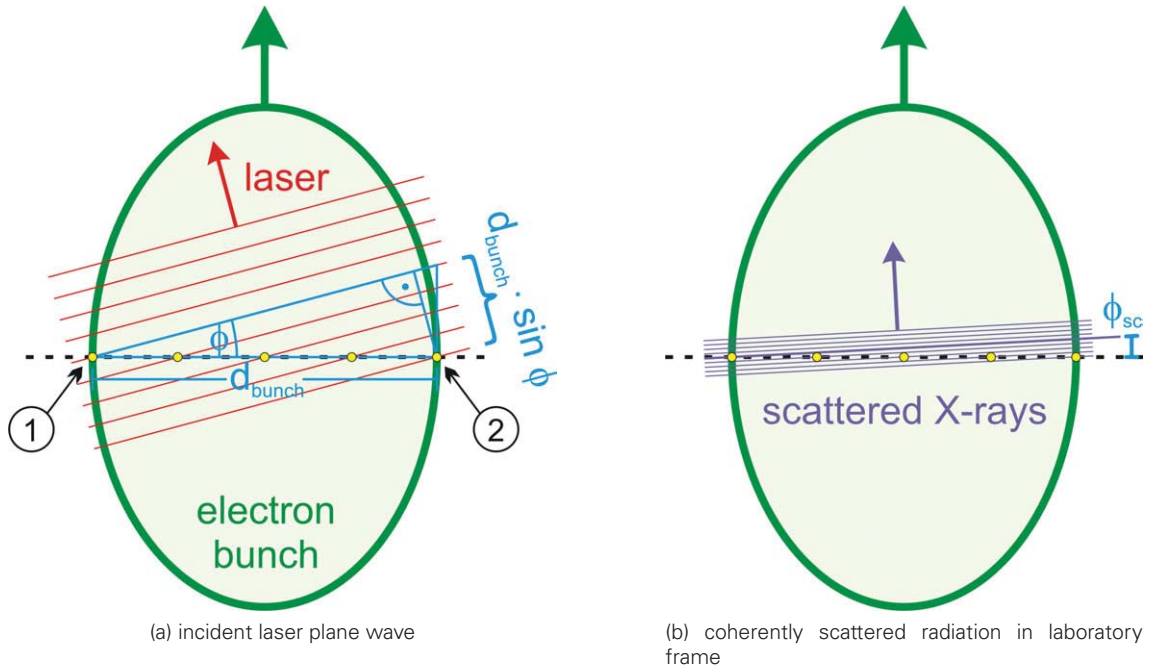


Figure 5.12: (a) depicts a laser plane wave (red) which is incident onto an electron bunch under an angle ϕ in the laboratory frame. Due to this angle there exists a relative phase difference transverse to the electron direction of propagation (between **1** and **2**). (b) shows the plane wave resulting from coherent scattering. Since the phase differences compared to the incident plane wave remain the same, but the scattered wavelength contracts by a factor proportional to γ_0^2 , this correspondingly leads to a contraction of the outgoing angle ϕ_{sc} with respect to the electron direction of propagation.

The first case represents light scattered at such small angles that in both the electron rest frame and the laboratory frame it is radiated into the forward direction without change in angle. The situation becomes more interesting above the angle $\phi > 1/\gamma_0$, where the backscattered radiation in the electron rest frame is radiated into the forward direction in the laboratory frame. In this case the resulting wavelength of the coherently scattered plane wave becomes

$$\begin{aligned} \lambda_{sc} &\simeq \frac{\lambda_u}{2\gamma_0^2} (1 + \gamma_0^2 \phi_{sc}^2) \\ &= \frac{\lambda_0}{2\gamma_0^2 \cdot (1 - \beta_0 \cos \phi)} \left(1 + \frac{1}{\gamma_0^2 \phi^2} \right). \end{aligned} \quad (5.44)$$

According to (5.43) and Fig. 5.13 the resulting angle ϕ_{sc} does for no incident angle ϕ become larger than $1/\gamma_0$. Thus the amplitude of the scattered wave remains comparable to the one at zero angle.

Another consequence of side-scattering is that the microbunching instability does not develop along the electron propagation direction, but along the direction of the scattered wave. Therefore the FEL resonant condition

$$\lambda_r = \frac{\lambda_u (1 - \beta_{z,0})}{\beta_{z,0}} \quad (5.45)$$

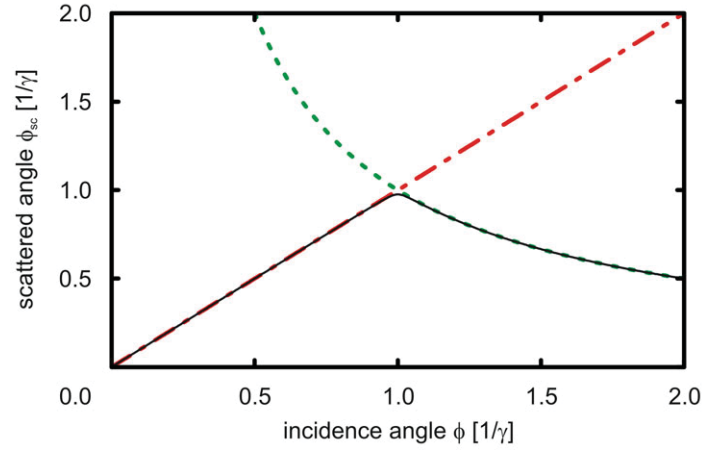


Figure 5.13: Scattering angle ϕ_{sc} of a coherently scattered plane wave with respect to the incident angle ϕ . The red (dash-dotted) curve and the green (dashed) curve, represent the forward- and backscattered contribution according to the approximations in (5.43). The black (solid) curve shows the numerical result from (5.42) for a $\gamma = 40$ electron beam and illustrates the validity of the approximation in (5.43).

for maintaining a constant “ponderomotive force phase” (2.34),

$$\phi_{pond} = 2\pi \left(\frac{1}{\lambda_r} + \frac{1}{\lambda_u} \right) z - \omega t + \Psi \quad (5.46)$$

has to be written with the effective undulator wavelength $\lambda_u \rightarrow \lambda_u / \cos \phi_{sc}$ and the electron velocity $\beta_{z,0} = \beta_0 \cdot \cos \phi_{sc}$, both projected into the direction of the scattered wave. Hence, the new resonance condition becomes

$$\begin{aligned} \lambda_r &= \frac{\lambda_u (1 - \beta_0 \cdot \cos \phi_{sc})}{\beta_0 \cdot \cos^2 \phi_{sc}} \\ &\simeq \lambda_u \left(1 - \left(1 - \frac{1}{2\gamma_0^2} \right) \cdot \left(1 - \frac{\phi_{sc}^2}{2} \right) \right) \\ &\simeq \frac{\lambda_u}{2\gamma_0^2} (1 + \gamma_0^2 \phi_{sc}^2). \end{aligned} \quad (5.47)$$

Together with eq. (5.43) and $\lambda_u = \lambda_0 / (1 - \beta_0 \cos \phi)$ one obtains the resonant condition for traveling-wave Thomson scattering based free-electron lasers

$$\lambda_r = \frac{\lambda_0}{2\gamma_0^2 \cdot (1 - \beta_0 \cos \phi)} \cdot \left(1 + \frac{1}{\gamma_0^2 \phi^2} \right), \quad (5.48)$$

which is the same as the wavelength λ_{sc} for coherent and oblique scattering (5.44) and thus is in agreement with TWTS driving an FEL instability.

However, the angle ϕ_{sc} between electron trajectory and the resulting radiation causes the latter to leak out of the interaction zone and thus loss of radiation to the amplification process. For the SASE process not to be affected, it is necessary for that leakage to be much smaller than the FEL gain. Therefore the radiation walk-off over one gain length needs to be smaller than the

width of the interaction zone, which corresponds to the electron bunch diameter $d_{\text{bunch}} \simeq 2\sigma_b$.

$$\underbrace{\phi_{\text{sc}} \cdot L_{\text{gain}}}_{\propto \gamma^{-2} \phi^{-13/3}} \ll d_{\text{bunch}} \simeq 2\sigma_b \quad (5.49)$$

Due to the strong γ_0 scaling, (5.49) can become an issue for lower electron energies. In the 13 nm example of Table 5.2, the leakage offset is with 18 μm already a significant fraction of the 40 μm beam diameter, which will lead to a longer effective gain and saturation length. In the other 1 \AA example with the higher electron energy, the leakage offset is merely 2 % of the electron bunch diameter and is thus negligibly small.

Requirements on laser beams

In contrast to undulators it is experimentally more challenging to precisely tune the spatial and temporal envelope of the field – and especially so for high power lasers. In order to stay tuned on the FEL resonance $\Delta\lambda_{\text{sc}}/\lambda_r \ll 2\rho$ for all electrons over the entire interaction length, the laser field has to meet requirements on both spatial and temporal field envelopes or equivalently intensity profiles.

Since high laser fields shift the FEL resonance through the nonlinear laser-electron interaction by a factor of $(1 + a_0^2/2)$, it is necessary to keep variations in the laser field δa , small enough to satisfy

$$\begin{aligned} \frac{1 + (a_0 + \delta a)^2/2}{1 + a_0^2/2} - 1 &\ll 2\rho \\ \frac{a_0 \delta a + \delta a^2/2}{1 + a_0^2/2} &\ll 2\rho. \end{aligned} \quad (5.50)$$

In addition field variations are field gradients that lead to ponderomotive forces, that expel the electrons out of the laser region of highest intensity. The resulting change in direction by the angle θ leads to a change in the radiated wavelength λ_{sc} according to (5.2). Hence for continuous FEL resonance

$$\frac{\gamma^2 \theta^2}{1 + a_0^2/2} \ll 2\rho, \quad (5.51)$$

the relativistic expression for the ponderomotive force (2.92) is

$$\mathbf{F}_p = \frac{d\mathbf{p}}{dt} = -mc^2 \nabla \bar{\gamma}, \quad (5.52)$$

with the cycle averaged $\bar{\gamma}$ -factor for linearly polarized laser fields

$$\bar{\gamma} = \sqrt{\gamma_0^2 + \frac{a_0(\mathbf{r})^2}{2}} \stackrel{a_0 \ll \gamma_0}{\simeq} \gamma_0 + \frac{a_0^2}{4\gamma_0}. \quad (5.53)$$

For an upper estimate of the ponderomotive force (5.52) and thus the ensuing angular deflection θ_{pond} , the force can be assumed to be at constant maximum over the entire electron

interaction time $\Delta t = L_{\text{int}}/c$, the resulting ponderomotive deflection angle can for $\gamma \gg 1$ and $a_0 \ll \gamma_0$ be written as

$$\theta_{\text{pond}} = \frac{d\bar{p}}{dt} \cdot \frac{\Delta t}{\rho_{\parallel}} \simeq \frac{|\nabla\bar{\gamma}| \cdot L_{\text{int}}}{\gamma_0}. \quad (5.54)$$

Inserting (5.53) and (5.54) into (5.51) yields the condition

$$\frac{\gamma^2 \theta_{\text{pond}}^2}{1 + a_0^2/2} = \frac{L_{\text{int}}^2}{1 + a_0^2/2} \left(\frac{|\nabla a_0^2(\mathbf{r})|}{4\gamma_0} \right)^2 \ll 2\rho. \quad (5.55)$$

When supposing $\mathbf{a}_0 \perp \beta_0$, an order of magnitude estimate can be made by setting the intensity gradient $\nabla a_0^2(\mathbf{r}) \approx \delta a^2/w_0$, where w_0 denotes the laser beam waist size.

In practical terms the conditions (5.50) and (5.55) mean that optical wiggler schemes with a_0 approaching or even exceeding unity require near perfect beams $\delta a/a_0 \ll \rho$ that are “flat top” in transverse profile and rectangular in the temporal profile, which makes optical wiggler FELs extremely demanding for technical realization and is one major reason optical wigglers have not been built yet. This however is different for TWTS-FEL scenarios: In contrast to head-on setups, the maximum interaction length is not anymore limited by the Rayleigh length, which makes it possible to trade lower laser intensities for longer gain lengths and avoid nonlinearities and ponderomotive effects. In the example of the XUV and X-ray TWTS-FEL scenarios in Table 5.2 at $a_0 = 0.1$, according to (5.50), the maximum relative variation of laser beam intensity $\delta I/I_{0,\text{TWTS}} \simeq 2(\delta a/a_0)$ only needs to be smaller than 58% and 4% respectively, which is clearly within the capabilities of existing laser technology. The corresponding restrictions arising from (5.55) are even weaker: smaller than 111% for the XUV and smaller than 72% for the X-ray scenario. Therefore one of the advantages of a potential TWTS-FEL is that it is much less of an optical wiggler, rather than an optical undulator. Also on the experimental side, the TWTS mechanism (Fig. 5.4) has the advantage that the electrons are stationary with respect to the temporal envelope of the beam and thus remain in the laser beam center where less intensity variation occurs, so that intensity variations mainly originate from the transverse laser profile, which is easier to modify in a laser system.

Requirements on electron beams

In order to remain within the FEL resonance, there are two main conditions on the electron beam. First the energy spread has to be

$$\frac{\sigma_{\gamma}}{\gamma_0} \ll \rho, \quad (5.56)$$

which is equivalent to $\Delta\lambda_{\text{sc}}/\lambda_r \ll 2\rho$. Then according to (5.2), the off-axis Doppler effect $\Delta\lambda_{\text{sc}}/\lambda_r \propto \gamma_0^2 \theta^2$ has a similar effect than an energy spread and leads to a constraint on the normalized transverse emittance

$$\begin{aligned} \gamma_0^2 \theta^2 &\ll 2\rho \\ \left(\frac{\epsilon_n}{\sigma_b} \right)^2 &\ll 2\rho, \end{aligned} \quad (5.57)$$

where σ_b denotes the RMS beam diameter. An alternative notation of (5.57)

$$\varepsilon_n \ll \frac{4\rho\beta_{\text{ph}}\gamma_0\lambda_r}{\lambda_0}(1 - \beta_0 \cos \phi) \quad (5.58)$$

includes the so called β -parameter $\beta_{\text{ph}} = \gamma \cdot \sigma_b^2/\varepsilon_n$, as defined in accelerator physics [36], where it parameterizes the phase space ellipse of an electron beam.

However for side-scattering the angle ϕ in (5.2) becomes also relevant, because electrons propagating off-axis in a direction $\Delta\phi$ have also a different laser incidence angle $\phi + \Delta\phi$. Hence the condition for a central side-scattering angle $\phi_0 \gg 1/\gamma_0$ is

$$\frac{\Delta\lambda_{\text{sc}}}{\lambda_r} = \left| \frac{\beta_0 \sin \phi_0}{1 - \beta_0 \cos \phi_0} \right| \cdot \Delta\phi \ll 2\rho. \quad (5.59)$$

After identifying $\Delta\phi$ with the divergence from transverse emittance $\Delta\phi = \varepsilon_{n,\text{trans}}/(\gamma_0\sigma_b)$, inserting (5.36) for ρ and approximating for small angles (5.59) becomes an additional transverse emittance constraint

$$\varepsilon_{n,\text{trans}} \ll \left(\frac{l_p}{l_A} \left(\frac{\lambda_0 a_0}{2\sqrt{2}\pi\sigma_b} \right)^2 \right)^{1/3} \frac{\sigma_b(1 - \beta_0 \cos \phi)^{1/3}}{\beta_0 \sin \phi} \stackrel{\phi \ll 1}{\propto} \phi^{-1/3} \sigma_b^{1/3}, \quad (5.60)$$

which in practice is far more strict than (5.57). Additionally, the condition only scales weakly in ϕ , such there is no big difference between the emittance requirement of the 1 Å and 13 nm TWTS-FEL example of Table 5.2, which are 0.19π mm mrad and 0.25π mm mrad respectively.

For incoherent TWTS, where much larger angles ϕ are being used, this is much less an issue. Here it is useful to examine (5.59) for the condition that its broadening contribution becomes negligible

$$\begin{aligned} \gamma_0^2 \Delta\phi \cdot \Delta\phi &\ll (\Delta\omega_{\text{sc}}/\omega_{\text{sc}}) \\ \Rightarrow \left| \frac{\sin \phi_0}{1 - \beta_0 \cos \phi_0} \right| &\ll \gamma_0^2 \Delta\phi, \end{aligned} \quad (5.61)$$

when compared to (5.57). It is thus clear that the side-scattering term only can be neglected for $\gamma_0 \frac{\varepsilon_n}{\sigma_b} \gg 1$. From (5.61) it follows that there exists a minimum scattering angle

$$\phi_{\text{min}} = \arccos \left(\frac{(\gamma_0 \varepsilon_n / \sigma_b)^2 - 1}{(\gamma_0 \varepsilon_n / \sigma_b)^2 + 1} \right), \quad (5.62)$$

which has to be exceeded, before the contribution of wavelength spread from (5.59) becomes smaller than (5.57). For most practical cases (5.62) is small compared to the large interaction angles. For example the LWFA-driven TWTS Thomson source in Table 5.1 features a ϕ_{min} of 8.4°, which is much smaller than the targeted 120°. In principle it is also possible to exploit this limit for TWTS-FEL, but note that according to (5.39) the Pierce parameter ρ becomes smaller towards larger angles ϕ .

5.8 OUTLOOK ON TRAVELING-WAVE THOMSON SCATTERING

Since a short Rayleigh length is a limiting factor to many light-matter interactions, the basic idea and the tools provided here in the scope of efficient Thomson scattering can be applied to a large range of experiments and applications.

The pulse front tilt in combination with the line focus provides a small interaction volume of the size of the laser focus which, depending on the tilting angle, moves with velocities comparable to the speed of light. Therefore, if the interacting matter or some generic excitation mode moves with the same speed, the result is an effective interaction length, which can be much longer than the Rayleigh length. Consequently, this scheme is interesting not only for relativistic, charged beams, which can be made up of electrons, protons, ions, positrons or ionized clusters, but can be also be extended towards light-matter interactions that take place in gases, solids, liquids or plasmas. This broad applicability is motivated in the following by two examples.

Phase-matching in nonlinear light-matter interactions

In general, TWTS could be used in nonlinear light-matter interactions to improve conversion efficiencies. Hereby frequency conversion through sum-frequency or second harmonic generation such as in KDP (*Potassium Dihydrogen Phosphate*) crystals is a well known and prominent example, where the total energy efficiency for the frequency upconversion is largely determined by the degree of phase-matching [37] between the interacting modes. In order to achieve phase-matching between ordinary and extraordinary beams in type-II second-harmonic generation processes, non-collinear geometries are widely used. However, this usually comes at the cost of having only a limited overlapping region. This can be circumvented by a traveling-wave interaction scheme as shown in Fig. 5.14. When compared to other techniques such as quasi phase-matching techniques [37], where the nonlinear properties of a medium are spatially modulated, for example through periodic poling, to achieve a net phase-matching effect over longer distances, this technique has the main advantage of being independent of the crystal material. Quasi-phase matched crystals have to be manufactured for a specific process and can not be realized for all crystal materials. Also, parasitic higher-order processes can generate light at additional wavelengths, which can be disturbing in various ways. Hence, for many applications it could be easier and cheaper to utilize a traveling-wave setup with VLS gratings and a homogeneous nonlinear crystal without microstructure. Since it is easier to manufacture homogeneous large aperture nonlinear crystals of considerable thicknesses, this technique is in principle also useful for high-power applications. Also, the flexibility provided by the line focus and the dispersion correction through VLS gratings, makes it possible to break the symmetry in angle ϕ of the two beams with respect to the focal line and account for some additional energy walk-off angle within the nonlinear medium.

As an example there is High Harmonics Generation (HHG) in gases [38, 39]. Here especially for higher order harmonics, phase matching between the laser pulse driving the process and the resulting emitted light is one of the grand challenges [40] for increasing photon fluxes. In general the gas is a mixture of ionized and non-ionized atoms at a certain gas pressure. The

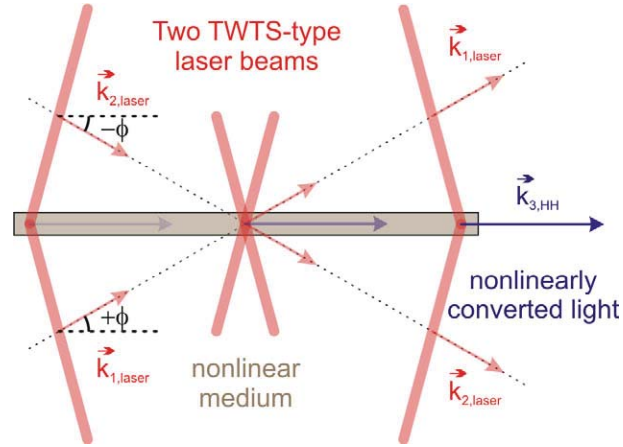


Figure 5.14: The nonlinear medium is aligned with the line focus and two counterpropagating, pulse-front tilted laser pulses $\mathbf{k}_{1,\text{laser}}$ and $\mathbf{k}_{2,\text{laser}}$ at angle ϕ and $-\phi$ overlap within the nonlinear medium. The angle ϕ is chosen according to the nonlinear medium to satisfy the phase matching condition (5.63) to allow for sum-frequency generation $\mathbf{k}_{1,\text{laser}} + \mathbf{k}_{2,\text{laser}} = \mathbf{k}_{3,\text{HH}}$. The advantage of this approach is that it enables angle-based phase matching over long propagation lengths in the nonlinear material without loss of overlap. Since direction and velocity of the laser pulse envelopes along the region of interaction can be controlled independently of the two laser beam \mathbf{k} -vectors, it is thus possible to arrange the laser beams such that their main pulse energy follows the energy flow (*Poynting vector*) of the radiation generated in the nonlinear material. Hence, this has the effect of eliminating energy walk-off.

differences in phase velocities between laser and HHG radiation lead to phase mismatch. Especially a high degree of ionization, leads to laser phase velocities greater than the speed of light and dominates other dispersive contributions to laser and the HHG. A novel approach to achieve full phase matching could be two TWTS-type laser-beams focused along the line of interaction as in Fig. 5.14, one at some angle ϕ and the other one at an angle $-\phi$. The superposition of both beams then leads to a wave propagating along the focus with a longer phase velocity and a standing wave pattern in the transversal direction. A particular choice of angle ϕ , can reduce the enough to fully compensate for the phase dispersion

$$\cos \phi \cdot qk_{\text{laser}} - k_q = 0, \quad (5.63)$$

where k_q denotes the wavenumber of the q^{th} radiated harmonic. For a plasma with an electron density of $\sim 10^{19} \text{ cm}^{-3}$ and a $1 \mu\text{m}$ laser, the angle would be about 5° . This design of phase matching works without a waveguide in a long gas jet geometry, so the laser is for most of its time propagating outside of the gas, which make it much less prone to propagation effects, such as density and intensity induced defocusing or frequency shifts. Since the focusing happens perpendicular to the focal line, the Gouy phase shift is not contributing. This approach needs a reasonably high electron density, such that the required angle ϕ is large enough to be realized in some realistic experimental setup, but on the other hand the angle needs to be small enough to allow for a sizable coherence length in the transverse direction, which is defined by the period of the standing wave in transversal direction $L_{\text{trans}} = \lambda_0 / \sin \phi$. If this length becomes comparable with the wavelength of the radiated harmonic, the periodic phase-structure has the same effect as a refractive phase-grating and leads to diffraction of the higher harmonic to higher (diffraction) orders into other angles, thus reducing intensity in the main direction (0^{th} order).

Electron cooling

Right after electron energy and bunch charge, transverse electron beam emittance is crucial to many experiments in accelerator physics, but advances in smaller beam emittances have been slow and mostly depend on better electron beam guns. Therefore it was proposed [41–43] to improve emittances by a cooling process during circulation in a storage ring (Fig. 5.15). For cooling it was proposed to use the electron recoil of Compton backscattering to decelerate all electrons in the direction opposite their individual direction of propagation. By reacceleration by a RF-cell the original electron energy is restored. However, as the reacceleration takes place in the mean direction of propagation of the entire electron bunch, the transverse velocity components of the individual electrons are not restored. The result is a decrease in divergence and hence transverse emittance. The net effect of alternating Compton scattering and reacceleration over many round trips in a storage ring is a cooling of the electron beam. The number of round trips n_d required to damp away an e^1 -fold of the initial electron energy E is according to [42] in practical units

$$n_d = \left(\frac{\Delta E_\gamma}{E} \right)^{-1} \simeq \frac{1.6 \times 10^5 \lambda_0 [\mu\text{m}] Z_0 [\text{mm}]}{E_L [\text{J}] E [\text{MeV}]} = \frac{5.0 \times 10^{-4} \lambda_0 [\mu\text{m}] w_0^2 [\mu\text{m}]}{E_L [\text{J}] E [\text{MeV}]} . \quad (5.64)$$

For a laser with $\lambda_0 = 1 \mu\text{m}$ with $E_L = 1 \text{ J}$ pulse energy and a Rayleigh length of 1 mm the characteristic number of round trips for cooling is 1600. This formula is valid only for the linear Compton regime, where transverse electron velocities are sub-relativistic $a_0 \ll 1$.

Neglecting other sources of emittance growth, this process could in principle cool the beam down to the limit, where the quantized nature of the Compton process with its photon recoil $\hbar k$ limits further cooling. The resulting lower limit in normalized transverse emittance [42]

$$\varepsilon_{n,\min} = \frac{3}{10} \frac{\lambda_c}{\lambda_0} \beta_{x,y}^* = \frac{3}{10} \frac{\lambda_c}{\lambda_0} \gamma_0 \frac{\sigma_{x,y}^2}{\varepsilon_{n,0}} \quad (5.65)$$

could with $\lambda_0 = 1 \mu\text{m}$ and $\beta_{x,y}^* = 1 \text{ cm}$ be much lower $\varepsilon_{n,\min} = 7.3 \times 10^{-9} \text{ m}$ than any known electron source. Here $\beta_{x,y}^*$ and $\lambda_c = h/mc \simeq 2.43 \times 10^{-13} \text{ m}$ denote the electron beta function (also: depth of electron focus) in the x or y direction [36] at the laser interaction region and the electron Compton wavelength respectively.

The energy spread on the other hand can grow due to the energy fluctuations of the scattered photons, but is also damped in a storage ring. The scaling of the minimum energy spread at equilibrium [42]

$$\left(\frac{\sigma_\gamma}{\gamma} \right)_{\min} = \sqrt{\frac{7}{5} \frac{\lambda_c}{\lambda_0} \gamma_0} \quad (5.66)$$

is proportional to $\sqrt{\gamma}$ and for moderate electron energies at 100 MeV the energy spread can be already as high as 2.6%.

Although the physics of the cooling process is straight forward and well-known, the technical realization of such an electron cooling concept is challenging and has not been realized yet. Especially the average power requirements of the required laser system are demanding. Also the energy spread issue prevents many interesting applications such as free-electron lasers that require electron beams with both small emittance and small energy spread.

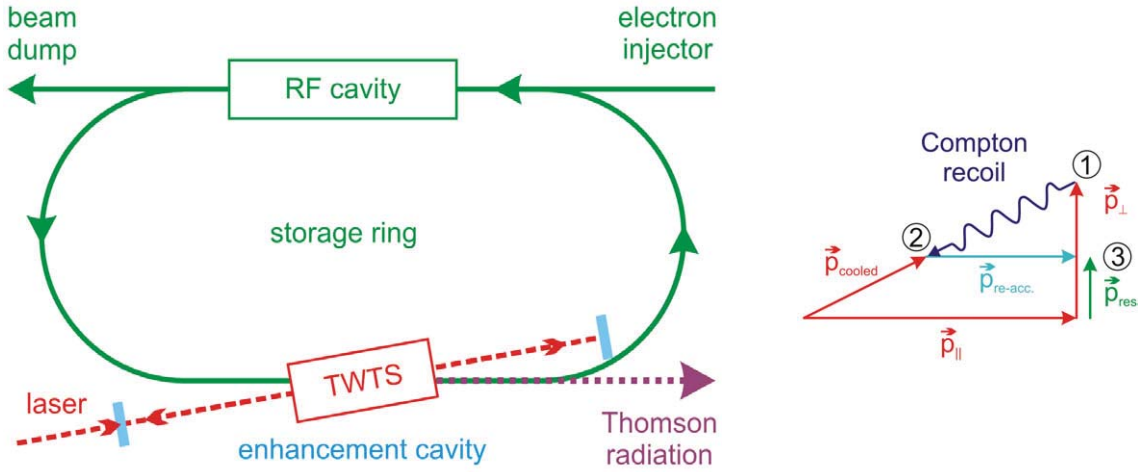


Figure 5.15: An electron beam is circulating in a storage ring. A laser beam in a TWTS scattering geometry oscillates in a power enhancement cavity and requires TWTS-specific dispersive elements inside the cavity. By Compton/Thomson scattering (1 \rightarrow 2) the individual electrons are decelerated opposite their direction of propagation. In the RF cavity, all electrons are re-accelerated (2 \rightarrow 3) into the common forward direction. The result is a reduction in transverse momentum of the individual electrons. Over many round trips, this leads to a cooling effect of the electrons from reduction of transverse momenta.

This problem is analogous to efficient Thomson sources, where high photon yields are limited by the requirement of non-relativistic intensities $a_0 \ll 1$ and the Rayleigh limit $L_{int} \leq 2 \cdot Z_0$.

Sufficiently low intensities and long interaction lengths are again achieved with ultrashort lasers by using small interaction diameters and long interaction lengths, so it is possible to increase E_L and decrease w_0 in (5.64) without approaching laser strengths a_0 near unity. Scattering at small angles ϕ becomes especially useful at a later stage of cooling, when the cooling process has decreased emittance to a level where both the electron focus and the laser waist w_0 can be reduced. In (5.64) to (5.66) the effective laser wavelength becomes $\lambda_0 \rightarrow \lambda_0 \cdot 2/(1 - \beta_0 \cos \phi)$, so in the limit of small angles $\phi \ll 1$

$$n_d = \frac{E}{(\Delta E)_\gamma} \simeq \frac{5.0 \times 10^{-4} \lambda_0 [\mu\text{m}] w_0^2 [\mu\text{m}]}{E_L [\text{J}] E [\text{MeV}]} \cdot \frac{4}{\phi^2} \quad (5.67)$$

$$\varepsilon_{n,\min} = \frac{3}{10} \frac{\lambda_c}{\lambda_0} \beta_{x,y}^* \cdot \frac{\phi^2}{4} \quad (5.68)$$

$$\left(\frac{\sigma_\gamma}{\gamma} \right)_{\min} = \sqrt{\frac{7}{5} \frac{\lambda_c}{\lambda_0}} \gamma_0 \cdot \frac{\phi}{2}, \quad (5.69)$$

the final limits on transverse emittance and energy spread are considerably decreased. One of the main technical challenges in realizing a TWTS scenario inside a power enhancement cavity is the reduction of intensity losses within the dispersive elements of TWTS.

In these examples it has become apparent, that the methods presented here in the framework of traveling-wave Thomson scattering can go far beyond the originally intended goal and could possibly open up interesting experiments and applications in other fields. The next major step in developing the technology for these applications is to demonstrate TWTS-type laser beams in experiment.

6 CONCLUSIONS

In this work the use of laser wakefield accelerated electrons and optical undulators for brilliant radiation sources was explored both in experiment and theory.

The ultrashort duration of laser-wakefield accelerated electron bunches, which is an essential requirement for brilliant X-ray sources was confirmed in an experiment at the ASTRA laser (500 mJ, 45 fs) at RAL for the first time in an experiment to be shorter than the laser pulse and comparable to the plasma period. The duration of these laser-accelerated electron bunches was determined by electro-optic measurements of coherent transition radiation to be 32 fs (FWHM) at the best fit with an upper confidence limit at 38 fs. Due to this ultrashort bunch duration, these low-emittance electron beams are attractive for use in table-top-scale undulators as a potential driver of compact, synchrotron source or free-electron lasers (FEL). Such an application of laser-accelerated electron beams as a synchrotron radiation source was then demonstrated in a first proof-of-principle experiment at the JETI laser (430 mJ, 85 fs) in Jena.

Theoretical investigations targeted the potential and scalability of optically driven X-ray sources at keV and MeV photon energies from Thomson scattering at ultrashort electron bunches using high-power lasers. For optimization, a general radiation code CLARA (*CL*assical *RA*diation Code) was created that in combination with a particle tracker takes into account all non-ideal effects from overlap, phase-space, space-charge as well as ponderomotive effects. This code was consequently used to optimize for high scattered photon fluxes from both low-intensity, high-repetition and high-power, single shot laser systems. Hereby, high-power lasers in traditional, head-on Thomson scattering geometries were found to have severe scaling limitations due to the finite Rayleigh length, when aiming for small bandwidth and high-photon yields on a single shot basis.

As a consequence, an alternative Thomson scattering setup that entirely avoids the Rayleigh length limitation became necessary and it was discovered that this is indeed possible by using a line-focused, side-scattering geometry with tilted laser pulse fronts. This novel traveling-wave Thomson scattering (TWTS) scheme was established from the fact that the laser pulse needs to achieve the target beam properties only at time and position of the interactions with the electrons. The payoff is that both small interaction diameters in the range of micrometers and interaction

lengths up to meters become possible.

Towards experimental realization of such an approach using ultrashort laser pulses, it has been shown that precompensation of higher-order dispersion is essential. Furthermore, it has been shown in theory, that this becomes feasible with grating compressor designs that use varied-line spacing (VLS) gratings, i.e. gratings with a chirp. An extension of the Kostenbauder formalism to higher orders has been provided to analytically calculate and numerically optimize the required VLS spacing functions. The scope of this new technique is not restricted to Thomson sources only – instead it is a general, non-Rayleigh limited scheme for interactions with targets moving close to the speed of light.

For incoherent Thomson sources this novel approach can potentially increase photon yields per shot by several orders of magnitudes. Especially ultrashort, high-power laser systems that are being built in the coming years benefit from the new technique. Furthermore, the additional flexibility through the interaction angle in the TWTS geometry leads to tunability of the scattered photon energy even for electron beams with no adjustability in energy.

Coherent X-ray sources could become possible. Since, interaction lengths with at the same time small diameters can be so long, such that the radiation field amplitude becomes large enough to significantly act back onto the electrons, the regime of optically driven SASE-FELs seems attainable – even for sub-relativistic laser field strengths $a_0 \ll 1$.

In summary, this work has shown that ultrashort, high-power lasers can provide both, sources of ultrashort electron bunches and optical undulators that are truly scalable in length. Laser-accelerated electrons can be combined with magnetic undulators and conventional electron beams go together with optical undulators. Ultimately however, this provides a foundation for a compact, all-optical radiation source that integrates both a laser-wakefield accelerator and an optical undulator for hard X-rays of high brilliance.

On the medium time scale of a decade, ultrashort, monochromatic and intense, hard X-ray beams of a small source size from novel radiation sources, such as incoherent undulator and Thomson radiation by LWFA, table-top FELs or optical FELs, have a broad applicability with regard to structure analysis [1, 2], pump probe experiments [3, 4] and imaging [5, 6]. Such advanced radiation sources are of special interest to life science, material sciences, medicine and semiconductor industries.

The idea of a quantum FEL (QFEL) [7, 8], however, is more of a long shot that drives basic research. It relies on the classical FEL resonance ρmc^2 becoming more narrow in energy than the resulting photon energy $\hbar\omega_r$. As a result quantum effects become relevant and allow only one energy transition. This leads to each electron emitting a single photon at the same energy, so the resulting spectrum consists of a single line, whose width is Fourier limited $(\Delta\omega/\omega_r) = \lambda_r/L_{\text{bunch}}$. In contrast to a classical SASE-FEL, where the beam consists of many different frequency modes around the resonant frequency, a QFEL contains a single mode and thus is truly coherent in time. There are daunting requirements with regard to both undulators – magnetic undulators would need to be **km** long – and electron bunches, which require relative energy spreads below 10^{-4} . Here, TWTS could provide compact optical undulators with long interaction lengths and be a driver for electron cooling technology to improve electron beam parameters.

Likewise on a longer term perspective, brilliant, hard X-ray beams could be even used to probe the vacuum, when perturbed by intense counter-propagating laser beams on the petawatt scale and above [9]. Quantum electrodynamics predicts that the QED vacuum dressed by an intense field becomes birefringent and thus introduces a small ellipticity in the polarization of an X-ray beam passing this region. Using a sufficiently intense X-ray pulse from Thomson scattering, this change could be measured.

Since its discovery [10] fifty years ago, lasers have become an indispensable tool for science and engineering. Numerous applications ranging from fundamental science, over medicine to entertainment have emerged and now permeate everyday life. In the last decade, an amazing drive in laser technology towards higher intensities has given access to the field of relativistic optics, where the laser light has become intense enough to accelerate particles to relativistic energies. Now, the vision is to realize table-top accelerator technology using lasers and make it available to scientists and engineers across all fields. Since brilliant electron and X-ray beams are both window and scalpel on the spatial and temporal scale of atoms and molecules, applications for these “dream beams” extend from the life sciences to semi-conductor industry. One can only guess what the advances of the next five decades will be, but most certainly lasers are continuing to surprise and their future is bright.

A RAY-TRACING OF VLS GRATINGS

The Kostenbauder formalism [1–4] is a first order theory for arbitrary optical systems using matrices to describe the mapping of input to output rays and thus the beam characteristics. All rays are denoted relative to a central ray as position, angle, time and frequency deviations x_{in} , θ_{in} , Δt_{in} , $\Delta \nu$. An optical system, which can be optical elements like mirrors or gratings, empty space or comprise an entire optics arrangement, is formally parameterized by an input and output plane that are connected by a mapping between the rays entering at the input plane and the rays exiting at the output plane. These planes can in principle be chosen arbitrarily for analytical convenience, do not need to be parallel to one another and can also intersect. This approach is especially useful when the aforementioned mapping constitutes a linear transform, which makes it straightforward to chain several optics elements one after another to form a combined optical system that is again described by a linear mapping of ray coordinates. From a practical point of view, the Kostenbauder formalism is useful for quickly extending calculations to optical setups consisting of many different optical elements. From a theoretical point of view the formalism is at the intersection between geometrical optics and wave optics, since the matrices considered here describe geometrical optics, but can also be used as a point-to-point eikonal in a integral formulation of Fermat's principle, such as the Kirchhoff integral [1, 5], to extend to a wave-optics description. This derivation shows how this Kostenbauder formalism can be extended to include VLS-gratings.

In general a Kostenbauder matrix

$$\begin{pmatrix} x_{out} \\ \theta_{out} \\ \Delta t_{out} \\ \Delta \nu \end{pmatrix} = \underbrace{\begin{pmatrix} \frac{\partial x_{out}}{\partial x_{in}} & \frac{\partial x_{out}}{\partial \theta_{in}} & 0 & \frac{\partial x_{out}}{\partial \Delta \nu} \\ \frac{\partial \theta_{out}}{\partial x_{in}} & \frac{\partial \theta_{out}}{\partial \theta_{in}} & 0 & \frac{\partial \theta_{out}}{\partial \Delta \nu} \\ \frac{\partial \Delta t_{out}}{\partial x_{in}} & \frac{\partial \Delta t_{out}}{\partial \theta_{in}} & 1 & \frac{\partial \Delta t_{out}}{\partial \Delta \nu} \\ 0 & 0 & 0 & 1 \end{pmatrix}}_{\mathbf{M}} \cdot \begin{pmatrix} x_{in} \\ \theta_{in} \\ \Delta t_{in} \\ \Delta \nu \end{pmatrix} \quad (\text{A.1})$$

$$\mathbf{M} = \begin{pmatrix} A & B & 0 & E \\ C & D & 0 & F \\ G & H & 1 & I \\ 0 & 0 & 0 & 1 \end{pmatrix} = \begin{pmatrix} \text{spatial magn.} & \text{offset by angle} & 0 & SD \\ \text{focus} & \text{angular magn.} & 0 & AD \\ \text{pulse front tilt} & \text{time-angle} & 1 & GDD \\ 0 & 0 & 0 & 1 \end{pmatrix} \quad (\text{A.2})$$

consists of constant first order derivatives, which is a valid assumption for small changes in the ray coordinates. For plane waves the matrix elements of \mathbf{M} have direct physical meanings, such as spatial magnification for element A or group delay dispersion (GDD) for element I . The zero elements arise from assuming stationary (i.e. time-invariant) optical elements without frequency conversion. Furthermore, it can be shown [1], that in a first-order theory only six matrix elements are independent of each other. Therefore there exist three additional relations

$$\begin{aligned} AD - BC &= 1 \\ BF - ED &= \lambda_0 H \\ AF - EC &= \lambda_0 G \end{aligned} \quad (\text{A.3})$$

between the nine non-zero elements. Other dispersion phenomena, such as the pulse front tilt (PFT) directly depend on these six dispersion quantities, so that in this framework the pulse front tilt by angular dispersion is defined as

$$\begin{aligned} PFT &\equiv c \frac{\partial \Delta t}{\partial x_{in}} \frac{\partial x_{in}}{\partial x_{out}} \\ &= \frac{cG}{A} = \frac{c(AF - EC)}{\lambda_0 A} \\ &= \frac{cF}{\lambda_0}, \text{ for } C=0 \text{ in collimated beams,} \end{aligned} \quad (\text{A.4})$$

where the last relation in (A.3) is used.

In the following it is shown how this formalism has to be extended for VLS gratings, where the spatial variation in the grating period leads to non-negligible higher order terms in the ray coordinate x_{in} .

For a general, planar VLS grating it is necessary to derive the behavior of spatially displaced rays and include the position dependency in all other relations involving the grating constant. As shown in Fig. A.1 the ray displaced by a distance x_{in} hits the VLS grating at the grating surface coordinate $s = \overline{AB} = -x_{in}/\cos \psi_{in}$, which determines a diffraction angle $\psi_{out}(x_{in})$ different from the central ray outgoing angle $\psi_{out,0}$. The two reference planes represent the wavefront of the incoming and outgoing beam. All changes to the ray characteristics have to be considered relative to the central ray and its reference planes. Thus the resulting spatial displacement with respect to the central ray is the distance \overline{AC} and the temporal delay is the difference $(\overline{DB} - \overline{BC})/c$. Using Fig. A.1 one finds for the angles $\alpha = \psi_{out,0}$, $\beta = \pi/2 - \psi_{out}(x_{in})$ and $\gamma = \pi/2 - (\psi_{out,0} - \psi_{out}(x_{in}))$.

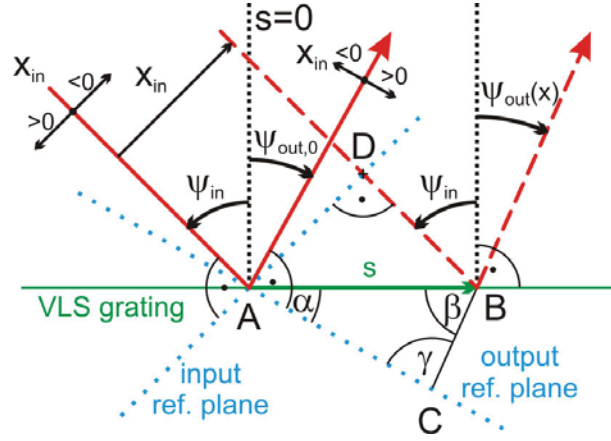


Figure A.1: Two rays (red), spatially displaced by $x_{in} = -s \cdot \cos \psi_{in}$, are incident on a varied-line spacing (VLS) grating (green). Due to the varying line spacing of the grating the ray incident at **B** is deflected at a different angle $\Psi_{out}(x_{in})$ than at **A**.

After applying the law of sines, one arrives at

$$A(x_{in}) \cdot x_{in} = \overline{AC} = -\frac{\cos \psi_{out}(x_{in})}{\cos(\psi_{out,0} - \psi_{out}(x_{in}))} \cdot \frac{x_{in}}{\cos \psi_{in}} \quad (A.5)$$

$$G(x_{in}) \cdot x_{in} = (\overline{DB} - \overline{BC})/c = \frac{\sin \psi_{out,0}}{\cos(\psi_{out,0} - \psi_{out}(x_{in}))} \cdot \frac{x_{in}}{c \cdot \cos \psi_{in}}. \quad (A.6)$$

In contrast to uniformly spaced grating, VLS gratings have focusing properties because the outgoing angle ψ_{out} changes with the incident position on the grating surface, hence

$$C(x_{in}) \cdot x_{in} = \psi_{out,0} - \psi_{out}(x_{in}). \quad (A.7)$$

The angular magnification $D(x_{in}) = \partial \theta_{out} / \partial \theta_{in}$ and the angular dispersion $F(x_{in}) = \partial \theta_{out} / \partial \Delta \nu_{in}$ are both derivatives of the grating equation.

$$D(x_{in}) = -\frac{\partial \psi_{out}(x_{in})}{\partial \psi_{in}} \quad (A.8)$$

$$AD(x_{in}) = F(x_{in}) = -\frac{\partial \psi_{out}(x_{in})}{\partial \nu} \quad (A.9)$$

As in the linear case [1], the matrix elements B, E, H and I are zero, because rays reflect at the grating surface without time delay or spatial displacement. The remaining matrix elements can be obtained by substituting the custom grating spacing function

$$d(s) = d_0 + a_g \lambda_0 s + b_g \lambda_0 s^2, \quad (A.10)$$

which is chosen to be a second order polynomial into the grating equation

$$\psi_{out}(x_{in}) = \arcsin(c/(\nu \cdot d(x_{in}/\cos \psi_{in})) + \sin \psi_{in}), \quad (A.11)$$

and by inserting the result into eqs. (A.5) to (A.9).

Finally, all matrix elements are expanded to the first order in a Taylor series around $x_{in} = 0$, so one arrives at:

$$\begin{aligned}
A(x_{in}) &= -\cos \psi_{out} / \cos \psi_{in} \\
&\quad + a_g x_{in} \tan \psi_{out} \cdot (\tan \psi_{in} - \sin \psi_{out} / \cos \psi_{in})^2 \\
C(x_{in}) &= -a_g \frac{(\sin(\psi_{in}) - \sin(\psi_{out}))^2}{\cos(\psi_{in}) \cos(\psi_{out})} \\
&\quad + x_{in} (4b_g + 4b_g \cos(2\psi_{out}) + 8a_g^2 \sin(\psi_{in}) - a_g^2 \sin(2\psi_{in} - \psi_{out}) \\
&\quad \quad - 7a_g^2 \sin \psi_{out} - a_g^2 \sin(3\psi_{out}) + a_g^2 \sin(2\psi_{in} + \psi_{out})) \\
&\quad \cdot (\tan \psi_{in} - \sin \psi_{out} / \cos \psi_{in})^2 / (8 \cos^3 \psi_{out}) \\
D(x_{in}) &= -\cos \psi_{in} / \cos \psi_{out} - a_g x_{in} (\cos^2 \psi_{out} \sin \psi_{in} + \cos^2 \psi_{in} \sin \psi_{out}) \\
&\quad \cdot (\tan \psi_{in} - \sin \psi_{out} / \cos \psi_{in})^2 / \cos^3 \psi_{out} \\
F(x_{in}) &= (\lambda_0 / c (\tan \psi_{out} - \sin \psi_{in} / \cos \psi_{out})) \\
&\quad - a_g x_{in} \lambda_0 / c (\sin \psi_{in} - \sin \psi_{out})^2 \\
&\quad \cdot (\sin \psi_{in} \sin \psi_{out} - 1) / (\cos \psi_{in} \cos^3 \psi_{out}) \\
G(x_{in}) &= (-\sin \psi_{out} / \cos \psi_{in} + \tan \psi_{in}) / c
\end{aligned} \tag{A.12}$$

The Taylor-expansion is justified on practical grounds, because the grating chirps are in most cases gradual and of non-oscillatory nature. As a result the matrix becomes a nonlinear vector function

$$\mathbf{v}_{out} = \mathbf{O}_{VLS}(\mathbf{v}_{in}), \tag{A.13}$$

which operates on input ray vectors $\mathbf{v}_{in} = (x_{in}, \theta_{in}, \Delta t_{in}, \Delta \nu)$. Because the nonlinearity of \mathbf{O}_{VLS} exists only in the spatial displacement coordinate x_{in} , it remains linear in the other coordinates. Thus locally, the structure of the new operator still corresponds to a Kostenbauder matrix as in eq. (A.1),

$$\begin{aligned}
x_{out}(x_{in}, \theta_{in}, \Delta \nu) &= A(x_{in}) \cdot x_{in} + B(x_{in}) \cdot \theta_{in} + E(x_{in}) \cdot \Delta \nu \\
\theta_{out}(x_{in}, \theta_{in}, \Delta \nu) &= C(x_{in}) \cdot x_{in} + D(x_{in}) \cdot \theta_{in} + F(x_{in}) \cdot \Delta \nu \\
\Delta t_{out}(x_{in}, \theta_{in}, \Delta t_{in}, \Delta \nu) &= G(x_{in}) \cdot x_{in} + H(x_{in}) \cdot \theta_{in} \\
&\quad + \Delta t_{in} + I(x_{in}) \cdot \Delta \nu \\
\Delta \nu &= \Delta \nu_{in} = \Delta \nu_{out} \\
\text{here: } B(x_{in}) &= E(x_{in}) = H(x_{in}) = I(x_{in}) = 0.
\end{aligned} \tag{A.14}$$

In the limit of uniform gratings, i.e. a_g and $b_g \rightarrow 0$, (A.14) assumes as expected the usual form

of a Kostenbauder matrix for a standard grating

$$\mathbf{M}_g = \begin{pmatrix} -\frac{\cos \psi_{out}}{\cos \psi_{in}} & 0 & 0 & 0 \\ 0 & -\frac{\cos \psi_{in}}{\cos \psi_{out}} & 0 & \frac{\lambda_0(\sin \psi_{out} - \sin \psi_{in})}{c \cos \psi_{out}} \\ \frac{\sin \psi_{in} - \sin \psi_{out}}{c \cos \psi_{in}} & 0 & 1 & 0 \\ 0 & 0 & 0 & 1 \end{pmatrix}. \quad (\text{A.15})$$

For the optical setup of chapter 5, in which a laser from an arbitrary stretcher-compressor system reflects off a VLS grating and propagates further to the interaction zone, the operators have to be successively applied to the input rays

$$\mathbf{v}_{out} = \mathbf{M}_p(\overline{\mathbf{AB}}) \cdot \mathbf{O}_{VLS}(\psi_{in}, \psi_{out}, b_g) (\mathbf{M}_{gen}(SD, GDD) \cdot \mathbf{v}_{in}), \quad (\text{A.16})$$

where the second factor in (A.16) denotes the nonlinear part of the system that operates on non-delayed, collimated input rays $\mathbf{v}_{in} = (x_{in}, \theta_{in} = 0, \Delta t_{in} = 0, \Delta\nu)$. The matrix \mathbf{M}_{gen} represents the first order or the Kostenbauder matrix for a generic stretcher-compressor system, as depicted by Fig. 5.8, that introduces a defined group delay dispersion (GDD) and spatial dispersion (SD).

$$\mathbf{M}_{gen}(SD, GDD) = \begin{pmatrix} 1 & 0 & 0 & SD \\ 0 & 1 & 0 & 0 \\ 0 & -SD & 1 & GDD \\ 0 & 0 & 0 & 1 \end{pmatrix} \quad (\text{A.17})$$

The Kostenbauder matrix for free space propagation $\mathbf{M}_p(L)$ is denoted by

$$\mathbf{M}_p(L) = \begin{pmatrix} 1 & L & 0 & 0 \\ 0 & 1 & 0 & 0 \\ 0 & 0 & 1 & 0 \\ 0 & 0 & 0 & 1 \end{pmatrix}. \quad (\text{A.18})$$

Note, that in general the combined operator expression of (A.16) does not solely depend on the input displacement x_{in} , but rather all input ray coordinates. Thus for a collimated input beam $(\Delta x_{in}, 0, 0, \Delta\nu)$ the output beam components $(x_{out}(x_{in}, \Delta\nu), \theta_{out}(x_{in}, \Delta\nu), \Delta t_{out}(x_{in}, \Delta\nu), \Delta\nu)$ in this example denote higher order polynomials in x_{in} and $\Delta\nu$, with the coefficients being functions of the setup parameters, such as the distances, angles and grating chirps.

When designing optical systems using VLS gratings, it is useful to reduce the complexity of the grating function, such that at a given order it modifies only one matrix element. According

to (A.12) the lowest order is exclusively affected by a linear chirp a_g that modifies the focusing element

$$C(x_{in}) = -a_g \frac{(\sin(\psi_{in}) - \sin(\psi_{out}))^2}{\cos(\psi_{in}) \cos(\psi_{out})} + \mathcal{O}(x_{in}). \quad (\text{A.19})$$

The corresponding effective focusing distance f_{eff} can be derived, by calculating in first order the distance a ray requires to propagate to the beam center.

$$\begin{aligned} (C_0 \cdot f_{\text{eff}} + A_0) \cdot x_{in} &= 0 \\ \Rightarrow f_{\text{eff}} &= \frac{-\cos^2 \psi_{out}}{a_g(\sin \psi_{in} - \sin \psi_{out})^2} \end{aligned} \quad (\text{A.20})$$

However, a_g has to remain zero, since focusing the beam is not the goal in this work. Instead, the lowest order behavior of a quadratic grating chirp b_g becomes important. Of all matrix elements, only

$$C(x_{in}) = x_{in} \underbrace{(4b_g + 4b_g \cos(2\psi_{out})) \cdot \frac{(\tan \psi_{in} - \sin \psi_{out} / \cos \psi_{in})^2}{8 \cos^3 \psi_{out}}}_{C_1} + \mathcal{O}(x_{in}^2) \quad (\text{A.21})$$

is modified, such that it is proportional to x_{in} . In chapter 5, that property is exploited in spatially chirped beams to introduce an additional angular dispersion, that varies linearly across the beam diameter. According to (A.1) and (A.17), the angular dispersion of (A.16) yields

$$F_{\text{gen+VLS}} = 1 \cdot F_{\text{VLS}} + E_{\text{gen}} \cdot C_{\text{VLS}} + 0 \cdot D_{\text{VLS}} \quad (\text{A.22})$$

$$\Rightarrow AD(x_{in}) = AD_0 + \underbrace{SD_0 C_1}_{AD_1 = \text{const.}} \cdot x_{in}, \quad (\text{A.23})$$

for quadratic line spacing gratings as in (A.10). Accordingly, if such a beam propagates over a distance ΔL , this leads to the desired linear variation of spatial dispersion

$$SD(x_{in}) = SD_0 + \Delta L \cdot (AD_0 + AD_1 x_{in}) \quad (\text{A.24})$$

across the laser beam diameter.

BIBLIOGRAPHY FOR CHAPTER 1

- [1] T. H. Maiman, "Stimulated Optical Radiation in Ruby," *Nature* **187**, 493–494 (Aug. 1960), pp. 1 and 139.
- [2] D. Strickland and G. Mourou, "Compression of amplified chirped optical pulses," *Optics Communications* **56**, 219–221 (Dec. 1985), p. 1.
- [3] M. D. Perry and G. Mourou, "Terawatt to petawatt subpicosecond lasers," *Science* **264**, 917–924 (1994), p. 1.
- [4] T. Guo, "More power to x-rays: New developments in x-ray spectroscopy," *Laser & Photonics Rev.* **3**, 591–622 (2009), pp. 1 and 138.
- [5] W. P. Leemans, R. W. Schoenlein, P. Volfbeyn, A. H. Chin, T. E. Glover, P. Balling, M. Zolotarev, K. J. Kim, S. Chattopadhyay, and C. V. Shank, "X-ray based subpicosecond electron bunch characterization using 90° Thomson scattering," *Phys. Rev. Lett.* **77**, 4182–4185 (1996), pp. 1 and 32.
- [6] G. L. Sage, S. Anderson, T. Cowan, J. Crane, T. Ditmire, and J. Rosenzweig, "Development of an RF photoinjector for relativistic thomson scattering short-pulse x-ray source," *AIP Conf. Proc.* **569**, 391 (2001), p. 1.
- [7] D. Gibson, S. Anderson, C. Barty, S. Betts, R. Booth, W. Brown, J. Crane, R. Cross, D. Fittinghoff, F. Hartemann, J. Kuba, G. Le Sage, D. Slaughter, A. Tremaine, A. Wootton, E. Hartouni, P. Springer, and J. Rosenzweig, "PLEIADES: A picosecond Compton scattering x-ray source for advanced backlighting and time-resolved material studies," *Phys. of Plasmas* **11**, 2857–2864 (2004), pp. 1 and 4.
- [8] W. J. Brown, S. G. Anderson, C. P. J. Barty, S. M. Betts, R. Booth, J. K. Crane, R. R. Cross, D. N. Fittinghoff, D. J. Gibson, F. V. Hartemann, E. P. Hartouni, J. Kuba, G. P. Le Sage, D. R. Slaughter, A. M. Tremaine, A. J. Wootton, P. T. Springer, and J. B. Rosenzweig, "Experimental characterization of an ultrafast thomson scattering x-ray source with three-dimensional time and frequency-domain analysis," *Physical Review Special Topics – Accelerators and Beams* **7**, 060702 (2004), p. 1.
- [9] G. Priebe, D. Laundry, L. Jones, G. Diakun, S. Jamison, D. Hodler, P. Phillips, M. Macdonald, S. Smith, G. Hirst, N. Naumova, G. Krafft, F. Hartemann, J. Rosenzweig, F. Grüner, R. Beach, U. Schramm, S. Chattopadhyay, and E. Seddon, "Inverse Compton backscattering source driven by the multi 10 TW-laser installed at Daresbury," *Laser and Particle Beams* **26**, 649–660 (2008), p. 1.
- [10] E. Esarey, C. B. Schroeder, and W. P. Leemans, "Physics of laser-driven plasma-based electron accelerators," *Reviews of Modern Physics* **81**, 1229–1285 (2009), pp. 1, 2, 3, 37, 40, and 50.
- [11] W. Leemans and E. Esarey, "Laser-driven plasma-wave electron accelerators," *Physics Today* **62**, 44 (2009), p. 1.

- [12] H. Schwöerer, B. Liesfeld, H. Schlenvoigt, K. Amthor, and R. Sauerbrey, "Development of an RF photoinjector for relativistic thomson scattering short-pulse x-ray source," *Phys. Rev. Lett.* **96**, 014820 (2006), pp. 1 and 65.
- [13] F. V. Hartemann, D. J. Gibson, W. J. Brown, A. Rousse, K. T. Phuoc, V. Malka, J. Faure, and A. Pukhov, "Compton scattering x-ray sources driven by laser wakefield acceleration," *Physical Review Special Topics – Accelerators and Beams* **10**, 011301 (2007), p. 1.
- [14] D. A. Jaroszynski, R. Bingham, E. Brunetti, B. Ersfeld, J. Gallacher, B. van Der Geer, R. Issac, S. P. Jamison, D. Jones, A. de Loos, M. Lyachev, V. Pavlov, A. Reitsma, G. Saveliev, Y. Vieux, and S. M. Wiggins, "Radiation sources based on laser-plasma interactions," *Phil. Trans. R. Soc. A* **364**, 689–710 (2006), pp. 1 and 77.
- [15] S. P. D. Mangles, C. D. Murphy, Z. Najmudin, A. G. R. Thomas, J. L. Collier, A. E. Dangor, E. J. Divall, P. S. Foster, J. G. Gallacher, C. J. Hooker, D. A. Jaroszynski, A. J. Langley, W. B. Mori, P. A. Norreys, F. S. Tsung, R. Viskup, B. R. Walton, and K. Krushelnick, "Monoenergetic beams of relativistic electrons from intense laser-plasma interactions," *Nature* **431**, 535 (2004), pp. 1, 2, 42, and 56.
- [16] C. G. R. Geddes, C. Toth, J. Van Tilborg, E. Esarey, C. B. Schroeder, D. Bruhwiler, C. Nieter, J. Cary, and W. P. Leemans, "High-quality electron beams from a laser wakefield accelerator using plasma-channel guiding," *Nature* **431**, 538 (2004), pp. 1, 2, and 42.
- [17] J. Faure, Y. Glinec, A. Pukhov, S. Kiselev, S. Gordienko, E. Lefebvre, J.-P. Rousseau, F. Burgy, and V. Malka, "A laser-plasma accelerator producing monoenergetic electron beams," *Nature* **431**, 541 (2004), pp. 1, 2, and 42.
- [18] W. Leemans, E. Esarey, C. Geddes, C. Schroeder, and C. Tóth, "GeV electron beams from a centimetre-scale accelerator," *Nature Physics* **2**, 696–699 (2006), pp. 1, 3, 46, 77, 79, 106, and 124.
- [19] J. Osterhoff, A. Popp, Zs. Major, B. Marx, T. P. Rowlands-Rees, M. Fuchs, M. Geissler, R. Hörlein, B. Hidding, S. Becker, E. A. Peralta, U. Schramm, F. Grüner, D. Habs, F. Krausz, S. M. Hooker, and S. Karsch, "Generation of Stable, Low-Divergence Electron Beams by Laser-Wakefield Acceleration in a Steady-State-Flow Gas Cell," *Phys. Rev. Lett.* **101**, 085002 (2008), pp. 1, 46, and 126.
- [20] S. Karsch, J. Osterhoff, A. Popp, T. P. Rowlands-Rees, Zs. Major, M. Fuchs, B. Marx, R. Hörlein, K. Schmid, L. Veisz, S. Becker, U. Schramm, B. Hidding, G. Pretzler, D. Habs, F. Grüner, F. Krausz, and S. M. Hooker, "GeV-scale electron acceleration in a gas-filled capillary discharge waveguide," *New Journal of Physics* **9**, 415 (2007), pp. 1, 46, and 126.
- [21] T. Tajima and J.M. Dawson, "Laser electron accelerator," *Phys. Rev. Lett.* **43**, 267–270 (1979), pp. 2 and 37.
- [22] R. Sah, R. P. Johnson, M. Neubauer, M. Conde, W. Gai, A. Moretti, M. Popovic, K. Yonehara, J. Byrd, D. Li, M. Bastaninejad, and M. Elmustafa, "RF Breakdown Studies Using a 1.3-GHz Test Cell," in *Particle Accelerator Conference, PAC'09, Vancouver BC, Canada* (2010) pp. 1–4, p. 2.

- [23] A. Grudiev, S. Calatroni, and W. Wuensch, "New local field quantity describing the high gradient limit of accelerating structures," *Physical Review Special Topics – Accelerators and Beams* **12**, 102001–9 (2009), pp. 2 and 36.
- [24] J. Faure, C. Rechatin, A. Norlin, A. Lifschitz, Y. Glinec, and V. Malka, "Controlled injection and acceleration of electrons in plasma wakefields by colliding laser pulses," *Nature* **444**, 737–9 (Dec. 2006), pp. 2 and 47.
- [25] A. Irman, M. J. H. Luttikhof, A. G. Khachatryan, F. A. van Goor, J. W. J. Verschuur, H. M. J. Bastiaens, and K.-J. Boller, "Design and simulation of laser wakefield acceleration with external electron bunch injection in front of the laser pulse," *Journal of Applied Physics* **102**, 024513 (2007), pp. 2 and 47.
- [26] A. Pukhov and S. Gordienko, "Bubble regime of wake field acceleration: similarity theory and optimal scalings.." *Philosophical transactions. Series A, Mathematical, physical, and engineering sciences* **364**, 623–33 (2006), pp. 3 and 42.
- [27] W. Lu, C. Huang, M. Zhou, M. Tzoufras, F. S. Tsung, W. B. Mori, and T. Katsouleas, "A nonlinear theory for multidimensional relativistic plasma wave wakefields," *Physics of Plasmas* **13**, 056709 (2006), pp. 3, 42, 44, 45, and 47.
- [28] M. Geissler, J. Schreiber, and J. Meyer-ter Vehn, "Bubble acceleration of electrons with few-cycle laser pulses," *New Journal of Physics* **8**, 186 (2006), pp. 3, 42, 45, 47, and 65.
- [29] E. Brunetti, R. Shanks, G. Manahan, M. Islam, B. Ersfeld, M. Anania, S. Cipiccia, R. Issac, G. Raj, G. Vieux, G. Welsh, S. Wiggins, and D. Jaroszynski, "Low Emittance, High Brilliance Relativistic Electron Beams from a Laser-Plasma Accelerator," *Phys. Rev. Lett.* **105**, 3–6 (Nov. 2010), p. 3.
- [30] F. Grüner, S. Becker, U. Schramm, T. Eichner, M. Fuchs, R. Weingartner, D. Habs, J. Meyer-ter Vehn, M. Geissler, M. Ferrario, L. Serafini, B. van der Geer, H. Backe, W. Lauth, and S. Reiche, "Design considerations for table-top, laser-based VUV and x-ray free electron lasers," *Applied Physics B: Lasers and Optics* **86**, 431–435 (Feb. 2007), pp. 4 and 65.
- [31] D. J. Gibson, C. P. J. Barty, S. M. Betts, J. K. Crane, and I. Jovanovic, *Proceedings of the 2005 Particle Accelerator Conference* (IEEE, 2005) pp. 1347–1349, p. 4.
- [32] D. Gibson, F. Albert, S. Anderson, S. Betts, M. Messerly, H. Phan, V. Semenov, M. Shverdin, A. Tremaine, F. Hartemann, C. Siders, D. McNabb, and C. Barty, "Design and operation of a tunable MeV-level Compton-scattering-based γ -ray source," *Physical Review Special Topics – Accelerators and Beams* **13**, 1–12 (Jul. 2010), p. 4.
- [33] E. Esarey, S. K. Ride, and P. Sprangle, "Nonlinear Thomson scattering of intense laser pulses from beams and plasmas," *Phys. Rev. E* **48**, 3003–3021 (Oct. 1993), pp. 4, 31, 33, 34, 82, and 107.

BIBLIOGRAPHY FOR CHAPTER 2

- [1] James A. Clarke, *The Science and Technology of Undulators and Wigglers (Oxford Series on Synchrotron Radiation)* (Oxford University Press, USA, 2004) ISBN 0198508557, p. 244, pp. 8, 11, 16, 75, and 79.
- [2] Walter D. Jackson, *Classical Electrodynamics*, 3rd ed. (John Wiley & Sons, 1999), pp. 11, 32, 53, and 80.
- [3] H. Onuki and P. Elleaume, *Undulators, Wigglers and their Applications* (Taylor and Francis Inc., 2003), pp. 11, 74, 75, and 82.
- [4] David Attwood, *Soft X-Rays and Extreme Ultraviolet Radiation: Principles and Applications* (Cambridge University Press, 1999) ISBN 978-0521029971, p. 504, p. 11.
- [5] J. B. Murphy and C. Pellegrini, "Introduction to the Physics of the Free Electron Laser," in *Frontiers of Particle Beams*, Lecture Notes in Physics, Vol. 296, edited by M. Month and S. Turner (Springer-Verlag, Berlin/Heidelberg, 1988) pp. 163–219, pp. 12, 19, 22, and 24.
- [6] E. L. Saldin, E. V. Schneidmiller, and M. V. Yurkov, *The Physics of Free Electron Lasers* (Springer, 2000) ISBN 3540662669, p. 464, pp. 12, 13, and 27.
- [7] S. Reiche, *Numerical studies for a single pass high gain free-electron laser*, Phd thesis, Universität Hamburg (1999), pp. 12, 27, and 125.
- [8] C. Pellegrini and S. Reiche, "The Development of X-Ray Free-Electron Lasers," *IEEE Journal of Selected Topics in Quantum Electronics* **10**, 1393–1404 (2004), pp. 12 and 113.
- [9] John M. J. Madey, "Stimulated emission of bremsstrahlung in a periodic magnetic field," *Journal of Applied Physics* **42**, 1906–1913 (1971), p. 13.
- [10] F. A. Hopf, P. Meystre, M. O. Scully, and W. H. Louisell, "Classical theory of a free-electron laser," *Phys. Rev. Lett.* **37**, 1215–1218 (1976), p. 13.
- [11] C. Maroli, V. Petrillo, and M. Ferrario, "One-dimensional free-electron laser equations without the slowly varying envelope approximation," *Physical Review Special Topics – Accelerators and Beams* **14**, 1–7 (Jul. 2011), p. 21.
- [12] R. Bonifacio, C. Pellegrini, and L. M. Narducci, "Collective instabilities and high-gain regime in a free electron laser," *Optics Communications* **50**, 373–378 (1986), pp. 22 and 113.
- [13] R. Bonifacio, F. Casagrande, and C. Pellegrini, "Hamiltonian model of a free electron laser," *Optics Communications* **61**, 55–60 (Jan. 1987), p. 22.
- [14] Paul Gibbon, *Short Pulse Laser Interactions with Matter: An Introduction* (World Scientific Pub Co, 2005) ISBN 978-1860941351, pp. 29, 31, 37, 40, and 42.
- [15] E. S. Sarachik and G. T. Schappert, "Classical Theory of the Scattering of Intense Laser Radiation by Free Electrons," *Physical Review D* **1**, 2738 (1970), pp. 29 and 31.
- [16] E. Esarey, S. K. Ride, and P. Sprangle, "Nonlinear Thomson scattering of intense laser pulses from beams and plasmas," *Phys. Rev. E* **48**, 3003–3021 (Oct. 1993), pp. 4, 31, 33, 34, 82, and 107.

- [17] S. K. Ride, E. Esarey, and M. Baine, "Thomson scattering of intense lasers from electron beams at arbitrary interaction angles," *Physical Review E* **52**, 5425–5442 (Oct. 1995), pp. 31 and 34.
- [18] Y. Y. Lau, F. He, D. P. Umstadter, and Kowalczyk R., "Nonlinear Thomson scattering: A tutorial," *Physics of Plasmas* **10**, 2155 (2003), pp. 31 and 34.
- [19] A. Debus, S. Bock, M. Bussmann, T. E. Cowan, A. Jochmann, T. Kluge, S. D. Kraft, R. Sauerbrey, K. Zeil, and U. Schramm, "Linear and Non-Linear Thomson-Scattering X-Ray Sources Driven by Conventionally and Laser Plasma Accelerated Electrons," *Proc. of SPIE* **7359**, 735908 (2009), pp. 31, 65, and 107.
- [20] D. Seipt and B. Kämpfer, "Scaling law for the photon spectral density in the nonlinear Thomson-Compton scattering," *Physical Review Special Topics – Accelerators and Beams* **14**, 040704 (2011), pp. 31 and 34.
- [21] D. Seipt and B. Kämpfer, "Nonlinear Compton scattering of ultrashort intense laser pulses," *Physical Review A* **83**, 1–12 (Feb. 2011), pp. 31 and 34.
- [22] W. P. Leemans, R. W. Schoenlein, P. Volfbeyn, A. H. Chin, T. E. Glover, P. Balling, M. Zolotarev, K. J. Kim, S. Chattopadhyay, and C. V. Shank, "X-ray based subpicosecond electron bunch characterization using 90° Thomson scattering," *Phys. Rev. Lett.* **77**, 4182–4185 (1996), pp. 1 and 32.
- [23] O. Klein and T. Nishina, "Über die Streuung von Strahlung durch freie Elektronen nach der neuen relativistischen Quantendynamik von Dirac," *Zeitschrift für Physik* **52**, 853–868 (Nov. 1929), p. 32.
- [24] W. Heitler, *The Quantum Theory of Radiation*, 3rd ed. (Dover Publications, 1954) ISBN 0486645584, p. 464, p. 32.
- [25] D. D. Meyerhofer, "High-intensity-laser-electron scattering," *IEEE Journal of Quantum Electronics* **33**, 1935–1941 (1997), ISSN 00189197, p. 32.
- [26] P. Luchini and H. Motz, *Undulators and Free-electron Lasers (International Series of Monographs on Physics)* (Oxford University Press, USA, 1990) ISBN 0198520190, p. 336, p. 33.
- [27] T. Heinzl, D. Seipt, and B. Kämpfer, "Beam-shape effects in nonlinear Compton and Thomson scattering," *Physical Review A* **81**, 1–17 (Feb. 2010), p. 34.
- [28] T. Eichner, F. Grüner, S. Becker, M. Fuchs, D. Habs, R. Weingartner, U. Schramm, H. Backe, P. Kunz, and W. Lauth, "Miniature magnetic devices for laser-based, table-top free-electron lasers," *Physical Review Special Topics – Accelerators and Beams* **10**, 1–9 (2007), p. 35.
- [29] A. Mikhailichenko, *Proceedings of the 2005 Particle Accelerator Conference* (IEEE, 2005) pp. 3676–3678, p. 35.
- [30] K. L. F. Bane, "Wakefields of sub-picosecond electron bunches," *International Journal of Modern Physics A* **22**, 3736–3758 (2007), p. 35.
- [31] Karl L. F. Bane and Matthew Sands, *The Short-Range Resistive Wall Wakefields*, Tech. Rep. AP-87 (SLAC Report, 1991), p. 35.

- [32] O. Henry and O. Napoly, "The resistive pipe wake potentials for short bunches," Part. Accel **35**, 235–248 (1991), p. 35.
- [33] J. D. Lawson, "Radiation from a ring charge passing through a resonator," Part. Accel **25**, 107–112 (1990), p. 35.
- [34] Helmut Wiedemann, *Particle Accelerator Physics*, 3rd ed. (Springer-Verlag Berlin Heidelberg, 2007), pp. 36, 74, 132, and 135.
- [35] A. Grudiev, S. Calatroni, and W. Wuensch, "New local field quantity describing the high gradient limit of accelerating structures," Physical Review Special Topics – Accelerators and Beams **12**, 102001–9 (2009), pp. 2 and 36.
- [36] A. Büchner, H. Büttig, M. Justus, U. Lehnert, P. Michel, C. Schneider, G. Staats, and J. Teichert, "Experiences with TESLA cavities in CW-operations at ELBE," Proceedings of ERL07, 62–64(2007), p. 36.
- [37] J.D. Lawson, "Lasers and accelerators," IEEE Trans. Nuc. Sci. **26**, 4217–4219 (1979), p. 37.
- [38] P.M. Woodward, "A method of calculating the field over a plane.." J. Inst. Electr. Eng. **93**, 1554–1558 (1947), p. 37.
- [39] E. Esarey, C. B. Schroeder, and W. P. Leemans, "Physics of laser-driven plasma-based electron accelerators," Reviews of Modern Physics **81**, 1229–1285 (2009), pp. 1, 2, 3, 37, 40, and 50.
- [40] G. Malka, E. Lefebvre, and J. Miquel, "Experimental Observation of Electrons Accelerated in Vacuum to Relativistic Energies by a High-Intensity Laser," Phys. Rev. Lett. **78**, 3314–3317 (Apr. 1997), p. 37.
- [41] P. Musumeci, S. Tochitsky, S. Boucher, C. Clayton, A. Doyuran, R. England, C. Joshi, C. Pellegrini, J. Ralph, J. Rosenzweig, C. Sung, S. Tolmachev, G. Travish, A. Varfolomeev, A. Varfolomeev, T. Yarovoi, and R. Yoder, "High Energy Gain of Trapped Electrons in a Tapered, Diffraction-Dominated Inverse-Free-Electron Laser," Phys. Rev. Lett. **94**, 1–4 (Apr. 2005), p. 37.
- [42] T. Tajima and J.M. Dawson, "Laser electron accelerator," Phys. Rev. Lett. **43**, 267–270 (1979), pp. 2 and 37.
- [43] A. Modena, Z. Najmudin, AE Dangor, CE Clayton, KA Marsh, C. Joshi, V. Malka, CB Darrow, C. Danson, D. Neely, and Others, "Electron acceleration from the breaking of relativistic plasma waves," Nature **377**, 606–608 (1995), p. 37.
- [44] Eric Esarey and Mark Pilloff, "Trapping and acceleration in nonlinear plasma waves," Physics of Plasmas **2**, 1432–1436 (1995), p. 40.
- [45] L. M. Gorbunov and V. I. Kirsanov, "The excitation of plasma waves by an electromagnetic wave packet," Sov. Phys. JETP **66**, 290–4 (1987), p. 40.
- [46] P. Sprangle, E. Esarey, A. Ting, and G. Joyce, "Laser wakefield acceleration and relativistic optical guiding," Appl. Phys. Lett. **46**, 2146–2148 (1988), p. 40.

- [47] E. Esarey, A. Ting, P. Sprangle, and G. Joyce, "The laser wakefield accelerator," *Comments on Plasma Physics and Controlled Fusion* **12**, 191–204 (1989), p. 40.
- [48] A. Pukhov and J. Meyer-ter Vehn, "Laser wake field acceleration: the highly non-linear broken-wave regime," *Applied Physics B* **74**, 355–361 (2002), pp. 42 and 45.
- [49] S. P. D. Mangles, C. D. Murphy, Z. Najmudin, A. G. R. Thomas, J. L. Collier, A. E. Dangor, E. J. Divall, P. S. Foster, J. G. Gallacher, C. J. Hooker, D. A. Jaroszynski, A. J. Langley, W. B. Mori, P. A. Norreys, F. S. Tsung, R. Viskup, B. R. Walton, and K. Krushelnick, "Monoenergetic beams of relativistic electrons from intense laser-plasma interactions," *Nature* **431**, 535 (2004), pp. 1, 2, 42, and 56.
- [50] C. G. R. Geddes, C. Toth, J. Van Tilborg, E. Esarey, C. B. Schroeder, D. Bruhwiler, C. Nieter, J. Cary, and W. P. Leemans, "High-quality electron beams from a laser wakefield accelerator using plasma-channel guiding," *Nature* **431**, 538 (2004), pp. 1, 2, and 42.
- [51] J. Faure, Y. Glinec, A. Pukhov, S. Kiselev, S. Gordienko, E. Lefebvre, J.-P. Rousseau, F. Burgy, and V. Malka, "A laser-plasma accelerator producing monoenergetic electron beams," *Nature* **431**, 541 (2004), pp. 1, 2, and 42.
- [52] W. Lu, C. Huang, M. Zhou, M. Tzoufras, F. S. Tsung, W. B. Mori, and T. Katsouleas, "A non-linear theory for multidimensional relativistic plasma wave wakefields," *Physics of Plasmas* **13**, 056709 (2006), pp. 3, 42, 44, 45, and 47.
- [53] John Dawson, "Particle simulation of plasmas," *Reviews of Modern Physics* **55**, 403–447 (Apr. 1983), p. 42.
- [54] M. Geissler, J. Schreiber, and J. Meyer-ter Vehn, "Bubble acceleration of electrons with few-cycle laser pulses," *New Journal of Physics* **8**, 186 (2006), pp. 3, 42, 45, 47, and 65.
- [55] R. A. Fonseca, L. O. Silva, F. S. Tsung, V. K. Decyk, W. Lu, C. Ren, W. B. Mori, S. Deng, S. Lee, T. Katsouleas, and J. C. Adam, "OSIRIS: A Three-Dimensional, Fully Relativistic Particle in Cell Code for Modeling Plasma Based Accelerators," *Lecture Notes in Computer Science* **2331**, 342–351 (2002), p. 42.
- [56] C. Nieter, "VORPAL: a versatile plasma simulation code," *Journal of Computational Physics* **196**, 448–473 (May 2004), p. 42.
- [57] S. Gordienko and A. Pukhov, "Scalings for ultrarelativistic laser plasmas and quasimonoenergetic electrons," *Physics of Plasmas* **12**, 043109 (2005), p. 42.
- [58] A. Pukhov and S. Gordienko, "Bubble regime of wake field acceleration: similarity theory and optimal scalings." *Philosophical transactions. Series A, Mathematical, physical, and engineering sciences* **364**, 623–33 (2006), pp. 3 and 42.
- [59] B. Hidding, K.-U. Amthor, B. Liesfeld, H. Schwöerer, S. Karsch, M. Geissler, L. Veisz, K. Schmid, J. Gallacher, S. Jamison, D. Jaroszynski, G. Pretzler, and R. Sauerbrey, "Generation of Quasimonoenergetic Electron Bunches with 80-fs Laser Pulses," *Phys. Rev. Lett.* **96**, 3–6 (Mar. 2006), pp. 44 and 72.

- [60] W. Lu, M. Tzoufras, C. Joshi, F. Tsung, W. Mori, J. Vieira, R. Fonseca, and L. Silva, "Generating multi-GeV electron bunches using single stage laser wakefield acceleration in a 3D nonlinear regime," *Physical Review Special Topics – Accelerators and Beams* **10**, 1–12 (Jun. 2007), pp. 44 and 45.
- [61] A. Pukhov, S. Gordienko, S. Kiselev, and I. Kostyukov, "The bubble regime of laser-plasma acceleration: monoenergetic electrons and the scalability," *Plasma Physics and Controlled Fusion* **46** (2004), p. 45.
- [62] Francis F. Chen, *Klassische Mechanik*, 11th ed. (AULA-Verlag Wiesbaden, 1991), p. 46.
- [63] Jorge v. José and Eugene J. Saletan, *Classical Dynamics – A Contemporary Approach* (Cambridge University Press, 1998), p. 46.
- [64] W. Leemans, E. Esarey, C. Geddes, C. Schroeder, and C. Tóth, "GeV electron beams from a centimetre-scale accelerator," *Nature Physics* **2**, 696–699 (2006), pp. 1, 3, 46, 77, 79, 106, and 124.
- [65] A. Debus, *Guiding a high-energy laser beam through a plasma channel*, Master's thesis, University of Texas at Austin (Dec. 2004), pp. 46 and 106.
- [66] H. M. Milchberg, K. Y. Kim, V. Kumarappan, B. D. Layer, and H. Sheng, "Clustered gases as a medium for efficient plasma waveguide generation," *Philosophical transactions. Series A, Mathematical, physical, and engineering sciences* **364**, 647–61 (2006), pp. 46 and 106.
- [67] S. Karsch, J. Osterhoff, A. Popp, T. P. Rowlands-Rees, Zs. Major, M. Fuchs, B. Marx, R. Hörlein, K. Schmid, L. Veisz, S. Becker, U. Schramm, B. Hidding, G. Pretzler, D. Habs, F. Grüner, F. Krausz, and S. M. Hooker, "GeV-scale electron acceleration in a gas-filled capillary discharge waveguide," *New Journal of Physics* **9**, 415 (2007), pp. 1, 46, and 126.
- [68] J. Osterhoff, A. Popp, Zs. Major, B. Marx, T. P. Rowlands-Rees, M. Fuchs, M. Geissler, R. Hörlein, B. Hidding, S. Becker, E. A. Peralta, U. Schramm, F. Grüner, D. Habs, F. Krausz, S. M. Hooker, and S. Karsch, "Generation of Stable, Low-Divergence Electron Beams by Laser-Wakefield Acceleration in a Steady-State-Flow Gas Cell," *Phys. Rev. Lett.* **101**, 085002 (2008), pp. 1, 46, and 126.
- [69] J. Faure, C. Rechatin, A. Norlin, A. Lifschitz, Y. Glinec, and V. Malka, "Controlled injection and acceleration of electrons in plasma wakefields by colliding laser pulses," *Nature* **444**, 737–9 (Dec. 2006), pp. 2 and 47.
- [70] C. Geddes, K. Nakamura, G. Plateau, Cs. Toth, E. Cormier-Michel, E. Esarey, C. Schroeder, J. Cary, and W. Leemans, "Plasma-Density-Gradient Injection of Low Absolute-Momentum-Spread Electron Bunches," *Phys. Rev. Lett.* **100**, 1–4 (May 2008), p. 47.
- [71] R. M. G. M. Trines, R. Bingham, Z. Najmudin, S. Mangles, L. O. Silva, R. Fonseca, and P. A. Norreys, "Electron trapping and acceleration on a downward density ramp: a two-stage approach," *New Journal of Physics* **12**, 045027 (Apr. 2010), p. 47.
- [72] A. Irman, M. J. H. Luttikhof, A. G. Khachatryan, F. A. van Goor, J. W. J. Verschuur, H. M. J. Bastiaens, and K.-J. Boller, "Design and simulation of laser wakefield acceleration with external electron bunch injection in front of the laser pulse," *Journal of Applied Physics* **102**, 024513 (2007), pp. 2 and 47.

- [73] W. van Dijk, M. J. van Der Wiel, and G. J. H. Brussaard, "Electron bunch compression using a laser-plasma compressor," *Physical Review Special Topics – Accelerators and Beams* **12**, 1–12 (Nov. 2009), p. 47.

BIBLIOGRAPHY FOR CHAPTER 3

- [1] J. van Tilborg, C. B. Schroeder, C. V. Filip, Cs. Tóth, C. G. R. Geddes, G. Fubiani, R. Huber, R. A. Kaindl, E. Esarey, and W. P. Leemans, "Temporal Characterization of Femtosecond Laser-Plasma-Accelerated Electron Bunches Using Terahertz Radiation," *Phys. Rev. Lett.* **96**, 014801 (2006), pp. 49 and 56.
- [2] T. Ohkubo, A. Maekawa, R. Tsujii, T. Hosokai, K. Kinoshita, K. Kobayashi, M. Uesaka, A. Zhidkov, K. Nemoto, Y. Kondo, and Y. Shibata, "Temporal characteristics of monoenergetic electron beams generated by the laser wakefield acceleration," *Phys. Rev. Spec. Top. - Accel. and Beams* **10**, 031301 (2007), p. 49.
- [3] M. Tzoufras, W. Lu, F. S. Tsung, C. Huang, W. B. Mori, T. Katsouleas, J. Vieira, R. A. Fonseca, and L. O. Silva, "Beam Loading in the Nonlinear Regime of Plasma-Based Acceleration," *Phys. Rev. Lett.* **101**, 145002 (2008), pp. 50 and 65.
- [4] I. Kostyukov and E. Nerush, "Electron Self-Injection in Multidimensional Relativistic-Plasma Wake Fields," *Phys. Rev. Lett.* **103**, 1–4 (Oct. 2009), p. 50.
- [5] I. Kostyukov, E. Nerush, A. Pukhov, and V. Seredov, "A multidimensional theory for electron trapping by a plasma wake generated in the bubble regime," *New Journal of Physics* **12**, 045009 (Apr. 2010), p. 50.
- [6] E. Esarey, C. B. Schroeder, and W. P. Leemans, "Physics of laser-driven plasma-based electron accelerators," *Reviews of Modern Physics* **81**, 1229–1285 (2009), pp. 1, 2, 3, 37, 40, and 50.
- [7] K. Phuoc, S. Corde, R. Shah, F. Albert, R. Fitour, J.-P. Rousseau, F. Burgy, B. Mercier, and A. Rousse, "Imaging Electron Trajectories in a Laser-Wakefield Cavity Using Betatron X-Ray Radiation," *Phys. Rev. Lett.* **97**, 1–4 (Nov. 2006), p. 50.
- [8] K. Németh, B. Shen, Y. Li, H. Shang, R. Crowell, K. Harkay, and J. Cary, "Laser-Driven Coherent Betatron Oscillation in a Laser-Wakefield Cavity," *Phys. Rev. Lett.* **100**, 1–4 (Mar. 2008), p. 50.
- [9] M.L. Ter-Mikaelian, *High-energy Electromagnetic Processes in Condensed Media (Tracts on Physics & Astronomical)* (John Wiley & Sons Inc, 1972) ISBN 0471851906, p. 468, p. 51.
- [10] V.L. Ginzburg and I.M. Frank, "To the Theory of Transition Radiation," *Sov. Phys. JETP* **16** (1946), p. 51.
- [11] I.M. Frank, "Transition radiation and optical properties of matter," *Soviet Physics Uspekhi* **8**, 729–742 (May 1966), p. 51.

- [12] V.L. Ginzburg, "Transition radiation and transition scattering," 16th International Cosmic Ray Conference **14**, 42–50 (1979), p. 51.
- [13] C. B. Schroeder, E. Esarey, J. Van Tilborg, and WP Leemans, "Theory of coherent transition radiation generated at a plasma-vacuum interface," *Physical Review E* **69**, 16501–12 (2004), pp. 51 and 68.
- [14] J. van Tilborg, C. B. Schroeder, E. Esarey, and W. P. Leemans, "Pulse shape and spectrum of coherent diffraction-limited transition radiation from electron beams," *Laser and Particle Beams* **22**, 415–422 (2004), pp. 52, 58, 65, and 68.
- [15] Walter D. Jackson, *Classical Electrodynamics*, 3rd ed. (John Wiley & Sons, 1999), pp. 11, 32, 53, and 80.
- [16] S. Casalbuoni, B. Schmidt, and P. Schmüser, *TESLA REPORT: Far-Infrared Transition and Diffraction Radiation*, Tech. Rep. 2005-15 (DESY Hamburg, 2005), p. 53.
- [17] G. Berden, S. Jamison, A. MacLeod, W. Gillespie, B. Redlich, and A. van Der Meer, "Electro-Optic Technique with Improved Time Resolution for Real-Time, Nondestructive, Single-Shot Measurements of Femtosecond Electron Bunch Profiles," *Phys. Rev. Lett.* **93**, 1–4 (Sep. 2004), pp. 55, 56, and 57.
- [18] Bernhard Schmidt, "Overview on diagnostics for X-and XUV-FEL," in *Proceedings of the 28th International Free Electron Laser Conference (FEL 2006), Berlin, Germany* (2006) p. 761, p. 55.
- [19] Sara Casalbuoni, H. Schlarb, B. Schmidt, B. Steffen, P. Schmuser, and A. Winter, *TESLA Report: Numerical Studies on the Electro-Optic Sampling of Relativistic Electron Bunches*, Tech. Rep. 2005-01 (DESY Hamburg, 2005), pp. 55, 58, 62, 66, and 68.
- [20] S. P. D. Mangles, C. D. Murphy, Z. Najmudin, A. G. R. Thomas, J. L. Collier, A. E. Dangor, E. J. Divall, P. S. Foster, J. G. Gallacher, C. J. Hooker, D. A. Jaroszynski, A. J. Langley, W. B. Mori, P. A. Norreys, F. S. Tsung, R. Viskup, B. R. Walton, and K. Krushelnick, "Monoenergetic beams of relativistic electrons from intense laser-plasma interactions," *Nature* **431**, 535 (2004), pp. 1, 2, 42, and 56.
- [21] R. A. Bosch, "Double-pulse THz radiation bursts from laser-plasma acceleration," *Phys. of Plasmas* **13**, 113107 (2006), p. 56.
- [22] H. C. Wu, Z. M. Sheng, Q. L. Dong, H. Xu, and J. Zhang, "Powerful terahertz emission from laser wakefields in inhomogeneous magnetized plasmas," *Phys. Rev. E* **75**, 016407 (2007), p. 56.
- [23] S. P. Jamison, J. Shen, A. M. MacLeod, W. A. Gillespie, and D. A. Jaroszynski, "High-temporal-resolution, single-shot characterization of terahertz pulses," *Opt. Lett.* **28**, 1710–1712 (2003), p. 57.
- [24] F. G. Sun, Z. Jiang, and X.-C. Zhang, "Analysis of terahertz pulse measurement with a chirped probe beam," *Applied Physics Letters* **73**, 2233 (1998), p. 57.
- [25] A. Pukhov and J. Meyer-ter Vehn, "Laser wake field acceleration: the highly non-linear broken-wave regime," *Appl. Phys. B* **74**, 355–361 (2002), p. 57.

- [26] S. Casalbuoni, H. Schlarb, B. Schmidt, P. Schmüser, B. Steffen, and A. Winter, "Numerical studies on the electro-optic detection of femtosecond electron bunches," *Physical Review Special Topics – Accelerators and Beams* **11**, 072802 (2008), pp. 58 and 62.
- [27] Joseph W. Goodman, *Introduction to Fourier Optics*, 3rd ed. (Roberts & Company Publishers, 2004) ISBN 978-0974707723, p. 61.
- [28] Edward Collett, *Field Guide to Polarization (SPIE Vol. FG05)* (SPIE Publications, 2005) ISBN 0819458686, p. 62.
- [29] R. Clark Jones, "A New Calculus for the Treatment of Optical Systems," *Journal of the Optical Society of America* **31**, 488 (Jul. 1941), p. 62.
- [30] T. G. Kolda, R. M. Lewis, and V. Torczon, "Optimization by direct search: new perspectives on some classical and modern methods," *SIAM Review* **45**, 385–482 (2003), p. 63.
- [31] M. Geissler, J. Schreiber, and J. Meyer-ter Vehn, "Bubble acceleration of electrons with few-cycle laser pulses," *New Journal of Physics* **8**, 186 (2006), pp. 3, 42, 45, 47, and 65.
- [32] A. Debus, S. Bock, M. Bussmann, T. E. Cowan, A. Jochmann, T. Kluge, S. D. Kraft, R. Sauerbrey, K. Zeil, and U. Schramm, "Linear and Non-Linear Thomson-Scattering X-Ray Sources Driven by Conventionally and Laser Plasma Accelerated Electrons," *Proc. of SPIE* **7359**, 735908 (2009), pp. 31, 65, and 107.
- [33] H. Schwoerer, B. Liesfeld, H. Schlenvoigt, K. Amthor, and R. Sauerbrey, "Development of an RF photoinjector for relativistic thomson scattering short-pulse x-ray source," *Phys. Rev. Lett.* **96**, 014820 (2006), pp. 1 and 65.
- [34] F. Grüner, S. Becker, U. Schramm, T. Eichner, M. Fuchs, R. Weingartner, D. Habs, J. Meyer-ter Vehn, M. Geissler, M. Ferrario, L. Serafini, B. van der Geer, H. Backe, W. Lauth, and S. Reiche, "Design considerations for table-top, laser-based VUV and x-ray free electron lasers," *Applied Physics B: Lasers and Optics* **86**, 431–435 (Feb. 2007), pp. 4 and 65.
- [35] N. H. Matlis, S. Reed, S. S. Bulanov, V. Chvykov, G. Kalintchenko, T. Matsuoka, P. Rousseau, V. Yanovsky, A. Maksimchuk, S. Kalmykov, G. Shvets, and M. C. Downer, "Snapshots of laser wakefields," *Nature Physics* **2**, 749–753 (Oct. 2006), p. 66.
- [36] Kim Ta Phuoc, Jean-philippe Rousseau, Victor Malka, Antoine Rousse, Rahul Shah, Donald Umstadter, Alexander Pukhov, Sergei Kiselev, and I Introduction, "Laser based synchrotron radiation," *Physics of Plasmas* **023101**, 1–8 (2005), p. 66.
- [37] Károly Németh, Baifei Shen, Yuelin Li, Hairong Shang, Robert Crowell, Katherine Harkay, and John Cary, "Laser-Driven Coherent Betatron Oscillation in a Laser-Wakefield Cavity," *Phys. Rev. Lett.* **100**, 1–4 (Mar. 2008), pp. 66 and 68.
- [38] H.-P. Schlenvoigt, K. Haupt, A. Debus, F. Budde, O. Jäckel, S. Pfotenhauer, H. Schwoerer, E. Rohwer, J. G. Gallacher, E. Brunetti, R. P. Shanks, S. M. Wiggins, and D. A. Jaroszynski, "A compact synchrotron radiation source driven by a laser-plasma wakefield accelerator," *Nature Physics* **4**, 130 (2008), pp. 71 and 77.

- [39] H.-P. Schlenvoigt, K. Haupt, A. D. Debus, F. Budde, O. Jäckel, S. Pfotenhauer, J. G. Gallacher, E. Brunetti, R. P. Shanks, S. M. Wiggins, D. A. Jaroszynski, E. Rohwer, and H. Schworer, "Synchrotron Radiation From Laser-Accelerated Monoenergetic Electrons," *IEEE Transactions on Plasma Science* **36**, 1773–1781 (Aug. 2008), p. 71.
- [40] J. G. Gallacher, M. P. Anania, E. Brunetti, F. Budde, A. D. Debus, B. Ersfeld, K. Haupt, M. R. Islam, O. Jäckel, S. Pfotenhauer, A. J. W. Reitsma, E. Rohwer, H.-P. Schlenvoigt, H. Schworer, R. P. Shanks, S. M. Wiggins, and D. A. Jaroszynski, "A method of determining narrow energy spread electron beams from a laser plasma wakefield accelerator using undulator radiation," *Physics of Plasmas* **16**, 093102 (2009), p. 71.
- [41] B. Hidding, K.-U. Amthor, B. Liesfeld, H. Schworer, S. Karsch, M. Geissler, L. Veisz, K. Schmid, J. Gallacher, S. Jamison, D. Jaroszynski, G. Pretzler, and R. Sauerbrey, "Generation of Quasimonoenergetic Electron Bunches with 80-fs Laser Pulses," *Phys. Rev. Lett.* **96**, 3–6 (Mar. 2006), pp. 44 and 72.
- [42] Fabian Budde, *Experiment zur Erzeugung von Undulatorstrahlung mit laserbeschleunigten Elektronen*, Diplomarbeit, Friedrich-Schiller Universität Jena (2006), p. 73.
- [43] Kazuo A. Tanaka, T. Yabuuchi, T. Sato, R. Kodama, Y. Kitagawa, T. Takahashi, T. Ikeda, Y. Honda, and S. Okuda, "Calibration of imaging plate for high energy electron spectrometer," *Review of Scientific Instruments* **76**, 013507 (2005), p. 73.
- [44] H. Onuki and P. Elleaume, *Undulators, Wigglers and their Applications* (Taylor and Francis Inc., 2003), pp. 11, 74, 75, and 82.
- [45] Helmut Wiedemann, *Particle Accelerator Physics*, 3rd ed. (Springer-Verlag Berlin Heidelberg, 2007), pp. 36, 74, 132, and 135.
- [46] James A. Clarke, *The Science and Technology of Undulators and Wigglers (Oxford Series on Synchrotron Radiation)* (Oxford University Press, USA, 2004) ISBN 0198508557, p. 244, pp. 8, 11, 16, 75, and 79.
- [47] W. Leemans, E. Esarey, C. Geddes, C. Schroeder, and C. Tóth, "GeV electron beams from a centimetre-scale accelerator," *Nature Physics* **2**, 696–699 (2006), pp. 1, 3, 46, 77, 79, 106, and 124.
- [48] D. A. Jaroszynski, R. Bingham, E. Brunetti, B. Ersfeld, J. Gallacher, B. van Der Geer, R. Issac, S. P. Jamison, D. Jones, A. de Loos, M. Lyachev, V. Pavlov, A. Reitsma, G. Saveliev, Y. Vieux, and S. M. Wiggins, "Radiation sources based on laser-plasma interactions," *Phil. Trans. R. Soc. A* **364**, 689–710 (2006), pp. 1 and 77.

BIBLIOGRAPHY FOR CHAPTER 4

- [1] W. Leemans, E. Esarey, C. Geddes, C. Schroeder, and C. Tóth, "GeV electron beams from a centimetre-scale accelerator," *Nature Physics* **2**, 696–699 (2006), pp. 1, 3, 46, 77, 79, 106, and 124.

- [2] James A. Clarke, *The Science and Technology of Undulators and Wigglers (Oxford Series on Synchrotron Radiation)* (Oxford University Press, USA, 2004) ISBN 0198508557, p. 244, pp. 8, 11, 16, 75, and 79.
- [3] Walter D. Jackson, *Classical Electrodynamics*, 3rd ed. (John Wiley & Sons, 1999), pp. 11, 32, 53, and 80.
- [4] S. B. van der Geer and M. J. de Loos, "General Particle Tracker (GPT)," www.pulsar.nl/gpt, p. 82.
- [5] S. B. van der Geer, O. J. Luiten, M. J. de Loos, G. Pöplau, and U. van Rienen, "Space-charge model for GPT simulations of high brightness electron bunches," Institute of Physics Conference Series, 101(2005), p. 82.
- [6] G. Pöplau, U. van Rienen, B. van der Geer, and M. de Loos, "Multigrid algorithms for the fast calculation of space-charge effects in accelerator design," IEEE Transactions on magnetics **40**, 714 (2004), p. 82.
- [7] E. Esarey, S. K. Ride, and P. Sprangle, "Nonlinear Thomson scattering of intense laser pulses from beams and plasmas," Phys. Rev. E **48**, 3003–3021 (Oct. 1993), pp. 4, 31, 33, 34, 82, and 107.
- [8] H. Onuki and P. Elleaume, *Undulators, Wigglers and their Applications* (Taylor and Francis Inc., 2003), pp. 11, 74, 75, and 82.
- [9] Inc. Wolfram Research, *Mathematica 6.0* (Wolfram Research, Inc., Champaign, Illinois, 2007), p. 82.
- [10] S. Agostinelli, "Geant4 – a simulation toolkit," Nuclear Instruments and Methods in Physics Research Section A: Accelerators, Spectrometers, Detectors and Associated Equipment **506**, 250–303 (Jul. 2003), p. 83.
- [11] J. Allison, K. Amako, J. Apostolakis, H. Araujo, P. Arce Dubois, M. Asai, G. Barrand, R. Capra, S. Chauvie, R. Chytracsek, *et al.*, "Geant4 developments and applications," IEEE Transactions on Nuclear Science **53**, 270–278 (Feb. 2006), p. 83.
- [12] ITRS, "International Technology Roadmap for Semiconductors: 2009," (2009), 1–17 pp., <http://www.itrs.net/Links/2009ITRS/Home2009.htm>, p. 89.
- [13] B. Wu and A. Kumar, "Extreme ultraviolet lithography: A review," Journal of Vacuum Science & Technology B: Microelectronics and Nanometer Structures **25**, 1743 (2007), p. 89.
- [14] Jeroen Jonkers, "High power extreme ultra-violet (EUV) light sources for future lithography," Plasma Sources Sci. Technol. **15**, S8–16 (2006), pp. 89 and 90.
- [15] Vadim Banine and Roel Moors, "Plasma sources for EUV lithography exposure tools," J. Phys. D: Appl. Phys. **37**, 3207–3212 (2004), p. 89.
- [16] Y. Socol, G. N. Kulipanov, O. A. Shevchenko, N. A. Vinokurov, and A. N. Matveenko, "13.5-nm Free Electron Laser for EUV Lithography," Proceedings of the FEL conference(2010), p. 89.

- [17] T. Eidam, S. Hanf, E. Seise, T. V. Andersen, T. Gabler, C. Wirth, T. Schreiber, J. Limpert, and A. Tünnermann, "Femtosecond fiber CPA system emitting 830 W average output power," *Optical Letters* **35**, 94–96 (2010), pp. 90, 95, and 123.
- [18] F. Röser, T. Eidam, J. Rothhardt, O. Schmidt, D. N. Schimpf, J. Limpert, and A. Tünnermann, "Millijoule pulse energy high repetition rate femtosecond fiber chirped-pulse amplification system," *Optical Letters* **32**, 3495–3497 (2007), pp. 90, 95, and 123.
- [19] R. Xiang, A. Arnold, H. Buettig, D. Janssen, M. Justus, U. Lehnert, P. Michel, P. Murcek, A. Schamlott, Ch. Schneider, R. Schurig, F. Staufenbiel, and J. Teichert, "Cs₂Te normal conducting photocathodes in the superconducting RF gun," *Physical Review Special Topics – Accelerators and Beams* **13**, 1–7 (Apr. 2010), p. 90.
- [20] A. Arnold, H. Büttig, D. Janssen, T. Kamps, G. Klemz, W. Lehmann, U. Lehnert, D. Lipka, F. Marhauser, P. Michel, P. K. Möller, P. Murcek, Ch. Schneider, R. Schurig, F. Staufenbiel, J. Stephan, J. Teichert, V. Volkov, I. Will, and R. Xiang, "A high-brightness SRF photoelectron injector for FEL light sources," *Nuclear Instruments and Methods in Physics Research A* **593**, 57–62 (2008), pp. 90 and 123.
- [21] A. Chao, R. Pitthan, T. Tajima, and D. Yeremian, "Space charge dynamics of bright electron beams," *Physical Review Special Topics – Accelerators and Beams* **6** (Feb. 2003), p. 91.
- [22] Alexander Wu Chao, *Physics of Collective Beam Instabilities in High Energy Accelerators (Wiley Series in Beam Physics and Accelerator Technology)* (Wiley-Interscience, 1993) ISBN 0471551848, p. 371, <http://www.slac.stanford.edu/~achao/wileybook.html>, pp. 91 and 125.
- [23] G. Fubiani, J. Qiang, Eric Esarey, W. Leemans, and G. Dugan, "Space charge modeling of dense electron beams with large energy spreads," *Physical Review Special Topics – Accelerators and Beams* **9**, 1–31 (2006), p. 91.
- [24] Alan Todd, "State-of-the-art electron guns and injector designs for energy recovery linacs (ERL)," *Nuclear Instruments and Methods in Physics Research Section A: Accelerators, Spectrometers, Detectors and Associated Equipment* **557**, 36–44 (Feb. 2006), pp. 94 and 95.
- [25] T. Rao, I. Ben-zvi, A. Burrill, X. Chang, P. D. Johnson, and J. Kewisch, "Diamond Amplifier For Photocathodes," *Physics*, 178–190(2004), p. 94.
- [26] J. Smedley, I. Ben-Zvi, J. Bohon, X. Chang, R. Grover, I. Abdel, R. Triveni, and W. Qiong, "Diamond Amplified Photocathodes," *Mater. Res. Soc. Symp. Proc.* **1039**, 1–6 (2008), p. 94.
- [27] K. L. Jensen, J. E. Yater, J. L. Shaw, R. E. Myers, B. B. Pate, J. E. Butler, and T. Feygelson, "Bunch characteristics of an electron beam generated by a diamond secondary emitter amplifier," (2010), p. 94.
- [28] Jens Limpert, Fabian Röser, Thomas Schreiber, and Andreas Tünnermann, "High-Power Ultrafast Fibre Laser Systems," *IEEE Journal of Selected Topics in Quantum Electronics* **12**, 233–243 (2006), p. 95.
- [29] A Tünnermann, T Schreiber, F Röser, A Liem, S Höfer, H Zellmer, S Nolte, and J Limpert, "The renaissance and bright future of fibre lasers," *Journal of Physics B: Atomic, Molecular and Optical Physics* **38**, S681–S693 (2005), p. 95.

- [30] I. Pupeza, T. Eidam, O. Pronin, J. Rauschenberger, B. Bernhardt, A. Ozawa, Th. Udem, R. Holzwarth, J. Limpert, A. Apolonski, T. W. Hänsch, A. Tünnemann, and F. Krausz, "Femtosecond high repetition rate external cavity beyond the average power limit for linear enhancement," (OSA Optics & Photonics Congress 2010, 2010), pp. 95 and 123.
- [31] Roderick J. Loewen, *A Compact Light Source: Design and Technical Feasibility Study of a Laser-Electron Storage Ring X-Ray Source*, Ph.D. thesis, Stanford University (2003), p. 95.
- [32] Christian Morawe and Markus Osterhoff, "Hard X-Ray Focusing with Curved Reflective Multilayers," *X-Ray Optics and Instrumentation* **2010**, 1–9 (2010), p. 99.

BIBLIOGRAPHY FOR CHAPTER 5

- [1] V. Karagodsky, D. Schieber, and L. Schächter, "Enhancing X-Ray Generation by Electron-Beam-Laser Interaction in an Optical Bragg Structure," *Phys. Rev. Lett.* **104**, 024801 (2010), p. 106.
- [2] W. Leemans, E. Esarey, C. Geddes, C. Schroeder, and C. Tóth, "GeV electron beams from a centimetre-scale accelerator," *Nature Physics* **2**, 696–699 (2006), pp. 1, 3, 46, 77, 79, 106, and 124.
- [3] H. M. Milchberg, K. Y. Kim, V. Kumarappan, B. D. Layer, and H. Sheng, "Clustered gases as a medium for efficient plasma waveguide generation," *Philosophical transactions. Series A, Mathematical, physical, and engineering sciences* **364**, 647–61 (2006), pp. 46 and 106.
- [4] A. Debus, *Guiding a high-energy laser beam through a plasma channel*, Master's thesis, University of Texas at Austin (Dec. 2004), pp. 46 and 106.
- [5] A. D. Debus, M. Bussmann, M. Siebold, A. Jochmann, U. Schramm, T. E. Cowan, and R. Sauerbrey, "Traveling-wave Thomson scattering and optical undulators for high-yield EUV and X-ray sources," *Applied Physics B* **100**, 61–76 (May 2010), p. 106.
- [6] A. Debus, S. Bock, M. Bussmann, T. E. Cowan, A. Jochmann, T. Kluge, S. D. Kraft, R. Sauerbrey, K. Zeil, and U. Schramm, "Linear and Non-Linear Thomson-Scattering X-Ray Sources Driven by Conventionally and Laser Plasma Accelerated Electrons," *Proc. of SPIE* **7359**, 735908 (2009), pp. 31, 65, and 107.
- [7] E. Esarey, S. K. Ride, and P. Sprangle, "Nonlinear Thomson scattering of intense laser pulses from beams and plasmas," *Phys. Rev. E* **48**, 3003–3021 (Oct. 1993), pp. 4, 31, 33, 34, 82, and 107.
- [8] R. W. Schoenlein, W. P. Leemans, A. H. Chin, P. Volfbeyn, T. E. Glover, P. Balling, M. Zolotarev, K.-J. Kim, S. Chattopadhyay, and C. V. Shank, "Femtosecond x-ray pulses at 0.4 Å generated by 90° Thomson scattering: a tool for probing the structural dynamics of materials," *Science* **274**, 236–238 (1996), p. 108.
- [9] J. Diehls, *Ultrashort Laser Pulse Phenomena*, 2nd ed. (Academic Press, 2006), pp. 110, 115, and 141.

- [10] Z. Bor, "Distortion of femtosecond laser pulses in lenses," *Optics Letters* **14**, 119–121 (1989), p. 110.
- [11] J. Hebling, "Derivation of the pulse front tilt caused by angular dispersion," *Optical and Quantum Electronics* **28**, 1759–1763 (Dec. 1996), p. 110.
- [12] S. Akturk, X. Gu, E. Zeek, and R. Trebino, "Spatial chirp and pulse-front tilt in ultrashort laser pulses and their measurement," in *14th International Conference on Ultrafast Phenomena* (Optical Society of America, 2004) p. ME39, pp. 110 and 141.
- [13] O. E. Martinez, "Pulse Distortions in tilted pulse schemes for ultrashort pulses," *Optics Communications* **59**, 229–232 (1986), p. 112.
- [14] C. Pellegrini and S. Reiche, "The Development of X-Ray Free-Electron Lasers," *IEEE Journal of Selected Topics in Quantum Electronics* **10**, 1393–1404 (2004), pp. 12 and 113.
- [15] R. Bonifacio, C. Pellegrini, and L. M. Narducci, "Collective instabilities and high-gain regime in a free electron laser," *Optics Communications* **50**, 373–378 (1986), pp. 22 and 113.
- [16] P. Michel, H. Buettig, F. Gabriel, M. Helm, U. Lehnert, Ch. Schneider, R. Schurig, W. Seidel, D. Stehr, J. Teichert, S. Winnerl, and R. Wünsch, "The Rossendorf IR-FEL ELBE," in *Proc. FEL* (2006) pp. 488–491, p. 113.
- [17] W. Seidel, E. Cizmar, O. Drachenko, M. Helm, M. Justus, U. Lehnert, P. Michel, M. Ozerov, H. Schneider, R. Schurig, D. Stehr, M. Wagner, S. Winnerl, D. Wohlfarth, and S. Zvyagin, "Three years of cw-operation at FELBE-Experiences and applications," in *Proceedings of the 30th International Free Electron Laser Conference, Gyeongbuk, Korea* (2008) pp. 382–385, p. 113.
- [18] W. Ackermann, G. Asova, V. Ayvazyan, A. Azima, N. Baboi, J. Bähr, V. Balandin, B. Beutner, A. Brandt, A. Bolzmann, *et al.*, "Operation of a free-electron laser from the extreme ultraviolet to the water window," *Nature Photonics* **1**, 336–342 (Jun. 2007), p. 113.
- [19] P. Emma, R. Akre, J. Arthur, R. Bionta, C. Bostedt, J. Bozek, A. Brachmann, P. Bucksbaum, R. Coffee, F.-J. Decker, Y. Ding, D. Dowell, S. Edstrom, A. Fisher, J. Frisch, S. Gilevich, J. Hastings, G. Hays, Ph. Hering, Z. Huang, R. Iverson, H. Loos, M. Messerschmidt, A. Miahnahri, S. Moeller, H.-D. Nuhn, G. Pile, D. Ratner, J. Rzepiela, D. Schultz, T. Smith, P. Stefan, H. Tompkins, J. Turner, J. Welch, W. White, J. Wu, G. Yocky, and J. Galayda, "First lasing and operation of an ångstrom-wavelength free-electron laser," *Nature Photonics* **4**, 641–647 (Aug. 2010), p. 113.
- [20] A. G. Kostenbauder, "Ray-Pulse Matrices: A Rational Treatment for Dispersive Optical Systems," *IEEE Journal of Quantum Electronics* **26**, 1148–1157 (1990), pp. 117, 141, 142, and 143.
- [21] R. Storn and K. Price, "Differential Evolution - A simple and efficient adaptive scheme for global optimization over continuous spaces," *J. Global Optimization* **11**, 341–359 (1997), p. 119.
- [22] F. Röser, T. Eidam, J. Rothhardt, O. Schmidt, D. N. Schimpf, J. Limpert, and A. Tünnermann, "Millijoule pulse energy high repetition rate femtosecond fiber chirped-pulse amplification system," *Optical Letters* **32**, 3495–3497 (2007), pp. 90, 95, and 123.

- [23] T. Eidam, S. Hanf, E. Seise, T. V. Andersen, T. Gabler, C. Wirth, T. Schreiber, J. Limpert, and A. Tünnermann, "Femtosecond fiber CPA system emitting 830 W average output power," *Optical Letters* **35**, 94–96 (2010), pp. 90, 95, and 123.
- [24] I. Pupeza, T. Eidam, O. Pronin, J. Rauschenberger, B. Bernhardt, A. Ozawa, Th. Udem, R. Holzwarth, J. Limpert, A. Apolonski, T. W. Hänsch, A. Tünnermann, and F. Krausz, "Femtosecond high repetition rate external cavity beyond the average power limit for linear enhancement," (*OSA Optics & Photonics Congress 2010*, 2010), pp. 95 and 123.
- [25] A. Arnold, H. Büttig, D. Janssen, T. Kamps, G. Klemz, W. Lehmann, U. Lehnert, D. Lipka, F. Marhauser, P. Michel, P. K. Möller, P. Murcek, Ch. Schneider, R. Schurig, F. Staufenberg, J. Stephan, J. Teichert, V. Volkov, I. Will, and R. Xiang, "A high-brightness SRF photoelectron injector for FEL light sources," *Nuclear Instruments and Methods in Physics Research A* **593**, 57–62 (2008), pp. 90 and 123.
- [26] K.-H. Hong, J. Gopinath, D. Rand, A. Siddiqui, S.-W. Huang, E. Li, B. Eggleton, J. Hybl, T. Y. Fan, and F. X. Kärtner, "Generation of 2-kHz, 40-mJ Picosecond Pulses from a Cryogenic Yb:YAG Chirped-Pulse Amplifier for OPCPA Pumping," (*OSA Optics & Photonics Congress 2010*, 2010), p. 123.
- [27] M. Siebold, J. Hein, M. Hornung, S. Podleska, M. C. Kaluza, S. Bock, and R. Sauerbrey, "Diode-pumped lasers for ultra-high peak power," *Applied Physics B: Lasers and Optics* **90**, 431–437 (2008), p. 123.
- [28] J. Hein, M. C. Kaluza, R. Bodefeld, M. Siebold, S. Podleska, and R. Sauerbrey, "POLARIS: An All Diode-Pumped Ultrahigh Peak Power Laser for High Repetition Rates," *Lect. Notes Phys.* **694**, 47–66 (2006), p. 123.
- [29] A. D. Debus, M. Bussmann, U. Schramm, R. Sauerbrey, C. D. Murphy, Zs. Major, R. Hörlein, L. Veisz, K. Schmid, J. Schreiber, K. Witte, S. P. Jamison, J. G. Gallacher, D. A. Jaroszynski, M. C. Kaluza, B. Hidding, S. Kiselev, R. Heathcote, P. S. Foster, D. Neely, E. J. Divall, C. J. Hooker, J. M. Smith, K. Ertel, A. J. Langley, P. Norreys, J. L. Collier, and S. Karsch, "Electron bunch length measurements from laser-accelerated electrons using single-shot THz time-domain interferometry," *Phys. Rev. Lett.* **104**, 084802 (2010), p. 124.
- [30] J. Gea-Banacloche, G. Moore, R. Schlicher, M. Scully, and H. Walther, "Proposal for a compact FEL with electromagnetic-wave undulator," *Nuclear Instruments and Methods in Physics Research A* **272**, 199–205 (1988), p. 125.
- [31] J. Gea-Banacloche, G. Moore, R. Schlicher, M. Scully, and H. Walther, "Soft X-Ray free-electron laser with a laser undulator," *IEEE Journal of Quantum Electronics* **QE-23**, 1558–1570 (1987), p. 125.
- [32] Alexander Wu Chao, *Physics of Collective Beam Instabilities in High Energy Accelerators (Wiley Series in Beam Physics and Accelerator Technology)* (Wiley-Interscience, 1993) ISBN 0471551848, p. 371, <http://www.slac.stanford.edu/~achao/wileybook.html> , pp. 91 and 125.
- [33] S. Reiche, *Numerical studies for a single pass high gain free-electron laser*, Phd thesis, Universität Hamburg (1999), pp. 12, 27, and 125.

- [34] J. Osterhoff, A. Popp, Zs. Major, B. Marx, T. P. Rowlands-Rees, M. Fuchs, M. Geissler, R. Hörlein, B. Hidding, S. Becker, E. A. Peralta, U. Schramm, F. Grüner, D. Habs, F. Krausz, S. M. Hooker, and S. Karsch, "Generation of Stable, Low-Divergence Electron Beams by Laser-Wakefield Acceleration in a Steady-State-Flow Gas Cell," *Phys. Rev. Lett.* **101**, 085002 (2008), pp. 1, 46, and 126.
- [35] S. Karsch, J. Osterhoff, A. Popp, T. P. Rowlands-Rees, Zs. Major, M. Fuchs, B. Marx, R. Hörlein, K. Schmid, L. Veisz, S. Becker, U. Schramm, B. Hidding, G. Pretzler, D. Habs, F. Grüner, F. Krausz, and S. M. Hooker, "GeV-scale electron acceleration in a gas-filled capillary discharge waveguide," *New Journal of Physics* **9**, 415 (2007), pp. 1, 46, and 126.
- [36] Helmut Wiedemann, *Particle Accelerator Physics*, 3rd ed. (Springer-Verlag Berlin Heidelberg, 2007), pp. 36, 74, 132, and 135.
- [37] Robert W. Boyd, *Nonlinear Optics*, 2nd ed. (Academic Press, 2003), p. 133.
- [38] Carsten Winterfeldt, Christian Spielmann, and Gustav Gerber, "Colloquium: Optimal control of high-harmonic generation," *Reviews of Modern Physics* **80**, 117–140 (Jan. 2008), p. 133.
- [39] Ferenc Krausz and Misha Ivanov, "Attosecond physics," *Reviews of Modern Physics* **81**, 163–234 (Feb. 2009), p. 133.
- [40] Xiaoshi Zhang, Amy L. Lytle, Tenio Popmintchev, Xibin Zhou, Henry C. Kapteyn, Margaret M. Murnane, and Oren Cohen, "Quasi-phase-matching and quantum-path control of high-harmonic generation using counterpropagating light," *Nature Physics* **3**, 270–275 (Feb. 2007), p. 133.
- [41] Valery Telnov, *Laser cooling of electron beams for linear colliders*, Tech. Rep. SLAC-PUB-7337 (Stanford Linear Accelerator Center, 1996), p. 135.
- [42] Zhirong Huang and Ronald Ruth, "Laser-Electron Storage Ring," *Phys. Rev. Lett.* **80**, 976–979 (Feb. 1998), p. 135.
- [43] Valery Telnov, "Laser cooling of electron beams at linear colliders," *Nuclear Instruments and Methods in Physics Research A* **455**, 80–89 (2000), p. 135.

BIBLIOGRAPHY FOR CHAPTER 6

- [1] R. Neutze, R. Wouts, D. van der Spoel, E. Weckert, and J. Hajdu, "Potential for biomolecular imaging with femtosecond X-ray pulses," *Nature* **406**, 752–7 (Aug. 2000), p. 138.
- [2] Ch. Song, H. Jiang, A. Mancuso, B. Amirbekian, L. Peng, R. Sun, S. Shah, Z. Zhou, T. Ishikawa, and J. Miao, "Quantitative Imaging of Single, Unstained Viruses with Coherent X Rays," *Phys. Rev. Lett.* **101**, 1–4 (2008), p. 138.
- [3] T. Guo, "More power to x-rays: New developments in x-ray spectroscopy," *Laser & Photonics Rev.* **3**, 591–622 (2009), pp. 1 and 138.
- [4] Ch. Bressler and M. Chergui, "Ultrafast X-ray absorption spectroscopy," *Chemical reviews* **104**, 1781–812 (May 2004), p. 138.

- [5] T. J. Davis, D. Gao, T. E. Gureyev, A. W. Stevenson, and S. W. Wilkins, "Phase-contrast imaging of weakly absorbing materials using hard X-rays," *Nature* **373**, 595–598 (1995), p. 138.
- [6] M. Bech, O. Bunk, Ch. David, R. Ruth, J. Rifkin, R. Loewen, R. Feidenhans'l, and F. Pfeifer, "Hard X-ray phase-contrast imaging with the Compact Light Source based on inverse Compton X-rays," *Journal of synchrotron radiation* **16**, 43–7 (2009), p. 138.
- [7] R. Bonifacio, N. Piovella, M. Cola, and L. Volpe, "Experimental requirements for X-ray compact free electron lasers with a laser wiggler," *Nuclear Instruments and Methods in Physics Research Section A: Accelerators, Spectrometers, Detectors and Associated Equipment* **577**, 745–750 (Jul. 2007), p. 138.
- [8] N. Piovella, M. Cola, L. Volpe, A. Schiavi, and R. Bonifacio, "Three-Dimensional Wigner-Function Description of the Quantum Free-Electron Laser," *Phys. Rev. Lett.* **100**, 1–4 (Jan. 2008), p. 138.
- [9] H. Gies, "Strong laser fields as a probe for fundamental physics," *The European Physical Journal D* **55**, 311–317 (Feb. 2009), p. 139.
- [10] T. H. Maiman, "Stimulated Optical Radiation in Ruby," *Nature* **187**, 493–494 (Aug. 1960), pp. 1 and 139.

BIBLIOGRAPHY FOR APPENDIX A

- [1] A. G. Kostenbauder, "Ray-Pulse Matrices: A Rational Treatment for Dispersive Optical Systems," *IEEE Journal of Quantum Electronics* **26**, 1148–1157 (1990), pp. 117, 141, 142, and 143.
- [2] S. Akturk, X. Gu, E. Zeek, and R. Trebino, "Spatial chirp and pulse-front tilt in ultrashort laser pulses and their measurement," in *14th International Conference on Ultrafast Phenomena* (Optical Society of America, 2004) p. ME39, pp. 110 and 141.
- [3] S. Akturk, X. Gu, P. Gabolde, and R. Trebino, "The general theory of first-order spatio-temporal distortions of Gaussian pulses and beams," *Optics Express* **13**, 8642–8661 (2005), p. 141.
- [4] J. Diehls, *Ultrashort Laser Pulse Phenomena*, 2nd ed. (Academic Press, 2006), pp. 110, 115, and 141.
- [5] Anthony E. Siegman, *Lasers* (University Science Books, 1986), p. 141.

PUBLICATIONS BY THE AUTHOR

- [1] A. D. Debus, M. Bussmann, U. Schramm, R. Sauerbrey, C. D. Murphy, Zs. Major, R. Hörlein, L. Veisz, K. Schmid, J. Schreiber, K. Witte, S. P. Jamison, J. G. Gallacher, D. A. Jaroszynski, M. C. Kaluza, B. Hidding, S. Kiselev, R. Heathcote, P. S. Foster, D. Neely, E. J. Divall, C. J. Hooker, J. M. Smith, K. Ertel, A. J. Langley, P. Norreys, J. L. Collier, and S. Karsch, "Electron bunch length measurements from laser-accelerated electrons using single-shot THz time-domain interferometry," *Phys. Rev. Lett.* **104**, 084802 (2010)
- [2] A. D. Debus, M. Bussmann, M. Siebold, A. Jochmann, U. Schramm, T. E. Cowan, and R. Sauerbrey, "Traveling-wave Thomson scattering and optical undulators for high-yield EUV and X-ray sources," *Applied Physics B* **100**, 61–76 (May 2010), *Invited paper*.
- [3] H.-P. Schlenvoigt, K. Haupt, A. Debus, F. Budde, O. Jäckel, S. Pfotenhauer, H. Schwöerer, E. Rohwer, J. G. Gallacher, E. Brunetti, R. P. Shanks, S. M. Wiggins, and D. A. Jaroszynski, "A compact synchrotron radiation source driven by a laser-plasma wakefield accelerator," *Nature Physics* **4**, 130 (2008)
- [4] H.-P. Schlenvoigt, K. Haupt, A. D. Debus, F. Budde, O. Jäckel, S. Pfotenhauer, J. G. Gallacher, E. Brunetti, R. P. Shanks, S. M. Wiggins, D. A. Jaroszynski, E. Rohwer, and H. Schwöerer, "Synchrotron Radiation From Laser-Accelerated Monoenergetic Electrons," *IEEE Transactions on Plasma Science* **36**, 1773–1781 (Aug. 2008)
- [5] J. G. Gallacher, M. P. Anania, E. Brunetti, F. Budde, A. D. Debus, B. Ersfeld, K. Haupt, M. R. Islam, O. Jäckel, S. Pfotenhauer, A. J. W. Reitsma, E. Rohwer, H.-P. Schlenvoigt, H. Schwöerer, R. P. Shanks, S. M. Wiggins, and D. A. Jaroszynski, "A method of determining narrow energy spread electron beams from a laser plasma wakefield accelerator using undulator radiation," *Physics of Plasmas* **16**, 093102 (2009)
- [6] A. Debus, S. Bock, M. Bussmann, T. E. Cowan, A. Jochmann, T. Kluge, S. D. Kraft, R. Sauerbrey, K. Zeil, and U. Schramm, "Linear and Non-Linear Thomson-Scattering X-Ray Sources Driven by Conventionally and Laser Plasma Accelerated Electrons," *Proc. of SPIE* **7359**, 735908 (2009)
- [7] A. Debus and M. Bussmann, "Erzeugung kurzweiliger ultrakurzer Lichtpulse und deren Verwendung," Patent application: DE 10 2010 028994.9 (May 2010)
- [8] A. Debus, "Electron bunch duration measurements - Results from ASTRA," Annual Report of the Institute of Optics and Quantum Electronics, Friedrich-Schiller-University Jena (2005)
- [9] R. Lauck, V. Dangendorf, K. Tittelmeier, A. D. Debus, S. Pfotenhauer, K.-U. Amthor, R. Sauerbrey, D. Vartsky, and I. Mor, "Radiography with a Terawatt Laser γ -Source," *Optical Society of America*, 10–11(2006)
- [10] S. Karsch, Z. Major, R. Hörlein, L. Veisz, K. Schmid, J. Schreiber, K. Witte, S. Jamison, JG Gallacher, DA Jaroszynski, C. D. Murphy, M. C. Kaluza, A. D. Debus, H. Schwöerer, R. Sauerbrey, U. Schramm, B. Hidding, S. Kiselev, R. Heathcote, P. S. Foster, D. Neely, E. J. Divall, C. J. Hooker, J. M. Smith, K. G. Ertel, A. J. Langley, and J. L. Collier, "Time-resolved THz emission from laser-accelerated electron bunches," *Central Laser Facility Annual Report*, 30–33(2006)

- [11] F. Budde, A. Debus, H.-P. Schlenvoigt, K. Haupt, H. Schwoerer, E. Brunetti, J. Gallacher, R. Shanks, and D. Jaroszynski, "Undulator Radiation based on laser-accelerated electrons," Annual Report of the Institute of Optics and Quantum Electronics, Friedrich-Schiller-University Jena (2006)
- [12] H. Schwoerer, H. P. Schlenvoigt, K. Haupt, A. Debus, E. Rohwer, J. Gallacher, R. Shanks, and D. Jaroszynski, "An All-Optical Synchrotron Light Source," in *Ultrafast Phenomena XVI*, Springer Series in Chemical Physics, Vol. 92 (Springer Berlin Heidelberg, 2009) pp. 813–815
- [13] H. Burau, R. Widera, W. Hönig, G. Juckeland, A. Debus, T. Kluge, U. Schramm, T. E. Cowan, R. Sauerbrey, and M. Bussmann, "PICongPU: A fully relativistic particle-in-cell code for a GPU cluster," *IEEE Transactions on Plasma Science* **38**, 2831–2839 (2010)

CONFERENCE PRESENTATIONS BY THE AUTHOR

- [1] A. D. Debus, "Radiation from ultrashort electron bunches as source and diagnostic," **Talk** given at ENLITE 2009 – Exchange on Laser-Plasma Interaction Theory – Forschungszentrum Dresden-Rossendorf, Germany (Apr. 2009)
- [2] A. D. Debus, M. Bussmann, U. Schramm, R. Sauerbrey, C. D. Murphy, Zs. Major, R. Hörlein, L. Veisz, K. Schmid, J. Schreiber, K. Witte, S. P. Jamison, J. G. Gallacher, D. A. Jaroszynski, M. C. Kaluza, B. Hidding, S. Kiselev, R. Heathcote, P. S. Foster, D. Neely, E. J. Divall, C. J. Hooker, J. M. Smith, K. Ertel, A. J. Langley, P. Norreys, J. L. Collier, and S. Karsch, "All-optical Femtosecond Bunch Length Measurement of Laser-accelerated Electron Beams," **Talk** given at ULIS 2009 – Ultra-intense Laser Interactions Science 2009, INFN – Laboratori Nazionali di Frascati, Italy (May 2009)
- [3] A. D. Debus, M. Bussmann, U. Schramm, R. Sauerbrey, C. D. Murphy, Zs. Major, R. Hörlein, L. Veisz, K. Schmid, J. Schreiber, K. Witte, S. P. Jamison, J. G. Gallacher, D. A. Jaroszynski, M. C. Kaluza, B. Hidding, S. Kiselev, R. Heathcote, P. S. Foster, D. Neely, E. J. Divall, C. J. Hooker, J. M. Smith, K. Ertel, A. J. Langley, P. Norreys, J. L. Collier, and S. Karsch, "Electron bunch length measurements from laser-accelerated electrons using single-shot THz time-domain interferometry," **Talk** given at the TR18-Meeting, Bad Breisig, Germany (Mar. 2010)
- [4] A. D. Debus, M. Bussmann, U. Schramm, R. Sauerbrey, C. D. Murphy, Zs. Major, R. Hörlein, L. Veisz, K. Schmid, J. Schreiber, K. Witte, S. P. Jamison, J. G. Gallacher, D. A. Jaroszynski, M. C. Kaluza, B. Hidding, S. Kiselev, R. Heathcote, P. S. Foster, D. Neely, E. J. Divall, C. J. Hooker, J. M. Smith, K. Ertel, A. J. Langley, P. Norreys, J. L. Collier, and S. Karsch, "Electron bunch length measurements from laser-accelerated electrons using single-shot THz time-domain interferometry," **Talk** given at the DPG Frühjahrstagung Hannover (Mar. 2010)
- [5] A. Debus, M. Bussmann, A. Jochmann, M. Siebold, T. Cowan, U. Schramm, and R. Sauerbrey, "Experimental challenges of Traveling-wave Thomson Scattering," **Poster** presented at the 32nd International Free Electron Laser Conference, Malmö, Sweden (Aug. 2011)
- [6] A. Debus, M. Bussmann, A. Jochmann, M. Siebold, T. Cowan, U. Schramm, and R. Sauerbrey, "Traveling-wave Thomson scattering for scaling optical undulators towards the FEL

regime," **Poster** presented at the 32nd International Free Electron Laser Conference, Malmö, Sweden (Aug. 2011)

- [7] A. Debus, S. Bock, M. Bussmann, T. E. Cowan, A. Jochmann, T. Kluge, S. D. Kraft, R. Sauerbrey, K. Zeil, and U. Schramm, "Traveling-wave Thomson scattering: a source of X-ray photons with high per-shot yield and tunable energy and bandwidth," **Talk** given at the Optics + Optoelectronics 2011, Prague, Czech Republic (Apr. 2011)
- [8] A. Debus, K. Steiniger, M. Siebold, A. Jochmann, A. Irman, M. Bussmann, U. Schramm, T. Cowan, and R. Sauerbrey, "Long optical undulators with Traveling-Wave Thomson Scattering," **Talk** given at the DPG Frühjahrstagung Münster (Mar. 2011)
- [9] A. Debus, M. Bussmann, U. Schramm, R. Sauerbrey, and S. Karsch, "Duration measurement of laser-accelerated electron bunches using single-shot THz time-domain interferometry," **Poster** presented at the DPG Frühjahrstagung Münster (Mar. 2011)
- [10] A. Debus, K. Steiniger, M. Siebold, A. Jochmann, A. Irman, M. Bussmann, U. Schramm, T. Cowan, and R. Sauerbrey, "Experimental challenges of Traveling-wave Thomson Scattering," **Poster** presented at the DPG Frühjahrstagung Münster (Mar. 2011)
- [11] A. Debus, K. Steiniger, M. Siebold, A. Jochmann, A. Irman, M. Bussmann, U. Schramm, T. Cowan, and R. Sauerbrey, "Traveling-wave Thomson Scattering towards tunable, high-yield sources in the hard X-ray range," **Talk** given at the DPG Frühjahrstagung Kiel (Mar. 2011)
- [12] A. Debus, K. Steiniger, M. Siebold, A. Jochmann, A. Irman, M. Bussmann, U. Schramm, T. Cowan, and R. Sauerbrey, "Design and scaling considerations of Traveling-wave Thomson sources," **Poster** presented at the DPG Frühjahrstagung Kiel (Mar. 2011)
- [13] A. Debus, K. Steiniger, M. Siebold, A. Jochmann, A. Irman, U. Schramm, T. Cowan, R. Sauerbrey, and M. Bussmann, "Long optical undulators with Traveling-Wave Thomson Scattering towards tunable, high-yield sources in the hard X-ray range," **Talk** given at RREPS 2011 – Radiation from Relativistic Electrons in Periodic Structures, Royal Holloway, University of London, UK (Sep. 2011)

ACKNOWLEDGEMENT

Research seldom happens in isolation - instead, Physics is done by many people and I would like to thank all that have accompanied or guided me towards the completion of this work.

First of all I would like to thank Prof. Roland Sauerbrey for the opportunity to work on this exciting field of laser-plasma physics from so many different aspects and angles. Despite busy schedules, he manages to make time available for his students. It is always great fun to talk with him about physics and as a student it is almost impossible to leave his office without a new challenge.

I am grateful to our institute leaders Prof. Ulrich Schramm for his support and advice, as well as to Prof. Tom Cowan, whose enthusiasm and passion for dense plasma physics is dangerously contagious.

Most of my scientific sparring-matches were done with my main supervisor Michael Bussmann who passionately loves fighting against group-think, but for clarity and brevity in physics. He extended my theoretical profile, taught me about supercomputing and has shown me a great deal about academic politics. Also I would like to express my gratitude to Arie Irman and Mathias Siebold for the many fruitful discussions.

I would like to thank the entire "laser-plasma gang" for making research possible at a world-class level in a friendly, inspiring atmosphere and in general for a good time that among the professional concerns included: cake & coffee, grilling sessions and shared weekend activities. In no particular order I would like to call: Thomas Kluge (thanks also for enduring me in office), Karl Zeil, Axel Jochmann, Jurjen Couperus, Josephine Metzkes, Stephan Kraft, Markus Löser, Stefan Bock, Uwe Helbig, Wolfgang Seidel, Trevor Burris-Mog, Lingen Huang, René Widera, Lukas Zühl, Fabian Röser, Bhuvanesh Ramakrishna, Christoph Erler, Tom Richter, Franziska Kroll and of course the next generation: Klaus Steiniger, Axel Hübl, Richard Pausch, Omid Zarini, Anne Seidel, Anton Helm and Heiko Burau.

In case of problems with the HPC cluster or software equipment I always found help from Henrik Schulz, Matthias Schlett and Niels SchmeiSSer. Also, I want to express my gratitude to our secretary and administrative staff Petra Neumann, Anne Liebezeit, Franka Seifert and Katrin Thiele for the organizational support, all the paper work and realizing swift orders to optics companies.

I would like to thank my former supervisor Prof. Heinrich Schwoerer who guided my experimental work in Jena. It has been a pleasure to work with Enrico Brunetti, Fabian Budde and Jordon Gallacher at the construction of the undulator experiment. I am grateful to my former colleagues Hans-Peter Schlenvoigt, Kerstin Haupt, Sebastian Pfoth and Oliver Jäckel. In a combined effort of extended and grueling measurement campaigns, we finally saw light at the end of the undulator. Hereby, it cannot be emphasized enough that without the great technical support of Burgard Beleites, Falk Ronneberger and Wolfgang Ziegler the experiments would not have been possible. Special thanks go to Prof. Dino Jaroszynski for his continuous interest in the current experimental status.

Prof. Ken Ledingham, an avid fan of laser-driven nuclear physics (and golf), was a regular visitor both in Jena and Dresden. I would like to thank him for his long-standing support, his friendly advice and the refreshing discussion about the big lines of research.

It is an honor for me to thank Prof. Stefan Karsch and his team at MPQ in Garching and the other collaborators for the opportunity to participate at his electron bunch duration measurement campaign at the Rutherford Appleton Laboratories (UK). I found it remarkable how readily he and his team included me in the experiment and subsequent analysis.

Special thanks go to Prof. Michael Downer from the University of Texas at Austin – without his skills in advertisement and persuasion at the very beginning of my research activities I would not have gone into this wonderful, diverse mess which is laser-plasma physics.

Finally, I want to thank my parents for their encouragement at all times, for providing logistical and organizational help and in general their unconditional support in this and so many other endeavors before.

Thank you!

EIDESSTATTLICHE ERKLÄRUNG

Hiermit versichere ich, Alexander Alfred Darius Debus, geboren am 23.5.1980 in Heilbronn-Neckargartach, im Rahmen meines Promotionsverfahrens an der Fakultät Mathematik und Naturwissenschaften der Technischen Universität Dresden und an Eides statt, dass

1. ich die vorliegende Arbeit ohne unzulässige Hilfe Dritter und ohne Benutzung anderer als der angegebenen Hilfsmittel angefertigt habe; die aus fremden Quellen direkt oder indirekt übernommenen Gedanken sind als solche kenntlich gemacht. Die Arbeit wurde bisher weder im Inland noch im Ausland in gleicher oder ähnlicher Form einer anderen Prüfungsbehörde vorgelegt.
2. ich die vorliegende Arbeit am Helmholtz-Zentrum Dresden-Rossendorf am Institut für Strahlphysik unter der wissenschaftlichen Betreuung von Prof. Roland Sauerbrey angefertigt habe.
3. mir die geltende Promotionsordnung (Stand 23.02.2011, Fakultät Mathematik und Naturwissenschaften der TU Dresden) bekannt ist und ich diese anerkenne.

Dresden, 7. Oktober 2011



Postfach 51 01 19
01314 Dresden
Tel. +49 351 260-2619
Fax +49 351 260-3700
a.debus@hzdr.de
<http://www.hzdr.de>